

**CONSTRUCTION MONITORING, LABORATORY TESTING,  
AND FINITE ELEMENT ANALYSIS  
TO EVALUATE REUSE POTENTIAL  
OF STRUCTURAL STEEL**

by

Philipp Keller

A dissertation submitted to the Faculty of the University of Delaware  
in partial fulfillment of the requirements for the degree of  
Doctor of Philosophy in Civil Engineering

Spring 2019

© 2019 Philipp Keller  
All Rights Reserved

**CONSTRUCTION MONITORING, LABORATORY TESTING,  
AND FINITE ELEMENT ANALYSIS  
TO EVALUATE REUSE POTENTIAL  
OF STRUCTURAL STEEL**

by

Philipp Keller

Approved: \_\_\_\_\_

Sue McNeil, Ph.D.

Chair of the Department of Civil & Environmental Engineering

Approved: \_\_\_\_\_

Levi T. Thompson, Ph.D.

Dean of the College of Engineering

Approved: \_\_\_\_\_

Douglas J. Doren, Ph.D.

Interim Vice Provost for Graduate and Professional Education

I certify that I have read this dissertation and that in my opinion it meets the academic and professional standard required by the University as a dissertation for the degree of Doctor of Philosophy.

Signed:

---

Jennifer Righman McConnell, Ph.D.  
Professor in charge of dissertation

I certify that I have read this dissertation and that in my opinion it meets the academic and professional standard required by the University as a dissertation for the degree of Doctor of Philosophy.

Signed:

---

Harry W. Shenton III, Ph.D.  
Member of dissertation committee

I certify that I have read this dissertation and that in my opinion it meets the academic and professional standard required by the University as a dissertation for the degree of Doctor of Philosophy.

Signed:

---

Thomas Schumacher, Ph.D.  
Member of dissertation committee

I certify that I have read this dissertation and that in my opinion it meets the academic and professional standard required by the University as a dissertation for the degree of Doctor of Philosophy.

Signed:

---

Erik T. Thostenson, Ph.D.  
Member of dissertation committee

## **ACKNOWLEDGMENTS**

I would like to express my deepest appreciation to my advisor Dr. Jennifer McConnell for offering me this great opportunity. Your patience and encouragement during this entire time were vital to my success. I will always cherish you as a great role model who found the perfect balance between academic excellence, personal life, and great advising. Thank you for everything!

I would also like to extend my sincere thanks to my committee members Dr. Thomas Schumacher, Dr. Erik Thostenson, and Dr. Tripp Shenton. Your questions, advice, and comments were instrumental in making me the researcher I am today. I am humbled by your knowledge and your modesty.

This dissertation would not have been possible without the support of the National Science Foundation.

I would like to acknowledge the assistance of the University of Delaware Facilities and Auxiliary Services (namely Peter Krawchyk, Marcia Hutton, and Brian Saint), project managers at Whiting Turner (particularly Greg Ritter, Ian Wood, and Dan Maniscalco), Craig Sams from Bancroft Construction, and personnel at RC Fabricators, Mid-Atlantic Steel, and East Coast Erectors. Special thanks to Melissa Boulden of Mid-Atlantic Steel who was instrumental during the construction monitoring phase of this project.

The completion of this research project and dissertation would not have been possible without the support and boundless technical knowledge of Gary Wenczel. When I started at UD you were our lab manager, and now you are my office mate and

friend. I will always remember our instrumentation field trips, and us digging through the fireproofing in the BPI Building to relocate those darn nodes. Thank you for the help, the friendship, and the beer!

Many thanks to Michael Davidson for your help with electrical circuits and for all the things you do for the students in DuPont Hall. I'm not sure if this place would run without you.

I am also grateful to my lab group for their help and support during this project. Specifically, Tayler Wennick, Shafique Ahmed, Matija Radovic, Hongbo Dai, Tian Bai, Asmaa Abo Alouk, Megan Beachy, and JT Rupp, you were there when I needed help in the lab and in the field or when I needed academic advice. For that I thank you.

Particularly helpful to me during this time as a PhD student were our main office staff. Chris Reoli, Sarah Palmer, Christine Murray, Marikka Beach, and Karen Greco. Thank you for all the emails, the reminders and the organized events. My time at UD would have been much more complicated without your help.

Many thanks to all my friends that supported me during my graduate school time. Sabine, Jonas, Manuel, Nadine, Samuel, Renate, Mike, and Barbara, thank you for staying in contact with me during all this time away from Switzerland. It is great to know you have wonderful friends across the ocean. To my West Coast friends, Liz, Jeff, Amanda, Hugh, Lisa, Kirk, Francisco, and Joelyn, thank you for the hospitality, conversations, and the support whenever Keely and I are in town. To my Lehigh friends, Frank, Courtney, Ellen, Aly, and Vasileios, leaving Lehigh wasn't an easy decision but I cherish the friendship we built during that "short" time. Thank you for the good memories. To my two roommates, Danielle and Jil, thank you for your

friendship and for keeping the house in good shape! To my UD offices mates, Ali, Hadi, Omar, Arsha, Matt, Andrew, Matija, Shafique, and Cortney, thank you for the great discussions, and the friendship. You guys made my time here at UD fly by.

Very special thanks to Rachel and Dave Riley. When Keely and I came to UD we didn't know very many people. You barely knew us but still invited us to your wedding and the rest is history. Thank you for the many great memories and thank you for the support.

More special thanks to Kelsea and Thomas Schumacher. You two are the reason for me being in the United States getting my PhD! Not only did you convince me to take the leap and get my master's degree in Corvallis, you introduced me to my wife, you convinced us to move to Delaware, and you let us live with you for a year! No words can express how thankful I am for everything you have done for me.

I would like to extend my deepest appreciation to my parents Ursula and Martin Keller and my sister Beatrice and her family, Dominik, Timo, and Jan Schmucki for letting me make my own decisions and for letting me figure out my own path even when it meant not seeing each other for extended periods of time. The last eight years have been the best but also hardest years of my life. I will never forget your support, your kind words, your advice, and of course the never-ending supply of Swiss chocolate and cheese. I love and miss you all very much!

I am also extremely grateful to my American family (Natasha and Brian Heintz and Megan, Justin and Marlowe Wilson) for welcoming me with open arms. I would have never thought I'd be supported so well by anyone besides my immediate family. Boy, was I wrong! I found an entire family that provided the necessary encouragement to complete a task like this. #blessed

I cannot begin to express my thanks to my wife Keely Ann Keller, who has been my steady rock (in a pretty rough sea at times) for the past 8 years. Since we met at OSU, you have been by my side every step of the way and you have supported me in every way possible. Here at UD, I got to marry you three times, which was probably the smartest thing I did during my entire PhD! You are the smartest, most loving, and most caring person I know and I don't know how I got that lucky to have you in my life. I am so thankful for you and I cannot wait to raise our first baby together! I love you very much!

Finally, I would like to recognize the assistance and support of Miss Coco Chanel Mademoiselle Keller and Miss Sterling Florence Keller. Both of you have kept me going during the last couple weeks of writing this dissertation with your boundless energy!



## **DEDICATION**

I would like to dedicate this dissertation to all my grandparents. Some of you I have never met which pains me. Some of you had to leave during my time at UD which makes me sad, but I'm so glad I had you in my life. Finally, I'm very happy that I get to spend some more time with my three sweet grandmas, Charlotte Gerber, Nelly Keller and Carol Heintz. Thank you all for the encouraging words and for always being there for me.

In loving memory:

Otto Gerber

Hanspeter Keller

June Slangal

Henry (Hank) Slangal

Robert Heintz

## TABLE OF CONTENTS

LIST OF TABLES .....	xiv
LIST OF FIGURES .....	xvi
ABSTRACT .....	xxii

### Chapter

1	REUSE OF STRUCTURAL STEEL .....	1
1.1	Motivation .....	1
1.1.1	Reducing the Environmental Impact of Steel.....	1
1.1.2	Climate Change .....	3
1.1.3	Influence of Structural Steel Production on Climate Change .....	5
1.1.4	Influence of Recycled Steel on Climate Change.....	6
1.1.5	Reuse of Structural Steel .....	8
1.1.6	Concerns about the Reuse of Structural Steel .....	9
1.2	Research Objectives .....	10
1.3	Scope and Organization.....	11
2	LITERATURE REVIEW.....	14
2.1	Reuse of Structural Steel .....	14
2.2	Construction Stress Evaluation in Structural Steel Members.....	16
2.3	Carbon Nanotube-Based Sensing Skin.....	16
2.4	Finite Element Analysis of Structural Steel Building Connections .....	18
3	CONSTRUCTION MONITORING .....	22
3.1	Wireless Sensor Network .....	22
3.2	General Data Analysis Process.....	24
3.2.1	Data Collection .....	25
3.2.2	Data Cleaning .....	25
3.2.2.1	General Procedure .....	26
3.2.2.2	Data Cleaning of Selected Strain Gauge Data.....	28

3.2.3	Initial Dead Load .....	29
3.2.4	Sustained Versus Impact Categorization.....	30
3.2.5	Member Force Calculation .....	31
	3.2.5.1 Three-Gauge Approach .....	31
	3.2.5.2 Optimization Approach .....	32
3.2.6	Data Analysis Considering Temperature Effects .....	35
3.3	Instrumented Buildings .....	39
	3.3.1 Purnell Hall Addition .....	40
	3.3.1.1 Building Information .....	40
	3.3.1.2 Instrumentation.....	41
	3.3.1.3 Field Data Collection.....	47
	3.3.1.4 Results .....	49
	3.3.1.4.1 Maximum Sustained and Impact Stress Results .....	50
	3.3.1.4.2 Stress Data by Construction Phases .....	55
	3.3.1.4.3 Member Forces Results .....	61
	3.3.1.4.4 Evaluation of Member Forces .....	65
	3.3.2 STAR Tower .....	69
	3.3.2.1 Building Information .....	69
	3.3.2.2 Instrumentation.....	70
	3.3.2.3 Field Data Collection.....	74
	3.3.2.4 Results .....	76
	3.3.2.4.1 Maximum Sustained and Impact Stress Results .....	76
	3.3.2.4.2 Member Forces Results .....	81
	3.3.2.4.3 Evaluation of Member Forces .....	83
	3.3.3 BPI Building.....	85
	3.3.3.1 Building Information .....	85
	3.3.3.2 Instrumentation.....	86
	3.3.3.3 Field Data Collection.....	93
	3.3.3.4 Results .....	94

3.3.3.4.1	Maximum Sustained and Impact Stress Results .....	94
3.3.3.4.2	Member Forces Results .....	100
3.3.3.4.3	Evaluation of Member Forces .....	103
3.4	Field Data Comparison.....	105
3.4.1	Stress Data Comparison .....	105
3.4.2	Member Force Comparison.....	106
3.5	Field Data Conclusions.....	109
4	CARBON NANOTUBE-BASED SENSOR.....	112
4.1	Sensor Fabrication .....	113
4.2	Sensor Location .....	114
4.3	Connecting the Sensing Skin to the Circuit Board Box .....	115
4.4	Field Installation of the Sensing Skin at the Steel Fabricator .....	118
4.5	Carbon Nanotube-Based Sensor Results .....	122
4.5.1	Sensing Skin Field Data Results.....	123
4.5.2	Comparison of Sensing Skin Data to Conventional Strain Gauge Data .....	125
4.6	Carbon nanotube-based sensor Conclusions .....	129
5	LABORATORY TESTING .....	131
5.1	Selection of Connection Detail for the Laboratory Test Setup .....	131
5.2	Laboratory Test Setup .....	133
5.2.1	Strain and Displacement Instrumentation .....	136
5.2.1.1	Angle Connection Section .....	139
5.2.1.2	Beam Start Section .....	140
5.2.1.3	Beam Connection Section .....	141
5.2.1.4	Beam Middle Section .....	142
5.2.1.5	Beam End Section .....	143
5.2.2	Carbon Nanotube-Based Sensing Skin Installation on the Test Setup Beam.....	144
5.3	Load Tests .....	148
5.3.1	Axial Load Test Setup Configuration.....	149

5.3.2	Strong Axis Bending Test Setup Configuration .....	150
5.3.3	Weak Axis Bending Test Setup Configuration .....	151
5.4	Test Results .....	152
5.4.1	Axial Force Tests.....	153
5.4.2	Strong Axis Bending Tests.....	155
5.4.3	Weak Axis Bending Tests .....	159
5.5	Conclusion.....	160
6	FINITE ELEMENT ANALYSIS .....	161
6.1	Finite Element Model Overview .....	162
6.1.1	Parts and Mesh .....	163
6.1.2	Materials .....	167
6.1.3	Boundary Conditions and Interactions .....	171
6.1.4	Steps and Applied Loads.....	174
6.2	Finite Element Model Validation .....	175
6.2.1	Axial Load.....	177
6.2.2	Strong Axis Load (Strong Axis Bending) .....	178
6.2.3	Weak Axis Load (Weak Axis Bending).....	181
6.2.4	Influence of Bolt Pretension Load and Friction Coefficient .....	184
6.3	Connection Field Data Evaluation Using the Finite Element Model ....	191
6.4	Finite Element Analysis Conclusions.....	197
7	SUMMARY AND CONCLUSIONS.....	200
7.1	Summary.....	200
7.1.1	Field Data Summary.....	200
7.1.2	Carbon Nanotube-Based Sensor Summary .....	202
7.1.3	Laboratory Test Setup Summary.....	203
7.1.4	Finite Element Analysis Summary .....	204
7.2	Conclusions .....	205
7.3	Lessons Learned .....	207
7.3.1	Instrumental Steps Taken for the Building Instrumentation .....	207
7.3.2	Lessons Learned After the Instrumentation .....	210

7.4 Future work .....	211
REFERENCES .....	213
Appendix	
COPYRIGHT RELEASE FORM FOR USED FIGURES .....	219

## LIST OF TABLES

Table 3.1:	Maximum and minimum threshold temperatures for data processing purposes.....	27
Table 3.2:	Details of instrumented Purnell Hall Addition members .....	43
Table 3.3:	Summary of sustained Purnell Hall member stress data .....	52
Table 3.4:	Summary of sustained Purnell Hall connection area stress data .....	55
Table 3.5:	Construction phase member stress data summary.....	57
Table 3.6:	Construction phase connection area stress data summary.....	60
Table 3.7:	Applied member forces and moments relative to multi-axial yield criteria.....	68
Table 3.8:	Details of instrumented STAR Tower members .....	71
Table 3.9:	Summary of sustained STAR Tower member stress data.....	78
Table 3.10:	Summary of sustained STAR Tower connection area stress data.....	80
Table 3.11:	Applied member forces and moments relative to multi-axial yield criteria for the STAR Tower .....	84
Table 3.12:	Details of instrumented BPI Building members.....	89
Table 3.13:	Summary of strain gauges with reduced data.....	96
Table 3.14:	Summary of sustained BPI Building member stress data .....	98
Table 3.15:	Summary of sustained BPI Building connection area stress data .....	100
Table 3.16:	Applied member forces and moments relative to multi-axial yield criteria for the BPI Building.....	104
Table 4.1:	Resistance values of sensing skin voltage breaker resistors.....	117
Table 5.1:	Material properties of the laboratory test setup parts .....	135

Table 5.2:	Uniaxial strain gauge instrumentation label details .....	137
Table 5.3:	Rosette strain gauge instrumentation label details .....	138
Table 5.4:	Displacement sensors instrumentation label details .....	138
Table 5.5:	Strain gauge information .....	138
Table 5.6:	Displacement sensor information .....	139
Table 6.1:	Material properties of FEM parts .....	168
Table 6.2:	Beam constitutive model (A992) .....	169
Table 6.3:	Bolt Constitutive Model (A325).....	170
Table 6.4:	Plate material properties (A36) .....	170
Table 6.5:	FEM result summary .....	196

## LIST OF FIGURES

Figure 1.1:	Highest to lowest environmental friendly uses of a material (adapted from Themelis and Mussche, 2014) .....	2
Figure 1.2:	U.S. Greenhouse gases in percentage of CO <sub>2</sub> equivalent by gas in 2016 (figure from USEPA, 2018) .....	4
Figure 1.3:	U.S. CO <sub>2</sub> Eq. emission sources in 2016 (figure from USEPA, 2018) 1 MMT = 1,102,311 ton .....	5
Figure 1.4:	Estimated U.S. steel shipments by market classification in 2017 (figure from AISI, 2018) .....	6
Figure 1.5:	Energy consumption in the U.S. by source in 2012, (figure from USEPA, 2018) .....	7
Figure 1.6:	Current and targeted demolition practice of structural steel buildings. (Figure by Dr. Thomas Schumacher) .....	8
Figure 3.1:	Schematic of wireless sensing network (WSN), only one node shown for simplicity .....	23
Figure 3.2:	Photograph of instrumented steel members at the fabrication facility ....	24
Figure 3.3:	Member forces acting on the Purnell Hall Addition Short Column .....	33
Figure 3.4:	Example strain gauge data for the Purnell Hall Addition Long Column showing temperature influence on data .....	38
Figure 3.5:	Purnell Hall Addition steel frame with instrumented members highlighted and named (Adapted from RC Fabricators Inc.) .....	42
Figure 3.6:	Long Column instrumentation drawing .....	45
Figure 3.7:	Short Column instrumentation drawing .....	45
Figure 3.8:	Cantilever instrumentation drawing .....	46
Figure 3.9:	Girder instrumentation drawing .....	46

Figure 3.10: Beam instrumentation drawing .....	47
Figure 3.11: Construction site camera image .....	48
Figure 3.12: Sample field monitoring data (bottom of Long Column), 100 MPa = 14.4 ksi .....	49
Figure 3.13: Overall maximum data, including impact values and maximum sustained data for the Purnell Hall Addition member strain gauges .....	51
Figure 3.14: Overall maximum data, including impact values and maximum sustained data for the Purnell Hall Addition connection area strain gauges .....	54
Figure 3.15: Sustained member stress data during different construction phases .....	56
Figure 3.16: Sustained connection area stress data during different construction phases .....	59
Figure 3.17: Overall maximum sustained RTE axial force data.....	62
Figure 3.18: Overall maximum sustained RTE bending moment data.....	63
Figure 3.19: Theoretical stress data (STAAD) compared to final hour field data.....	65
Figure 3.20: STAR Tower steel frame with instrumented members highlighted and named (Adapted from Mid Atlantic Steel, LLC) .....	70
Figure 3.21: STAR Tower Column instrumentation drawing .....	72
Figure 3.22: STAR Tower Girder instrumentation drawing.....	73
Figure 3.23: STAR Tower Beam instrumentation drawing.....	73
Figure 3.24: Construction site camera image of the construction progress on June 19, 2017 .....	74
Figure 3.25: STAR Tower Girder strain gauge data for the entire data collection period.....	75
Figure 3.26: Overall maximum data, including impact values and maximum sustained data for the STAR Tower member strain gauges .....	78
Figure 3.27: Overall maximum data, including impact values and maximum sustained data for the STAR Tower connection area strain gauges .....	80

Figure 3.28: Overall STAR Tower maximum sustained RTE axial force data .....	82
Figure 3.29: Overall STAR Tower maximum sustained RTE bending moment data .	83
Figure 3.30: BPI Building steel frame overview with instrumented members highlighted (Adapted from Mid Atlantic Steel, LLC).....	87
Figure 3.31: BPI Building steel frame details with instrumented members highlighted and named (Adapted from Mid Atlantic Steel, LLC) .....	88
Figure 3.32: BPI Building 1 <sup>st</sup> Floor Column instrumentation drawing .....	91
Figure 3.33: BPI Building 2 <sup>nd</sup> Floor Girder instrumentation drawing.....	91
Figure 3.34: BPI Building 2 <sup>nd</sup> Floor Beam instrumentation drawing.....	92
Figure 3.35: BPI Building 5 <sup>th</sup> Floor Column instrumentation drawing.....	92
Figure 3.36: BPI Building 6 <sup>th</sup> Floor Girder instrumentation drawing .....	93
Figure 3.37: Overall maximum data, including impact values and maximum sustained data for the BPI Building member strain gauges.....	97
Figure 3.38: Overall maximum data, including impact values and maximum sustained data for the BPI Building connection area strain gauges .....	99
Figure 3.39: Overall BPI Building maximum sustained RTE axial force data .....	102
Figure 3.40: Overall BPI Building maximum sustained RTE bending moment data	103
Figure 3.41: Overall maximum and minimum stress comparison for the three instrumented buildings .....	106
Figure 3.42: Overall maximum and minimum axial force comparison for the three instrumented buildings .....	107
Figure 3.43: Overall maximum and minimum bending moment comparison for the three instrumented buildings .....	109
Figure 4.1: Carbon nanotube-based sensor with electrode locations.....	114
Figure 4.2: Field instrumentation overview of the sensing skin.....	115
Figure 4.3: Sensing skin circuit diagram .....	116

Figure 4.4: Sensing skin circuit board box (CBB) layout.....	118
Figure 4.5: Sensing skin circuit board box (CBB) in the field .....	118
Figure 4.6: Sensing skin with attached wires (Photo credit: Gary Wenczel) .....	119
Figure 4.7: Placing the sensing skin on the girder on the adhesive layer (Photo credit: Gary Wenczel) .....	120
Figure 4.8: Sensing skin was bonded to the girder using the vacuum bag method (Photo credit: Gary Wenczel).....	121
Figure 4.9: Finished sensing skin on the girder with the CBB and WSN node wired (Photo credit: Gary Wenczel).....	122
Figure 4.10: Sensing skin data overview (WSN node output data).....	124
Figure 4.11: Sensing skin installed in the BPI Building.....	126
Figure 4.12: Strain gauges on the opposite side of the sensing skin.....	126
Figure 4.13: Sensing skin data compared to strain gauged and node temperature data (Data date: 05/15/2018 – 05/16/2018).....	129
Figure 5.1: Location of Girder to Long Column connection in Purnell Hall Addition. (Adapted from RC Fabricators) .....	132
Figure 5.2: Girder to Long Column connection detail including field instrumentation .....	132
Figure 5.3: Schematic of the laboratory test setup (north view).....	134
Figure 5.4: Instrumentation sections of the laboratory test setup (north view) .....	136
Figure 5.5: Angle connection instrumentation section schematic .....	140
Figure 5.6: Angle connection instrumentation.....	140
Figure 5.7: Beam start instrumentation section schematic .....	141
Figure 5.8: Beam connection instrumentation section schematic.....	142
Figure 5.9: Beam middle instrumentation section schematic .....	143
Figure 5.10: Beam end instrumentation section schematic .....	143

Figure 5.11: Adhesive layer application to install the sensing skin.....	144
Figure 5.12: Bonding the sensing skin to the beam using the vacuum bagging method.....	145
Figure 5.13: Installed sensing skin on the start of the beam including electrodes and strain gauges.....	147
Figure 5.14: Final beam end instrumentation with electrically insulated connection angle (north view) .....	148
Figure 5.15: South view of the laboratory test setup, axial load configuration .....	149
Figure 5.16: South view of the manual hydraulic jack, strong axis bending configuration .....	151
Figure 5.17: South view of the laboratory test setup, weak axis bending configuration .....	152
Figure 5.18: Beam connection cross-section stress data for applied axial tension force.....	154
Figure 5.19: Beam middle cross-section stress data for applied axial tension force .	155
Figure 5.20: Beam connection cross-section stress data for applied strong axis bending moment.....	156
Figure 5.21: Beam middle cross-section stress data for applied strong axis bending moment.....	157
Figure 5.22: Beam start displacement data compared to theoretical displacement data for applied strong axis bending moment .....	158
Figure 5.23: Beam connection cross-section stress data for applied weak axis bending moment.....	159
Figure 6.1: Annotated Overview of FEM of the laboratory test setup (isometric view).....	163
Figure 6.2: FEM of the beam with mesh .....	165
Figure 6.3: FEM of the colmun including mesh.....	166
Figure 6.4: FEM of the connection angle including mesh.....	166

Figure 6.5: FEM of the column bolt including mesh.....	167
Figure 6.6: FEM of the beam bolt including mesh .....	167
Figure 6.7: FEM boundary condition and spring element locations.....	172
Figure 6.8: Connection angles and bolt interactions surfaces.....	173
Figure 6.9: Bolt interaction surfaces .....	173
Figure 6.10: Load application locations.....	175
Figure 6.11: FEM validation at the middle of the beam using axial load test results	178
Figure 6.12: Location of displacement sensor and strain gauges for vertical tests....	179
Figure 6.13: Validation of the FEM using vertical displacement test results .....	181
Figure 6.14: Validation of the FEM using horizontal displacement test results.....	183
Figure 6.15: Vertical load laboratory test data compared to FEM data with different beam bolt loads and friction coefficients .....	185
Figure 6.16: Vertical load laboratory test data (top strain gauge data only) compared to FEM data with different beam bolt loads .....	188
Figure 6.17: Vertical load laboratory test data (bottom strain gauge data only) compared to FEM data with different beam bolt loads .....	189
Figure 6.18: Vertical load laboratory test data (middle strain gauge data only) compared to FEM data with different beam bolt loads .....	190
Figure 6.19: Flowchart of the field data extrapolation process using an FEM.....	192
Figure 6.20: Example rows of the superposition matrix.....	193
Figure 6.21: FEM contour plot of von Mises stresses for R10 max model (worst- case loading).....	197
Figure A.1: Copyright release for all figures from (U.S. Environmental Protection Agency (USEPA) 2018).....	220
Figure A.2: Copyright release form for Figure 1.4 (AISI, 2018) .....	221

## **ABSTRACT**

Iron and steel production is responsible for a significant environmental impact, contributing the third highest CO<sub>2</sub> emissions in the United States in 2016. To show one option of shifting towards a more sustainable built environment, this research explores the reuse of structural steel. Reuse of structural steel as primary load members in new buildings is presently rare, despite reduction in CO<sub>2</sub> emissions and other environmental advantages that could be achieved via this practice. The main concern preventing this is the lack of information about the stress history of a steel member during the member's service life. These concerns are most significant during construction, when fit-up issues, temporary loadings, and variable support conditions throughout the construction process may cause force effects to differ from designers' expectations, and in connection areas where localized stress concentrations occur.

To evaluate if a steel member can be reused after its service life, construction-induced strains in three typical steel-framed buildings were recorded. The field data were recorded using strain gauges connected to a wireless sensor network and a novel carbon nanotube (CNT) based sensor. The analysis revealed high variations in temperature throughout the structures and consequently significant temperature-induced stresses as well as greater magnitudes of flexural stress in columns than expected. The maximum measured stress (160 MPa, 23.2 ksi) was only 46% of the nominal yield strength (of 345 MPa, 50 ksi).

A validated FEM was used to extrapolate field stress data to more locations than feasible to physically instrument. This allowed for prediction and assessment of

the maximum stresses in a connection during construction. The FEM was validated using results of a full-scale laboratory test setup. The maximum absolute principal stress in the FEM was 216 MPa (31.4 ksi), 63% of the nominal yield strength. Therefore, collected strain gauge data and extrapolated connection area data indicate no yielding occurred during the construction phase of the instrumented buildings. These field and analytical results indicate that reuse of structural steel members is feasible given that all data collected in this work indicates that the material remains linear elastic during construction, including in connection areas.

# Chapter 1

## REUSE OF STRUCTURAL STEEL

### 1.1 Motivation

#### 1.1.1 Reducing the Environmental Impact of Steel

Climate change is one of the biggest societal concerns and the scientific community agrees that this is mainly a result of excessive emission of greenhouse gases (such as CO<sub>2</sub>) by humans. Furthermore, the production of iron and steel is responsible for the third highest CO<sub>2</sub> emissions in the year 2016 in the United States (USEPA, 2018) and the use of fossil fuels in this production creates additional emissions.

To reduce the impact of any material on the environment, the material (e.g., steel) should be used as shown in the waste management hierarchy in Figure 1.1. Since prevention of using steel is not possible or perhaps desirable in current construction (steel is currently one of the most common building materials), this step is not a viable option for this material. Reduction of steel use is currently achieved by highly researched and efficient design practices, with the help of accurate design software, to obtain efficient structural designs with minimized material use. Recycling is the next best option in the waste management hierarchy. This is well established practice at the current time in the steel industry and, today, steel is the most recycled material (by weight) in the United States (AISC, 2012 and Yellishetty et al., 2011). However, to create new structural steel from recycled steel, energy must be invested,

causing additional greenhouse gases. Energy recovery from steel fabrication is currently employed only in limited areas of the steel fabrication process (i.e. thermal energy of a hot output flow is used to preheat a cold incoming flow (McBrien et al., 2016)), mostly due to high implementation costs for the steel fabricators. However, this is a manufacturing related issue and discussed in more detail by the U.S. Department of Energy Industrial Technologies Program (2008). Disposal of a material has the biggest environmental impact as shown in the waste management hierarchy. However, only 2% of the structural steel is sent to landfills in the United States (AISC, 2012 and Yellishetty et al., 2011). Therefore, reuse of structural steel is presently the area with the most potential to decrease negative environmental effects of the steel industry for civil engineers. Reuse of structural steel is almost nonexistent in the United States, due to a lack of research in this area and therefore a lack of guidelines in the steel design industry.



Figure 1.1: Highest to lowest environmental friendly uses of a material (adapted from Themelis and Mussche, 2014)

In addition to preventing harmful greenhouse gases and therefore reducing climate change, this research will be helpful to design engineers in designing Leadership in Energy and Environmental Design (LEED) certified buildings (USGBC, 2018). LEED certified buildings are internationally recognized for their low environmental impact. The certification program awards points for many different building parameters that are beneficial to the environment, including the reuse of materials (category MR3). The more points awarded to one building, the higher the certification. Therefore, reusing structural steel members will not only lower the carbon footprint of the steel industry but also help design engineers archive LEED certified buildings to fulfill needs of their clients.

### **1.1.2 Climate Change**

The climate of the planet earth has changed. During the past 100 years, the average temperature has increased by 0.78°C (1.4°F) and the average temperature is predicted to increase by another 1.1 to 6.4°C (2.0 to 11.5°F) by 2114. Furthermore, each of the last four years (2015-2018) were the warmest years on record according to (NOAA, 2019). An increased global average temperature results in more severe weather patterns such as floods, heat waves, higher intensity hurricanes, and droughts. Also, due to an increased global average temperature, the world's oceans become warmer, and the ice caps melt, which results in increased sea levels (USEPA, 2016). Climate change is clearly one of the main concerns of the current era.

Climate change is created due to greenhouse gases in the atmosphere that are necessary to maintain a livable climate on earth. Over the past century, humans created enormous amounts of these gases (through industrialization, invention of the

automobile, etc.), which resulted in global warming. The group of greenhouse gases mainly consists of three gases: carbon dioxide (CO<sub>2</sub>), methane (CH<sub>4</sub>), nitrous oxide (N<sub>2</sub>O), and various other gases. All these greenhouse gases have different global warming potentials (GWP). To create comparable results, all the gases are converted into CO<sub>2</sub> equivalents (CO<sub>2</sub> Eq.) of global warming potential. The obtained normalized percentages are shown in Figure 1.2, which clearly shows that CO<sub>2</sub> is the major contributor to the greenhouse gases and thus global warming.

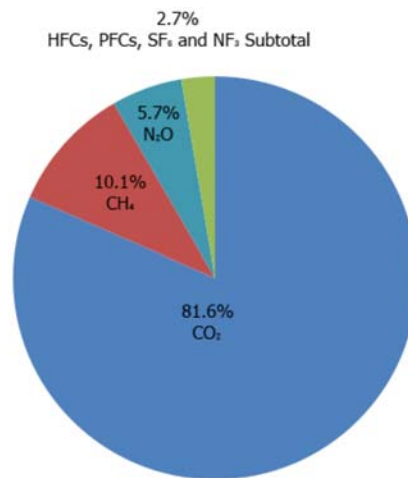


Figure 1.2: U.S. Greenhouse gases in percentage of CO<sub>2</sub> equivalent by gas in 2016 (figure from USEPA, 2018)

The CO<sub>2</sub> emissions shown in Figure 1.2 can be classified by their emission source as shown in terms of CO<sub>2</sub> Eq. global warming potential in Figure 1.3. The figure shows that fossil fuel combustion is by far the biggest CO<sub>2</sub> Eq. emission source. This is followed by non-energy use of fuels (for example production of bitumen or

lubricants) and then by iron and steel production. It should be noted that the CO<sub>2</sub> Eq. emissions for the steel and iron production given in the figure below are from the production process solely (of both recycled steel and steel from virgin iron ore) and do not include the emissions resulting from the energy demands of the processes. Rather, these emissions are included in the fossil fuel combustion category.

**1.1.3 Influence of Structural Steel Production on Climate Change**

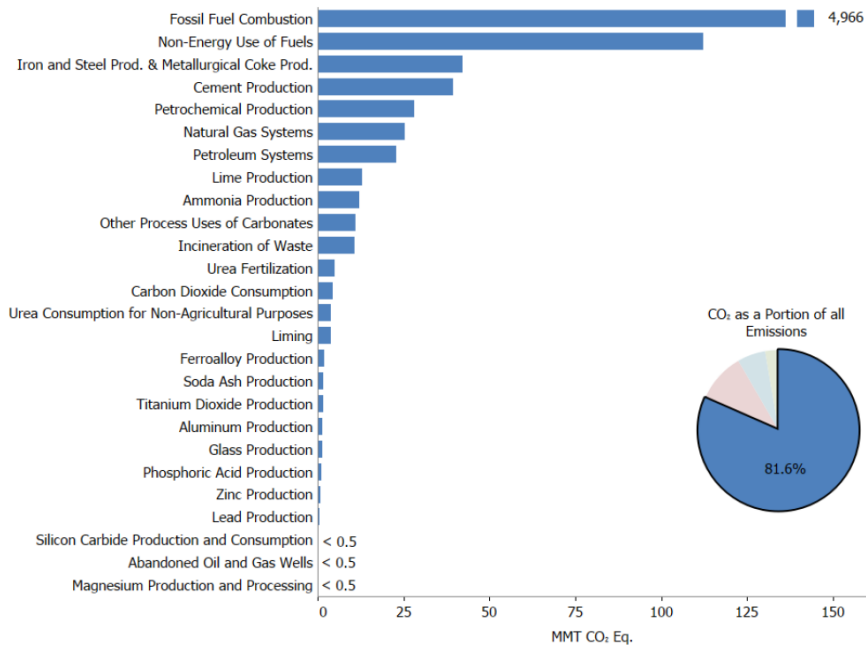


Figure 1.3: U.S. CO<sub>2</sub> Eq. emission sources in 2016 (figure from USEPA, 2018)  
 1 MMT = 1,102,311 ton

Not all of the produced iron and steel is used for structural engineering purposes, as shown in Figure 1.4. However, most of the produced steel is used by the construction industry (40%), followed by the automotive, machinery and equipment,

and energy industries. Therefore, civil engineering applications are the largest sector of steel use and consequently a significant contributor to the overall CO<sub>2</sub> production in the United States and climate change.

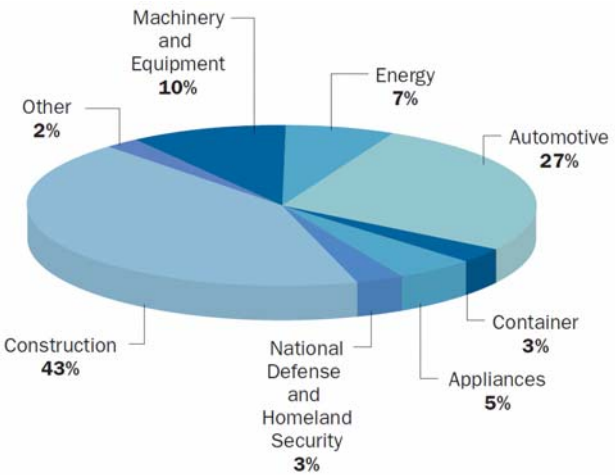


Figure 1.4: Estimated U.S. steel shipments by market classification in 2017 (figure from AISI, 2018)

**1.1.4 Influence of Recycled Steel on Climate Change**

Production of steel from virgin iron ore or from recycled steel requires a large amount of energy. However, recycling of steel is less energy demanding and pollutes the air with fewer greenhouse gases than does creating steel from virgin iron. Creating new steel from recycled steel, however, still requires between 2.52 and 8.57 MWh of energy per metric ton (10 and 34 GJ of energy per ton) of steel (Yellishetty et al., 2011 and New Steel Construction, 2010). Unfortunately, most of this energy comes from non-renewable energy sources, which create addition greenhouse gas emissions and/or other waste as only 9.3% of the produced energy in the United States originates from renewable energy sources as shown in Figure 1.5.

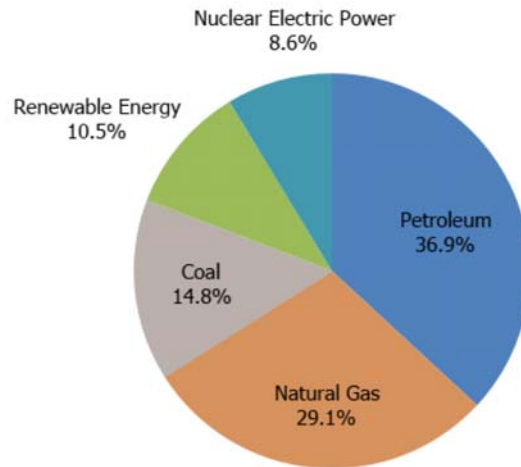


Figure 1.5: Energy consumption in the U.S. by source in 2012, (figure from USEPA, 2018)

Creating hot-rolled sections (which are mainly used as structural members) requires another 0.76 and 1.01 MWh per metric ton (3 to 4 GJ of energy per ton) of steel (Weisenberger, 2010) and creates between 0.76 and 1.94 metric tons of CO<sub>2</sub> per metric ton (0.73 and 2.10 tons of CO<sub>2</sub> per ton) of steel (AISC, 2012; Yellishetty et al., 2011; New Steel Construction, 2010; Weisenberger, 2010; and Webster et al., 2012). Therefore, a total of 3.28 to 9.58 MWh (13 to 38 GJ) are required to produce one metric ton (one ton) of steel while creating between 0.76 and 1.94 metric tons (0.73 and 2.10 tons) of CO<sub>2</sub>. This means, even though steel is the material that is recycled the most in the U.S. (Steel Recycling Institute, 2015), it is still the 3<sup>rd</sup> largest contributor to CO<sub>2</sub> emissions as shown in Figure 1.3, and thus the 3<sup>rd</sup> largest contributor to global warming in the United States.

### 1.1.5 Reuse of Structural Steel

Recycling of steel is a good start towards decreasing CO<sub>2</sub> emissions but there is a great potential left in the steel industry to increase the “greenness” of this material by reusing it before it must be recycled. The current demolition and rebuilding cycle of a steel building is shown in the bottom half of Figure 1.6. Once a building reaches the end of its design life, in most cases it is demolished. In current practice, the demolition process is performed without taking into consideration the possibility of reusing the structural steel. This means the entire building is demolished; the structural steel is sorted out and cut into smaller pieces for easier transportation and recycling purposes. It is then shipped to a recycling facility where the demolished steel is melted and new structural steel sections are produced, using energy and creating CO<sub>2</sub> emissions as mentioned in the previous section. Once the new steel sections are fabricated, they will be used in another new building.

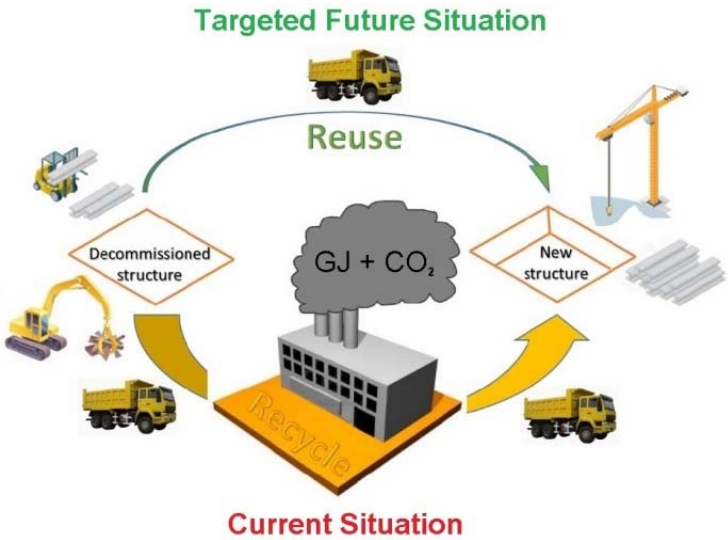


Figure 1.6: Current and targeted demolition practice of structural steel buildings. (Figure by Dr. Thomas Schumacher)

The future situation that is targeted with this project is shown in the top part of Figure 1.6. The demolition process of the old building is done by disassembling the structural steel, rather than demolishing the building. This results in reusable structural steel sections. Once the steel sections are disassembled, they are shipped to a storage facility and/or a fabrication shop to make necessary adjustments (e.g., drill new hole patterns, add stiffeners if necessary). The sections are ultimately shipped to the new building location and used in the new steel structure. This process has the potential of omitting the recycling of structural steel, and therefore reduces the energy consumption and CO<sub>2</sub> pollution caused by steel buildings.

#### **1.1.6 Concerns about the Reuse of Structural Steel**

Considering the environmental advantages of reusing of structural steel, the question arises why this is not already an established practice in the steel industry. This question was answered for the Canadian steel industry in a survey conducted by Gorgolewski et al. (2006). It was found that the major concern of structural engineers was the uncertainties associated with the use of reused structural steel. This research targets this concern. Even though Gorgolewski et al.'s survey was conducted in Canada, it can be assumed that similar results and concerns would be found in the United States.

Gorgolewski et al.'s survey was also given to construction shoring contractors. In the shoring industry, reuse of structural steel is common practice and has not resulted in any problems. Even though shoring is a temporary structure, the occurring construction stresses have a higher variability than in-service stresses. This could be a good indicator for the potential of structural steel reuse in new steel buildings.

The survey also showed that a few fabricators already apply the concept of reused structural steel. In this case, however, the structural steel was only used in secondary support structures due to the lack of appropriate codes or knowledge. This shows that reuse of structural steel is feasible and engineers and fabricators are interested in reusing structural steel. However, the lack of applicable standards limits the use of reused steel in new buildings.

## **1.2 Research Objectives**

To address the concern of structural engineers about the uncertainty associated with reused structural steel and to provide a basis for future standards, this research project evaluated the potential for reuse of structural steel members. The reusability of a structural steel member depends on the peak stresses experienced during its service life. Steel is elastic until the yield stress is reached, and therefore can be reused without concerns as long as the peak stress never exceeds the yield limit. If the peak stresses exceed the yield limit, a more thorough investigation could be warranted. Peak stresses can be accurately predicted (using modern design standards and design software) once the building is built. However, peak stresses during the construction process of a building are more difficult to predict due to random loads, such as fit-up stresses. Fit-up stresses are induced in a structural steel member during erection if the member needs to be forced into its location due to either fabrication tolerances or inexact construction site work. Therefore, peak stresses of structural steel members during construction have to be evaluated. Furthermore, construction-induced peak stresses in connections have to be known if the connection areas of structural steel members are to be reused. To reach these overall goals the following research tasks were pursued:

- Task 1: Monitor structural steel members and connection area stresses during erection of three steel buildings to capture peak construction stresses and to evaluate if the yield limit of the steel members was exceeded during the construction process.
- Task 2: Perform laboratory testing of a beam-to-column connection to validate a finite element model (FEM) of the same connection.
- Task 3: Extrapolate construction stress data collected in the vicinity of the connection using finite element analysis (FEA) to estimate the maximum stress experienced at any point in a connection.

### **1.3 Scope and Organization**

A literature review for the different dissertation tasks was performed and the findings are discussed in Chapter 2. This includes a discussion of the literature on the reuse of structural steel and construction stress evaluation in structural steel members. Next, carbon nanotube-based sensors were briefly reviewed. Finite element analysis of structural steel building connections are also reviewed.

To monitor and evaluate construction stresses during erection, structural steel members of three steel buildings erected on the University of Delaware campus were instrumented using a wireless sensor network. Columns and beams in each building were instrumented with weldable strain gauges and one member was instrumented with a CNT-based sensing skin. The installation of these instruments onto the steel members was performed at the fabrication shop. This ensured that all erection stresses were recorded. In addition, the construction sites were monitored with a camera

installed in the surrounding area of the buildings. These video recordings were used to correlate recorded erection stresses of the instruments with events that occurred on the construction site at the same time. The construction monitoring of the three buildings and the associated results are described in Chapter 3.

As a pilot study, a CNT-based sensing skin was installed to the connection area of a steel member, at the steel fabricator location. The instrumented steel member was placed into one of the instrumented steel buildings and the sensing skin was used to record connection area data during construction. This part of the project is described in Chapter 4.

To validate the finite element model of a connection area, a full-scale laboratory test setup was created. For the test setup, one of the instrumented connections was replicated and densely instrumented. The selected connection was a beam-to-column connection that used two angles as shear connectors. The test setup was instrumented using uniaxial and rosette strain gauges and displacement sensors. Furthermore, a CNT-based sensing skin was installed on the test beam in the connection area. The test setup is described in Chapter 5.

A finite element model of a connection instrumented in one of the buildings was created using the commercial finite element software *ABAQUS* (*ABAQUS*, 2015). The finite element model was focused on a connection area, in which high localized stresses were most likely. The finite element results were used to extrapolate field data from strain gauges installed close to the connection area to all locations within the connection area to determine the peak stresses that likely occurred in the connection during construction. The finite element model and the corresponding results are discussed in Chapter 6.

In the last chapter of this dissertation the research is summarized and conclusions are drawn. Furthermore, the lessons learned from the unique building instrumentation are listed and ideas for future work are given in Chapter 7.

## **Chapter 2**

### **LITERATURE REVIEW**

The literature review is divided into four sections. An overview of reuse of structural steel is given in Section 2.1. Then, each of the remaining sections of the literature review corresponds to one of the research tasks previously defined in Section 1.2. The previously performed research on construction and erection stresses was explored and are summarized in Section 2.2. Section 2.3 focuses on the origin and the current state of practice of CNT-based sensors. Finally, the literature was searched for information on structural building connections modeled using finite element software and the obtained information is presented in Section 2.4.

#### **2.1 Reuse of Structural Steel**

Once a structure has been constructed, with all connections formed and occupied as intended, the governing stresses can be conveniently and reasonably estimated in most cases using established structural engineering calculations. However, one situation where stresses are known with less confidence is during construction, when field conditions such as fit-up issues and temporary loadings may differ from the designers' expectations. Specifically, Gorgolewski et al. (2006) find that the major concern of structural engineers regarding steel reuse is the uncertainties related to the load scenarios during construction. This research directly addresses this concern by providing construction-induced strain data for a typical steel building, a topic for which there are no prior similar studies found in the literature.

Reuse of structural steel has the potential to significantly reduce greenhouse gas emissions resulting from the civil engineering sector (Yellishetty et al., 2011; McConnell et al., 2014). Given the high yield stress relative to other construction materials and elastic properties of steel, reuse is also viable from a structural engineering perspective. LEED standards (USGBC, 2018) acknowledge the environmentally advantageous practice of material reuse by giving credits for it. Therefore, reusing structural steel members helps lower the carbon footprint of the steel and construction industries and aids in achieving LEED certified buildings. The environmental benefits of steel reuse are further demonstrated by the data reported by the American Institute of Steel Construction (2012), New Steel Construction (2010), Pongiglione and Calderini (2014), Webster et al. (2012), Weisenberger (2010), and Winters-Downey (2010). Specifically, a theoretical study performed by Pongiglione and Calderini (2014) shows that up to 30% energy savings and CO<sub>2</sub> reduction can be achieved when reusing steel. Furthermore, Brimacombe et al. (2005) concludes that the sustainability of steel is dependent on future reuse and recycling of today's steel.

More broadly, this study is part of an effort to move the construction industry away from using finite natural resources and mass material disposal in landfills to an industry of deconstruction and reuse as described by Fujita and Iwata (2008). However, availability of reusable material, lack of customer demand, lack of technical guidance, and lack of governmental leadership are other factors which need to be addressed as described by Densley et al. (2017), Dunant et al. (2017) and Cooper and Gutowski (2017). It is also important to develop methods to automatically characterize structural steel members in existing buildings (for example 3D point cloud data) to quantify available steel as demonstrated in Yeung et al. (2015). Furthermore, with

current design practices it is usually less expensive for a demolition contractor to demolish the building and recycle the steel instead of spending more time to deconstruct the building and reuse some of the material. This issue is being addressed by developing new steel connections following the “design for deconstruction” philosophy, such as described in Eckelman et al. (2018), Matis et al. (2018a), Matis et al. (2018b), and Wang et al. (2019).

## **2.2 Construction Stress Evaluation in Structural Steel Members**

An extensive literature search was performed to find information on construction-induced stresses. However, none of the found papers contained information on construction-induced stresses during erection of a conventional multistory steel frame building. Furthermore, no information on fit-up stresses in connections during building erection could be found. Most of the found information centered on erection and construction sequences of bridge girders. However, no information was found on erection or fit-up stresses in bridge girders either. Therefore, the conclusion was drawn that no documented research in this particular area has been performed.

## **2.3 Carbon Nanotube-Based Sensing Skin**

To monitor the connection areas during construction, strain gauges are placed in the vicinity of connections and connection bolts. However, strain gauges only provide data from a very localized spot, and therefore many strain gauges are needed to capture the highly nonlinear stress distribution of a connection area. However, newly developed CNT-based sensors have the potential to be used for this application.

Carbon nanotubes and their different properties have been studied in great detail since their first observation by Iijima (1991) almost three decades ago. An extensive review of their use in science and technology has been performed by Thostenson et al. (2001). A more recent overview of CNT-based fibers and composites has been performed by Chou et al. (2010). Furthermore, Thostenson and Chou (2006) showed that CNT networks can be used for sensing of distributed strain.

Schumacher and Thostenson (2014) used CNT-based sensing on concrete structures and Dai et al. (2015) developed a CNT-based sensors that can be installed on steel and therefore used for sensing strain in the vicinity of connections. The developed sensor was made of aramid nonwoven fabric that was coated with a CNT solution. The coated aramid fabric was infused with epoxy resin to create the final sensor. Electrodes were attached to the sensor to measure the resistance change between two points while load was applied. The resistance change in the sensor was a result of electrical connections breaking between the CNTs when load was applied. The resistance change correlated well with measured strain. However, these sensors only used two electrodes and therefore measured resistance only between two points, which resulted in one measurement similar to a strain gauge.

To measure a strain distribution in a connection, a CNT-based sensor with multiple electrodes is necessary. This type of sensor was developed for spatial damage detection in electrically anisotropic fiber-reinforced composites by Gallo and Thostenson (2016) and by Dai et al. (2016). Dai et al. used multiplexing of 32 electrodes and electrical impedance tomography to detect flaws that were introduced manually in a CNT-based sensor using multiple electrodes. The results showed that flaws could be detected but their sizes were difficult to capture.

Carbon nanotube-based sensors have a great potential to detect the strain distribution in the vicinity of steel member connections. However, previously described experiments were all performed in a laboratory setting and with data acquisition equipment that would be hard to connect to a wireless sensing network on a steel member in the field.

#### **2.4 Finite Element Analysis of Structural Steel Building Connections**

Finite element analysis of steel building connections has become more important during the last several years for the civil engineering research community. Thanks to increased computational power, connections can be modeled with increased detail (for example, by including pretension forces in the bolts or contact interaction between bolts and connection angles). Modeling a connection using a finite element model is still a complex task and more research in this area needs to be performed. However, a large variety of publications on this topic can be found. It is prudent, therefore, to limit this review to only include publications with connection types used in the instrumented buildings (i.e. double angle shear connections).

A preliminary literature review on structural connections modeled using finite element models was performed to assess strengths, weaknesses, and other common features of prior work. First, five papers were considered to evaluate the use of solid versus shell finite elements. The five selected papers were: Takhirov and Popov (2002), Swanson et al. (2002), Citipitioglu et al. (2002), Bursi and Jaspart (1998) and Shi et al. (2008). These papers were selected since they discussed different methods of modeling double angle shear connections while providing sufficient detail about the finite element model such as element type, bolt pretension force, and friction coefficient for the connection interactions. Other papers could have been included, but

weren't because not enough information about the finite element model was provided. Takhirov and Popov (2002) used shell elements to model the global behavior of the entire connection and a solid element model to model the behavior of the T-stub (a piece of T-shaped steel that connects the top flange of the beam to the column flange) under tension loads. The bolts in the shell element model were replaced by springs. Parts of the connections from Takhirov and Popov (2002) were remodeled using solid elements including bolt holes and bolts. No interactions between the different parts were defined or explicitly mentioned in either of the two models. In general, shell elements were used to model the overall behavior of the connection and solid elements were used to model detailed behavior of connections. The purpose of the finite element model for this research project was to model the detailed stress distribution in the connection. Therefore, the finite element model for this project was created using solid finite elements.

The selected connection that was recreated as a full-scale laboratory setup and therefore created as finite element model was a double angle shear connection. The connection consisted of a beam-to-column connection using two connection angles, three bolts between the beam and the connection angles, and two bolts per connection angle to connect the angle to the column (i.e. four column bolts). A very similar finite element model was created by Hantouche and Sleiman (2016) for a study comparing shear endplate connections to double angle connections at elevated temperatures. The force-rotation response of the created models were compared to experimental test results found in the literature. Both force-rotation response and failure modes of the finite element models were in agreement with the experimental results making the modeling approach a success. The finite element model was created using ABAQUS,

and therefore the described processes could be easily adapted since the finite element model for this project was created in ABAQUS as well. Even though the dimension of the two connections were different, the basic modeling principle could be adapted. Hantouche and Sleiman (2016) use C3D8R (ABAQUS eight node brick elements with reduced integration) solid elements for their model. Furthermore, they used AISC (2017) minimum required pretension forces as pretension load for the bolt loads. The surface interactions between the connection surfaces were modeled using finite sliding with a friction coefficient of 0.25.

A friction coefficient of 0.25 was also used by Saedi and Yahyai (2009). These authors chose the friction coefficient based on their study (obtained FE results were in better agreement with laboratory test results), after considering values from AISC (2017) of 0.33 and 0.1 from Kishi et al. (2001) and Ahmed et al. (2001). Pirmoz et al. (2008) also used a friction coefficient of 0.25 for their study of the behavior of bolted angle connections subjected to combined shear force and moment. Furthermore, Pirmoz et al. (2008) used AISC (2017) minimum required pretension forces to pretension the used bolts. Takhirov and Popov (2002) and Weigand et al. (2016) used a friction coefficient of 0.30 while Swanson et al. (2002) used a value of 0.33, and Green et al. (2005) used a value of 0.2. Therefore, the friction coefficient in the relevant literature varied between 0.1 and 0.33.

Based on this literature review, a finite element model was created using ABAQUS eight node brick elements with reduced integration, AISC (2017) minimum required pretension forces to pretension the bolts, and a friction coefficient of 0.3. The friction coefficient was chosen since it was close to the AISC (2017) value but also

took into account that the friction coefficient in the literature were generally smaller (i.e. less external force was required to overcome the friction force).

## **Chapter 3**

### **CONSTRUCTION MONITORING**

The literature review demonstrated that obtaining information on construction-induced and fit-up stresses was necessary to meet the objectives of this research. To obtain these data, three steel buildings were instrumented during construction using a wireless sensor network (WSN). All three buildings were instrumented using the same WSN and the same general data analysis process was used for the three data sets. Therefore, these two topics are discussed at the beginning of this chapter (in Sections 3.1 and 3.2, respectively).

The instrumented buildings, including field data results for each building, are described in Section 3.3. The first instrumented building was a four-story addition to the existing Purnell Hall building on the University of Delaware main campus and was therefore labeled Purnell Hall Addition (Subsection 3.3.1). The second instrumented building was a ten-story tower built on the University of Delaware STAR campus and was labeled STAR Tower (Subsection 3.3.2). The third instrumented building was a 6-story building built next to the STAR Tower on the STAR campus, known as the BPI Building (Subsection 3.3.3). The field data of the three buildings is compared in Section 3.4.

#### **3.1 Wireless Sensor Network**

To collect data during the erection of a steel-framed building without interfering with the construction process, a WSN was used. The selected network was

the V-Link<sup>®</sup>-LXRS<sup>®</sup> wireless node network manufactured by LORD Sensing. This network consisted of one USB data gateway (WSDA<sup>®</sup>-Base -104 -LXRS<sup>®</sup>) and ten V-Link<sup>®</sup>-LXRS<sup>®</sup> wireless network nodes. The USB data gateway wirelessly received data from the nodes located on the steel members and transmitted these to a laptop as shown in Figure 3.1. Each of the nodes collected data from four strain gauges as well as ambient air temperature at the node.

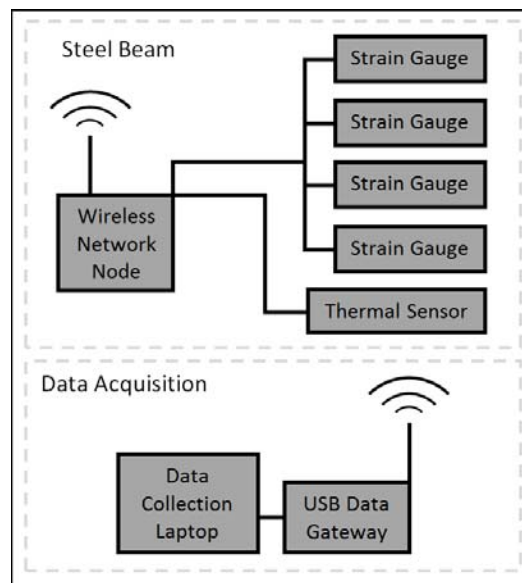


Figure 3.1: Schematic of wireless sensing network (WSN), only one node shown for simplicity

Each node was connected to prefabricated, weatherproofed, weldable uniaxial strain gauges and strain rosettes. The strain gauges and rosettes were covered using foil tape to protect them from the environment and were fabricated by Hitec Products, Inc., using Micro Measurements foil strain gauges with a gauge length of 3.18 mm (0.125 in.) and overall length of 5.59 mm (0.22 in.). These were placed on the same

side of the web of the same member on which the node was installed using conventional strain gauge wiring as shown in Figure 3.2 (for two representative Purnell Hall Addition members further described in Subsection 3.3.1.2, the Long Column and the Short Column). This node placement allowed all wires to be placed on the interior surfaces of the I-shaped members, where the equipment was relatively sheltered from potential impacts that may occur during the construction process. The nodes were connected to two batteries to supply power and collectively placed inside a protective hard plastic casing. The wireless system was validated for use in this application by Wennick (2016).

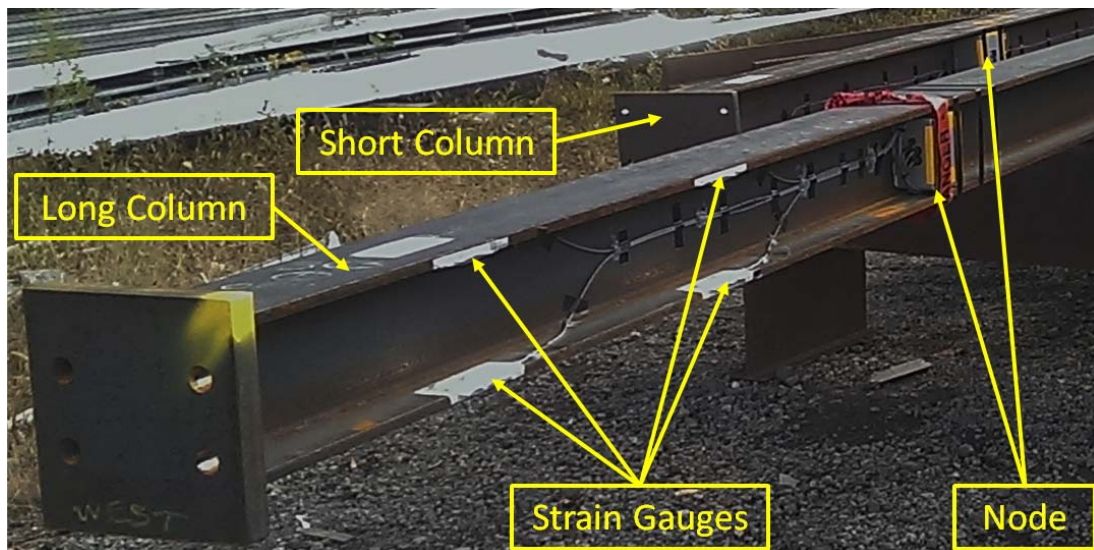


Figure 3.2: Photograph of instrumented steel members at the fabrication facility

### 3.2 General Data Analysis Process

The same data analysis process was used for all three instrumented buildings and is discussed in this section. First, the data was collected using the WSN during the

construction phase of the instrumented buildings as explained in Subsection 3.2.1. The collected data had to be cleaned as described in Subsection 3.2.2 to remove strain data values that were unreasonably high. Once the data was cleaned, the collected strain gauge data was zeroed based on the self-weight of the steel member while the member was hanging on the crane as described in Subsection 3.2.3. After cleaning and zeroing, the data was divided into sustained and impact data in Subsection 3.2.4. The obtained sustained data was used to calculate the member forces at selected locations as described in Subsection 3.2.5. The changes of temperature during the data collection period influenced the collected data. This is summarized in Subsection 3.2.6.

### **3.2.1 Data Collection**

Once all strain gauges were installed and their functionality tested, the WSN nodes were switched to sleep mode, which was a battery saving setting where the WSN nodes did not transmit any data. Once the steel members arrived on the construction site, where the data acquisition laptop was placed previously, the WSN nodes were woken from the sleep mode and data collection began before the steel members were unloaded from the delivery truck. More information regarding the data collection for each building is provided in Subsection 3.3.1.3 for the Purnell Hall Addition, Subsection 3.3.2.3 for the STAR Tower, and 3.3.3.3 for the BPI Building.

### **3.2.2 Data Cleaning**

The data for each strain gauge and for each temperature node were organized as vectors that were a function of time. Vector notation is used in the following equations where appropriate, where the vector variable is written in bold. Because all vectors were time dependent, this is omitted in the following equations for

conciseness. In order to work with conventional units of more practical significance, the collected strain data were converted to stress data using Hooke's law assuming a Young's modulus of 200,000 MPa (29,000 ksi). In the discussion that follows, strain is used when referring to a direct measurement from a strain gauge while stress is used in the data analysis.

The collected data for all three instrumented buildings was processed using the steps described in Section 3.2.2.1. Most of the collected data (97 out of 104 gauges) could be analyzed with this general procedure only, without any additional steps for the data analysis. However, the rest of the data had to be examined more carefully as described in Section 3.2.2.2 since the recorded strain values were much higher than expected.

### **3.2.2.1 General Procedure**

An initial screening of the collected data showed some suspicious random discontinuities in the data with seemingly impossibly high strain and temperature values. These were deemed spurious and the first step in processing the data was to assess the maximum and minimum node temperatures that were recorded. A conservative range of reasonable maximum and minimum temperature threshold values was set, as shown in Table 3.1, based on weather data for Newark, DE for the data recording months for each building. Any temperature value that was outside of these threshold values as well as the strain value collected at the same timestamp was deleted. This process reduced the suspicious strain values significantly.

Table 3.1: Maximum and minimum threshold temperatures for data processing purposes

<b>Building</b>	<b>Data collection period</b>	<b>Maximum temperature threshold [°C] (*F)</b>	<b>Minimum temperature threshold [°C] (*F)</b>
Purnell Hall Addition	November – December 2014	38 (100)	-10 (14)
STAR Tower	May – June 2017	49 (120)	0 (32)
BPI Building	March 2018 – November 2018	66 (150)	-18 (0)

The next step in the data processing was to check if the strain values were similar before and after the suspicious values. If they were similar and the maximum strain value was a single datum point, the suspicious maximum value was deleted. For the remaining suspicious values, the corresponding timestamps were found and the corresponding video records were checked to make sure the given values were not occurring simultaneously with construction events that could have caused such strains. After this was verified, these values were also deleted. This process deleted 2% of the total collected strain values for Purnell Hall Addition (0 – 3 % for 36 of the total 40 strain gauges and 13% for the other 4 strain gauges), 4% of the STAR Tower data (2 – 3% for 23 of the 24 strain gauges and 59% for the remaining strain gauge, G03 that will be discussed in more detail in Subsection 3.2.2.2), and 8% of the BPI Building data (0 – 5% for 32 of the total 40 strain gauges and between 10% and 95% for the other 8).

### **3.2.2.2 Data Cleaning of Selected Strain Gauge Data**

Once the general data processing for each strain gauge was completed, it was found that one STAR Tower gauge (G3) and 6 BPI Building gauges (G6, G7, G27, G28, G33, and G34) needed further examination since the recorded strain values for these strain gauges were much higher than expected. These steps are explained in this section based on an example strain gauge (STAR Tower, G3). First, the entire collected data for G3 was plotted together with all the other strain gauges on the same steel member. The other strain gauges were included on the same plot to verify G3 was the only strain gauge acting differently, i.e. high strain values.

Comparing G3 to the other gauges on the steel member showed that G3 was the only gauge increasing significantly, from -30 micro strain ( $\mu\epsilon$ .) to more than -3000 micro strain ( $\mu\epsilon$ .), instantaneously at a given timestamp. Therefore, the collected video recording of the construction process of the building was used to check if any work was completed in the area of G3 at selected timestamp. The video showed that during the given time no construction was performed (due to bad weather). Given this information it was determined that the high strain values in G03 were very likely a result of moisture penetrating the weather proofing of the strain gauge. Therefore, all G3 data collected after this event were deleted.

The same process was performed for the 6 BPI Building gauges. Three possible causes for these strain gauge results being different from typical strain gauge data (for this field instrumentation) are listed below.

- Damaged strain gauge due to construction work impact
- Moisture penetrating the weatherproofing
- Inadequate connectivity between the data collection laptop and the wireless network nodes normal

### **3.2.3 Initial Dead Load**

It was necessary to have a common reference point for all data that included dead load (because this was an important aspect of the goals of this work) but discounted unknown temperature changes between when the gauges were installed at the fabricator and when erection began. It was decided that the most certain way of doing this was to set the strain gauge data to the theoretically calculated strain value during the time period each instrumented steel member was hanging on the crane because the boundary conditions and loads were known with high certainty in this situation. The theoretical strain value was calculated based on the self-weight, the strain gauge location, and how the steel members were hanging on the crane. The columns were attached to the crane using a chain that was attached to the top of the columns. Therefore, only the self-weight of the column that was below the strain gauge was included, as an axial force, in the calculation. The beams were attached to the crane at the center of the beam. Therefore, the strain was calculated based on the moment produced by the self-weight of the beam assuming the self-weight acted as a uniformly distributed load on the beam while it was hanging on the crane and that the midpoint of the beam acted as the end of a cantilever beam.

The exact points in time when each steel member was lifted off the ground to be lifted to its final location and before the steel member was installed in the building were found using the video data. Between these two time points, the average recorded strain value for each strain gauge was calculated. The obtained average values were then subtracted from the theoretically calculated strain values. The resulting difference was the value that was needed to shift the time history data so the recorded data matched the calculated strain data during the time the steel member was hanging on the crane. Therefore, the calculated difference was subtracted from the time history of

that strain gauge. This process had the consequence that the temperature at this point in time, when each member was hanging from the crane, became the reference temperature for all temperature changes in that member.

#### **3.2.4 Sustained Versus Impact Categorization**

The next step in the data analysis was to separate sustained loads and impact loads. Impact loads were defined as short duration loads resulting from the construction process, such as one member hitting against another during the fit-up process, in contrast to more sustained loads resulting from more predictable sources. Separating the data into these two categories was necessary to evaluate if a peak data point occurred during an impact event or if it was a result from a sustained load. Since it is difficult to predict impact loads during construction, it was important to find peak data values due to impact and compare these values to peak sustained values and the yield strength of the steel members. The obtained data was used to evaluate if impact loads caused yielding in the instrumented steel members during construction. Yielding of steel members due to impact during the construction phase is one of the main concerns preventing reuse of structural steel.

To distinguish between impact and sustained loads, several different statistical methods were considered. However, since the collected data sets did not follow any consistent statistical patterns (i.e., it was not normally distributed, bimodal, etc.), an alternative approach was used, based on dividing the strain history from each strain gauge into moving one-second segments. For each one-second segment, the maximum and minimum stress was determined and their absolute difference calculated. If the absolute difference was more than 6.89 MPa (1.00 ksi), defined as the threshold range and informed by visual assessment of the data and the statistical analyses that were

piloted, the one second time segment was classified as impact data and separated from the remaining sustained data set.

For the BPI Building, the data collection frequency was reduced from 16 Hz to 1 Hz during the data collection period. The previously described approach for identifying impact analyzed one second segments of the data for impact. This approach would not be applicable for the 1 Hz data. Therefore, the collected data for the BPI Building was split into two data sets (16 Hz and 1 Hz). The first set was the data collected at 16 Hz. The above process to characterize impact loads was used on this set. Once the impact loads and the sustained loads were separated, the second data set (1Hz data) was added to the sustained data set. This process ensured a complete data set with only sustained data. Furthermore, including all the data from the 1 Hz data set was the conservative approach since all the peak values were included in the data.

### **3.2.5 Member Force Calculation**

#### **3.2.5.1 Three-Gauge Approach**

The data from groups of three strain gauges on common cross-sections were used to calculate the axial force ( $P$ ), strong axis moment ( $M_x$ ), and weak axis moment ( $M_y$ ) (assuming these were the only force effects). Three strain gauges on a common cross-section were labeled as “gauge sets”, GS, and will be defined in more detail in Subsection 3.3.1.2. One way to calculate member forces was via a system of three simultaneous equations using the three measured stresses on the cross-section to solve for the three unknown force effects as shown by Eqn 1.

$$\epsilon_{Gi,m} * E = \sigma_{Gi,m} = \frac{P}{A} \pm \frac{M_x * c_y}{I_x} \pm \frac{M_y * c_x}{I_y} \quad (3.1)$$

In Eqn. 3.1,  $\epsilon_{Gi,m}$ , is the measured strain data vector of strain gauge  $i$ ;  $\sigma_{Gi,m}$  is the stress vector of strain gauge  $i$ ;  $E$  is Young's modulus of steel;  $A$  is the cross-sectional area of the member;  $c_y$  and  $c_x$  are the distances from the center of gravity of the cross-section to the strain gauge in the strong and weak axis directions, respectively; and  $I_x$  and  $I_y$  are the strong and weak axes moments of inertia, respectively. Thus, it is noted that in Eqn. 3.1, the moment terms represent the internal moment at the cross-section under consideration, regardless of the cause of this moment (e.g., end moment or horizontal force applied at the end of the member). This approach of using Eqn. 3.1 to solve for external forces was termed the “three-gauge approach” (TGA) and used where only a single gauge set existed.

### 3.2.5.2 Optimization Approach

For four of the five instrumented columns (Purnell Hall Addition: Long and Short Column, STAR Tower: 1<sup>st</sup> Floor Column, and BPI Building: 1<sup>st</sup> Floor Column), there were sufficient longitudinal gauges installed to consider the longitudinal variation in stress when calculating member forces. For example, Figure 3.3 shows a schematic of the Purnell Hall Addition Short Column and the possible forces that acted on it during construction (neglecting wind, which was transient and assumed to be negligible for the time scale considered in this work).

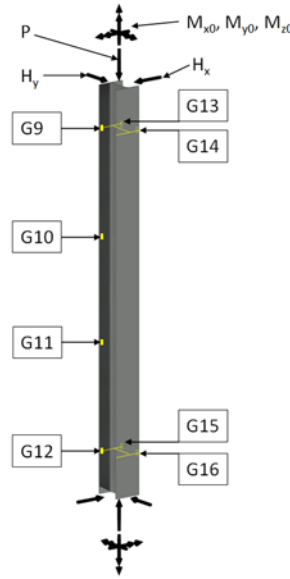


Figure 3.3: Member forces acting on the Purnell Hall Addition Short Column

Based on these assumed forces, the stress in each gauge as a function of forces and moments in all three global directions (i.e., six unknowns) can be expressed as follows:

$$\sigma_{Gi,m} = \frac{P}{A} \pm \frac{(M_{x0} + H_y * z_i) * c_y}{I_x} \pm \frac{(M_{y0} + H_x * z_i) * c_x}{I_y} \pm E * W_{ns} * \theta'' \quad (3.2)$$

where  $P$  is the calculated axial force at the strain gauge location,  $M_{x0}$  is the strong axis end moment,  $M_{y0}$  is the weak axis end moment, and  $H_x$  and  $H_y$  are horizontal forces along each primary axis of the member that together with leverage  $z_j$  (the distance from the top of the beam to each strain gauge) result in changing moments along the length of the beam (as displayed in Figure 3.3). To calculate the warping stress due to torsion (which was the only stress due to torsion in the longitudinal direction of the beam and therefore measured by the strain gauges) the second derivative of  $\theta$  (the

angle of rotation due to torsion with respect to  $z$ , which was the unknown) was multiplied by  $E$  and the normalized warping function ( $W_{ns}$ ) at point  $s$  (gauge location along the width of the flange, 12.7mm (0.5 in.) from the tip of the flange, Seaburg and Carter (2003)). All other variables are as defined in Eqn. 3.1. When Eqn. 3.2 was applied, the axial force and torsion were directly calculated. The internal moments at a given cross-section (previously defined as  $M_x$  and  $M_y$ ) resulted from the sum of the effects of the moment and horizontal terms in Eqn. 3.2 for the axis under consideration, consistent with the philosophy of Eqn. 3.1.

Furthermore, because four of the five previously mentioned columns had more than six longitudinal gauges, the patternsearch function from the Global Optimization Toolbox in Matlab (*MATLAB and Global Optimization Toolbox Release, 2017b*) was used to optimize the fit of the six unknowns in Eqn. 3.2 by minimizing the error between calculated and measured values. This approach of using Eqn. 3.2 to solve for external forces was termed the “optimization approach” (OA). Because of the more comprehensive nature of the OA compared to the TGA, this approach was used where there were sufficient gauges to do so. However, because of the computational demands of this approach, the TGA was first used to determine the time when the maximum and minimum force and moments occurred in each gauge set. The optimization program was then executed over a time range starting 1.5 seconds before and ending 1.5 seconds after this time. When comparing the calculated stresses from the optimization program to the measured stresses, for the Purnell Hall Addition data, it was found that 75% of the calculated stresses were within 5%, and 91% were within 20% of the measured stresses. For the Purnell Hall Addition data it was found that high differences between calculated and measured stresses that were more than 30%

were typically associated with measured stresses of 10 MPa (1 ksi) or less. The maximum stress difference between calculated and measured stress was 15 MPa (2 ksi) for the Purnell Hall addition data.

### **3.2.6 Data Analysis Considering Temperature Effects**

The next step in the data analysis process was to consider the influence of temperature. Temperature changes could significantly influence the strain data but would not necessarily have an effect on the resulting stress. For instance, change in strain due to temperature change in a steel member that was free to expand and contract would not cause stress. Conversely, if a member was restrained, temperature change would result in stress in proportion to the change in strain. In the instrumented building and most practical scenarios, the members have end conditions that vary between free and fully fixed and it is not a trivial task to determine the degree of fixity for each member. Initially, an upper- and lower-bound approach was considered for the data analysis with respect to temperature. One bound was labeled restrained thermal expansion (RTE). For this dataset, the stress values were calculated by assuming that thermal expansion and contraction were restrained and all temperature-induced strain was converted to stress. The second bound was labeled as free thermal expansion (FTE). For this bound, it was assumed that the instrumented members were free to expand and contract and none of the temperature strain was converted to stress in the steel member.

Calculation of the RTE stresses simply involved multiplying the recorded strains by Young's modulus of 200,000 MPa (29,000 ksi) (as all strain values were in the elastic range).

$$\sigma_{Gi,RTE} = \epsilon_{Gi,m} * E \quad (3.3)$$

Calculation of the FTE stresses required quantifying the temperature-induced strain and subtracting this effect from the total strain to obtain the load-induced strain. This load-induced strain was then converted to stress by multiplying it by Young's modulus:

$$\sigma_{Gi,FTE} = (\epsilon_{Gi,m} - \epsilon_{Temperature}) * E \quad (3.4)$$

where

$$\epsilon_{Temperature} = \alpha * \Delta T \quad (3.5)$$

and  $\alpha$  is the thermal expansion coefficient of steel and  $\Delta T$  is the change of temperature in the steel member.

To account for temperature, one strain gauge was installed transversely on the flange of one of the instrumented members for the purpose of measuring temperature change as all strain in this direction could be reasonably assumed to be due to temperature change (excluding the Poisson's effect from the longitudinal strains, which were not captured by the strain gauges). Furthermore, each node measured air temperature, which was anticipated to be used as a means for accounting for temperature differences throughout the structure.

However, this manner of accounting for temperature change in the data analysis did not result in reasonable stress estimates. Further analysis of temperature effects using the increased instrumentation for measuring temperature in the BPI Building, described in Subsection 3.3.3, showed that this was likely due to the tremendous variation in temperature throughout I-shaped cross-sections exposed to the environment. On average over 4 days during construction, temperature variations of 6.6 °C (12 °F) throughout the same cross-section were observed. The maximum variation in temperature throughout a cross-section during these four days was 8.8 °C

(16 °F). Using Eqn. 3.5 this corresponds to a strain of 111  $\mu\epsilon$  and if this strain was converted to axial stress, a stress difference of 22.2 MPa (3.2 ksi) occurred throughout the cross-section due to temperature which was 46 % of the maximum strain during the given time period.

An example graph for the influence of the temperature on strain gauges placed on both sides of the web along the Purnell Hall Addition Long Column is shown in Figure 3.4. The strain gauge locations are shown later in Figure 3.6. The collected strain gauge data follows the same trend as the temperature data. This can be best observed during nights when no work was performed.

It was also observed that there was high sensitivity to the angle of the sunlight relative to each web and flange surface of the steel member, which varied for each point on a cross-section and member. Direct sunlight exposure compared to being in variable shadows cast by adjacent buildings, members, surfaces, or clouds throughout the day also appeared to influence the recorded strain data. Furthermore, the steel heated and cooled at a different rate than the air. For all of these reasons, the air temperature measured by the node was inadequate to determine the temperature at different points in the steel.

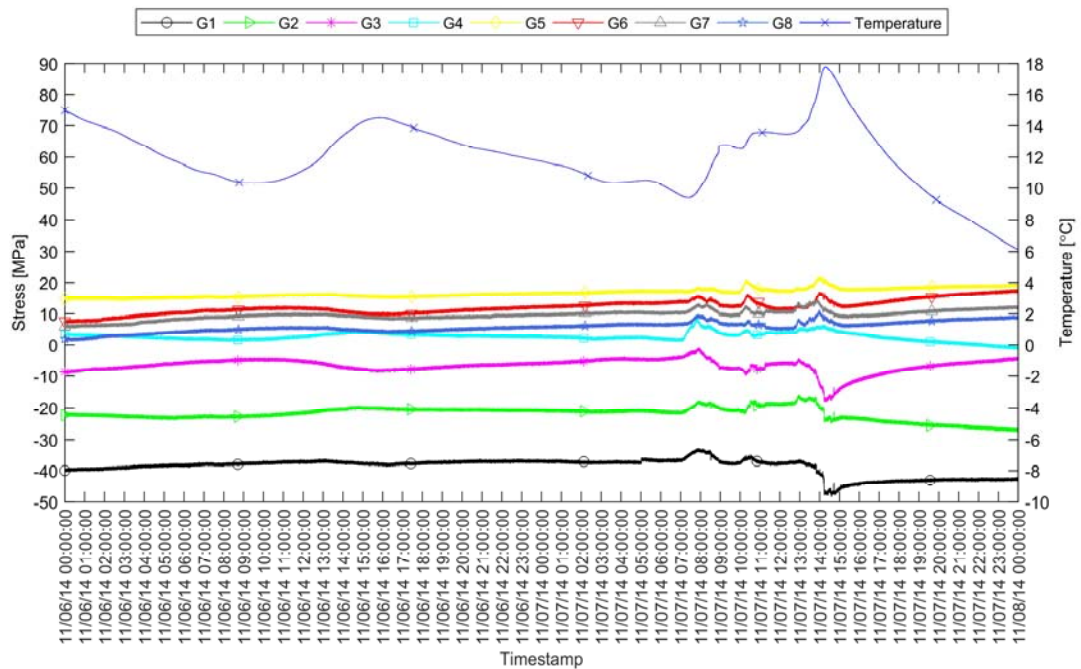


Figure 3.4: Example strain gauge data for the Purnell Hall Addition Long Column showing temperature influence on data

Thus, without having the ability to know the steel temperature at each gauge location, the FTE bound could not be estimated with sufficient confidence. Furthermore, the error resulting from the optimization program discussed above was calculated using both the FTE and RTE assumptions and was found to be less in the RTE scenario. This suggested that the actual conditions were closer to the RTE condition. For these reasons, the RTE is presented as a conservative but reasonable estimate of the stresses experienced in the instrumented members.

### **3.3 Instrumented Buildings**

The three instrumented buildings are described in the following sections. The first instrumented building was the Purnell Hall Addition. Data for this building was collected during November and December of 2014. The collected member data for this building was analyzed and summarized in Keller et al. (2019). The published data was supplemented with data in the vicinity of member connection in Section 3.3.1. The second instrumented building was the STAR Tower. Data for this building was collected during May and June of 2017. Unfortunately, the data collection had to be ended due to the building owner's request. Therefore, only three steel members were instrumented for this building and the results are summarized in Section 3.3.2. The third and final instrumented building was the BPI Building. Continuous data collection for this building started in March 2018 and ended in November 2018. However, three of the five instrumented steel members of this building are still instrumented, and data is periodically collected to monitor the steel member behavior during the entire construction process and during the building service life. The continuous data is reported in Section 3.3.3.

### **3.3.1 Purnell Hall Addition**

For this building, five steel members of a multi-story steel frame building were instrumented after fabrication and prior to shipping to the construction site. Data were continuously collected for 48 days, from the day the first instrumented steel member arrived on the building site until the day before the fire proofing was applied (which required removal of the WSN nodes). The data were considered in terms of impact versus sustained stresses and how stresses varied throughout the construction process. Calculated stresses based on maximum recorded strains were compared to the yield strength of the steel. Additionally, the data were used to calculate multi-axial loading effects and these forces were compared to multi-axial yield capacities of the members and the loading effects that would be expected based on typical design assumptions.

#### **3.3.1.1 Building Information**

The first structure selected for construction monitoring was an addition to an existing building on the University of Delaware campus located in Newark, DE, USA. This choice of structure satisfied the objectives of being a multi-story steel-framed structure for which access to the site could be facilitated with relative ease. This site also offered nearby enclosed spaces (via other campus buildings) for storing data collection equipment and a video camera to produce a video archive of the construction sequence.

The building had four floors, a gross area of 743 m<sup>2</sup> (8,000 ft.<sup>2</sup>), and is used as office space and conference rooms. An isometric rendering of the steel frame of the building is shown in Fig. 3.5 (which is discussed in more detail in Section 3.3.1.2). The overall dimensions of the structure are 15.6 m (51 ft.-2 1/6 in.) x 13.5 m (44 ft.-3 1/2 in.) and it was 15.0 m (49 ft.-1 1/2 in.) tall. The members of the structural frame

were hot-rolled wide flange shapes fabricated from A992 steel with a minimum specified tensile yield strength of 345 MPa (50 ksi). The column sections range from W200x42 (W8x28) to W250x131 (W10x88) with a story height of 3 m (9 ft-10 in.) and the beam sections consisted of W200x42 (W8x10) to W530x219 (W21x147) with a maximum span of 9 m (29 ft.-6 in.). The beams of the building were built composite with 80 mm (3.25 in.) concrete slab floors, which were fabricated using stay-in-place metal deck forms. The metal deck forms were put in place in two phases, each phase starting after two floors of the steel frame were erected. The concrete floor slabs were poured on two consecutive days. The building addition was connected to the existing building using field welds and anchors.

### **3.3.1.2 Instrumentation**

The instrumented members included the columns and beams where maximum local and global strains were theoretically expected, based on the assumed load transfer throughout the building. Here the term local strains refers to strains due to strain concentrations or other localized effects near member connections, while global strains refer to the strains resulting from the force effects that are typically considered in design, such as maximum moments in beams and maximum compression in columns. Both types of strains were important to consider as the latter governs design, while the former presents concerns for member reuse. It was also prioritized that the instrumented members connect to one another so that there were greater opportunities for understanding force transfer throughout the structure. Furthermore, by choosing members near the top of the structure, the force transfer into the columns was more straightforward.

Since the utilized WSN consisted of 10 nodes, and one node was required on each side of the instrumented member for wiring logistics, a total of five structural steel members were instrumented. As shown in Figure 3.5, these represented two columns and three beams, with specific labels for each member as identified in Figure 3.5. The circles indicate the general location of the installed strain gauges.

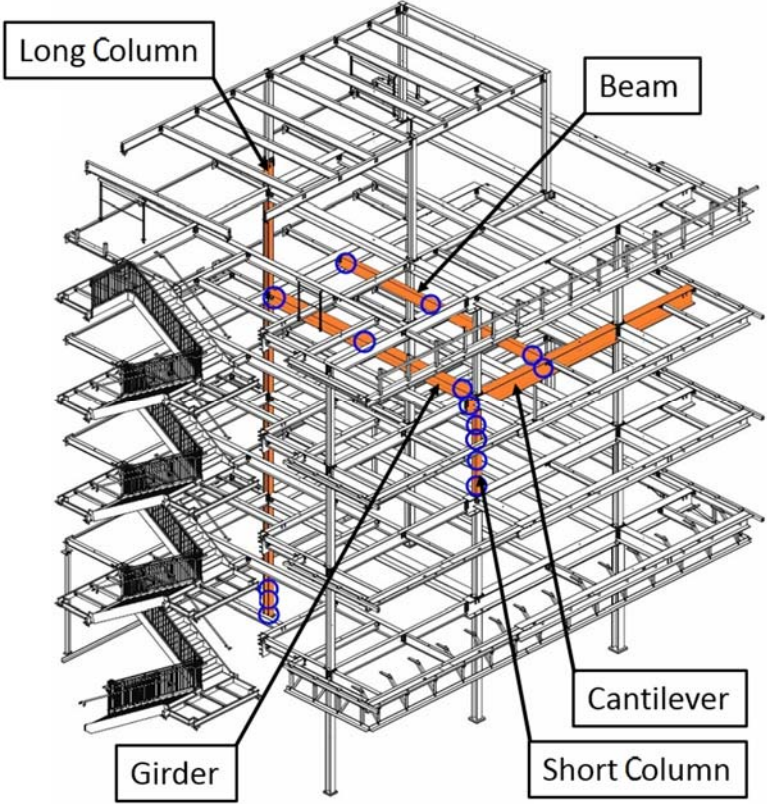


Figure 3.5: Purnell Hall Addition steel frame with instrumented members highlighted and named (Adapted from RC Fabricators Inc.)

The Long Column was selected for monitoring because it spanned most of the height of the structure. Furthermore, it was one of the first members erected and thus

data collection time could be maximized. The Girder was a typical member, connecting to the Long Column. The Short Column was a typical column connecting to the Girder. The Cantilever also connected to the Short Column as well as to the Girder and represented a unique member that had the potential to experience the governing strains. For the reason of member connectivity previously discussed in this section and to represent a typical flexural member in this structure, the Beam was instrumented. More information regarding each instrumented member is given in Table 3.2.

Table 3.2: Details of instrumented Purnell Hall Addition members

<b>Label</b>	<b>Cross-Section</b>	<b>Length [m] (ft.-in.)</b>	<b>Floor(s)</b>	<b>Date of Installation</b>	<b>Detail drawings</b>
Long Column	W200x71 (W8x48)	16 (52-5)	1 – Roof	11/03/2014	Figure 3.6
Short Column	W200x46 (W8x31)	3 (9-10)	3 – 4	11/07/2014	Figure 3.7
Cantilever	W530x219 (W21x147)	9.8 (32-1 3/8)	4	11/07/2014	Figure 3.8
Girder	W360x147 (W14x99)	8.8 (29-5/8)	4	11/07/2014	Figure 3.9
Beam	W360x57 (W14x38)	9 (29-4 1/2)	4	11/07/2014	Figure 3.10

Figures 3.6 through 3.10 provide the instrumentation layout for the strain gauges on each member (previously identified in Figure 3.5), where each gauge is

labeled by “G” followed by an arbitrary numeric identifier. A gauge layout consisting of three strain gauges per cross-section was commonly used, e.g., see Figure 3.6, Sections A-A and B-B. This three gauge layout was chosen to allow for the calculation of three unknown member forces - axial force, as well as weak and strong axes moments as described in Section 3.2.5.1. An assumption made in developing this was that torsion on the cross-section was negligible. This was later validated for Purnell Hall Addition data, and BPI data, however, STAR Tower display some torsion in the results. When strain gauges were installed in this configuration, the group was termed a “gauge set”, which was labeled as “GS” followed by an arbitrary numeric identifier (see Figure 3.6 through 3.10). The strain gauges were installed 12.7 mm (0.5 in.) away from the tip of the flange unless otherwise indicated. To measure temperature changes in the steel during erection, a strain gauge (labeled G4 in all three instrumented buildings) was installed at the outer edge of the flange on Section C-C of the Long Column to measure strain perpendicular to the length of the column. The strain measured by this gauge was only due to temperature change because: (1) strains due to construction at the given location only occurred perpendicular to the gauge, (2) the strain gauges internally accounted for Poisson effects, and (3) warping of the cross-section was found to be negligible.

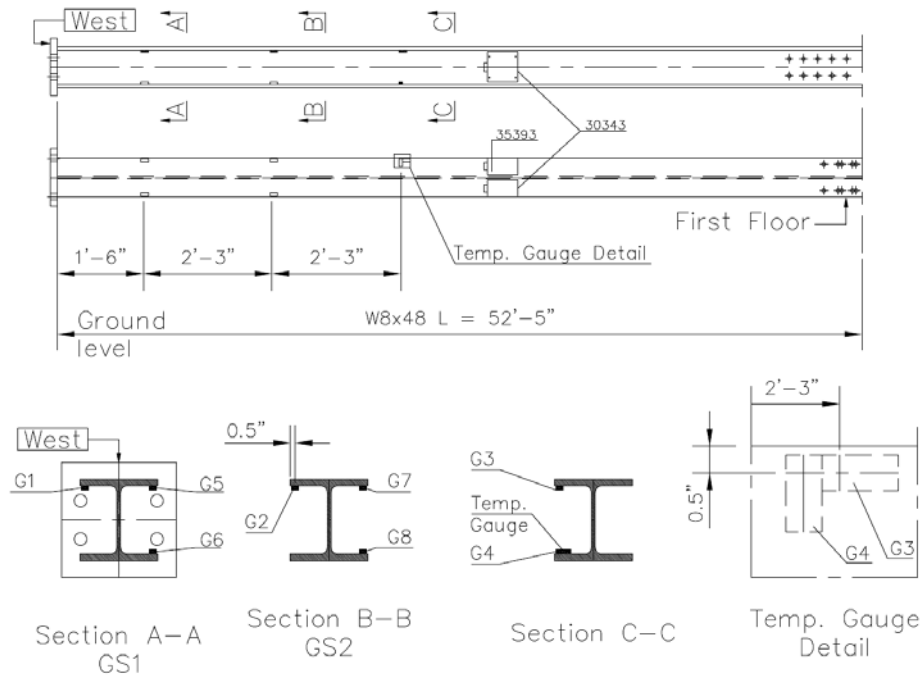


Figure 3.6: Long Column instrumentation drawing

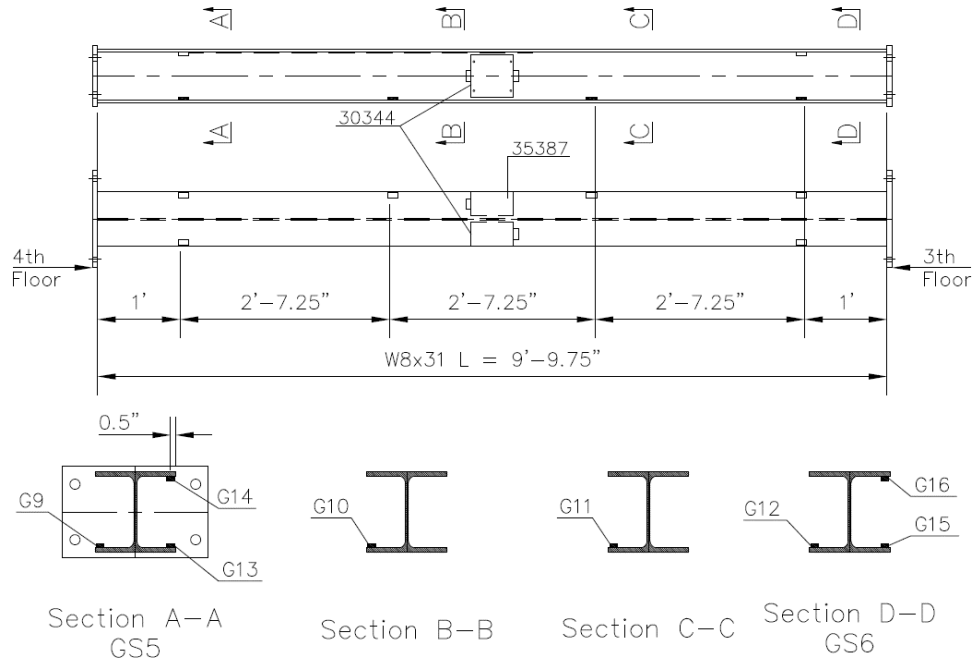


Figure 3.7: Short Column instrumentation drawing

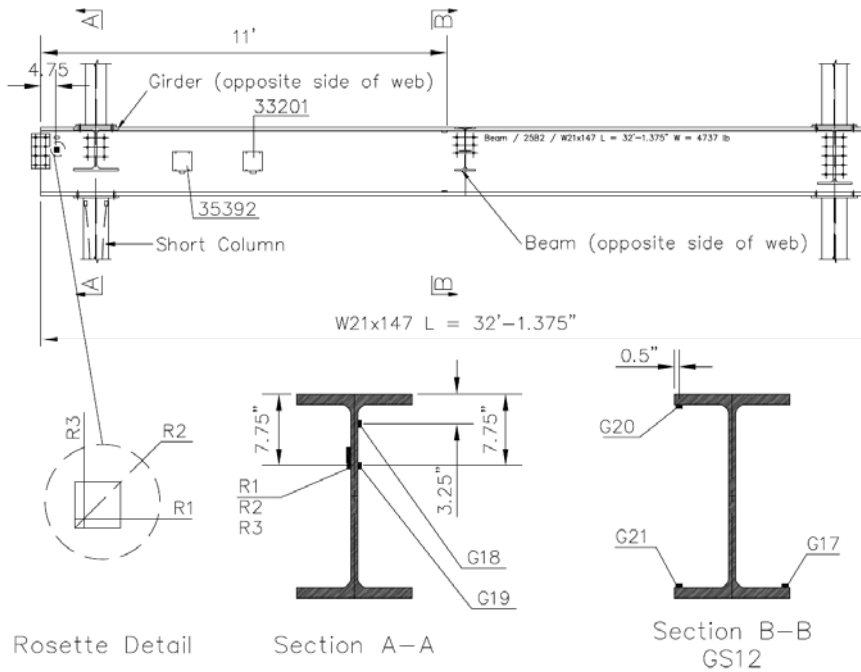


Figure 3.8: Cantilever instrumentation drawing

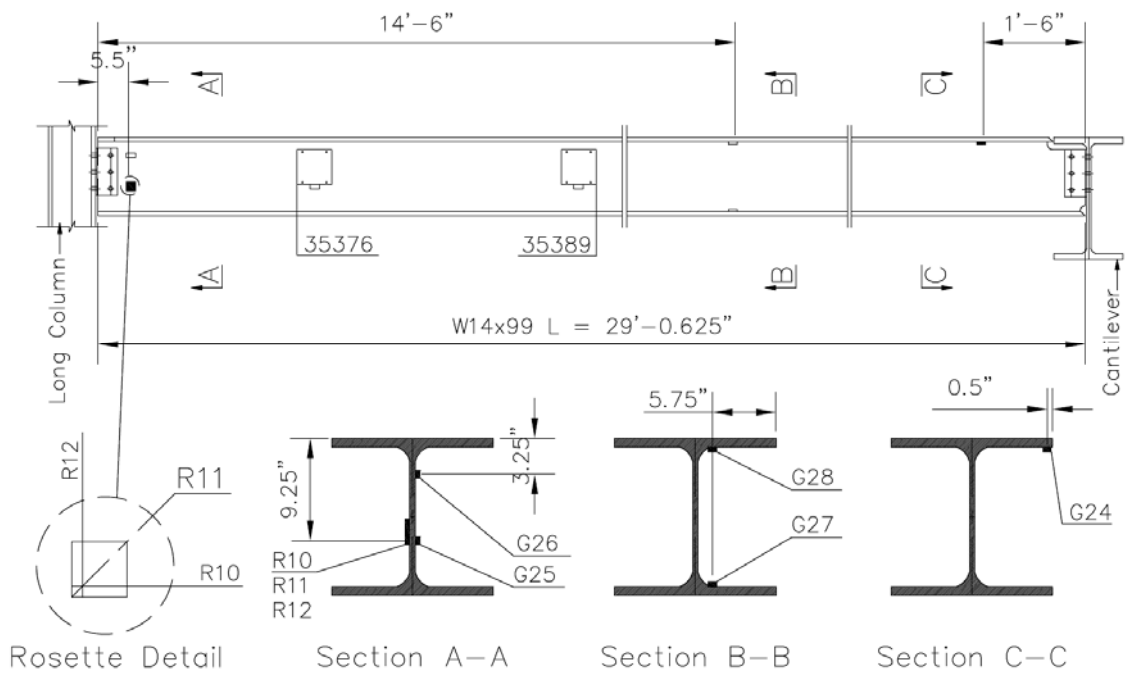


Figure 3.9: Girder instrumentation drawing

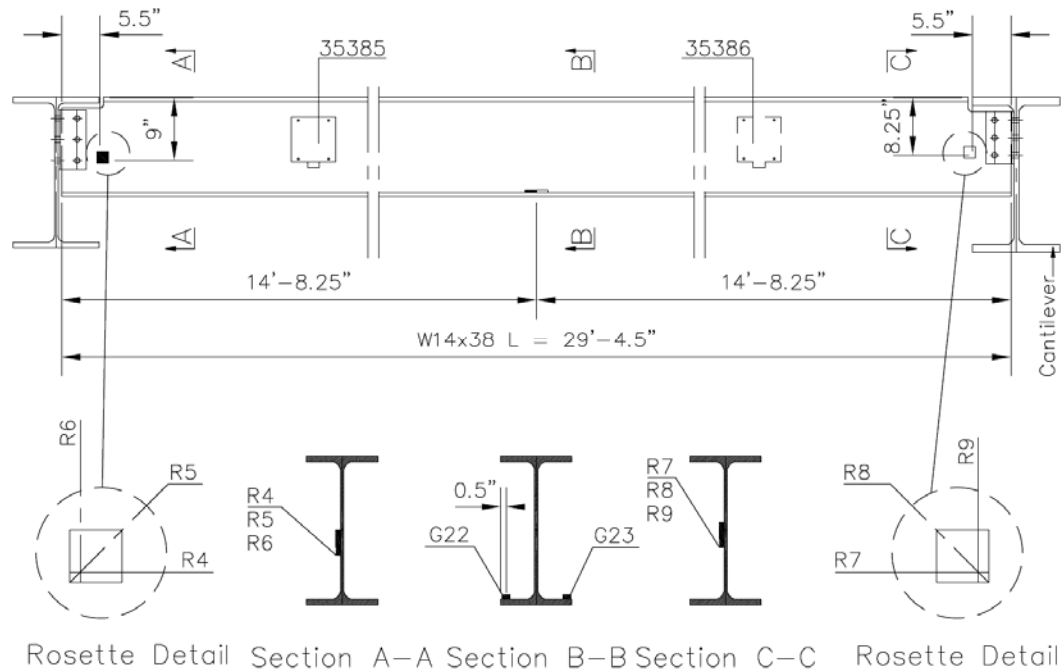


Figure 3.10: Beam instrumentation drawing

### 3.3.1.3 Field Data Collection

Data collection began on the morning of November 3, 2014 when the first steel delivery truck arrived on the construction site with the instrumented Long Column. Continuous data collection continued until December 20, 2014. Strain gauge and temperature data were collected at a sampling rate of 16 Hz. This rate was selected based on the available battery life of the WSN nodes, and to maximize data density during possible sudden construction events resulting in impacts, as described in more detail in Wennick (2016). At the beginning of data collection, data were collected continuously for 24 hours per day. The data collection was later paused during nights and restarted each morning before work on the construction site continued in order to preserve the WSN node battery life. During the time period recorded, the entire steel structure was erected, plumbed, and the concrete floors were poured. The data

collection ended immediately before the fireproofing material was applied to the steel structure because the WSN nodes needed to be removed from the steel members for future use and removing them after this time would have inhibited the required fire resistance of the structure.

In order to later relate the collected strain data with specific construction events, a video camera was utilized to record the entire construction process. The camera was setup behind a window in an office adjacent to the building site. The camera recording speed was two frames per second at a resolution of 800 x 600 pixels. A sample image from the camera is shown in Figure 3.11.



Figure 3.11: Construction site camera image

### 3.3.1.4 Results

A sample plot of stress data versus time, for the entire data collection period of the three strain gauges located at the bottom of the Long Column (G1, G5, and G6), along with recorded node temperature, is shown in Figure 3.12. As described in Section 3.3.1.3, data were initially collected continuously, which is reflected by the continuous portions of the data in Figure 3.12. Later, data were only collected during working hours, which is reflected by the discontinuous data in Figure 3.12.

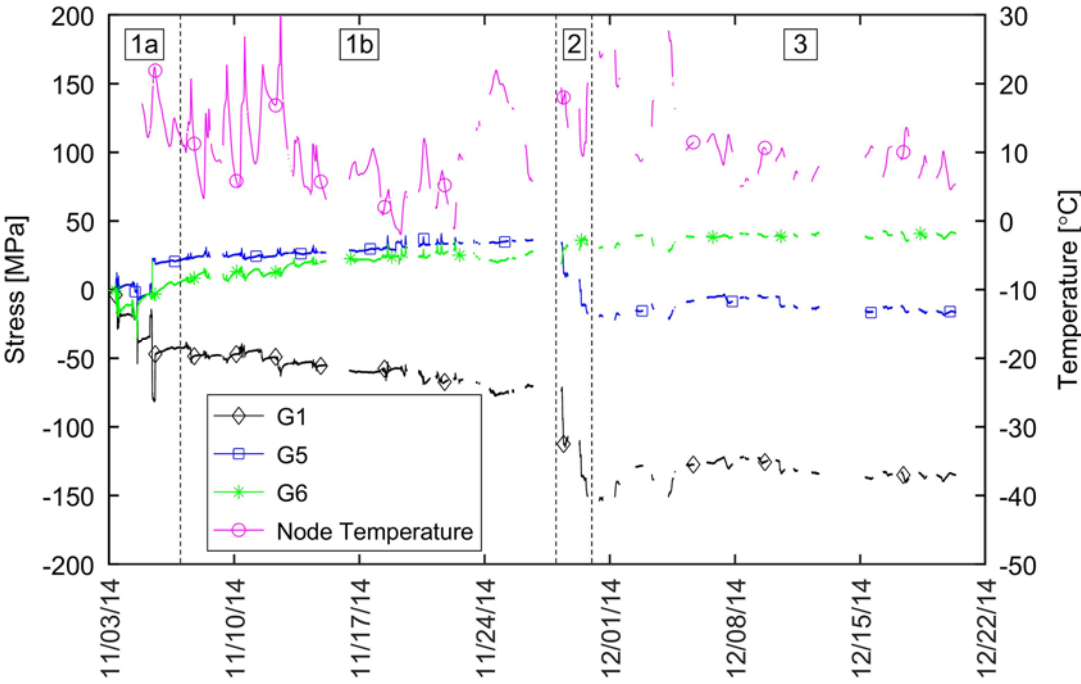


Figure 3.12: Sample field monitoring data (bottom of Long Column), 100 MPa = 14.4 ksi

For the Purnell Hall Addition, the strain gauge data was separated into three general construction phases. The first was the pre-concrete phase, which was further divided into two sub-phases, the second was the concrete pouring phase, and the third

was the post-concrete phase. These four time periods were labeled as phases “1a”, “1b”, “2”, and “3”, respectively, which were separated by vertical lines in Figure 3.12. Phase 1 included data between November 3 and 27. During this phase, all the steel members were put in place, the steel frame was plumbed, and the stay-in-place metal deck forms were connected to the steel frame. The two sub-phases in Phase 1 were introduced to distinguish the difference in stress data at the bottom of the Long Column during first and second floor installation (Phase 1a) versus third and fourth floor installation (Phase 1b). During Phase 1a, the Long Column was delivered to the building site and installed, the first and second floor steel members were attached to the Long Column, and the first two floors were plumbed. During Phase 1b, the stress changed more gradually, as shown in Figure 3.12, while the third and fourth floor steel was installed and plumbed. On November 28 and 29 (Phase 2) the concrete floors for all four floors were poured, two floors per day. The increased compression strain recorded by G1 and G5 was a clear indicator of the increased dead load during Phase 2. However, G6 strain remained constant during Phase 2, which indicated an asymmetric strain distribution that is discussed in Section 3.3.1.4.3. Phase 3 occurred between November 30 and December 20. The strain at the bottom of the Long Column remained relatively constant during this time because no significant dead load was added to the structure.

#### **3.3.1.4.1 Maximum Sustained and Impact Stress Results**

The range of values from member strain gauges throughout the recording period in both the measured data set, which included impact values, and from the sustained data set (computed as described in Section 3.2.4) is compared in Figure 3.13. The member stain gauges were located along the length of the steel member away

from the connection area. Positive values indicated tensile stress, whereas negative values indicated compressive stress. If the maximum values for a strain gauge were the same in both data sets, the maximum value was a sustained value. If the values differed, the maximum value was an impact value.

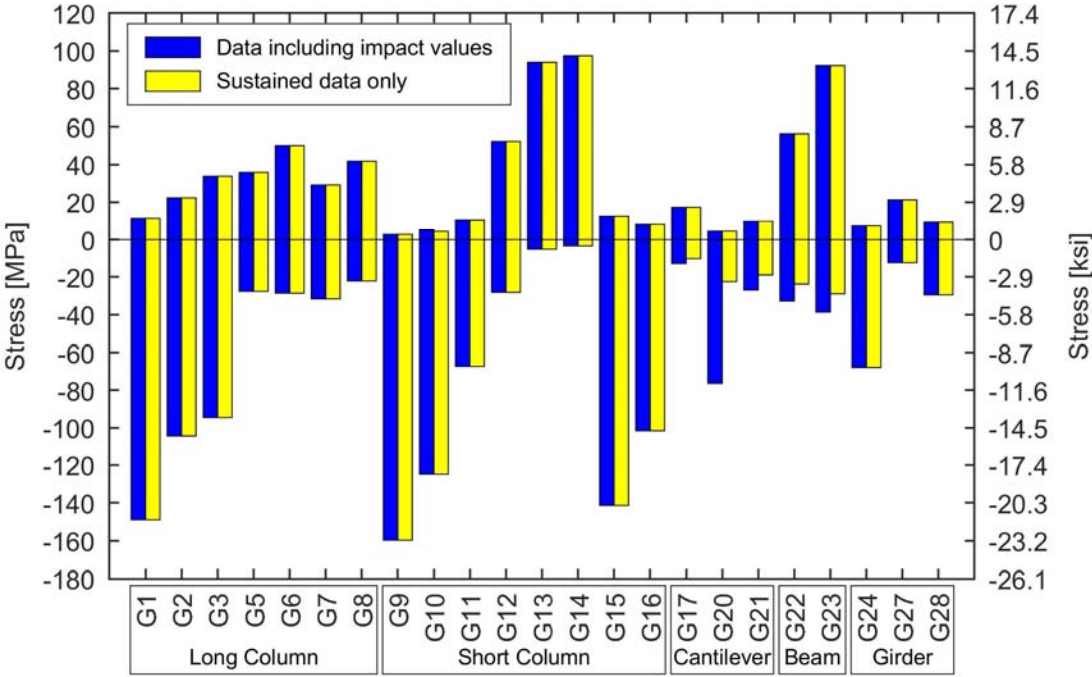


Figure 3.13: Overall maximum data, including impact values and maximum sustained data for the Purnell Hall Addition member strain gauges

Figure 3.13 shows that for 17 of these 23 strain gauges the maximum stress values were sustained stresses, including the overall minimum and maximum stresses that were recorded throughout the dataset for the member strain gauges. The maximum compression and tension values (i.e. member stress values) for the sustained data for the member strain gauges for all instrumented steel members are summarized

in Table 3.3. The connection area strain gauge results are discussed later in this section (Figure 3.14 and Table 3.4).

Table 3.3: Summary of sustained Purnell Hall member stress data

Steel Member Name	Maximum Compression		Maximum Tension	
	MPa (ksi)	Location	MPa (ksi)	Location
Long Column <sup>a</sup>	-149 (-21.6)	G1	50.0 (7.30)	G6
Short Column <sup>b</sup>	-160 (-23.2)	G9	97.4 (14.1)	G14
Cantilever <sup>c</sup>	-22.4 (-3.20)	G20	17.3 (2.50)	G17
Girder <sup>d</sup>	-67.9 (-9.80)	G24	21.3 (3.10)	G27
Beam <sup>e</sup>	-28.9 (-4.20)	G23	92.2 (13.4)	G23

<sup>a</sup> See Figure 3.6 for strain gauge location

<sup>b</sup> See Figure 3.7 for strain gauge location

<sup>c</sup> See Figure 3.8 for strain gauge location

<sup>d</sup> See Figure 3.9 for strain gauge location

<sup>e</sup> See Figure 3.10 for strain gauge location

Values shown in Table 3.3 are the maximum stress values for each steel member except for the Cantilever, for which the maximum recorded compression stress was an impact value. The maximum compression stress value, and also the stress with the largest absolute value, was -160 MPa (-23.2 ksi), at G9 located at the top of the Short Column. Therefore, the maximum stress value was 46% of the yield stress (of 345 MPa, 50 ksi). Adding conservative estimates of factored live loads based

on ASCE/SEI 7-16 (2016) and residual stresses from rolling the wide flange shapes equal to 0.3 times the nominal yield stress, (i.e., 15 ksi; Quayyum and Hassan, 2017), the total estimated stress of 303.4 MPa (44 ksi) remained below the yield stress. The maximum tensile stress value was 97.4 MPa (14.1 ksi), at G14, was also located at the top of the Short Column.

For six strain gauges the maximum value was due to impact. Five of these values occurred in the Cantilever and the Beam. The maximum difference between impact stress and sustained stress was 54.0 MPa (7.90 ksi) and recorded in G20, which was located on the top flange of the Cantilever. This corresponded to an impact stress of -76.4 MPa (-11.1 ksi) versus a sustained stress of -22.4 MPa (-3.20 ksi). The largest absolute change in stress in a one second interval was found to be 63.7 MPa (9.20 ksi), which also occurred in G20, when the stress value changed from -9.70 MPa (-1.40 ksi) to -73.4 MPa (-10.7 ksi) within one second.

The maximum sustained and impact stress values for the strain gauges located in the connection areas of the instrumented steel members as shown in Figure 3.14. The figure shows that only one of these 16 strain gauges (R4) had an impact value which was greater than the sustained value. Both the overall maximum and minimum stress in the connection area strain gauges (R3 and R7) were sustained values and both values were smaller than the maximum and minimum values found in the member strain gauges in Figure 3.13.

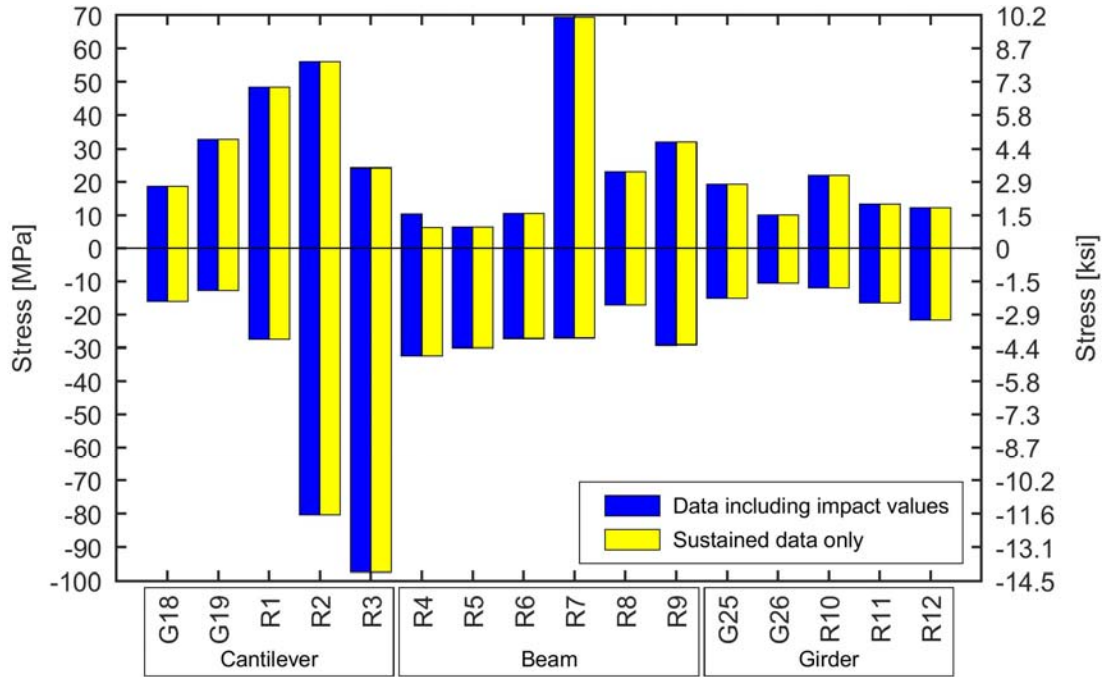


Figure 3.14: Overall maximum data, including impact values and maximum sustained data for the Purnell Hall Addition connection area strain gauges

The maximum and minimum values for the connection area strain gauge results are summarized in Table 3.4. The maximum compressive stress was -97.4 MPa (-14.1 ksi) in gauge R3. The maximum tensile stress was 69.4 MPa (10.1 ksi) in gauge R7. Both values were well below the yield stress of the instrumented members of 345 MPa (50 ksi). Based on the finding that maximum stress values were typically sustained stresses, because no impact value in any strain gauge approached the steel member yield stress, and for conciseness, only the sustained dataset is used in the following sections.

Table 3.4: Summary of sustained Purnell Hall connection area stress data

Steel Member Name	Maximum Compression		Maximum Tension	
	MPa (ksi)	Location	MPa (ksi)	Location
Cantilever <sup>a</sup>	-97.4 (-14.1)	R3	56.0 (8.12)	R2
Girder <sup>b</sup>	-21.7 (-3.15)	R12	22.0 (3.19)	R10
Beam <sup>c</sup>	-32.4 (-4.70)	R4	69.4 (10.1)	R7

<sup>a</sup> See Figure 3.8 for strain gauge location

<sup>b</sup> See Figure 3.9 for strain gauge location

<sup>c</sup> See Figure 3.10 for strain gauge location

### 3.3.1.4.2 Stress Data by Construction Phases

The collected data were also analyzed based on the three (pre-concrete, during concrete, and post-concrete) construction phases introduced at the beginning of Section 3.3.1.4 and the ranges of this data was plotted in Figure 3.15. In addition, the average value of the last hour of collected data for each strain gauge was calculated and plotted in Figure 3.15. The last hour value was compared to the last minute value and the two values were similar for all the strain gauges. Therefore, this value was representative of the stress when the structural framing was completed and the concrete floors were poured. The maximum compression and tension values for the sustained data for all instrumented steel members for each construction phase are summarized in Table **Error! Reference source not found.**

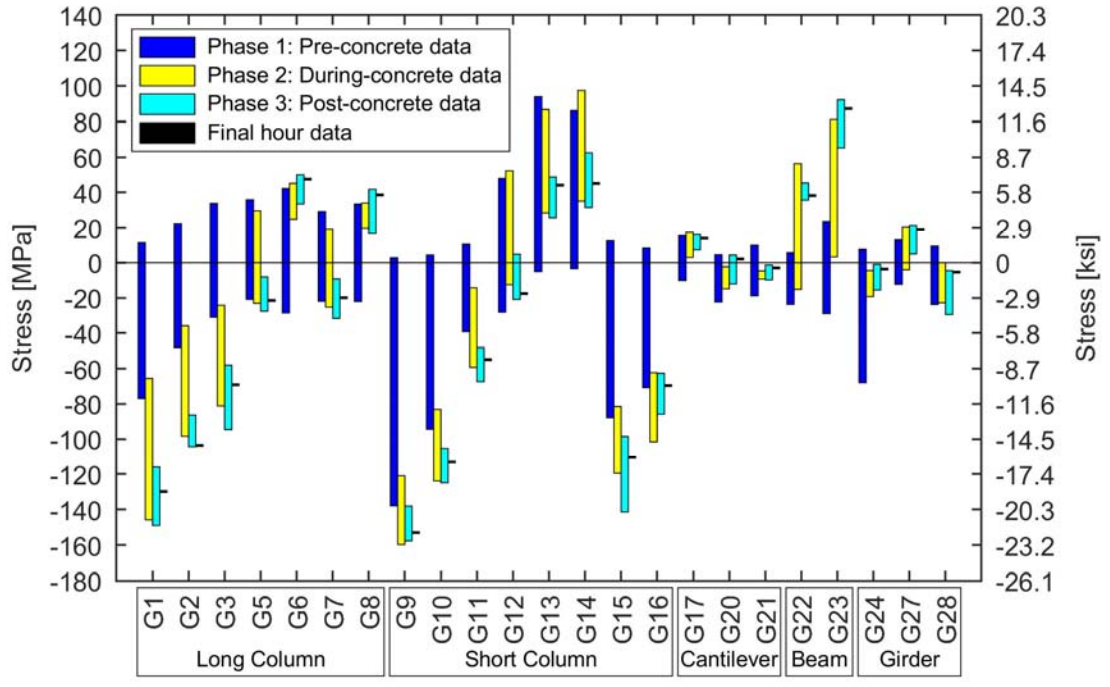


Figure 3.15: Sustained member stress data during different construction phases

Table 3.5: Construction phase member stress data summary

Steel Member Name	Maximum Compression						Maximum Tension					
	Pre-Concrete		During Concrete		Post-Concrete		Pre-Concrete		During Concrete		Post-Concrete	
	MPa (ksi)	Loc.	MPa (ksi)	Loc.	MPa (ksi)	Loc.	MPa (ksi)	Loc.	MPa (ksi)	Loc.	MPa (ksi)	Loc.
Long Column <sup>a</sup>	-76.9 (-11.2)	G1	-146 (-21.8)	G1	-149 (-21.6)	G1	42.3 (6.10)	G6	45.2 (6.50)	G6	50.0 (7.30)	G6
Short Column <sup>b</sup>	-138 -20	G9	-160 (-23.2)	G9	-158 (-22.9)	G9	93.9 (13.6)	G13	97.4 (14.1)	G14	62.5 (9.10)	G14
Canti-lever <sup>c</sup>	-22.4 (-3.20)	G20	-14.9 (-2.20)	G20	-12.1 (-1.80)	G20	15.5 (2.30)	G17	17.3 (2.50)	G17	16.1 (2.30)	G17
Girder <sup>d</sup>	13.0 (1.90)	G27	-22.8 (-3.30)	G28	-29.5 (-4.30)	G28	-67.9 (-9.80)	G24	20.5 (3.00)	G27	21.3 (3.10)	G27
Beam <sup>e</sup>	-28.9 (-4.20)	G23	-15.2 (-2.20)	G22	N/A	N/A	23.6 (3.40)	G23	81.1 (11.8)	G23	92.2 (13.4)	G23

<sup>a</sup> See Figure 3.6 for strain gauge location

<sup>b</sup> See Figure 3.7 for strain gauge location

<sup>c</sup> See Figure 3.8 for strain gauge location

<sup>d</sup> See Figure 3.9 for strain gauge location

<sup>e</sup> See Figure 3.10 for strain gauge location

From Figure 3.15 the change in stress ranges during the different construction phases can be observed. A large stress range indicated high variability in loads and/or structural stiffness. As expected, the stress range was highest during the pre-concrete construction phase for all expect two of the strain gauges (i.e., 91% of the gauges; exceptions were G22 and G23, two Beam gauges). This likely occurred because during this construction phase the members were subjected to variable loads (including fit-up loads) and variable connectivity to other members, affecting their

stiffness and boundary conditions. The maximum stress during this phase was -138 MPa (-20.0 ksi, at G9, located on the Short Column). The overall maximum stress, which was compressive, and maximum tension stress occurred during concrete pouring and were a compression stress of -159.8 MPa (-23.2 ksi) at G9 and tensile stress of 97.4 MPa (14.1 ksi) at G14. Both of these maxima occurred in the Short Column, as shown in Figure 3.15. The final hour data were less than the maximum value for all strain gauges. As one measure of the variability in the data versus time, it was found that the average of the data recorded during the final hour of data collection represented between 5 and 99% of the maximum stress recorded in the corresponding gauge.

Whether compression or tension was observed in the data shown in Figure 3.15 was generally as expected (e.g., compressive stresses in the columns and a combination of compressive and tensile stresses in the flexural members). However, it was not expected to see column stress values in tension, which were observed for Long Column gauges G6 and G8 as well as Short Column gauges G13 and G14. A closer look at this data revealed that there was a compression stress on one side of the neutral axis (NA) and a tensile stress on the other side of the NA of these members, which was an indication of moment in both columns. This will be discussed in more detail in Section 3.3.1.4.3.

The connection area strain gauge results sorted by the construction phases are plotted in Figure 3.16. Similar to the member strain gauge results shown in Figure 3.15, the stress range for only 2 (G25 and R10 both located on the Girder) of the 16 (12.5%) strain gauges shown in Figure 3.16 was greater during the post-concrete phase than during the pre-concrete phase. Furthermore, four strain gauges (G19 and

R1; G25 and R10) were placed “back to back” on the web as shown in Figure 3.8 and 3.9, respectively. Comparing the final hour data of the Cantilever gauges (G19 and R1) shows that the two values differ by 12 MPa (1.74 ksi) which indicates the presence of a weak axis moment in that connection. However, the final hour data for the gauge combination on the Girder (G25 and R10) only differed by 0.78 MPa (0.11 ksi) which indicates no or a very small weak axis moment was present.

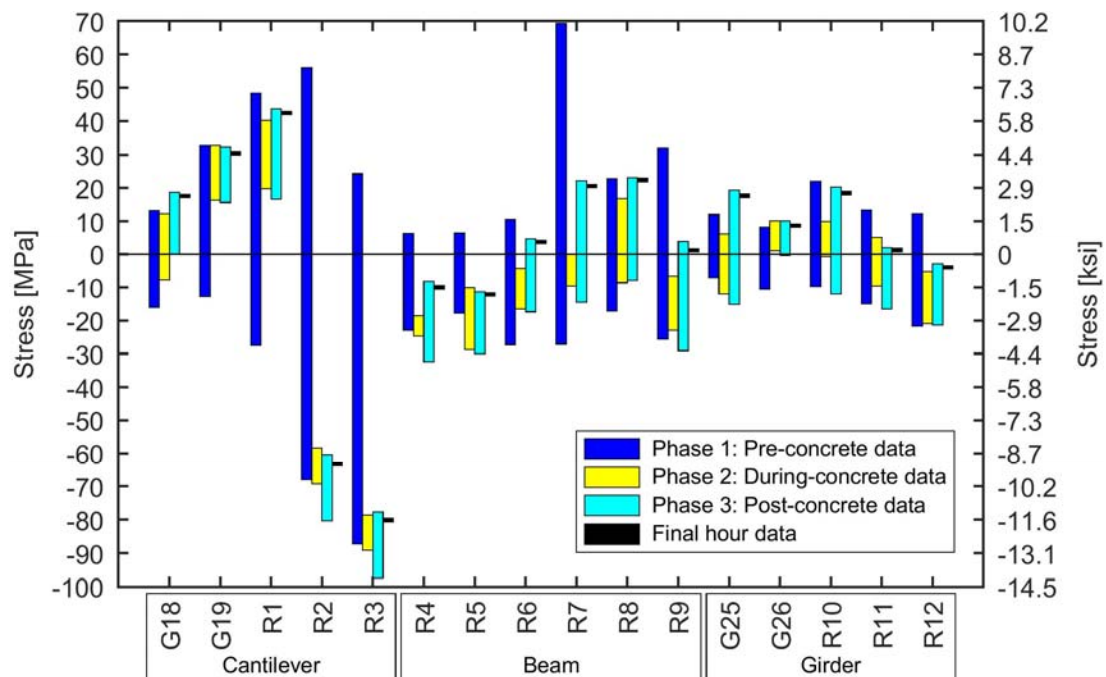


Figure 3.16: Sustained connection area stress data during different construction phases

The maximum compressive and tensile stresses for each construction phase for each member with connection area gauges are summarized in Table 3.6. The maximum compression stress for all phases was recorded in R3 which was the gauge measuring strain perpendicular to the Cantilever length. This is a reasonable result

since the gauge was placed next to a support (Short Column, supporting the Cantilever) and therefore high stresses at that point were expected. The maximum tension stress location varied by construction phase. However, the overall maximum tension stress was 69.4 MPa (10.1 ksi) during the pre-construction phase in gauge R7. The absolute maximum stress value in the connection areas of the instrumented members was 97.4 MPa (14.1 ksi) which is 28.2% of the yield stress of the instrumented steel members.

Table 3.6: Construction phase connection area stress data summary

Steel Member Name	Maximum Compression						Maximum Tension					
	Pre-Concrete		During Concrete		Post-Concrete		Pre-Concrete		During Concrete		Post-Concrete	
	MPa (ksi)	Loc.	MPa (ksi)	Loc.	MPa (ksi)	Loc.	MPa (ksi)	Loc.	MPa (ksi)	Loc.	MPa (ksi)	Loc.
Cantilever <sup>a</sup>	-87.2 (-12.6)	R3	-89.1 (-12.93)	R3	-97.4 (-14.1)	R3	56.0 (8.12)	R2	40.2 (5.83)	R1	43.7 (6.34)	R1
Girder <sup>b</sup>	-21.7 (-3.15)	R12	-20.9 (-3.04)	R12	-21.3 (-3.10)	R12	22.0 (3.19)	R10	10.1 (1.47)	G26	10.1 (1.47)	G26
Beam <sup>c</sup>	-27.3 (-3.96)	R6	-28.7 (-4.17)	R5	-32.4 (-4.70)	R4	69.4 (10.1)	R7	16.8 (2.44)	R8	23.2 (3.36)	R8

<sup>a</sup> See Figure 3.8 for strain gauge location

<sup>b</sup> See Figure 3.9 for strain gauge location

<sup>c</sup> See Figure 3.10 for strain gauge location

### 3.3.1.4.3 Member Forces Results

The ranges of axial forces obtained using the methodology for determining member forces described in Section 3.2.5 and final hour averages are shown in Figure 3.17. The maximum axial compression value was found to be -361 kN (-81 kip) in GS6 (at the bottom of the Short Column). The maximum axial tension force was found to be 254 kN (57 kip) in GS12 (on the Cantilever close to its connection to the Beam). The highest axial forces being compressive in both the Long and the Short Column was as expected based on conventional design assumptions. The expected magnitude of these forces resulting from conventional design assumptions was found by creating a simple structural model of the building using STAAD.Pro v8i software (*STAAD.Pro. 8i*). These are shown as theoretical values in Figure 3.17. This showed that the Long Column values compared well to theoretical expectations (3.5% difference on average for the two gauge sets) but that there was a 76% difference on average for the two gauge sets of the Short Column.

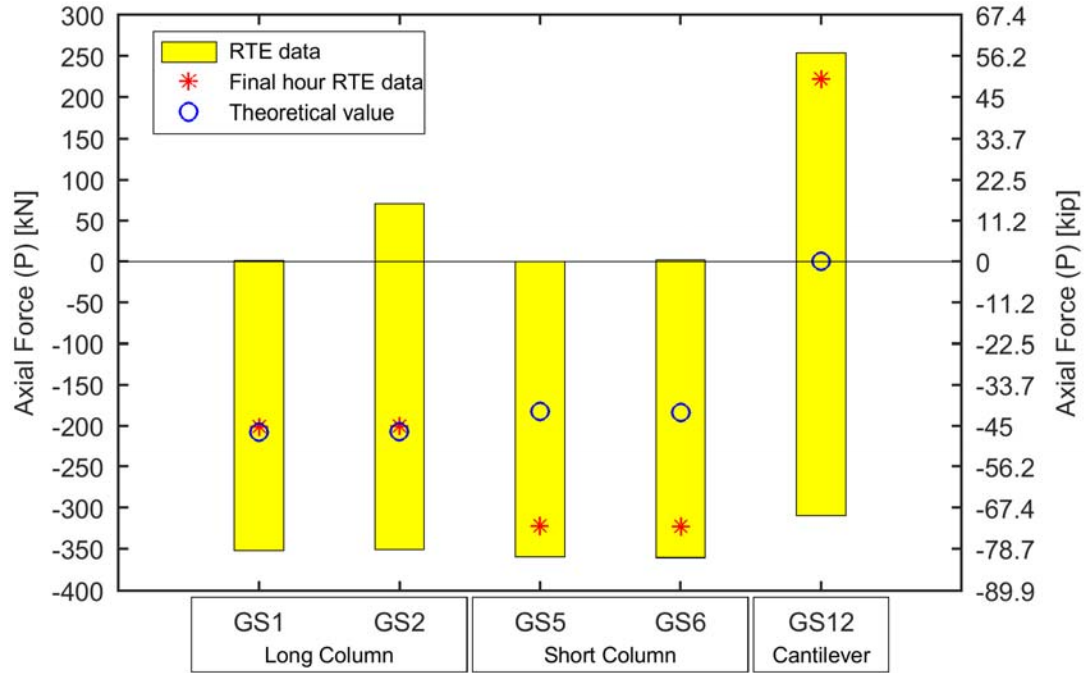


Figure 3.17: Overall maximum sustained RTE axial force data

One possible explanation for this was the effect of temperature. If the Short Column was fully restrained and exposed to 1 °C (1.8 °F) temperature change, the resulting axial force would be 14 kN (3.1 kip). Therefore, the difference between the average final hour value and the theoretical value of 139 kN (31 kip) for GS5 and GS6 corresponded to a 10 °C (18 °F) temperature difference, which was reasonable compared to the actual temperature change of 15 °C (26 °F) experienced by the member. The axial force at the center of the Cantilever (in GS12), significantly differed from typical assumptions about building behavior, which would presume that the axial force in this member would be small. This could be due to temperature or other forces being axially restrained. It was also noted that this calculation was based on the simpler three gauge approach for solving for member forces because there were

only three gauges measuring strain in the Cantilever gauge set and that this gauge set was only 60 mm (2.5 in.) from the connection between the Beam and the Cantilever. Thus, local warping affects may have contributed error to this calculation.

The ranges of internal moments and final hour averages calculated on each cross-section are plotted in Figure 3.18. The maximum strong axis moment was found to be 52 kNm (38 kip\*ft.). This was recorded in GS12, at mid-span of the Cantilever, which was expected due to the applied gravity loads.

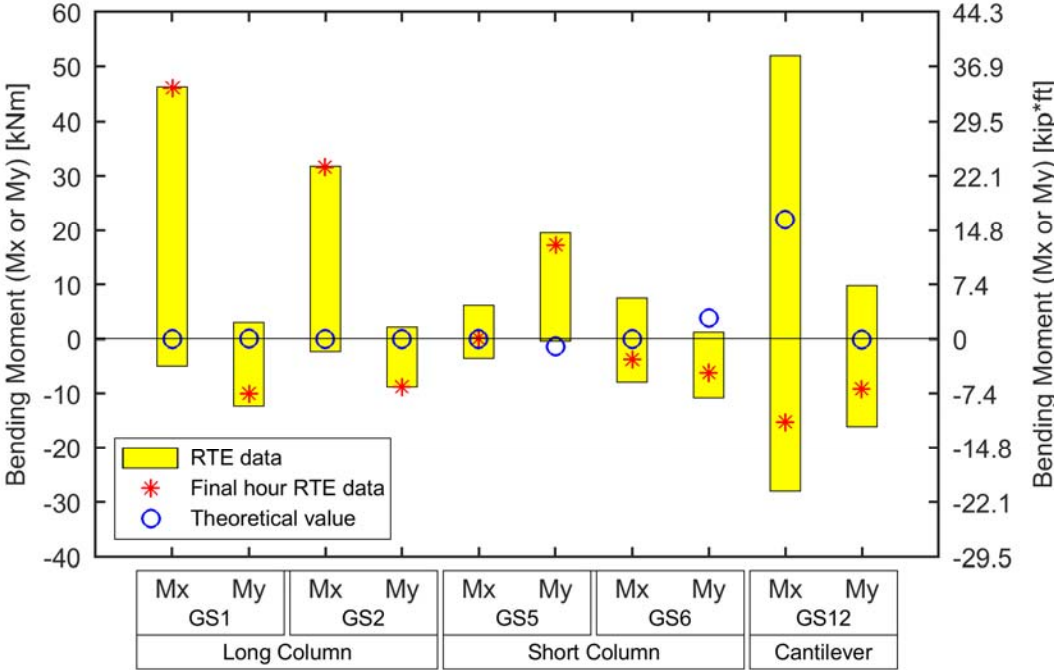


Figure 3.18: Overall maximum sustained RTE bending moment data

The weak axis moment recorded in the Cantilever was unexpected relative to traditional design assumptions, which would typically neglect weak axis bending in this member. However, the reported values were not unreasonable considering the

instrumented location was near the Beam-to-Cantilever connection and it was possible that the adjoining member caused translation and / or rotation of the Cantilever. This was also a possible explanation for why the final hour strong axis moment in GS12 was negative, the opposite of the theoretical value, based on a more detailed review of the individual gauge readings at this location. The maximum absolute weak axis moment was 19.6 kNm (14.4 kip\*ft.) and was recorded in GS5 (at the top of the Short Column). Other magnitudes of strong and weak axis bending moments in the columns were also higher than expected. If these moments were solely due to eccentricity of the axial load, this would represent an eccentricity of 240 mm (9.45 in.) for the maximum strong axis moment in GS1. Thus, it was inferred that these moments were caused by some combination of eccentric loading, joint rotations at the columns (which could have resulted from unequal dead loads on the adjoining members), and a temperature gradient throughout the cross-section. It was also noted that the bending moments were not generally converging to zero at the end of the data collection process, as indicated by the final hour data. Therefore, these bending moments were not due to temporary eccentricity or asymmetry. The torsion results were found to be less than 1 kNm (0.7 kip\*ft.) throughout the recording period in all gauge sets and were thus not presented here for brevity.

To compare the field data to theoretical expectations, the stresses at each strain gauge location were calculated from the axial force and moments obtained from the STAAD model discussed above. These stresses were compared to the final hour stresses from the field data (previously shown in Figure 3.17 and 3.18) and the comparison is plotted in Figure 3.19. The observed stress values differed greatly in some cases. The maximum difference was for G9 where the difference was 120 MPa

(18 ksi), but in this case both the measured and expected stress were in compression. Other values matched better but were observed as being in tension where compression was expected (e.g., G6) or vice versa (e.g., G21). These differences were in agreement with findings discussed above, suggesting the presence of bending moments in columns and influence of temperature in the field data.

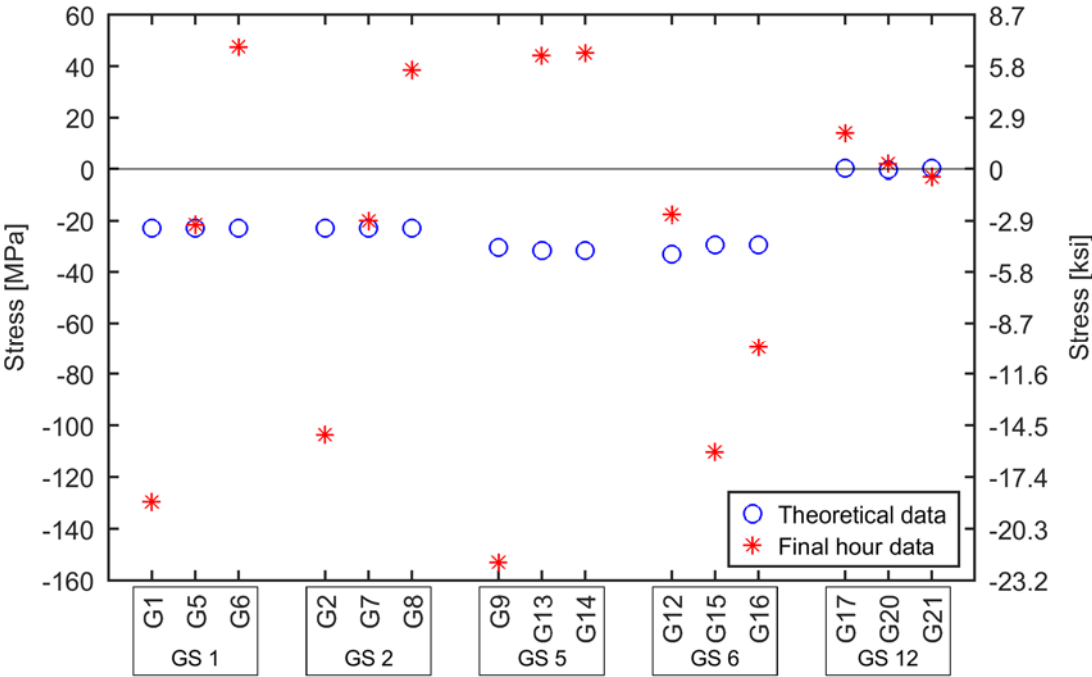


Figure 3.19: Theoretical stress data (STAAD) compared to final hour field data

**3.3.1.4.4 Evaluation of Member Forces**

The multi-axial member forces discussed in the previous section were assessed relative to member capacities under these stress states and thus their suitability for reuse. The AISC Steel Construction Manual (AISC, 2017), Chapter H equations (H1-

1a and H1-1b), reproduced as Eqns. 3.6 and 3.7, assess the applied axial and flexural stress relative to member capacity:

$$\text{When } \frac{P_r}{P_c} \geq 0.2: \quad \frac{P_r}{P_c} + \frac{8}{9} * \left( \frac{M_{rx}}{M_{cx}} + \frac{M_{ry}}{M_{cy}} \right) \leq 1.0 \quad (3.6)$$

$$\text{When } \frac{P_r}{P_c} < 0.2: \quad \frac{P_r}{2*P_c} + \left( \frac{M_{rx}}{M_{cx}} + \frac{M_{ry}}{M_{cy}} \right) \leq 1.0 \quad (3.7)$$

where  $P_r$  is the required axial strength,  $P_c$  is the design axial strength,  $M_{rx,y}$  and  $M_{ry,x}$  are the required flexural strengths for the strong and weak axis directions, respectively, and  $M_{ux}$  and  $M_{uy}$  are the design flexural strengths for the strong and weak axis direction, respectively. The flexural design strengths in Eqns. 3.6 and 3.7 ( $M_{cx}$  and  $M_{cy}$ ) have a maximum value of the plastic moment capacity ( $M_p$ ) in AISC (2017).

Since structural steel is only ideal for reuse if the yield limit has not been exceeded (no residual strain), design yield moments ( $M_{yx}$  and  $M_{yy}$  about the strong and weak axis, respectively) were conservatively computed by multiplying the respective section moduli by the minimum specified yield stress and the AISC flexural resistance factor of 0.9.  $M_{cx}$  and  $M_{cy}$  in Eqns. 3.6 and 3.7 were replaced with the design yield moment in Eqns. 3.8 and 3.9 to assess the measured stresses relative to suitability for reuse, after confirming this was less than the lateral torsional buckling capacity.

$$\text{When } \frac{P_r}{P_c} \geq 0.2: \quad \frac{P_r}{P_c} + \frac{8}{9} * \left( \frac{M_{rx}}{M_{yx}} + \frac{M_{ry}}{M_{yy}} \right) \leq 1.0 \quad (3.8)$$

$$\text{When } \frac{P_r}{P_c} < 0.2: \quad \frac{P_r}{2*P_c} + \left( \frac{M_{rx}}{M_{yx}} + \frac{M_{ry}}{M_{yy}} \right) \leq 1.0 \quad (3.9)$$

For tensile yield capacity, all gauge sets were located in gross cross-sections (no bolt holes in the cross-section), which resulted in applying a tension resistance

factor of 0.9 to the product of the area and the minimum specified yield stress. For compressive capacity, AISC (2017) equations were used with a resistance factor of 0.9 and a buckling coefficient ( $k$ ) assuming a fixed connection at the bottom of the Long Column and that all other connections were pinned, resulting in a value of 0.8 for the Long Column and 1.0 for the other members. Conservatively, all member cross-sections were assumed to be non-composite sections (including the Cantilever after concrete was poured). Eqns. 3.8 and 3.9 were used to calculate the yield ratios of each gauge set for each point in time where a maximum in the individual force effects occurred.

The overall maximum ratios resulting from this process and the corresponding axial forces ( $P_r$ ) and moments ( $M_{rx}$  and  $M_{ry}$ ) were summarized in Table 3.7. As shown in Table 3.7, the maximum calculated ratio from Eqn. 3.8 or 3.9 was found to be 0.55, at the top of the Short Column. Slightly lower ratios occurred in GS1 and GS2 corresponding to the Long Column. A very low maximum ratio of 0.07 was found in GS12 corresponding to the Cantilever. Therefore, it was concluded that the applied construction forces did not cause any yielding in any of the instrumented steel sections.

Table 3.7: Applied member forces and moments relative to multi-axial yield criteria

Gauge Set (GS)	Applied forces and moments			Yield forces and moment			Ratios			Eqn. 3.8 or Eqn. 3.9 Ratio
	$P_r$	$M_{rx}$	$M_{ry}$	$\phi P_c$	$\phi M_{yx}$	$\phi M_{yy}$	$P_r/P_c$	$M_{rx}/M_{yx}$	$M_{ry}/M_{yy}$	
	kN (kip)	kNm (kip*ft.)	kNm (kip*ft.)	kN (kip)	kNm (kip*ft.)	kNm (kip*ft.)				
1 <sup>a</sup>	352 (79.2)	38.5 (28.4)	12.3 (9.10)	2140 (481)	220 (162)	85.0 (62.5)	0.16	0.18	0.15	0.40
2 <sup>a</sup>	351 (78.9)	26.2 (19.3)	9.30 (6.90)	2140 (481)	220 (162)	85.0 (62.5)	0.16	0.12	0.11	0.31
5 <sup>b</sup>	360 (80.9)	1.80 (1.30)	16.6 (12.2)	1416 (318)	140 (103)	52.4 (38.6)	0.25	0.01	0.32	0.55
6 <sup>b</sup>	361 (81.1)	7.90 (5.90)	8.80 (6.50)	1416 (318)	140 (103)	52.4 (38.6)	0.25	0.06	0.17	0.46
12 <sup>c</sup>	254 (57.1)	21.2 (15.6)	9.90 7.30	5330 (1198)	1673 (1234)	340 (250)	0.05	0.01	0.03	0.07

<sup>a</sup> See Figure 3.6 for strain gauge location

<sup>b</sup> See 3.7 for strain gauge location

<sup>c</sup> See 3.8 for strain gauge location

### **3.3.2 STAR Tower**

Based on knowledge acquired during the Purnell Hall Addition field instrumentation the instrumentation for this building was planned. It was decided to instrument five structural steel members, three connected steel members on the first floor (one column and two 2<sup>nd</sup> floor beams) and two connected members on a higher floor (one column and one connected beam). However, the owner of the building requested to end the field instrumentation project after 43 days of data collection. During this time period only the first-floor steel members were erected and therefore, only three steel members are discussed in this section. The collected data is processed similar to the Purnell Hall Addition data and the results are organized in the same order.

#### **3.3.2.1 Building Information**

The second instrumented building was the STAR Tower on the University of Delaware STAR Campus in Newark, DE. The building was selected for instrumentation because of its close proximity to the University of Delaware's main campus, its multistory steel frame design and its use as a commercial building. For this building, the data acquisition laptop was stored in the construction site office and the camera was located outside the same office.

The building had 10 floors, a total area of 9,000 m<sup>2</sup> (97,500 ft.<sup>2</sup>), and was used for office space, conference rooms, and classrooms. A 3D overview of the steel frame of the building is shown in Figure 3.20. The building was 23 m (75 ft.) wide, 40 m (130 ft.) long and 49 m (160 ft.) tall. The steel frame was constructed of a wide range of hot rolled A992 W-sections with a yield strength of 345 MPa (50 ksi). The typical story height was approximately 4.5 m (15 ft.) and the maximum beam span was 12.8

m (42 ft.). The beams of the building were built composite with 80 mm (3.25 in.) concrete slab floors, which were fabricated using stay-in-place metal deck forms.

### 3.3.2.2 Instrumentation

The instrumentation for the STAR Tower was guided by the information gathered from the Purnell Hall Addition field instrumentation. Therefore, to collect data from the beginning of the erection phase of the building, one first floor column (labeled as Column) and two connecting 2<sup>nd</sup> floor flexural members (labeled as Girder and Beam) were selected for instrumentation as shown in Figure 3.20.

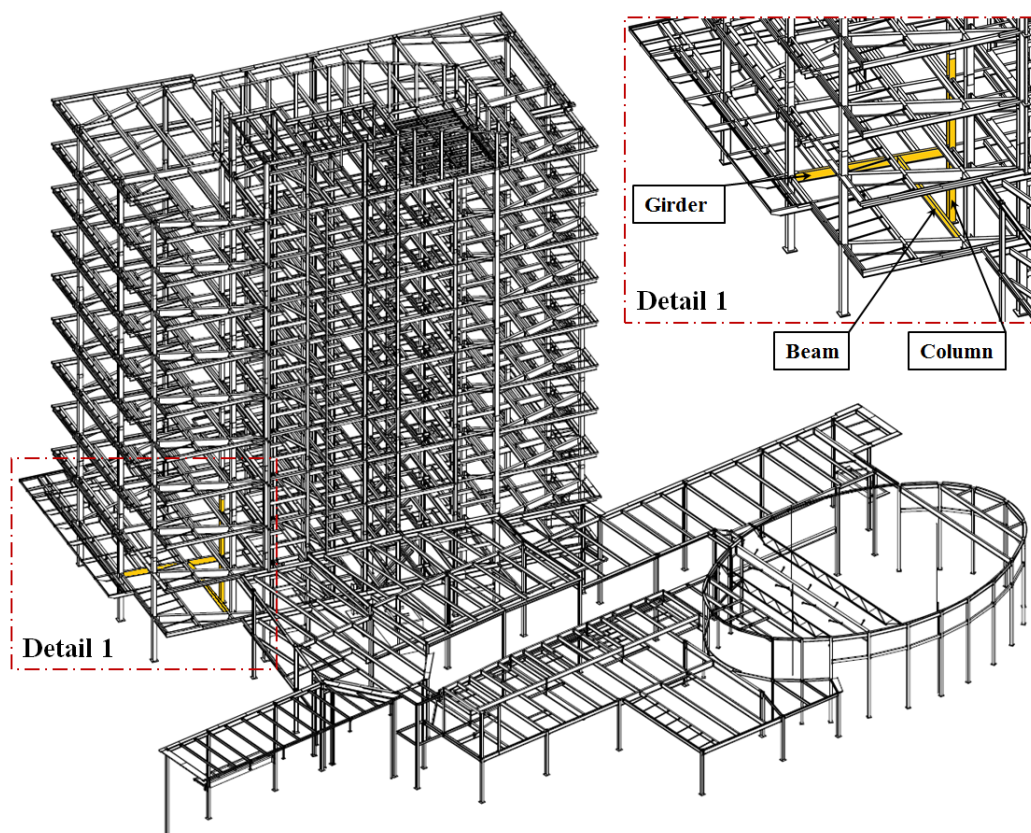


Figure 3.20: STAR Tower steel frame with instrumented members highlighted and named (Adapted from Mid Atlantic Steel, LLC)

The instrumented steel members were selected based on their location in the building (i.e. away from shear walls, elevator areas, and not connected to the façade, to simplify the load path to the instrumented members), the complexity of the connection (simple connections were preferred) and the generality of the member. The Beam was selected for instrumentation because it is a generally used floor beam in the entire building. The Girder was selected similar to the Beam based on its general use in the building and it was the steel member that connected the Beam to the Column. The Column was selected for instrumentation based on its proximity to the construction office and therefore the data acquisition laptop, and because it was a generally used interior column of the building. The instrumented steel members are summarized in Table 3.8.

Table 3.8: Details of instrumented STAR Tower members

<b>Label</b>	<b>Cross-section</b>	<b>Length [m] (ft.-in.)</b>	<b>Floor(s)</b>	<b>Date of installation</b>	<b>Detail drawings</b>
Column	W360x196 (W14x132)	10.6 (34-8 1/2)	1 – 3	05/09/2017	Figure 3.21
Girder	W610x101 (W24x68)	8.7 (28-7 9/16)	2	05/09/2017	Figure 3.22
Beam	W530x66 (W21x44)	11.5 (37-9 1/16)	2	05/09/2017	Figure 3.23

The instrumentation drawings for the three steel members are shown in Figure 3.21 through 3.23. Similar to the Purnell Hall Addition instrumentation layout, the strain gauges are labeled with “G” and followed by an arbitrary number. Furthermore,

the strain gauges were arranged in gauges sets (GS) as described in Section 3.3.1.2 and a temperature gauge (G4) was installed on the long column as shown in Figure 3.21 (Temp. Gauge Detail).

For this instrumentation two WSN were placed on the Column (either side of the web), three on the Girder (two on one side and one on the opposite side, as shown in Figure 3.22), and one WSN on the Beam as shown in Figure 3.23. All strain gauges on the flanges of the W sections were placed 12.7 mm (0.5 in.) away from the tip of the flange as shown in Section B-B in Figure 3.21. The locations of the strain gauges along the length of each member and on the web of the W sections are variable and are provided in the following drawings. The strain rosettes were created using three individual strain gauges as shown in the Rosette Detail in Figure 3.22.

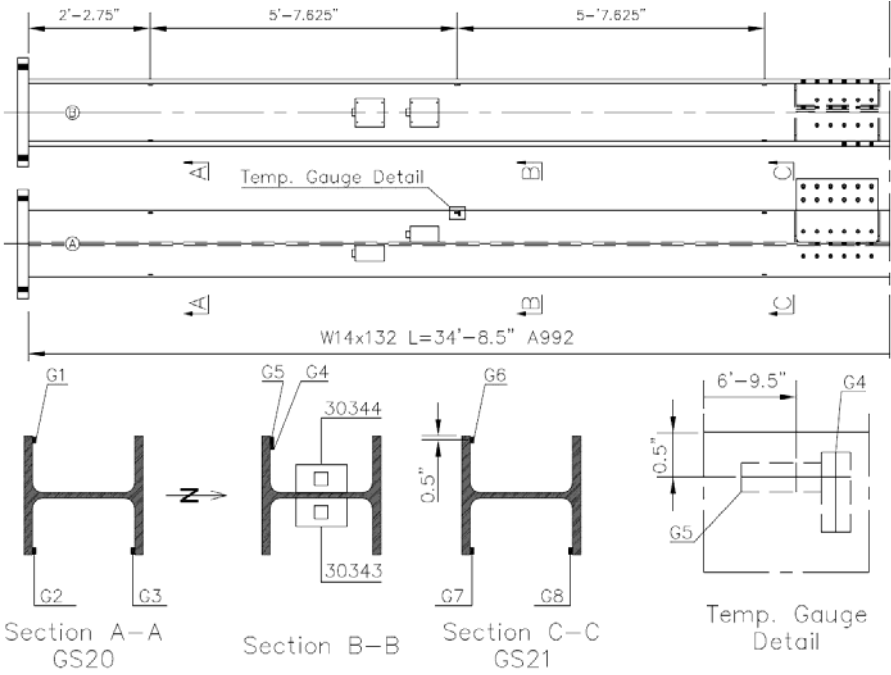


Figure 3.21: STAR Tower Column instrumentation drawing

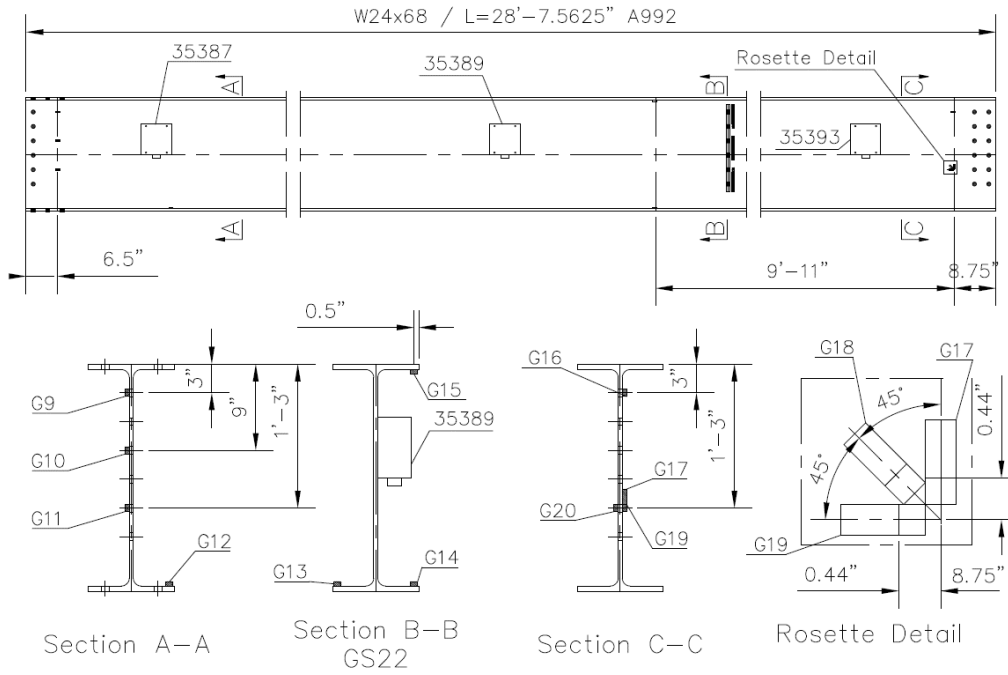


Figure 3.22: STAR Tower Girder instrumentation drawing

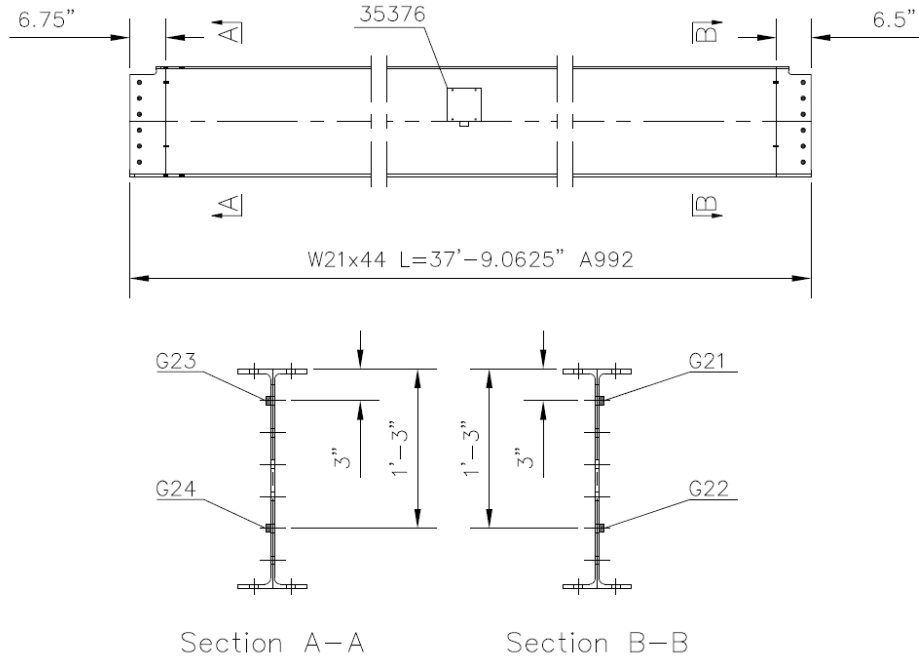


Figure 3.23: STAR Tower Beam instrumentation drawing

### 3.3.2.3 Field Data Collection

Data collection started on May 05<sup>th</sup> 2017, when the three instrumented steel members were delivered to the construction site. Data was collected continuously at 16 Hz for the first 4 weeks of building construction. On June 05<sup>th</sup> 2017 the data collection was halted during nights to conserve battery life of the WSN. The data collection was ended at the building owners request on June 19 2017. During the data collection period the steel structure for the first 7 floors of the tower were assembled (as shown in Figure 3.24), metal formwork for the first four floors was installed, and the concrete slab for the second floor was poured.



Figure 3.24: Construction site camera image of the construction progress on June 19, 2017

The strain gauge data for GS22 on the Girder (Figure 3.22) for the entire data collection period was converted to stress using Hooke's law with an assumed Young's modulus of 200,000 MPa (29,000 ksi) and is shown in Figure 3.25 for demonstration purposes. The collected WSN Temperature is shown on the top of the figure. The most distinctive change in the strain gauge data happens on June 7th, when the 2nd floor concrete floor was poured. The stress in the bottom flange strain gauges (G13 and G14) of the Girder increase (tension stress) and the values of top flange strain gauge (G15) decreases (compressive stress) indicating an expected positive moment in the Girder due to the increased dead load on top of the Girder due to the poured concrete.

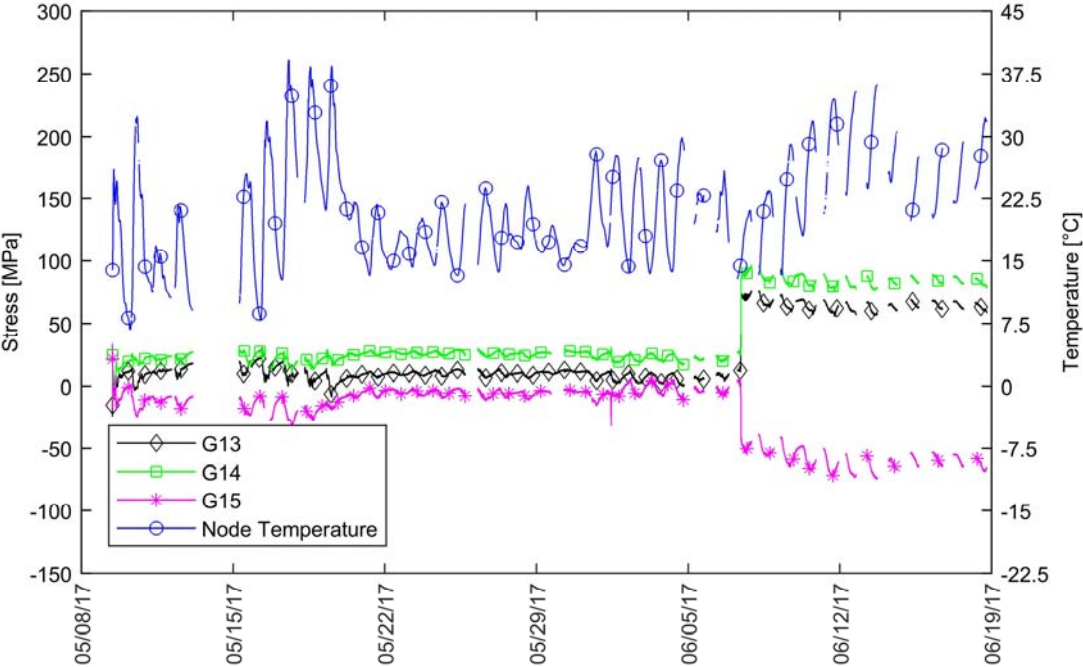


Figure 3.25: STAR Tower Girder strain gauge data for the entire data collection period

### **3.3.2.4 Results**

The result section for the STAR Tower data is organized similar to the Purnell Hall Addition data results. First the maximum sustained and impact stresses for each member and connection area strain gauge was calculated. Next, the member forces for the three GS locations on the Column and the Girder were calculated using the TGA and the OA. Lastly, the member forces were evaluated using the same approach as described in Section 3.3.1.4.4.

#### **3.3.2.4.1 Maximum Sustained and Impact Stress Results**

The collected strain data was separated into sustained and impact data as described in Section 3.2.4. The results for the strain gauges were split into member strain gauges and connection area strain gauges. The member strain gauges were located along the length of the steel member away from the connection area and the results are shown in Figure 3.26 and summarized in Table 3.9. The Beam did not have member strain gauges and was therefore not included in Figure 3.26 and in Table 3.9. The connection area strain gauges were located in the connection area of the steel members and their results are summarized in Figure 3.27 and Table 3.10. The column did not have any connection area strain gauges and was therefore not included in Figure 3.27 and Table 3.10.

Figure 3.26 shows that seven of the twelve maximums from the member strain gauges of the STAR Tower data were impact values. However, the magnitude of the recorded impact values was small (maximum impact value at G12 was -48.3 MPa (-7.00 ksi)) compared to the yield stress of the steel members of 345 MPa (50 ksi). Furthermore, the overall maximum value and minimum value of the member strain gauges were sustained values.

The maximum and minimum sustained stress values for the Column and the Girder are summarized in Table 3.9. The maximum (tension) sustained value was found, in G14, to be 96.7 MPa (14.0 ksi) and the minimum (compression) sustained value was -74.8 MPa (-10.8 ksi), in G15. Both, G14 and G15 were located at the center of the Girder as shown in Figure 3.22. These two gauges having the highest stresses seems logical, since only the concrete floor on the 2nd floor (right above the Girder) was poured before data collection was ended. This also explains the relatively small values in the maximum and minimum values for Column strain gauges. The values certainly increased significantly in compression (except strain gauge G4, which was the temperature gauge) once the concrete floors for the entire tower were poured. It is noted that for the Column the maximum tension stress was an impact value in G3 (23.1 MPa (3.35 ksi)) and the minimum compression stress was -38.0 MPa (-5.51 ksi).

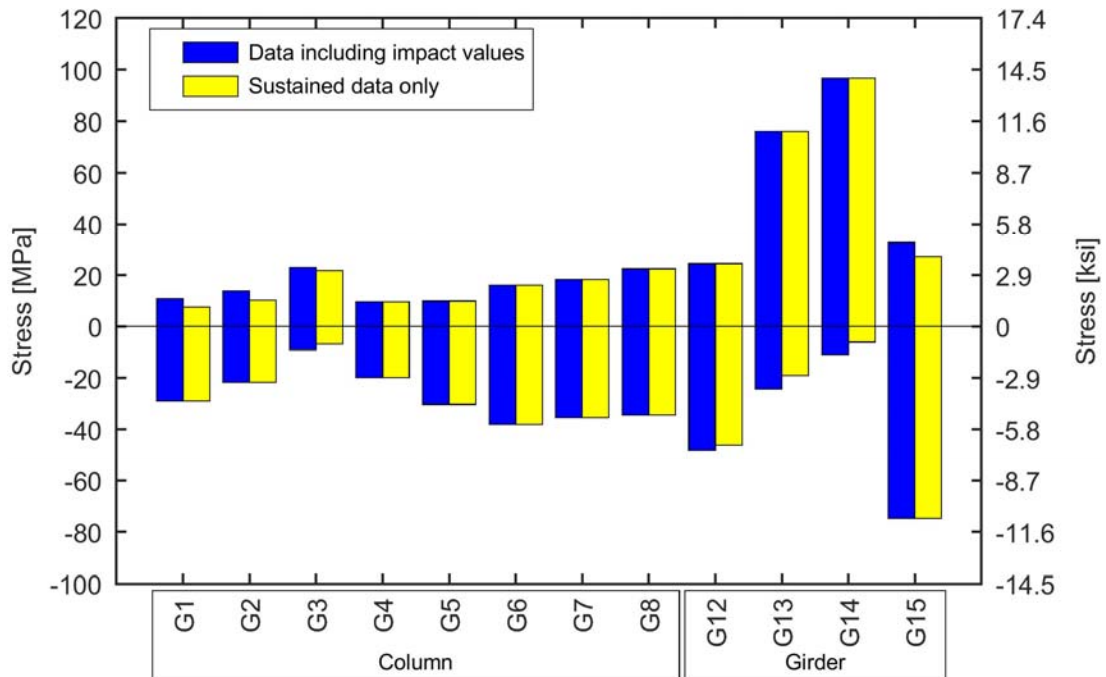


Figure 3.26: Overall maximum data, including impact values and maximum sustained data for the STAR Tower member strain gauges

Table 3.9: Summary of sustained STAR Tower member stress data

Steel Member Name	Maximum Compression		Maximum Tension	
	MPa (ksi)	Location	MPa (ksi)	Location
Column <sup>a</sup>	-38.0 (-5.51)	G6	23.1 (3.35)	G3 (impact value)
Girder <sup>b</sup>	-74.8 (-10.8)	G15	96.7 (14.0)	G14

<sup>a</sup> See Figure 3.21 for strain gauge location

<sup>b</sup> See Figure 3.22 for strain gauge location

The sustained and impact connection area strain gauge data for the STAR Tower is shown in Figure 3.27. Only two of the 12 connection strain gauges show an impact value greater than the sustained value (6.7 MPa (0.97 ksi) greater for G11 and 26.5 MPa (3.84 ksi) greater for G21, respectively). This indicates that the sustained stress in the connection area were greater than stresses caused by impact. Furthermore, the overall maximum tensile and compressive stresses for the connection area gauges was a sustained value. However, the maximum compressive stress in the connection areas of the Beam was an impact value -70.0 MPa (-10.1 ksi) in G21. Since for the Beam only connection area strain gauges were used, this stress was the highest stress recorded in the entire Beam. The maximum tension and compression stresses in the connection area are summarized in Table 3.10 (no Column data was included since the Column only had member strain gauges). The maximum tensile stress was 91 MPa (13.2 ksi), in G23 in the Beam. The maximum compressive stress was -88.2 MPa (-12.8 ksi), in G19 in the Girder.

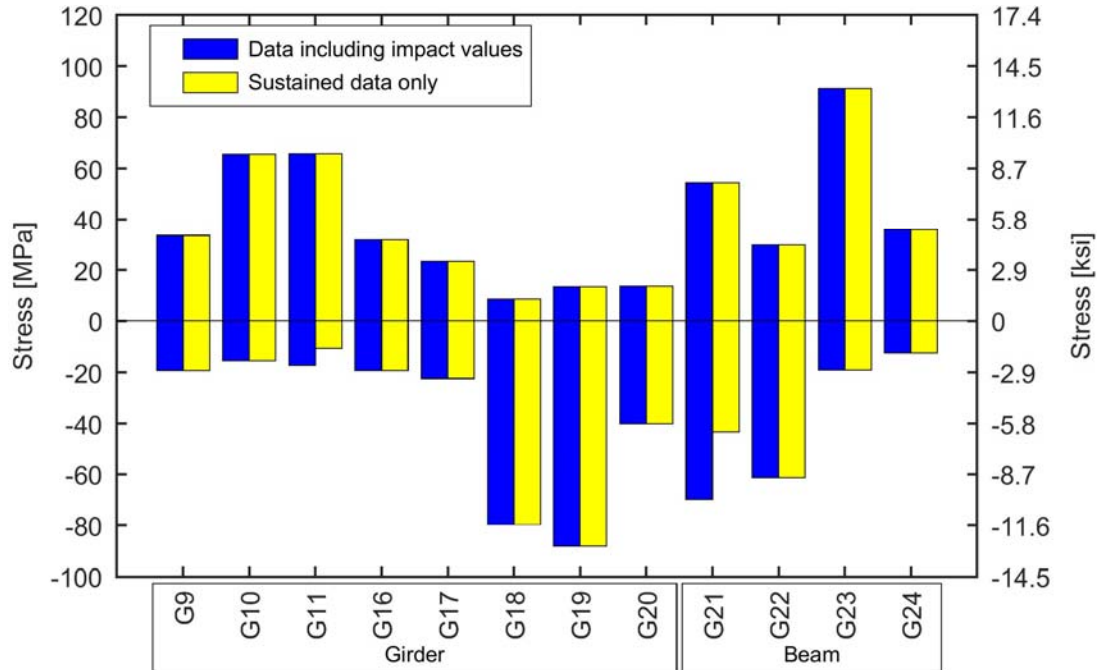


Figure 3.27: Overall maximum data, including impact values and maximum sustained data for the STAR Tower connection area strain gauges

Table 3.10: Summary of sustained STAR Tower connection area stress data

Steel Member Name	Maximum Compression		Maximum Tension	
	MPa (ksi)	Location	MPa (ksi)	Location
Girder <sup>a</sup>	-88.2 (-12.8)	G19	65.8 (9.54)	G11
Beam <sup>b</sup>	-61.4 (-8.91)	G22	91.1 (13.2)	G23

<sup>a</sup> See Figure 3.22 for strain gauge location

<sup>b</sup> See Figure 3.23 for strain gauge location

#### **3.3.2.4.2 Member Forces Results**

The member forces for the STAR Tower steel members were calculated using the same methods as described in Section 3.2.5. For the Column, a sufficient number of gauges existed to use the OA, but about 60% of G3 data was deleted during the data processing process (described in 3.2.2.2) and therefore the OA and the TGA could not be used for GS20 during the timestamps when G3 data was missing. For the Beam, only the TGA could be used based on the gauge layout of this member. The axial force results for the three GS are shown in Figure 3.28 and the bending moments are plotted in Figure 3.29. Both of these figures contain three series, the TGA data, the OA data, and the TGA data during the same times when the OA is possible to be calculated in order to evaluate the differences in the two calculation approaches.

The data shown in Figure 3.28 shows high axial compression forces (-701 kN (-158 kips)) for the TGA for GS21 since this data included the data collected during and after the second-floor concrete was poured while the OA data did not. This was confirmed by the limited TGA data for GS21. The OA for both GS20 and GS21 show a lower but similar axial force (-326 kN (-73.4 kips)) for both gauge sets. The tension axial forces for GS20 and GS21 were smaller than the compression forces which was expected since columns are theoretically expected to only have compression axial forces. The maximum axial tension force was 241 kN (54.2 kips) for GS22. This axial force was higher than expected, since floor beams are usually designed to have no axial force. However, the same trend was found in the Purnell Hall Addition data (Section 3.3.1.4.3, GS12).

The difference between the axial force for GS 20 and GS21 for the TGA was a result of missing data for strain gauge G3. Strain gauge G3 is used to calculate member force values for GS20. Therefore, it was expected that the TGA for GS 20

would show lower results than the TGA for GS21 since the data for GS20 only included data for the start of the building process and not all the data that was used for the GS21 results.

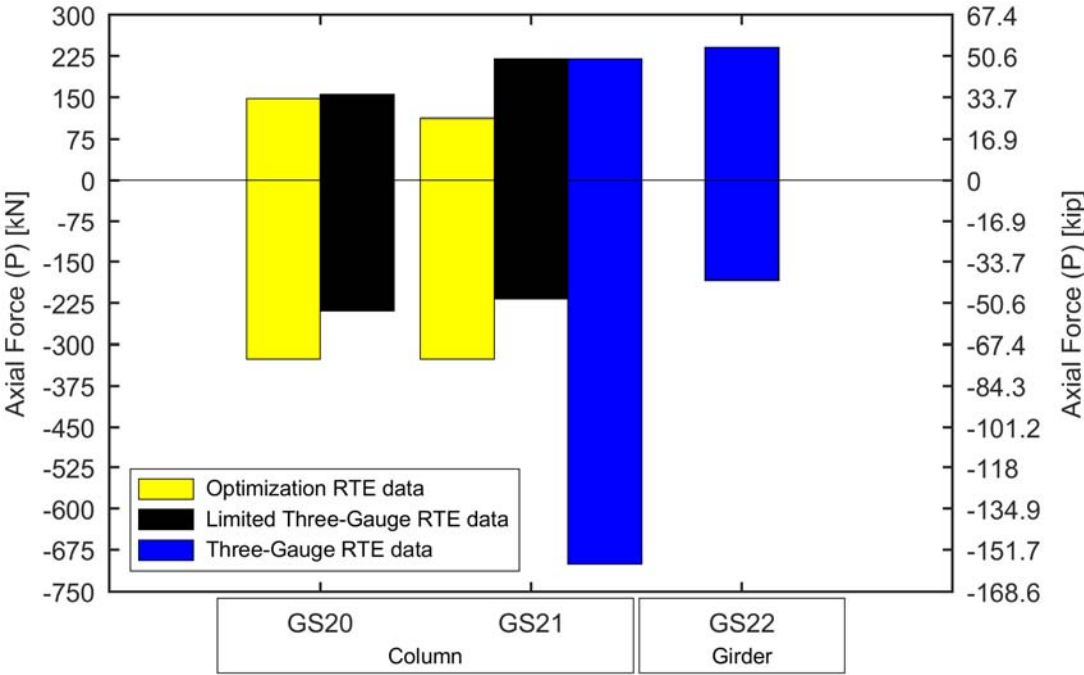


Figure 3.28: Overall STAR Tower maximum sustained RTE axial force data

The maximum strong axis moment for the three gauge sets shown in Figure 3.29 was calculated using the TGA for GS22 located on the Girder and was 204 kNm (150 kip\*ft). The moment was positive which was expected, since the gauge set was located at the center of the girder and had a uniformly distributed dead load (concrete floor) applied. The maximum weak axis moment was 35.1 kNm (25.9 kip\*ft) in GS20. Similar to the Purnell Hall Addition Data the moments calculated for the columns were higher than expected since these are usually assumed to be zero. The differences

between the TGA and the OA for the bending moments were assumed to be due to torsional forces that were accounted for in the OA but not in the TGA.

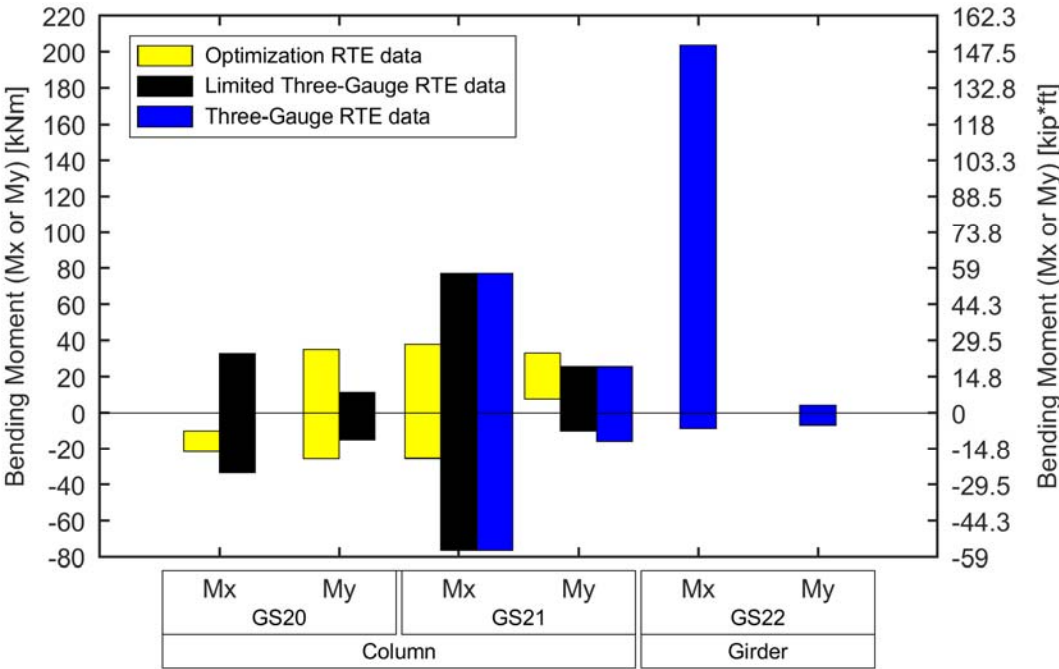


Figure 3.29: Overall STAR Tower maximum sustained RTE bending moment data

**3.3.2.4.3 Evaluation of Member Forces**

The calculated member forces from the previous section were evaluated using the same approach as described in Section 3.2.5. For compressive capacity, a buckling coefficient (*k*) assuming a fixed connection at the bottom of the Column and that all other connections were pinned, resulted in a value of 0.8 for the Column and 1.0 for the Girder. The Beam was not included in these calculations since member forces could not be calculated with the used strain gauge layout. Conservatively, all member cross-sections were assumed to be non-composite sections (including the Girder after

concrete was poured). Eqns. 3.8 and 3.9 were used to calculate the yield ratios of each gauge set for each point in time where a maximum in the individual force effects occurred.

The overall maximum ratios resulting from this process and the corresponding axial forces ( $P_r$ ) and moments ( $M_{rx}$  and  $M_{ry}$ ) were summarized in Table 3.11. The table shows the highest ratio from Eqn. 3.8 or 3.9 occurred at GS22, at the center of the Girder. This ratio is dominated by the strong axis moment, which was expected based on the primary loading being the distributed load of the concrete floor. The lower ratios for the Column GS were also expected since most of the design dead load from the concrete floors had not yet been applied. Therefore, it was concluded that the applied construction forces did not cause any yielding in any of the instrumented steel sections of the STAR Tower during the data collection period.

Table 3.11: Applied member forces and moments relative to multi-axial yield criteria for the STAR Tower

Gauge Set (GS)	Applied forces and moments			Yield forces and moment			Ratios			Eqn. 3.8 or Eqn. 3.9 Ratio
	$P_r$	$M_{rx}$	$M_{ry}$	$\phi P_c$	$\phi M_{yx}$	$\phi M_{yy}$	$P_r/P_c$	$M_{rx}/M_{yx}$	$M_{ry}/M_{yy}$	
	kN (kip)	kNm (kip*ft.)	kNm (kip*ft.)	kN (kip)	kNm (kip*ft.)	kNm (kip*ft.)				
20 <sup>a</sup>	239 (53.8)	33.0 (24.3)	15.0 (11.1)	6977 (1568)	1063 (784)	379 (279)	0.03	0.03	0.04	0.09
21 <sup>a</sup>	203 (45.6)	76.4 (56.3)	6.35 (11.1)	6977 (1568)	1063 (784)	379 (279)	0.03	0.07	0.02	0.10
22 <sup>b</sup>	107 (24.1)	204 (150)	3.03 (2.23)	2648 (595)	783 (578)	79.8 (58.9)	0.04	0.26	0.04	0.32

<sup>a</sup> See Figure 3.21 for strain gauge location

<sup>b</sup> See Figure 3.22 for strain gauge location

### **3.3.3 BPI Building**

This building was instrumented after the data collection of the STAR Tower ended. The instrumentation of five selected steel members was based on the knowledge gained from the Purnell Hall Addition and STAR Tower instrumentation. Two columns and three beams on two different floors of the building were selected for instrumentation. Furthermore, it was decided to keep part of the WSN (six nodes on three steel members) in the building to collect data during the entire construction process and during the service life of the building. Continuous data collection was started on March 9<sup>th</sup> 2018 and was ended on November 27<sup>th</sup> 2018. The continuous data collection was ended since the WSN was not able to connect to the data acquisition laptop anymore. The next step in the data collection process was to relocate the data acquisition laptop closer to the WSN nodes into the instrumented building. However, this data was not included in this dissertation.

#### **3.3.3.1 Building Information**

The third instrumented building was the Biopharmaceutical Innovation (BPI) Building located on the STAR Campus close to the University of Delaware main campus and in close proximity to the STAR Tower. The building is owned by the University of Delaware which facilitated the task of leaving some of the WSN nodes in the building after completion of the building, for future data collection. Both the BPI Building and the STAR Tower steel were fabricated by the same fabricator (Mid Atlantic Steel, LLC located in New Castle, DE), which simplified the instrumentation process. Furthermore, the general contractor for the Purnell Hall Addition and the BPI Building were the same (The Whiting-Turner Contracting Company), which facilitated this instrumentation.

The BPI Building has two parts. The laboratory part of the building houses research laboratories and the other part office space. The building has a total length of 89 m (292 ft.), a width of 35 m (116 ft.) and a height of 30 m (98 ft.). The first floor has a floor height of 5.5 m (18 ft.) while all other floors have a height of 4.9 m (16 ft.). The laboratory part of the building has a length of 60.5 m (198 ft) and the office part a length of 28.5 m (94 ft.). The steel frame was constructed of a wide range of hot rolled A992 W-sections with a yield strength of 345 MPa (50 ksi). The beams of the building were built composite with 114 mm (4.5 in.) concrete slab floors, which were fabricated using stay-in-place metal deck forms.

### **3.3.3.2 Instrumentation**

Based on the previous two building instrumentation projects (Purnell Hall Addition and STAR Tower) five steel member on two different floors of the BPI Building were instrumented using the WSN. The selected steel members were located in the office part of the building since in that part the used cross sections were smaller than the ones used in the laboratory part of the building. It was assumed higher construction-induced stresses would be found in smaller cross sections due to self-weight and dead load of the concrete floors.

The location of the instrumented steel members was marked in the BPI Building overview (Figure 3.30) in Detail 1 and Detail 2. The instrumented steel members are highlighted and better visible in Figure 3.31. As shown in Figure 3.31 two columns and three beams were selected for instrumentation. The 1<sup>st</sup> Floor Column (that extended into the 2<sup>nd</sup> floor) was connected to the 2<sup>nd</sup> Floor Girder which was connected to the 2<sup>nd</sup> Floor Beam. Only the edge of the 2<sup>nd</sup> Floor Beam was highlighted

in Figure 3.31, since a 3<sup>rd</sup> floor beam is blocking the view. The 5<sup>th</sup> Floor column (that extended into the 6<sup>th</sup> floor) was connected to the 6<sup>th</sup> Floor Girder.

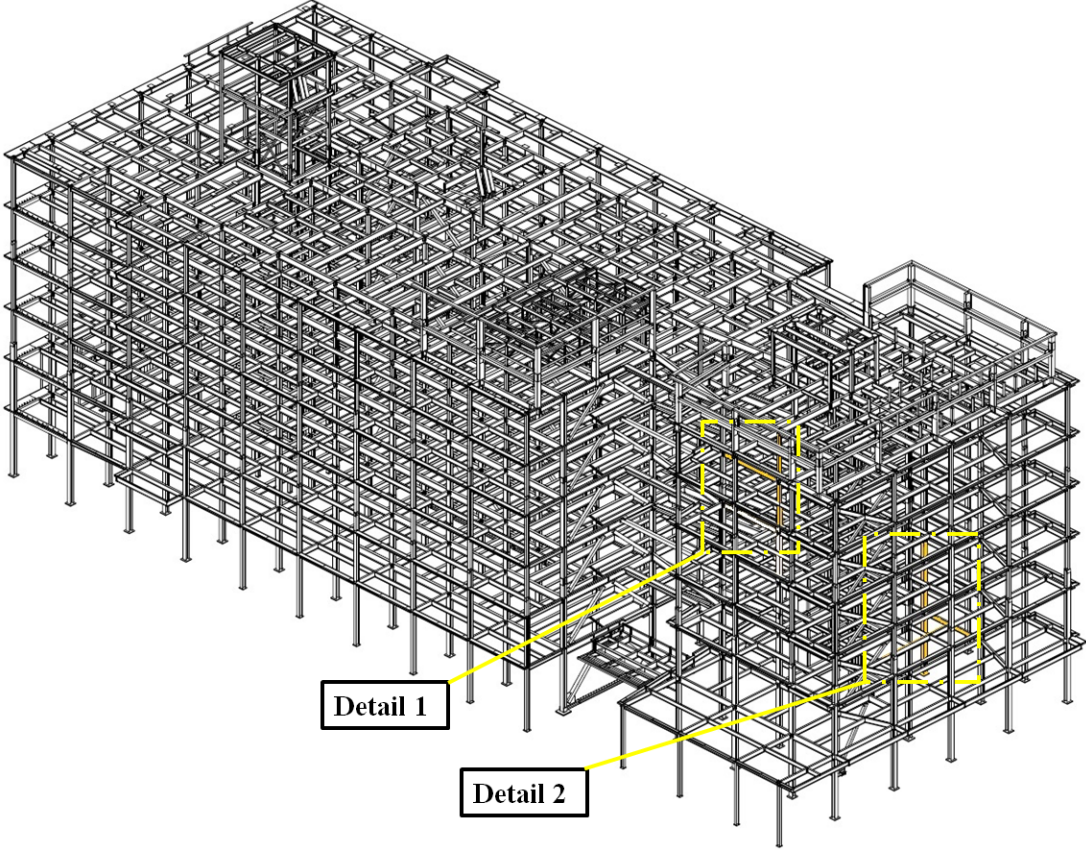


Figure 3.30: BPI Building steel frame overview with instrumented members highlighted (Adapted from Mid Atlantic Steel, LLC)

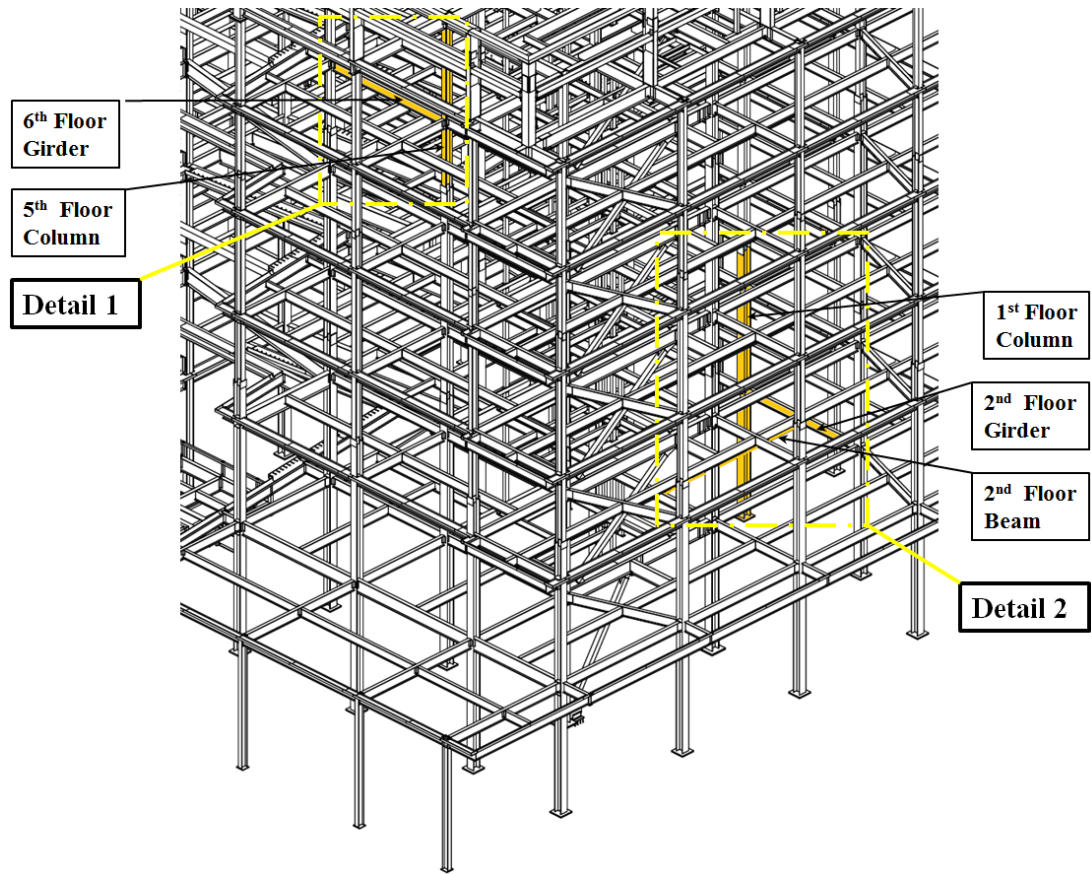


Figure 3.31: BPI Building steel frame details with instrumented members highlighted and named (Adapted from Mid Atlantic Steel, LLC)

The steel members were selected based on the Purnell Hall Addition instrumentation by selecting the 1<sup>st</sup> Floor Column as an interior column which was put in place at an early stage of the construction phase to maximize data collection time. The 2<sup>nd</sup> Floor Girder and Beam were selected since they represented a typical combination of flexural members and the Girder was connected to the 1<sup>st</sup> Floor column. The 5<sup>th</sup> Floor column was selected because it was an interior column which was representative of the columns used in multiple different locations. The 6<sup>th</sup> Floor

Girder was attached to the 5<sup>th</sup> Floor Column. The five selected steel members were summarized in Table 3.12.

Table 3.12: Details of instrumented BPI Building members

<b>Label</b>	<b>Cross-Section</b>	<b>Length [m] (ft.-in.)</b>	<b>Floor(s)</b>	<b>Date of Installation</b>	<b>Detail drawings</b>
1 <sup>st</sup> Floor Column	W360x216 (W14x145)	12.6 (41-3)	1 – 3	03/12/2018	Figure 3.32
2 <sup>nd</sup> Floor Girder	W460x52 (W18x35)	6.7 (21-9 3/4)	2	03/19/2018	Figure 3.33
2 <sup>nd</sup> Floor Beam	W460x60 (W18x40)	8.5 (27-10 1/8)	2	03/19/2018	Figure 3.34
5 <sup>st</sup> Floor Column	W360x216 (W14x145)	12.6 (41-3)	5 – Roof	05/09/2018	Figure 3.35
6 <sup>th</sup> Floor Girder	W460x52 (18x35)	6.5 (21-3 3/8)	6	05/09/2018	Figure 3.36

The instrumentation drawings for the five instrumented steel members are shown in Figure 3.32 through 3.36. The strain gauges were labeled with a “G” followed by an arbitrary number and the WSN nodes were labeled with their ID number. All the flange strain gauges were typically positioned 12.7 mm (0.5 in.) away from the flange tip unless otherwise noted. The connection area strain gauge locations were given in each drawing for the corresponding strain gauge. Similar to the STAR Tower project, the strain gauge rosettes were created manually by arrainging three strain gauges as shown in the rosette detail in Figure 3.33. Two WSN nodes were

attached to each steel member expect for the 2<sup>nd</sup> Floor Girder and the 2<sup>nd</sup> Floor Beam as shown in Figure 3.33 and 3.34.

For the BPI Building instrumentation, multiple temperature strain gauges were used. One of them was located on the 1<sup>st</sup> Floor Column (Figure 3.32, G4) and four on the 5<sup>th</sup> Floor Column (Figure 3.35, G25, G27, G29, and G31). The temperature strain gauges on the 5<sup>th</sup> Floor were each paired with a longitudinal strain gauge (Figure 3.35, G26, G28, G30, and G32) at all four flange tips of a common cross-section of the W-section to assess the temperature influence across the cross-section.

A CNT-based sensing skin was manufactured at the University of Delaware and installed to the 6<sup>th</sup> Floor Girder as shown in Figure 3.36. The sensing skin was connected to a circuit box and the WSN nodes on the 6<sup>th</sup> Floor Girder. To validate the sensing skin results, four conventional strain gauges were installed on the opposite side of the web, three of them were arranged as a strain rosette as shown in Figure 3.36. More detail about fabrication of the sensing skin, the field installation process and results are described in Chapter 4.

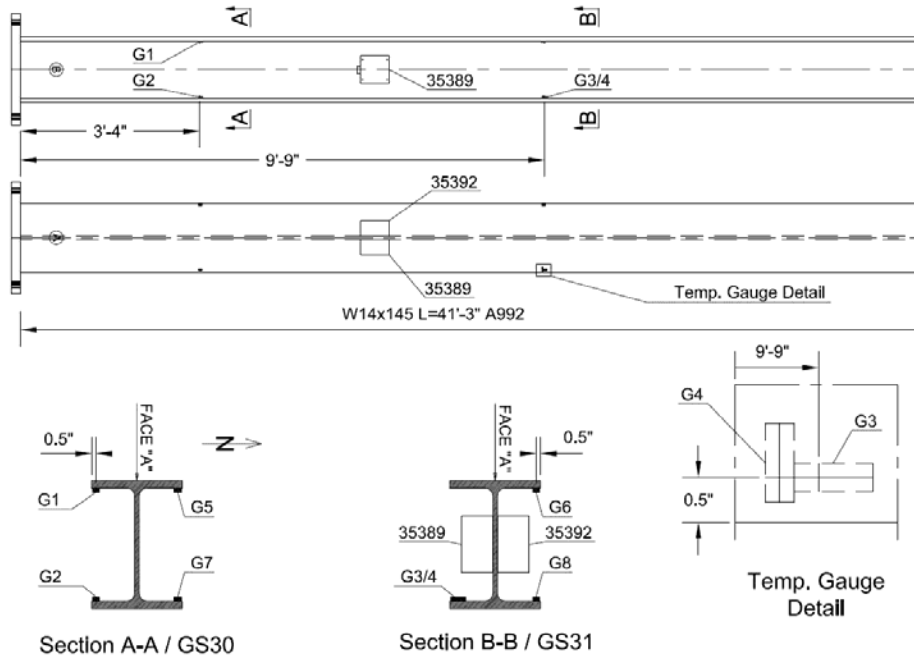


Figure 3.32: BPI Building 1<sup>st</sup> Floor Column instrumentation drawing

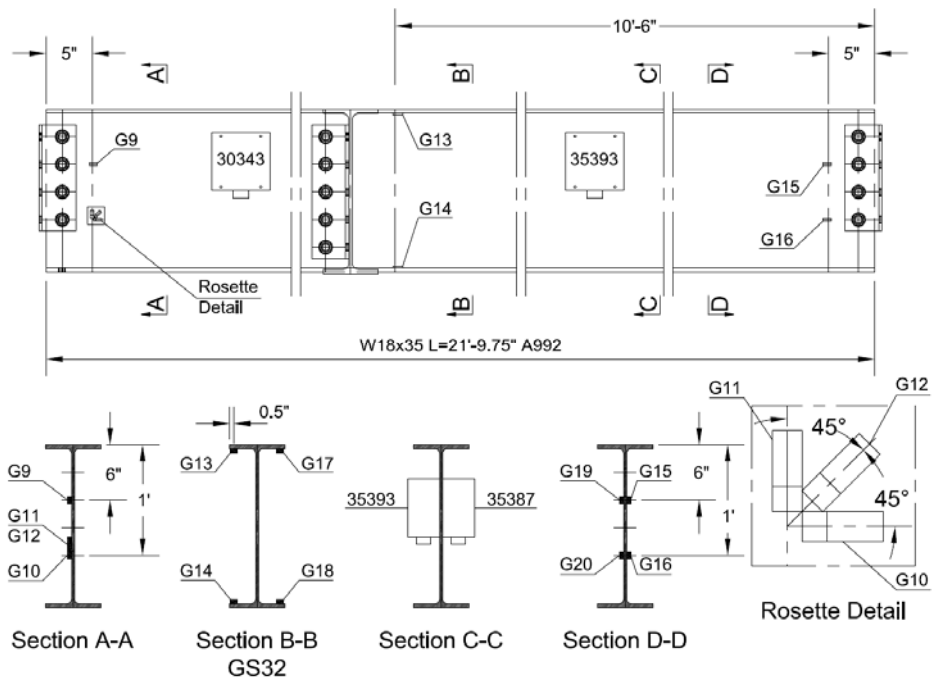


Figure 3.33: BPI Building 2<sup>nd</sup> Floor Girder instrumentation drawing

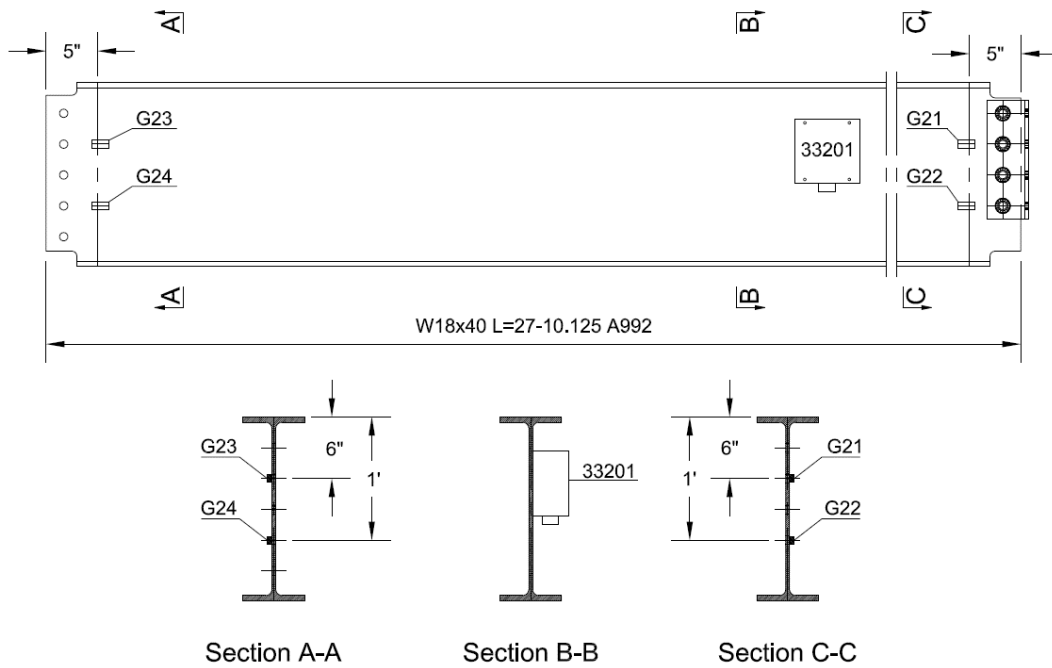


Figure 3.34: BPI Building 2<sup>nd</sup> Floor Beam instrumentation drawing

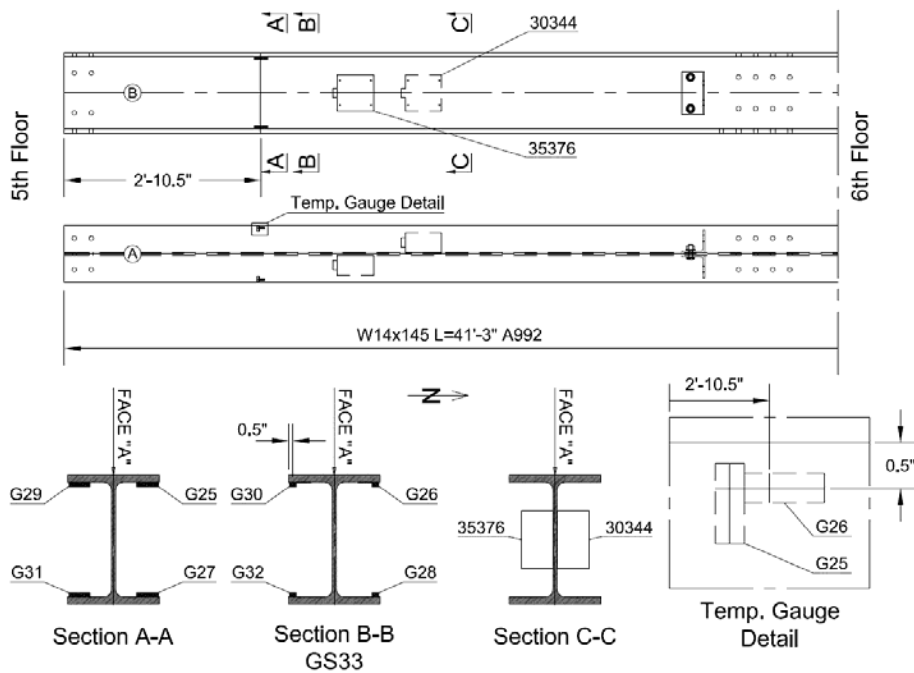


Figure 3.35: BPI Building 5<sup>th</sup> Floor Column instrumentation drawing

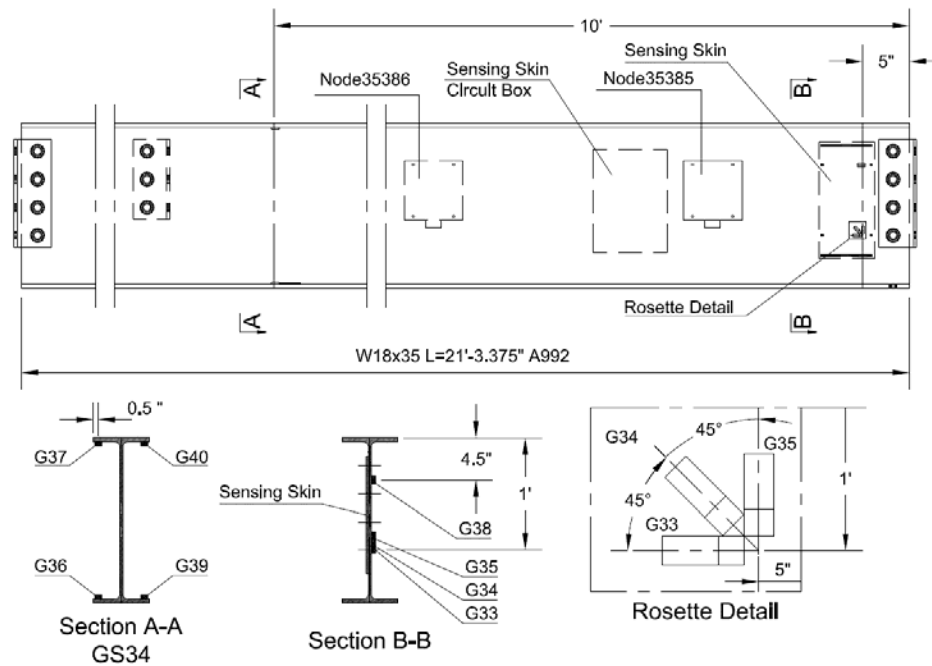


Figure 3.36: BPI Building 6<sup>th</sup> Floor Girder instrumentation drawing

### 3.3.3.3 Field Data Collection

For the BPI Building continuous data collection started on March 9<sup>th</sup> 2018 for the 1<sup>st</sup> Floor Column and the 2<sup>nd</sup> Floor Girder and Beam. Continuous data collection for the 5<sup>th</sup> Floor Column and the 6<sup>th</sup> Floor Girder started on May 8<sup>th</sup> 2018 once these members were delivered to the construction site. The WSN nodes for the 5<sup>th</sup> Floor Colum and the 6<sup>th</sup> Floor Girder were removed from the steel members on August 8<sup>th</sup> 2018 before the fire proofing was applied to these steel members. The continuous data collection for the first and second floor steel members was ended on November 27<sup>th</sup> 2018. The continuous data collection for these nodes was ended because the WSN nodes did not connect to the data acquisition laptop anymore due to increasing obstacles, like interior walls in the building. To conserve battery life of the WSN nodes the initial data acquisition frequency of in 16 Hz was reduced to 1 Hz on May

3<sup>rd</sup> 2018 for the first and second floor WSN nodes and on May 15<sup>th</sup> 2018 for the WSN nodes on the 5<sup>th</sup> and 6<sup>th</sup> floor.

#### **3.3.3.4 Results**

The results section for the BPI Building data is organized similar to the Purnell Hall Addition and the STAR Tower data results. First the maximum sustained and impact stresses for each member and connection area strain gauge was calculated. Next, the member forces for the three GS locations on the Column and the Girder were calculated using the three-gauge and the OA. At the end the member forces were evaluated using the same approach as described in Section 3.2.5.

##### **3.3.3.4.1 Maximum Sustained and Impact Stress Results**

Since the data acquisition frequency was changed from 16 Hz to 1 Hz during the data collection period, the data sets were split into two sets, one containing the data sampled at 16 Hz and one with the rest of the data. The collected strain data at 16 Hz was separated into sustained and impact data as described in Section 3.2.4.

Furthermore, the sustained data from the 16 Hz data set and the 1 Hz data set were added for the final, complete sustained data set which was used for this section.

The results for the strain gauges were split into member strain gauges and connection area strain gauges. The member strain gauges were located along the length of the steel member away from the connection area and the results are shown in Figure 3.37 and summarized in Table 3.14. The connection area strain gauges were located in the connection area of the steel members and their results are summarized in Figure 3.38 and Table 3.15.

As explained in Section 3.2.2.2, the time period of data collection from eight of the 40 strain gauges for the BPI Building was reduced significantly (i.e. values had to be deleted since they were unreasonably high or low values). The reduction of data for these strain gauges had an effect on the results, since not all the construction events were included in every strain gauge. Therefore, said strain gauges were summarized in Table 3.13 with data collection start and end date for the sustained data set and the amount of days data was collected. For comparison, G1 on the 1<sup>st</sup> Floor Column collected data for 263 days and G35 on the 6<sup>th</sup> Floor Girder collected data for 94 days. The percentage is given in respect to G1 for the 1<sup>st</sup> Floor Column and G35 for the 5<sup>th</sup> Floor Column and the 6<sup>th</sup> Floor Girder.

Even though only 8 of the 40 utilized strain gauges had reduced data, the impact of the missing data was very noticeable, especially during the member force calculations. For example, to calculate the member forces for GS31 the data for G8 was required. Therefore, the member forces at this location could only be calculated during the 3 days when G8 data was available. The same thing occurred for GS34 that included G36 and G40. Fortunately, member force calculations could still be calculated throughout the recording period for the remaining three gauge sets.

Table 3.13: Summary of strain gauges with reduced data

Steel Member Name	Strain Gauge	Data collection start date	Data collection end date	Data Collection Days	Percentage of G1 or G35 [%]
1 <sup>st</sup> Floor Column <sup>a</sup>	G7	03/09/2018	04/14/2018	36	14% of G1
	G8	03/09/2018	03/12/2018	3	1% of G1
5 <sup>th</sup> Floor Column <sup>b</sup>	G27	05/08/2018	05/13/2018	5	5% of G35
	G28	05/08/2018	05/14/2018	6	6% of G35
	G33	05/08/2018	07/13/2018	66	70% of G35
6 <sup>th</sup> Floor Girder <sup>c</sup>	G34	05/08/2018	5/29/2018	21	22% of G35
	G36	05/08/2018	06/03/2018	26	28% of G35
	G40	05/08/2018	06/27/2018	50	53% of G35

<sup>a</sup> See Figure 3.32 for strain gauge location

<sup>b</sup> See Figure 3.35 for strain gauge location

<sup>c</sup> See Figure 3.36 for strain gauge location

The collected field data for the BPI Building member strain gauges including impact values was compared to the sustained data from these gauges in Figure 3.37. Only one impact value (85.0 MPa (12.3 ksi), G17) was recorded for this data set.

As shown in Table 3.13 some of the strain gauges collected data only for a fraction of the time of others. This explained why column strain gauges G7 and G8 in Figure 3.37 only show tension forces and no compression forces. The tension force in the column strain gauges was probably a result of the temperature influence or an indication of moment being present. Furthermore, since the WSN nodes on the 5<sup>th</sup> and 6<sup>th</sup> floor steel members were removed earlier than all the other nodes and before the entire building was erected, 5<sup>th</sup> Floor Column stresses were small compared to the rest

of the gauge results. The temperature gauges G4, G25, G27, G29, and G31 are also included in Figure 3.37.

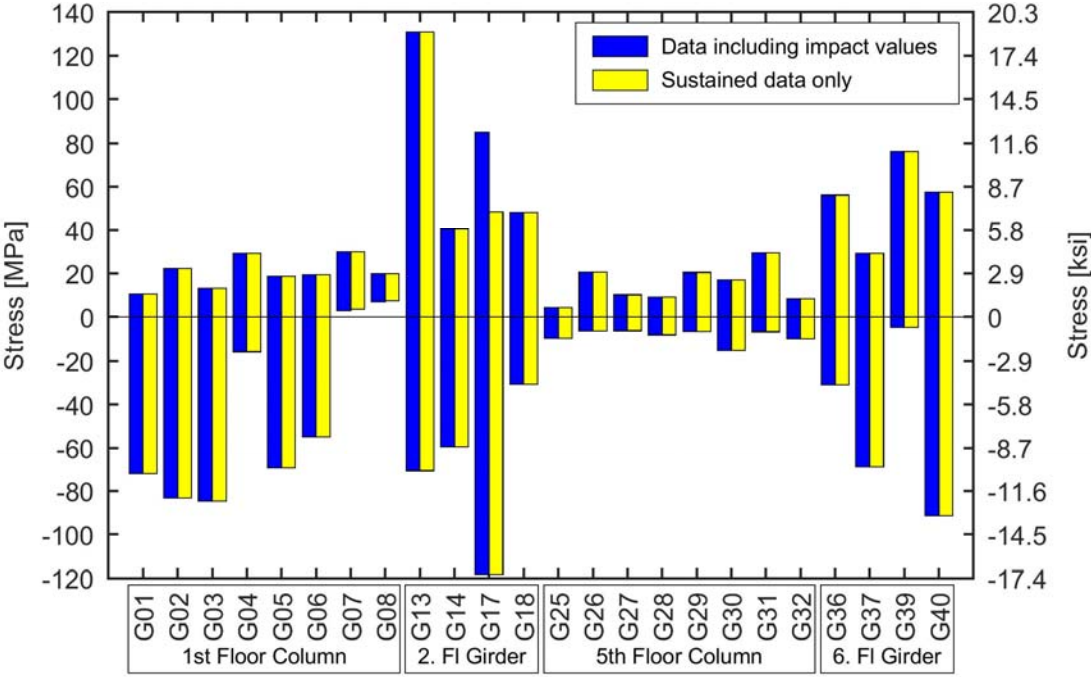


Figure 3.37: Overall maximum data, including impact values and maximum sustained data for the BPI Building member strain gauges

The maximum and minimum values of the member strain gauges for each instrumented steel member was summarized in Table 3.14. The overall maximum tension value was 131 MPa (19.0 ksi) in G13 on the 2nd Floor Girder and the maximum overall compression value was -91.4 MPa (-13.3 ksi) in G40 on the 6<sup>th</sup> Floor Girder. Therefore, the maximum stress value was 38% of the yield stress (of 345 MPa, 50 ksi).

Table 3.14: Summary of sustained BPI Building member stress data

Steel Member Name	Maximum Compression		Maximum Tension	
	MPa (ksi)	Location	MPa (ksi)	Location
1 <sup>st</sup> Floor Column <sup>a</sup>	-84.7 (-12.3)	G3	29.9 (4.33)	G7
2 <sup>nd</sup> Floor Girder <sup>b</sup>	-118 (-17.1)	G17	131 (19.0)	G13
5 <sup>th</sup> Floor Column <sup>c</sup>	-15.1 (-2.19)	G30	29.51 (4.28)	G31
6 <sup>th</sup> Floor Girder <sup>d</sup>	-91.4 (-13.3)	G40	11.1 (76.3)	G39

<sup>a</sup> See Figure 3.32 for strain gauge location

<sup>b</sup> See Figure 3.33 for strain gauge location

<sup>c</sup> See Figure 3.35 for strain gauge location

<sup>d</sup> See Figure 3.36 for strain gauge location

The impact and sustained connection area stress values are shown in Figure 3.38. From the figure it can be seen that both tension and compression maximum values were an impact value, 149 MPa (21.5 ksi) in G34 and -136 MPa (-19.7 ksi) in G20, respectively. However, besides these two impact values all other values were sustained values. The maximum values for all steel members were summarized in Table 3.14.

As described in the STAR Tower results Section (3.3.2.4.1) the connection area stresses did not follow any distinct patterns. Furthermore, to calculate the stresses in the connection area gauges, a linear behavior of the cross section was assumed by using Hook's law and an Elastic modulus of 200,000 MPa (29,000 ksi). Even though

the maximum stress values for the connection area strain gauges were impact values it was decided to only use the sustained data for the following sections.

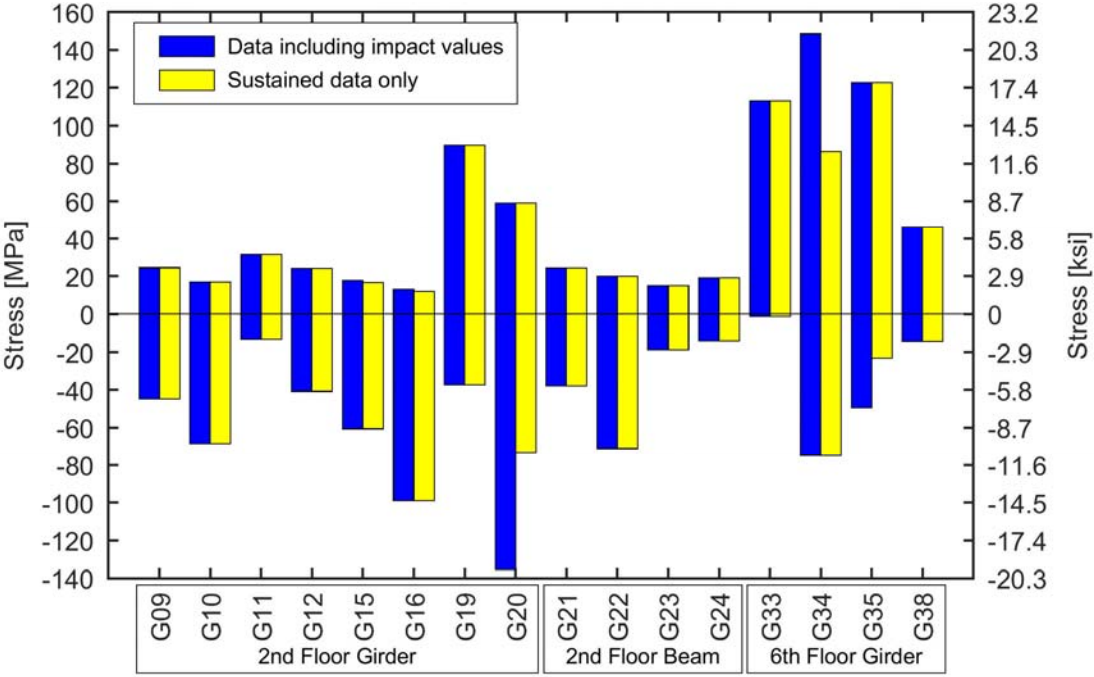


Figure 3.38: Overall maximum data, including impact values and maximum sustained data for the BPI Building connection area strain gauges

Table 3.15: Summary of sustained BPI Building connection area stress data

Steel Member Name	Maximum Compression		Maximum Tension	
	MPa (ksi)	Location	MPa (ksi)	Location
2 <sup>nd</sup> Floor Girder <sup>a</sup>	-136 (-19.7)	G20 (impact value)	89.6 (13.0)	G19
2 <sup>nd</sup> Floor Beam <sup>b</sup>	-71.2 (-10.3)	G22	24.4 (3.53)	G21
6 <sup>th</sup> Floor Girder <sup>c</sup>	-74.9 (-10.9)	G34	149 (21.5)	G34 (impact value)

<sup>a</sup> See Figure 3.33 for strain gauge location

<sup>b</sup> See Figure 3.34 for strain gauge location

<sup>c</sup> See Figure 3.36 for strain gauge location

### 3.3.3.4.2 Member Forces Results

The member forces for the BPI Building steel members were calculated using the same methods as described in Section 3.2.5. The axial force results for the five GS are shown in Figure 3.39 and the bending moments are plotted in Figure 3.40. As described in Section 3.2.5.2, to minimize computational time for the OA the TGA (described in 3.2.5.1) was used to determine the timestamps for the maximum and minimum member forces. However, since 99% of G8 data was deleted during the data processing process (described in 3.2.2.2 and Table 3.13) and therefore the OA could only be used during the time G8 data was available, the TGA results are also shown in Figures 3.39 and 3.40. All gauge sets for the BPI Building except GS31 consisted of four strain gauges as shown in Figures 3.32, 3.33, 3.35, and 3.36. To calculate the member forces with TGA, the strain gauge combinations with the maximum amount of data available were used. For GS30, G1, G2, and G5; for GS 32, G14, G17, and

G18; for GS33, G26, G30, and G32; and for GS34, G36, G37, and G39 were used. To compare the TGA to the OA for GS30, the maximum and minimum values for the TGA during the same timespan as the OA were added to the graph as limited TGA data.

The data shown in Figure 3.39 shows high axial compression forces (-1690 kN (-380 kips)) for the TGA for GS30. This value was expected to be high since GS 30 is located on the 1<sup>st</sup> Floor Column and the TGA method used the data from the entire data collection period. On the other hand, TGA data for GS 31 included G8 which reduced the available data by 99% as previously shown in Table 3.13 and thus the maximum recorded stress significantly. Comparing the limited TGA data from GS30 and GS31 it can be observed that the values are similar, particularly for compression. The OA for both GS30 and GS31 show tension axial forces only which was unexpected since columns are theoretically expected to only have compression axial forces. The maximum axial tension force was 296 kN (66.6 kips) for GS33 on the 5<sup>th</sup> Floor Column. However, the used data was recorded at the very beginning of data collection when the column was relatively free to expand and contract due to the temperature. Therefore, it can be assumed that the axial tension force was a result of the column expanding due to temperature changes. The axial force for the two Girders (GS32 and 34) were higher than expected, since these members are usually designed to have no axial force. However, the same trend was found in the Purnell Hall Addition data (Section 3.3.1.4.3, GS12) and STAR Tower data (Section 3.3.2.4.2, GS22).

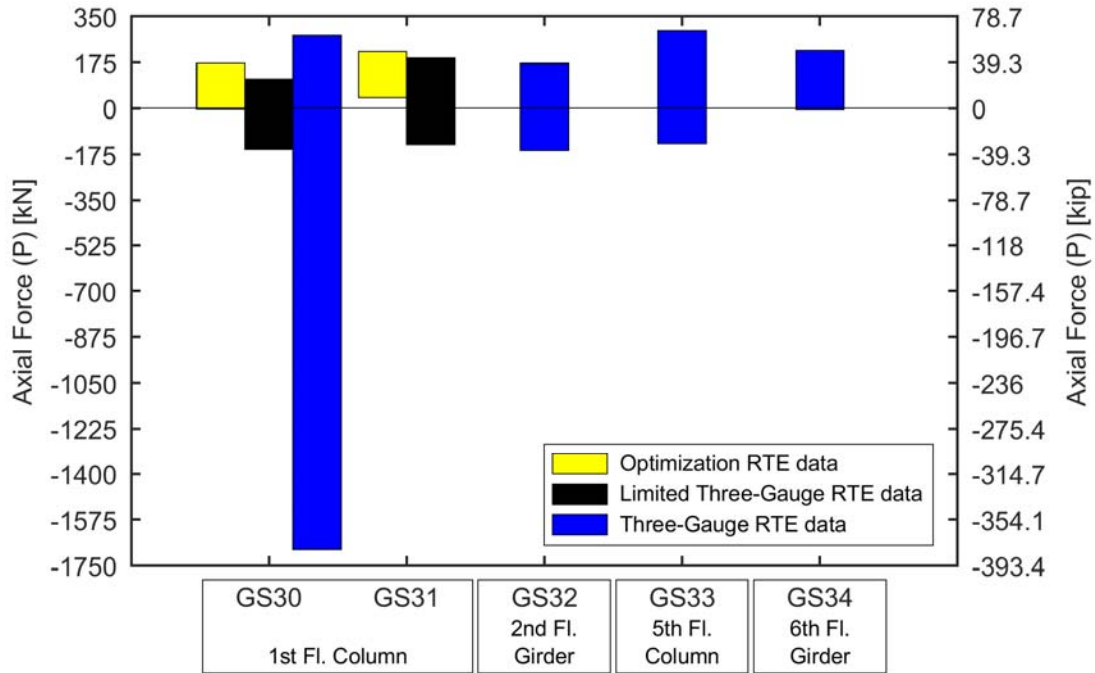


Figure 3.39: Overall BPI Building maximum sustained RTE axial force data

The maximum strong axis moment for the five gauge sets shown in Figure 3.40 was calculated using the TGA for GS31 located on the 1<sup>st</sup> Floor Column and was 54.6 kNm (40.2 kip\*ft). The maximum weak axis moment was 42.0 kNm (31 kip\*ft) in GS30. Similar to Purnell Hall Addition data the moments calculated for the columns were higher than expected since these are usually assumed to be zero. The high strong axis moment and low weak axis moment for the 2<sup>nd</sup> Floor and 6<sup>th</sup> Floor Girder were expected due to dead load of the concrete floor.

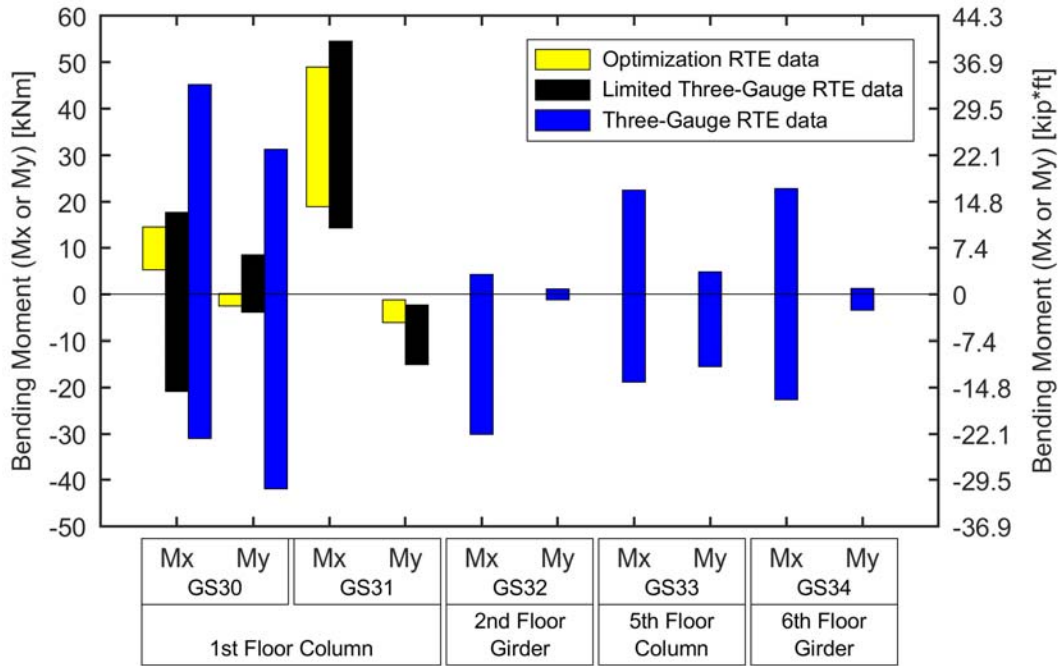


Figure 3.40: Overall BPI Building maximum sustained RTE bending moment data

### 3.3.3.4.3 Evaluation of Member Forces

The calculated member forces from the previous section were evaluated using the same approach as described in Section 3.3.1.4.4. For compressive capacity, a buckling coefficient ( $k$ ) assuming a fixed connection at the bottom of the 1<sup>st</sup> Floor Column and that all other connections were pinned, resulting in a value of 0.8 for the 1<sup>st</sup> Floor Column and 1.0 for all other members. Conservatively, all member cross-sections were assumed to be non-composite sections (including the floor girder and beams after concrete was poured). Eqns. 3.8 and 3.9 were used to calculate the yield ratios of each gauge set for each point in time where a maximum in the individual force effects occurred.

The overall maximum ratios resulting from this process and the corresponding axial forces ( $P_r$ ) and moments ( $M_{rx}$  and  $M_{ry}$ ) were summarized in Table 3.11. The

maximum ratio found was 0.30 for both GS 30 located on the 1<sup>st</sup> Floor Column and GS 34 located on the 6<sup>th</sup> Floor Girder. The highest component of the GS30 ratio was the axial force, which was expected since GS30 is located on a column where high axial stress were expected. For GS34, the highest ratio component was also the axial force component, which was unexpected and most likely caused by the influence of temperature. All of the calculated ratios were below 1. Therefore, it was concluded that the applied construction forces did not cause any yielding in any of the instrumented steel sections of the BPI Building during the data collection period.

Table 3.16: Applied member forces and moments relative to multi-axial yield criteria for the BPI Building

Gauge Set (GS)	Applied forces and moments			Yield forces and moment			Ratios			Eqn. 3.8 or Eqn. 3.9 Ratio
	$P_r$	$M_{rx}$	$M_{ry}$	$\phi P_c$	$\phi M_{yx}$	$\phi M_{yy}$	$P_r/P_c$	$M_{rx}/M_{yx}$	$M_{ry}/M_{yy}$	
	kN (kip)	kNm (kip*ft.)	kNm (kip*ft.)	kN (kip)	kNm (kip*ft.)	kNm (kip*ft.)				
30 <sup>a</sup>	1673 (376)	31.0 (22.9)	23.0 (17.0)	7251 (1630)	1180 (870)	444 (327)	0.23	0.03	0.05	0.30
31 <sup>a</sup>	134 (30)	54.4 (40.1)	15.0 (11.1)	7251 (1630)	1180 (870)	444 (327)	0.02	0.05	0.03	0.09
32 <sup>b</sup>	110 (24.8)	30.1 (22.2)	0.05 (0.04)	1142 (257)	229 (169)	26.0 (19.2)	0.10	0.13	0.00	0.18
33 <sup>c</sup>	262 (58.8)	11.3 (8.36)	15.5 (11.4)	7725 (1737)	1180 (870)	444 (327)	0.03	0.01	0.03	0.06
34 <sup>d</sup>	173 (38.9)	22.6 (16.7)	3.38 (2.49)	1142 (257)	229 (169)	26.0 (19.2)	0.15	0.10	0.13	0.30

<sup>a</sup> See Figure 3.32 for strain gauge location

<sup>b</sup> See Figure 3.33 for strain gauge location

<sup>c</sup> See Figure 3.35 for strain gauge location

<sup>d</sup> See Figure 3.36 for strain gauge location

### **3.4 Field Data Comparison**

The collected field data for the three instrumented buildings described in the previous sections are summarized in this section. First, the maximum and minimum member and connection area stresses were compared in Section 3.4.1. Next the calculated member forces (axial forces and bending moments) for all three buildings were summarized in Section 3.4.2.

#### **3.4.1 Stress Data Comparison**

The overall stress data comparison shown in Figure 3.41 was organized by member strain gauges and connection area strain gauges. Furthermore, the data was separated into column, beam and girder stresses. The maximum compression stress which was also the absolute maximum stress (including member and connection area stresses) for the three buildings was -160 MPa (-23.2 ksi) at the top of the Short Column of the Purnell Hall Addition. The maximum recorded tension stress was an impact stress of 149 MPa (21.5 ksi) in the connection area of the 6<sup>th</sup> Floor Girder in the BPI Building. The maximum sustained tension stress was 131 MPa (19.0 ksi) in G13 on the top flange of the 2<sup>nd</sup> Floor Girder of the BPI Building. Both maximum compression and tension stress were smaller than the yield stress of the instrumented steel member with the highest overall value (160 MPa (23.2 ksi)) being 46.4 % of the yield stress of 345 MPa (50 ksi).

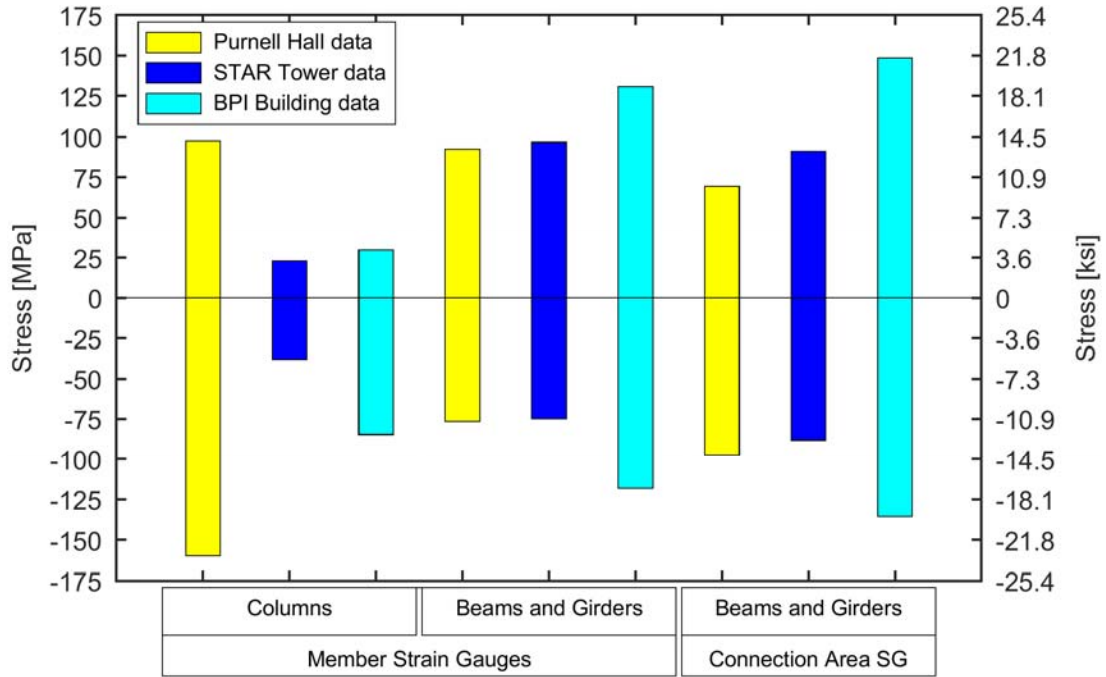


Figure 3.41: Overall maximum and minimum stress comparison for the three instrumented buildings

### 3.4.2 Member Force Comparison

The axial member forces from all three buildings were summarized in Figure 3.42. The maximum axial compression and tension forces were recorded in the BPI Building columns. The maximum compression force of -1690 kN (-380 kip) was calculated for the 1<sup>st</sup> Floor Column of the BPI Building and the maximum tension force of 296 kN (49.5 kip) was calculated for the 5<sup>th</sup> Floor column of the BPI Building. All column axial forces were higher than the beam and girder axial forces which was expected. The BPI Building had the highest compression force followed by the STAR Tower and the Purnell Hall Addition which was also expected, since the STAR Tower and the BPI Building were much bigger structures than the Purnell Hall Addition. The STAR Tower axial force only includes the dead load of one floor of the

entire building. Therefore, this value certainly increased after the data collection ended. While the axial forces for the beams and the girders were lower than the column forces, they were higher than expected, given that axial forces in beams are usually assumed to be zero during the design of a structure unless they are part of the lateral force resisting system, which these members were not. Furthermore, the highest axial forces for the beams and girders was found in the Purnell Hall Addition. The building was connected to an existing building, which could have introduced horizontal loads into the new steel structure if the connecting steel members (between Purnell Hall and the Purnell Hall Addition) were too long or too short creating fit up forces.

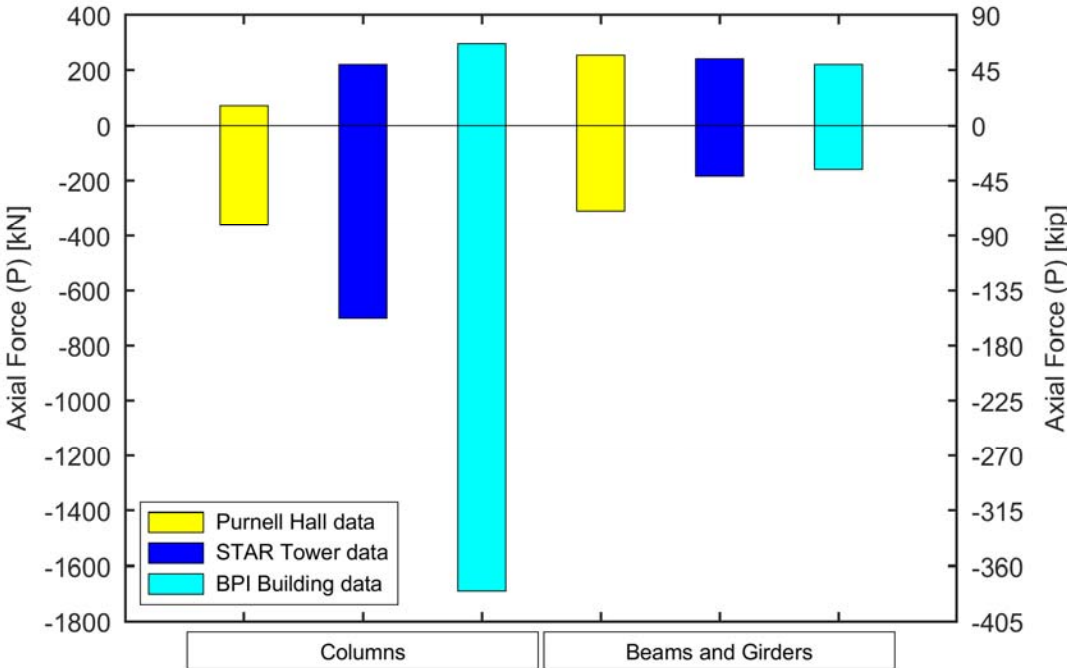


Figure 3.42: Overall maximum and minimum axial force comparison for the three instrumented buildings

The maximum and minimum strong and weak axis bending moments for the three instrumented buildings were summarized in Figure 3.43. The maximum absolute strong axis moment was 203 kNm (150 kip\*ft) and calculated at the center of the STAR Tower Girder. This strong axis moment was expected to be high, since the gauge set is located at the center of the Girder which supports the dead load of the concrete floor. The maximum absolute weak axis moment was 42.0 kNm (31 kip\*ft) and calculated for the 1<sup>st</sup> Floor Column of the BPI Building. The strong axis moments calculated for the beams and girders were expected, however, the moments found in the columns was unexpected, since columns are not usually explicitly designed for moments unless they are part of a lateral force resisting system, which these members were not. The high moments could be due to eccentric loading of the columns during the construction process or temperature influence in the field data.

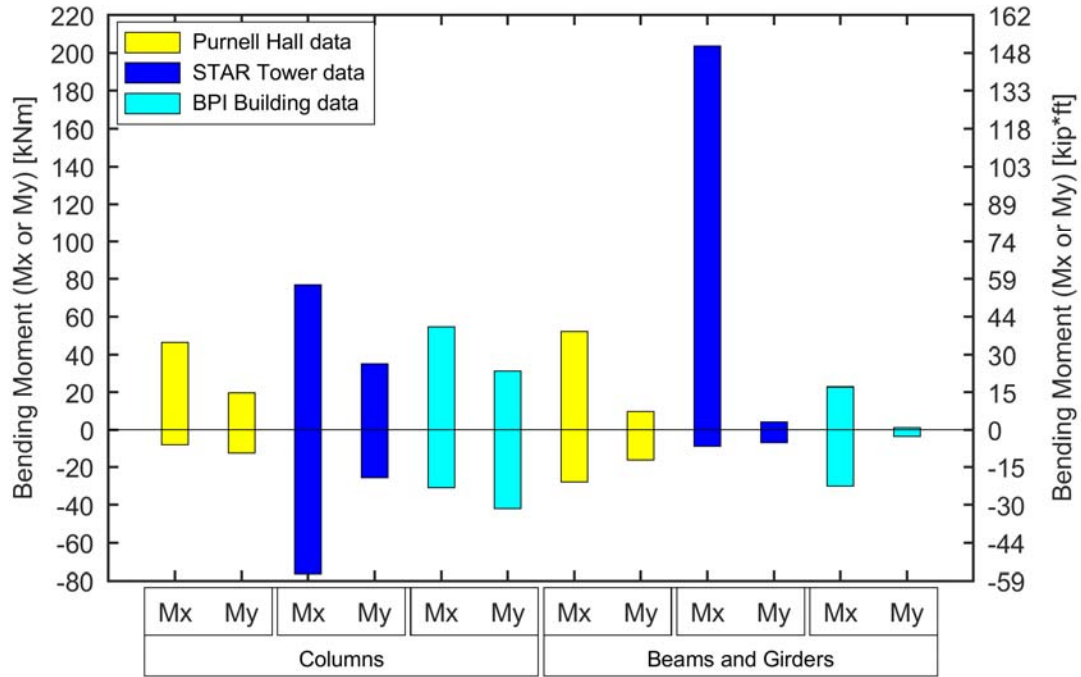


Figure 3.43: Overall maximum and minimum bending moment comparison for the three instrumented buildings

### 3.5 Field Data Conclusions

Three different steel frame buildings were instrument using a WSN. The WSN nodes were installed at the fabrication location and started recording data once the instrumented steel member arrived on the building site. For the first instrumented building (Purnell Hall Addition) and the last building (BPI Building) five steel members were instrumented (two columns and three beams). For the second instrumented building (STAR Tower) only one column and two beams were instrumented since the data collection had to be ended early for this project.

Continuous data was collected for all three buildings over a range of time. Data was collected at 16 Hz for all the buildings. However, to save battery life of the BPI Building WSN nodes the data acquisition frequency was lowered to 1 Hz. A total of

almost 3 billion strain data points and close to 750 million temperature data point were collected for the three buildings.

The collected data was processed, zeroed, and split into impact and sustained stress values. The maximum stress values for each building were summarized in Figure 3.41. The absolute maximum stress value was 160 MPa (-23.2 ksi) at the top of the Short Column of the Purnell Hall Addition. This value was 46.4% of the yield stress of 345 MPa (50 ksi) for the instrumented steel member. Therefore, it can be concluded that none of the instrumented areas reached yielding.

The calculated member forces (axial force, strong and weak axis bending) for the three buildings were calculated using the “three-gauge” approach and the “optimization” approach. The results were summarized in Figures 3.42 and 3.43. The maximum axial force was a compression force of -1690 kN (-380 kip) in the 1<sup>st</sup> Floor Column of the BPI Building. The maximum strong axis bending moment was 203 kNm (150 kip\*ft) at the center of the STAR Tower girder. The weak axis moments were small compared to the strong axis moments, the maximum weak axis moment was 42.0 kNm (31 kip\*ft) and calculated for the 1<sup>st</sup> Floor Column of the BPI Building. However, relatively high bending moments in the columns were recorded. The high moments could be due to eccentric loading of the columns during the construction process or temperature influence in the field data.

The calculated member forces were evaluated using the AISC Steel Construction Manual (AISC, 2017), Chapter H with modifications to assess yielding as discussed in Section 3.3.1.4.4. The maximum combination of member forces for each gauge set was found as well as the yield capacity for each steel member. The values were compared using Eqn. 3.8 or 3.9 and the calculated ratios were given in

Table 3.7 for the Purnell Hall Addition, Table 3.11 for the STAR Tower, Table 3.16 for the BPI Building. The maximum values were found to be 0.55 for Purnell Hall Addition data, 0.32 for STAR Tower data, and 0.30 for the BPI Building. All ratios were below 1.0 which indicated that none of the instrumented steel members experienced any yielding during the construction phase.

## Chapter 4

### CARBON NANOTUBE-BASED SENSOR

Reusing the complete structural steel member, including the connection area, is one of the main points of this dissertation. Therefore, the strain distribution in a connection area during construction should be determined. However, recording strain data close to connection areas is an involved task; because the strain distribution in this area is influenced by strain concentrations close to the connection bolts and does not follow general bending or shear theory, many strain gauges need to be applied to capture this strain distribution accurately. For example, when applying strain gauges to the connection area, peak strain data could be missed because the strain gauges measure strains only at discrete locations.

To address this challenge, a CNT-based sensor (see Section 2.3 for the literature review) was bonded next to the connection area of one of the instrumented steel members of the BPI Building and was also piloted on a laboratory specimen. CNT-based sensors take advantage of the electrical conductivity of carbon nanotubes. These sensors are fabricated by infusing carbon nanotubes in a fabric (nonwoven aramid fiber fabric). The created sensor is bonded to a substrate (steel beam). When the strain state of the substrate changes in the area of the CNT-based sensor, the electrical properties of the sensor changes as well. The electrical change in the sensor is measured and can be related to the change in strain in the substrate.

The sensing skin (label used in this chapter to describe the CNT-based sensor) was manufactured at the University of Delaware and installed onto the steel member at

the steel fabrication location before the steel member was shipped to the building site. The sensing skin was connected to a circuit box that provided the necessary power and to two WSN nodes that collected the output data and sent it to the data acquisition laptop.

In this chapter the fabrication and the field installation of the CNT-based sensor are discussed. Furthermore, the newly developed circuit box, that was necessary to connect the sensing skin to external power, is explained. Finally, field installation and data results of the sensing skin are compared to field data from strain gauges that were connected to the opposite side of the web of the sensing skin.

#### **4.1 Sensor Fabrication**

The carbon nanotube-based sensor was manufactured at the University of Delaware. The sensing skin was created by adding a nonwoven aramid fiber fabric (Optiveil aramid veil, Technical Fiber Products, Schenectady, New York) to a bath of CNT sizing agent. The sizing agent was made of one part sizing agent (SIZICTL XC R2G, Nanocyl, Sambreville, Belgium) and two parts distilled water. The aramid veil stayed in the sizing agent for 20 minutes and was dried afterwards for 30 minutes at 60°C (140°F) in an oven. Once the sensor was dry it was cut to the desired size of 152.4 mm (6 in.) by 317.5 mm (1 ft. 0.5 in.). Electrically conductive connections were painted on the sensing skin using conductive silver paint (Flash Dry, SPI Supplies, West Chester, Pennsylvania) at the locations E<sub>1</sub> – E<sub>6</sub> shown in Figure 4.1. Six electrodes were applied to the sensing skin since one WSN node could only record three additional data channels (capacity of utilized WSN node) and there were two WSN nodes on the BPI Building 6<sup>th</sup> Floor Girder (the location of the sensing skin for the field instrumentation). Each data channel measured the voltage between one

electrode and ground (i.e. E<sub>4</sub>). Therefore, voltage measurements were continuously measured between E<sub>2</sub> and E<sub>4</sub>, E<sub>3</sub> and E<sub>4</sub>, E<sub>5</sub> and E<sub>4</sub>, and E<sub>6</sub> and E<sub>4</sub>.

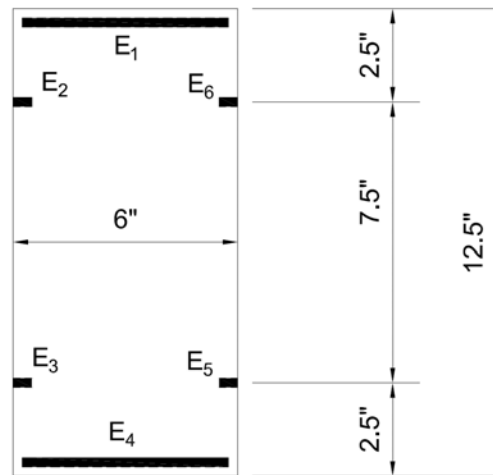


Figure 4.1: Carbon nanotube-based sensor with electrode locations

## 4.2 Sensor Location

The sensing skin was installed on the BPI Building 6<sup>th</sup> Floor Girder in the connection area where the girder was attached to the 5<sup>th</sup> Floor Column. The sensing skin was attached 12.7 mm (0.5 in) away from the connection angles as shown in Figure 4.2. The top electrodes (E<sub>2</sub> and E<sub>6</sub>) were vertically aligned halfway between the two top bolts of the connection, whereas the bottom electrodes (E<sub>3</sub> and E<sub>5</sub>) were vertically aligned with the bottom bolt of the connection. It was assumed (based on finite element results of connection areas) that the strain peaks in the connection area would occur at one of these two locations. Figure 4.2 also shows the how the sensing skin was connected to the circuit board box (CBB) and subsequently to the WSN nodes (where the dashed WSN node (Node35385) was located on the other side of the

web. The installation process of the sensing skin in the field is explained in more detail in Section 4.4. Furthermore, the sensing skin circuit diagram is shown in Figure 4.3 in the next section.

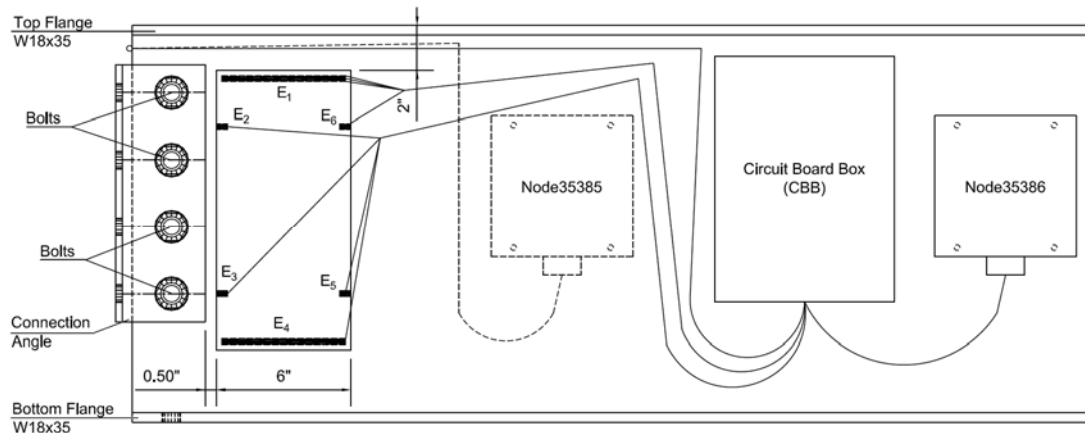


Figure 4.2: Field instrumentation overview of the sensing skin

### 4.3 Connecting the Sensing Skin to the Circuit Board Box

Six electrodes were placed on the sensing skin based on the number of available data collection channels from the WSN nodes. Therefore, six measurements could be recorded. To capture the overall behavior of the sensing skin, a voltage measurement ( $V_{E1}$ ) and a current measurement ( $I_{E1}$ ) between  $E_1$  and  $E_4$  were measured. A schematic of the circuit diagram was shown in Figure 4.3. Voltage measurements  $V_{E2}$ ,  $V_{E3}$ ,  $V_{E5}$ , and  $V_{E6}$  were all taken between the given electrodes and  $E_4$ , the ground electrode (GND).  $V_{E2}$ ,  $V_{E3}$  were placed close to the connection and  $V_{E5}$ , and  $V_{E6}$  were placed on the same axis but further away from the connection. This setup was used to measure the change in voltage between electrodes close to the connection

and electrodes away from the connection indicating a change in strain between the two points.

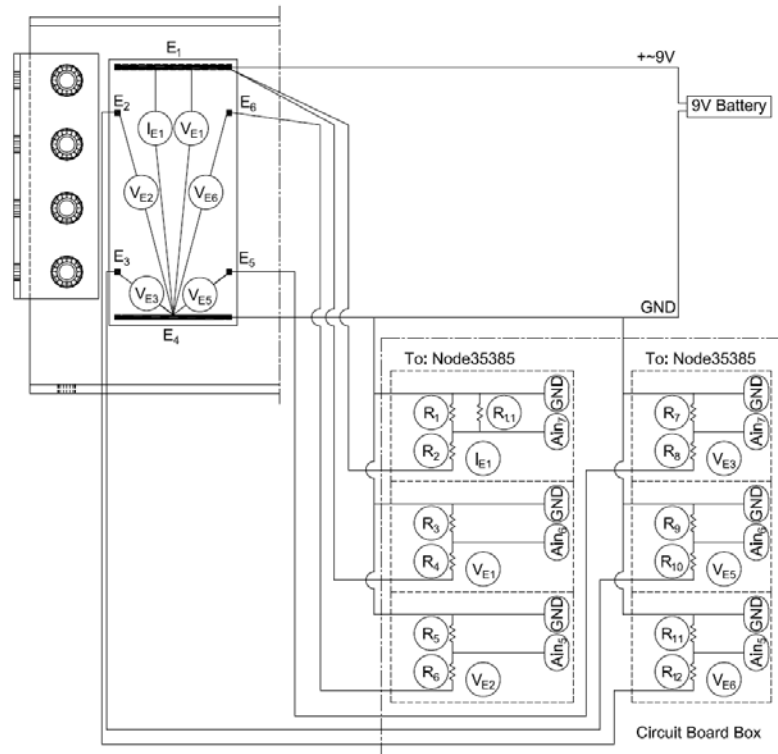


Figure 4.3: Sensing skin circuit diagram

To measure the voltage between the different electrodes, the sensing skin was connected to a 9 volt power source and to the WSN nodes as shown in Figure 4.3 and 4.4. However, the WSN nodes had a maximum voltage measuring range from 0 to 3 volts. Therefore, voltage divider circuits were designed based on information provided by the WSN manufacturer (Trutor, 2013). The voltage divider layout is shown in Figure 4.3 and 4.4 for the six channels and the resistance of the used resistors (R<sub>1</sub> –

$R_{12}$  and  $R_{1,1}$ ) are listed in Table 4.1. The resistors had three different nominal resistances. Two different resistances were required to create the voltage divider circuit for all channels and one resistor was used to convert the voltage measurement to a current measurement. The actual resistance for each resistor was measured and listed in Table 4.1. To measure the current between  $E_1$  and  $E_4$  ( $I_{E1}$ ) an additional resistor was used as shown in Figure 4.3, 4.4 and Table 4.1. The voltage dividers were created using  $\frac{1}{4}$  watt resistors with a tolerance of 1% (specified resistor resistance  $\pm$  1%) on a prototyping circuit board.

Table 4.1: Resistance values of sensing skin voltage breaker resistors

Measurement	Node & Channel	Resistor 1 [k $\Omega$ ]	Resistor 2 [k $\Omega$ ]	Resistor 3 [ $\Omega$ ]
$I_{E1}$	Node35385 Ain <sub>7</sub>	$R_1 = 10.0$	$R_2 = 27.1$	$R_{1,1} = 99.5$
$V_{E1}$	Node35385 Ain <sub>6</sub>	$R_3 = 9.95$	$R_4 = 26.9$	-
$V_{E2}$	Node35385 Ain <sub>5</sub>	$R_5 = 9.96$	$R_6 = 27.0$	-
$V_{E3}$	Node35386 Ain <sub>7</sub>	$R_7 = 9.95$	$R_8 = 27.1$	-
$V_{E5}$	Node35386 Ain <sub>6</sub>	$R_9 = 9.98$	$R_{10} = 26.9$	-
$V_{E6}$	Node35386 Ain <sub>5</sub>	$R_{11} = 9.96$	$R_{12} = 27.1$	-

The sensing skin and the WSN nodes were connected using the circuit board box (CBB) shown in Figures 4.4 and 4.5. The wires from the sensing skin electrodes were connected to one side of the circuit breakers and the WSN nodes were connected to the other side as shown in the schematic in Figure 4.4. The circuit was connected to

six 9-volt batteries as shown in Figure 4.5. The batteries were joined parallel to keep the voltage constant but increase their lifetime.

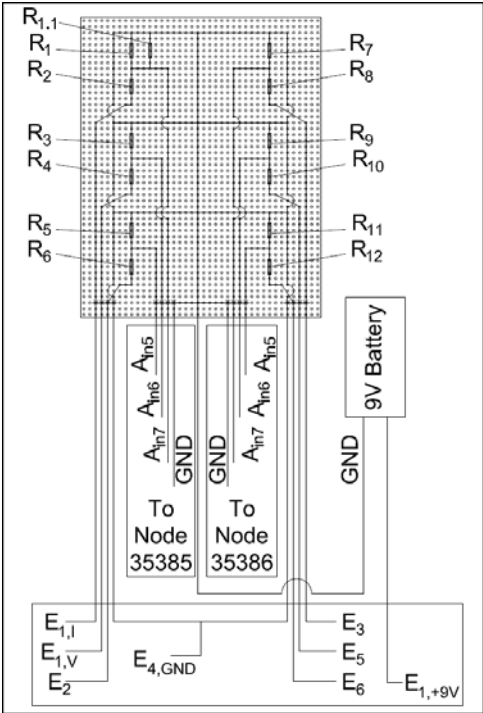


Figure 4.4: Sensing skin circuit board box (CBB) layout

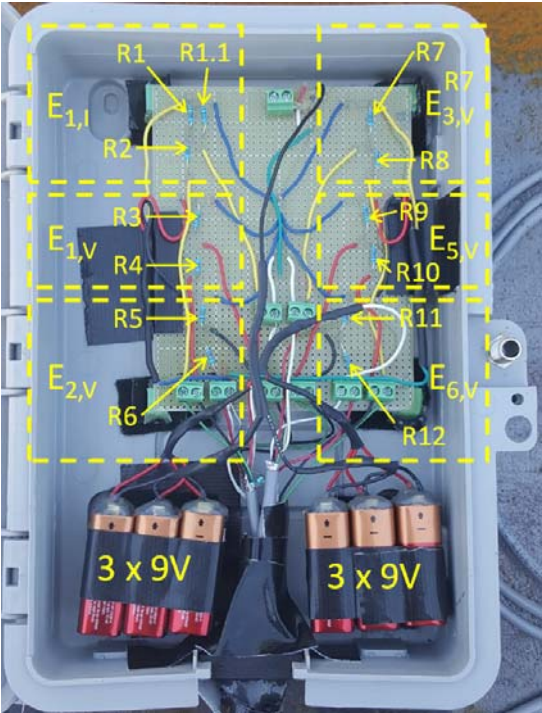


Figure 4.5: Sensing skin circuit board box (CBB) in the field

**4.4 Field Installation of the Sensing Skin at the Steel Fabricator**

The manufactured sensing skin was installed to the connection area of the 6<sup>th</sup> Floor Girder of the BPI Building as shown in Figure 4.2 at the steel fabricator’s facilities before the Girder was shipped to the construction site. The sensing skin was connected to the CBB and subsequently to two WSN nodes using wires. The wires

were attached to the sensing skin electrodes using electrically conductive silver epoxy (Epoxies Etc. 40-3900, Cranston, Rhode Island) as shown on Figure 4.6.

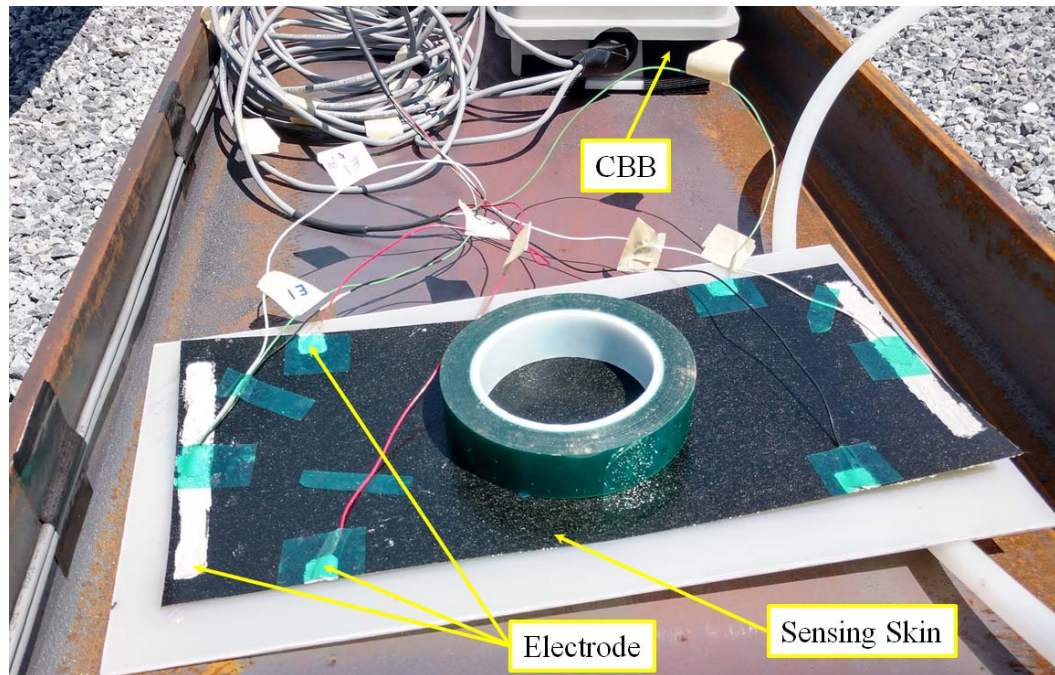


Figure 4.6: Sensing skin with attached wires (Photo credit: Gary Wenczel)

Once the wires were attached to the sensing skin, the sensing skin was bonded to the girder. Before bonding the sensing skin to the steel beam, the steel beam was sanded, removing any corrosion or mill scale, and cleaned with Acetone to remove any grease from the bonding area. The sensing skin was bonded to the web of the steel girder using a two-part epoxy paste adhesive (HYSOL 9309.3NA, Henkel Corporation) as shown in Figure 4.7. A thin adhesive layer of the epoxy paste was spread on the cleaned web surface of the girder and the sensing skin was placed on top of it.

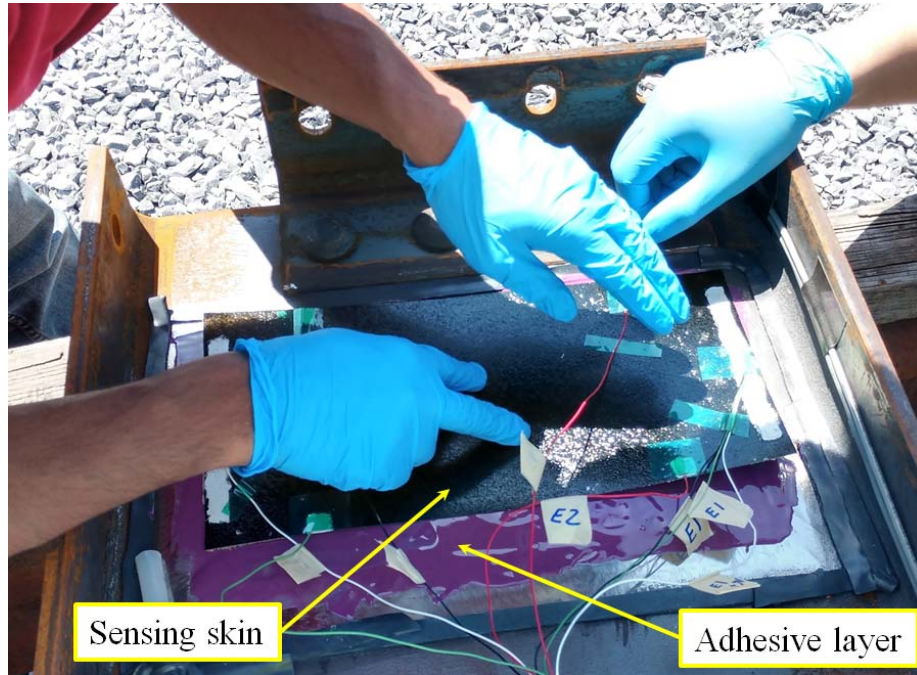


Figure 4.7: Placing the sensing skin on the girder on the adhesive layer (Photo credit: Gary Wenczel)

Once the sensing skin was in the correct place, a vacuum bagging method was used to attach the sensing skin as uniformly as possible to the steel surface. A rigid plate was wrapped in a breather material to protect the sensing skin from damage and enable uniform vacuum pressure to be applied as shown in Figure 4.8. Furthermore, the rigid plate wrapped in breather material was then wrapped in a release ply layer that did not bond to the two-part epoxy. The rigid plate assembly was then placed on top of the sensing skin between the sensing skin and the vacuum bag and the vacuum was created using a tube and a vacuum pump as shown in Figure 4.8.

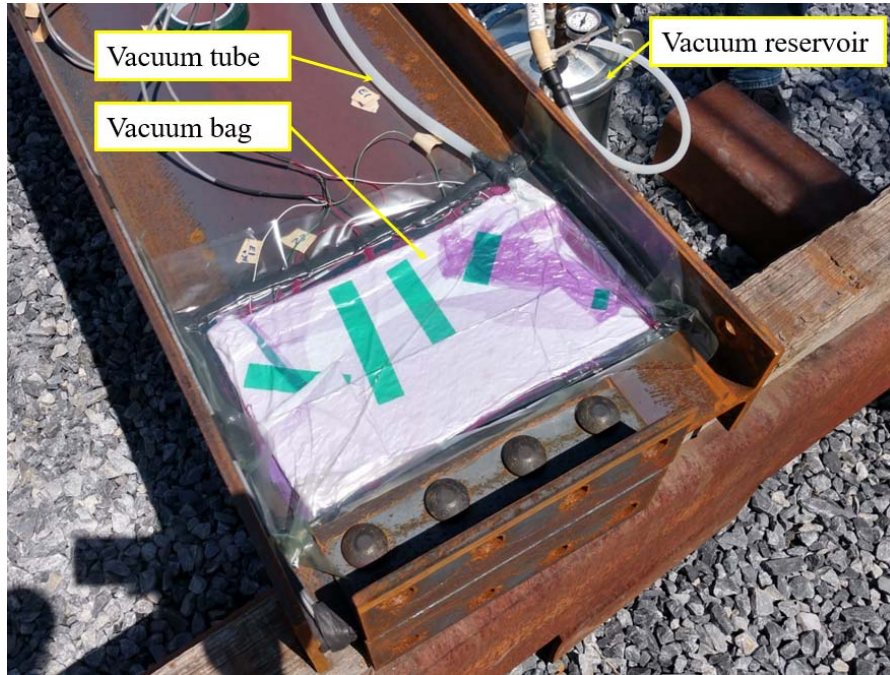


Figure 4.8: Sensing skin was bonded to the girder using the vacuum bag method (Photo credit: Gary Wenczel)

Once the vacuum was created, the assembly was left to cure for about 90 minutes. The curing of the two part epoxy was accelerated using heat guns and a temporary tent structure made of insulating foil. The curing ended after 90 minutes because the fabrication workshop closed for the day. The attached sensing skin was temporarily protected from weather using a plastic cover as shown in Figure 4.9. This precaution was taken to allow the two part epoxy to continue curing at ambient temperature while the beam was at the fabrication location.

The CBB and the WSN node were attached to the steel girder next to the sensing skin as shown in Figure 4.9. The second WSN node was attached on the other side of the web and cables were run through the space between the connection angle and the top flange of the girder as shown in the top left corner of Figure 4.9. The extra

cable attached to the girder in Figure 4.9 was left in place, in case the CBB and the WSN nodes had to be relocated from the girder once the girder was installed in the building.

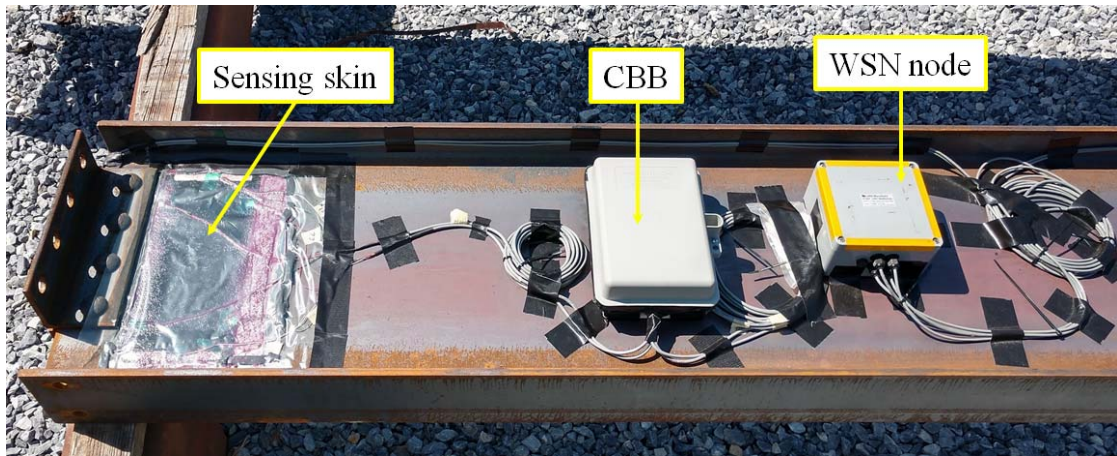


Figure 4.9: Finished sensing skin on the girder with the CBB and WSN node wired (Photo credit: Gary Wenczel)

#### 4.5 Carbon Nanotube-Based Sensor Results

The BPI Building 6<sup>th</sup> Floor Girder that had the sensing skin attached was installed in the building on May 9<sup>th</sup>, 2018. The connecting WSN nodes were removed from the BPI Building on August 10<sup>th</sup>, 2018 as described in Section 3.3.3.3.

Continuous data was collected at 16 Hz between May 9<sup>th</sup> and May 15<sup>th</sup> and at 1 Hz between May 15<sup>th</sup> and the end of the data collection period on August 10<sup>th</sup>.

The use of CNT-based sensors in the field is currently still being developed and the aim this project is proof of concept. Therefore, the results presented in this section are qualitative and more research is needed to fully understand the collected sensing skin data. A general overview of the collected sensing skin field data is given

in Section 4.5.1 and a more detail comparison between strain gauge data and sensing skin data at a selected moment in time was presented in Section 4.5.2.

#### **4.5.1 Sensing Skin Field Data Results**

A general overview of the collected sensing skin data for the entire data collection period was shown in Figure 4.10. The data presented was processed using the same approach as the strain gauge data as described in Section 3.2.2.

The batteries to power the sensing skin were changed two times. The first time a set of 9-volt batteries (6x Duracell Quantum, alkaline batteries) were connected to sensing skin while the Girder was still at the steel fabrication location on May 03<sup>rd</sup> 2018. The batteries provided enough power to collect voltage data until May 24<sup>th</sup> 2018 (right before the voltage dropped to zero as shown in Figure 4.10). The second set of 9V batteries (6x Energizer Ultimate, lithium batteries) were installed on June 28<sup>th</sup> 2018 and lasted until July 21 2018. Therefore, the two battery types lasted about the same amount of time, 21 and 23 days, respectively.

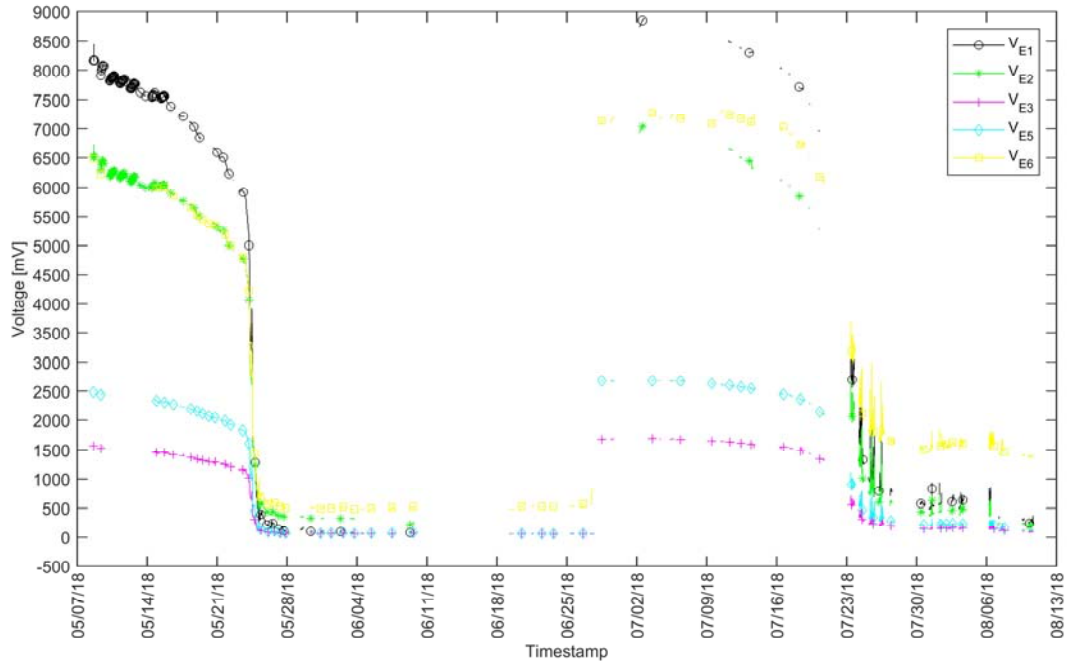


Figure 4.10: Sensing skin data overview (WSN node output data)

The data shown in Figure 4.10 had a lot of white space between collected data, which meant no data was collected during these times. The reason for this was a compromised wireless connection between the WSN nodes and the data acquisition laptop. However, general trends of the data were still noticeable and an example of continuously collected data was shown in Section 4.5.2.

The voltage readings of each of the electrodes were as expected: the value for  $V_{E1}$  close to 9 V when the batteries were new, the values for  $V_{E2}$  and  $V_{E6}$  similar in magnitude and lower than the values for  $V_{E1}$ , and the values for  $V_{E3}$  and  $V_{E5}$  lower than  $V_{E2}$  and  $V_{E6}$ , and all values decreasing overtime while the batteries were used. However, it was expected that  $V_{E3}$  and  $V_{E5}$  would have a similar magnitude. Therefore, the big difference between  $V_{E3}$  and  $V_{E5}$  that were located at the same distance from the

top electrode (i.e. E<sub>1</sub> see Figure 4.1) and the same distance from the bottom electrode (i.e. E<sub>4</sub>) was not expected. The values for  $V_{E3}$  and  $V_{E5}$  were expected to have had the same voltage readings, as was the case with  $V_{E2}$  and  $V_{E6}$  but with lower voltage than  $V_{E2}$  and  $V_{E6}$  since E<sub>3</sub> and E<sub>5</sub> were located farther away from E<sub>1</sub>. Lastly, the voltage measurement between E<sub>1</sub> and E<sub>4</sub> had the highest readings which was expected since the voltage was measured between the source (9 V in the sensing skin but around 2.4 V in the WSN node data) and the ground (GND).

Overall, the data did not show any major peaks or inconsistencies (which would show any major changes in the strain field of the sensing skin) during the two data collection periods (i.e. between May 7<sup>th</sup> 2018 and May 24<sup>th</sup> 2018 and June 28<sup>th</sup> 2018 and July 21 2018). Some data spikes were recorded at the end of the second data collection period (between 07/23/2018 and 07/29/2018), however, these were at the end of the batteries life span and therefore not considered. Furthermore, the voltage data did show some changes due to temperature changes which was expected. However, this will be addressed in more detail in the next section in Figure 4.13.

#### **4.5.2 Comparison of Sensing Skin Data to Conventional Strain Gauge Data**

In this section the sensing skin data was compared to strain gauge data collected on the opposite side of the web at the same location as electrodes E<sub>2</sub> and E<sub>3</sub>. The sensing skin on the 6<sup>th</sup> Floor Girder installed in the BPI Building was shown in Figure 4.11 and the strain gauges on the opposite side of the web were shown in Figure 4.12. The strain gauges were covered by weatherproofing and therefore not visible. However, their general location was indicated with the arrowheads of the strain gauge labels in the figure. The 6<sup>th</sup> floor girder was connected to the 5<sup>th</sup> Floor Column and the metal deck form was in place when these pictures were taken.



Figure 4.11: Sensing skin installed in the BPI Building

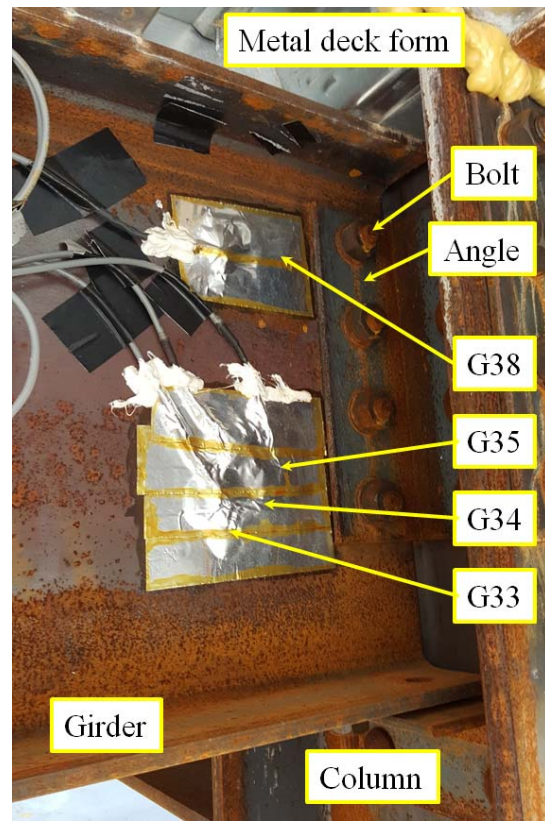


Figure 4.12: Strain gauges on the opposite side of the sensing skin

To compare the two different data sets a small portion of the collected data from May 15<sup>th</sup> at 12.00 pm until May 16<sup>th</sup> at 12:00 am was plotted in Figure 4.13. At that time, the steel structure was completed for the 5<sup>th</sup> floor and mostly completed for the 6<sup>th</sup> floor. The concrete floor for the first and second floor were poured and sheet metal formwork was completed for the 3<sup>rd</sup>, 4<sup>th</sup>, and 5<sup>th</sup> floor. This time window was selected based on having continuous data for all voltage measurements and strain gauge data as well as to show changes in sensing skin data were occurring. All voltage

data measurements except  $V_{E1}$  were shown in Figure 4.13. Furthermore, the difference between  $V_{E2}$  and  $V_{E6}$  as well as the difference between  $V_{E3}$  and  $V_{E5}$  were shown in the figure as an additional consideration. To have all data values in a similar range (to improve visibility of the trends of each data set), some of the voltage measurements were shifted by 850 to 5970 mV as shown in the legend of Figure 4.13. The temperature as well as the strain gauge data were not altered.

The strain gauges shown in Figure 4.13 were G34 and G38. G34 was the strain gauge that was at a 45° angle in the rosette on the 5<sup>th</sup> Floor Girder and strain gauge G38 was located on the opposite side of electrode E2 as shown in Figure 3.36 and 4.12. Gauge G38 was chosen since it was on the opposite side of E2 and G34 was chosen because it was the only strain gauge that provided reasonable data (of the three strain gauges located in this location, i.e. G33, G34, and G35) for this time window.

In Figure 4.13 it was shown that the sensing skin voltage measurements and the strain gauge data from both strain gauges had similar trends (i.e. change of voltage or strain due to temperature changes) and both showed a sudden change in data at around 7:00 PM (19:00:00 in the figure). However, the change due to temperature seems to be more prominent in the strain gauge data. However, this was probably due to the orientation of the 6<sup>th</sup> Floor Girder in the BPI Building, where the strain gauges were facing away from the building and the sensing skin was facing “into” the building. This statement was supported by the temperature data collected at the WSN nodes, where Node 35385 was located on the side of the strain gauges and Node 35386 was located on the side of the sensing skin and Node 35386 data was 5 °C (9 °F) lower than Node 35385 data.

Both voltage delta values ( $V_{E2} - V_{E6}$  and  $V_{E3} - V_{E5}$ ) showed a sudden change at the same timestamp as the strain gauged data did, which indicated that the sensing skin was able to record a change in the connection. Another observation was the voltage measurement at electrode E2 ( $V_{E2}$  that was located close to the connection) recorded the event but  $V_{E6}$  (that was located on the other edge of the sensing skin) did not record the event, showing that the event was localized to the area of electrode E2. Furthermore,  $V_{E3}$  did not record the event where as  $V_{E5}$  did record a change in voltage, showing the opposite behavior from  $V_{E2}$  and  $V_{E6}$ .

Finally, it was observed that the strain gauge data had higher electrical noise in the data than the sensing skin data did. This was unexpected since the strain gauges were directly connected to the commercially available WSN node and the sensing skin was connected to a custom circuit board prototype, where higher noise might be expected.

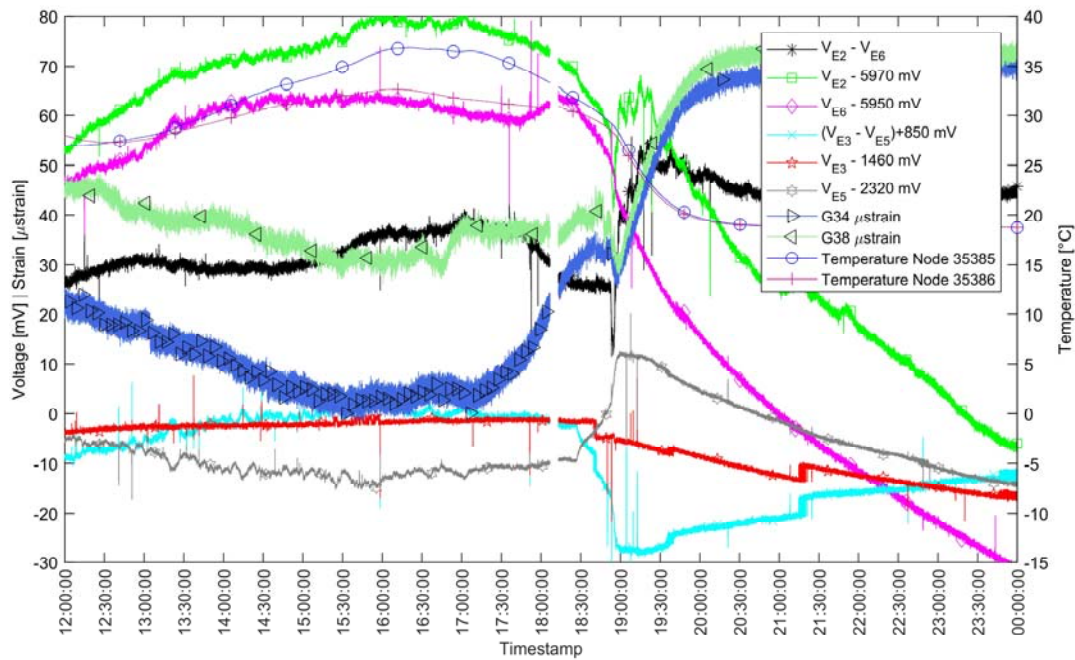


Figure 4.13: Sensing skin data compared to strain gauged and node temperature data (Data date: 05/15/2018 – 05/16/2018)

#### 4.6 Carbon nanotube-based sensor Conclusions

Carbon nanotube-based sensors with multiple electrodes haven't been used in the field for structural engineering applications. Therefore, this project was used to prove the concept of installing pre-manufactured CNT-based sensors in the field (not under laboratory conditions) and to collect data from the sensor via a commercially available WSN.

To collect deformation data in the connection area of a steel member, a sensing skin was bonded to the 6<sup>th</sup> Floor Girder of the BPI Building at the steel fabrication location. The sensing skin was installed in the field (outside the steel fabrication facility) using a pre-manufactured CNT-based sensor and a vacuum bagging method. The sensor was installed in one day, including preparing the steel surface, connecting

wires to the sensing skin, and bonding the sensor to the steel beam. The installed sensor was connected to two WSN nodes via a custom-made circuit board box (CBB). The instrumented Girder was installed in the BPI Building and two sets of data were collected for the sensing skin using two sets of six 9-volt batteries. The collected data was assessed and compared to strain gauge data that was collected in the same connection area on the opposite side of the web of the sensing skin. This project established the possibility of installing CNT-based sensors with multiple electrodes in the field to a building member without laboratory conditions.

The collected data was analyzed and the following conclusions were drawn. The voltage measurement data had a lower noise content than the commercially bought strain gauges, which was unexpected but positive. Furthermore, the collected voltage data recorded a data event at the same time as the strain gauges did, showing the monitoring capabilities of the sensing skin. Also, the sensing skin showed different voltage measurements during the data events at different electrode locations, showing the capability of the sensing skin to capture distributed strain behavior in a connection area.

## **Chapter 5**

### **LABORATORY TESTING**

Finite element models are used to quantify stresses in the vicinity of connections in Chapter 6. During the literature review (Section 2.3) it was found that these models can be very sensitive to input parameters, such as bolt pretension loads, friction coefficient for interactions, and mesh type and size. Therefore, it was necessary to validate the developed finite element model using a full-size laboratory test setup.

For the test setup, one of the instrumented connections of Purnell Hall Addition was replicated and densely instrumented. The selected connection was a beam-to-column connection that used two angles as shear connectors. The test setup was tested using three loading configurations. First, axial load was applied using a horizontal hydraulic actuator. Second, strong axis bending moment was applied using a manual hydraulic jack, and third, weak axis moment was applied using the same manual hydraulic jack.

#### **5.1 Selection of Connection Detail for the Laboratory Test Setup**

Since Purnell Hall Addition was the first building that was instrumented for this research project, it was decided to replicate one of the connections that was highly instrumented during this field monitoring. Furthermore, the selected connection was chosen to be a commonly used connection type, not overly complicated to replicate, and easy to disassemble (for the purpose of reuse). Therefore, the Girder to Long

Column connection, existing at the location highlighted with a circle in Figure 5.1 in the actual structure, was selected for replication. The connection consisted of the Girder (W360x147 [W14x99]) that was connected to the Long Column (W200x71 [W8x48]) using two angle sections (L100x100x8 [L4x4x5/16]) and nine bolts. Three of the bolts connected the web of the Girder to the two angle sections and six bolts connect the column to the angle sections as shown in Figure 5.2. In the field, the connection was instrumented using two uniaxial strain gauges on one side of the web of the Girder and one strain rosette on the opposite side of the web. The field instrumentation drawing is shown in Figure 5.2.

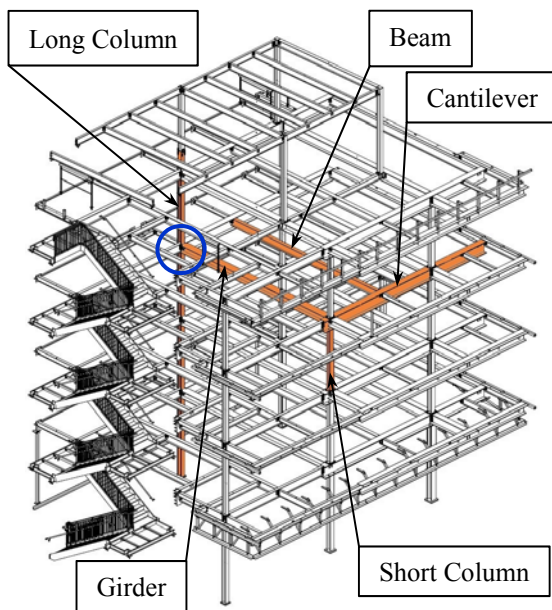


Figure 5.1: Location of Girder to Long Column connection in Purnell Hall Addition. (Adapted from RC Fabricators)

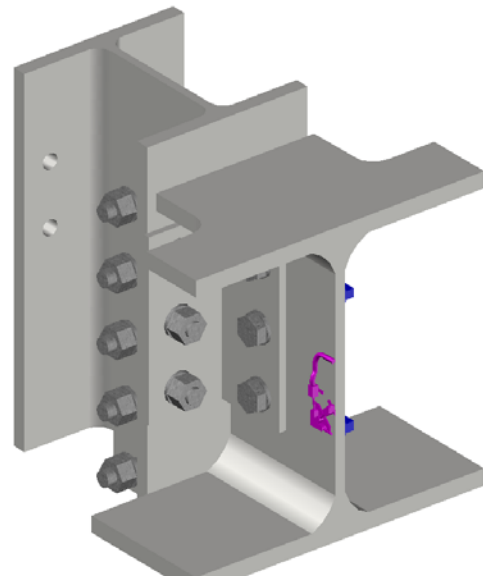


Figure 5.2: Girder to Long Column connection detail including field instrumentation

## 5.2 Laboratory Test Setup

The laboratory test setup consisted of a beam and a column with bracing as shown in Figure 5.3. The beam (W360x147 [W14x99]) had a length of 1.5 m (5 ft) and was attached to the column using two angles (L100x100x8 [L4x4x5/16]) and 7 bolts. The beam and angle dimensions are the same as those used in the actual structure. The column used in the laboratory setup was a W360x147 [W14x99]. This column was larger than the column used in the field, a W200x71 (W8x48). The beam web was connected to the two angles using three M20 (3/4") bolts. The other legs of the angles were connected to the column using four (1-1/4") bolts. Four bolts were used for the test setup instead of the six bolts used in the field connection (Figure 5.2), so the hole pattern in the column was symmetric and the beam could be rotated 90 degrees to perform weak axis tests of the connection as described in Section 5.3.3 The center bolt on the legs of the angles connecting to the beam was located 21.6 mm (0.85 in) above the centerline of the beam, which resulted in an eccentric connection. This eccentricity caused positive strong axis bending moment when the beam was loaded axially in tension.

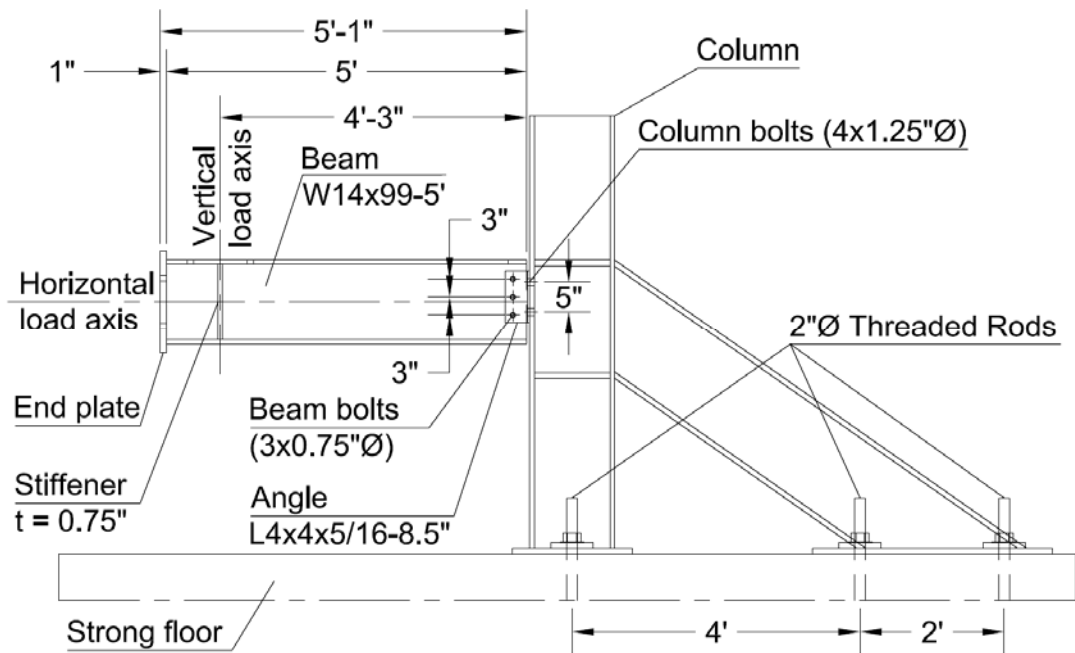


Figure 5.3: Schematic of the laboratory test setup (north view)

The column with bracing was an assembly of built-up sections which were readily available for use in the University of Delaware Structures Laboratory. The column with bracing was connected to the laboratory strong floor using six 50 mm (2 in.)  $\varnothing$  threaded rods. The fabrication drawings of the test setup can be found in the Appendix of Wennick (2016). The material properties of each part of the test setup are listed in Table 5.1, including the theoretical yield and ultimate stress limits of the respective materials. The material for the column with bracing was unknown. Therefore, it was conservatively assumed to be A36 steel.

Table 5.1: Material properties of the laboratory test setup parts

Part	Material	Minimum Specified Yield stress ( $F_y$ ) [MPa] (ksi)	Minimum Specified Ultimate stress ( $F_u$ ) [MPa] (ksi)
Beam (W360x147 [W14x99])	A992	345 (50)	450 (65)
Angle (L100x100x8 [L4x4x5/16])	A36	250 (36)	400 – 550 (58 – 80)
Beam to angle bolts (M20x65 [ø3/4"x2 1/2"])	A325N	635 (92)	825 (120)
Angle to column bolts (M30x 90 [ø1 1/4"x3 1/2"])	A325N	635 (92)	825 (120)
Column with bracing	Unknown Steel (A36 assumed)	250* (36)*	400* (58)*

\* Assumed values

Once the test setup was completely assembled and instrumented, the beam was whitewashed, which helped detect if any parts of the beam have yielded during the load tests. Yielding of the steel would have caused the whitewash to flake off.

The test setup was heavily instrumented using conventional uniaxial bondable strain gauges, bondable strain rosettes and displacement sensors. Furthermore, a novel carbon nanotube sensing skin was installed in the connection area. The conventional instrumentation is discussed in Section 5.2.1 and the novel instrumentation is discussed in Section 5.2.2.

### 5.2.1 Strain and Displacement Instrumentation

The conventional instrumentation was applied to five cross-sections (four beam cross-sections and one cross-section on each angle) as shown in Figure 5.4, which are described in the following subsections. The sections were labeled based on the location on the test setup. This labeling convention was also used to label each sensor. For example, each sensor in the beam end instrumentation section starts with the words “Beam End” and then with a specific sensor description, i.e. “Beam End North Vertical Displacement”, or BENVD. The different sensors are labeled in their respective instrumentation subsections. The label details are further explained in Table 5.2 for all uniaxial strain gauges, in Table for all rosette gauges, and in Table 5.4 for all the displacement sensors.

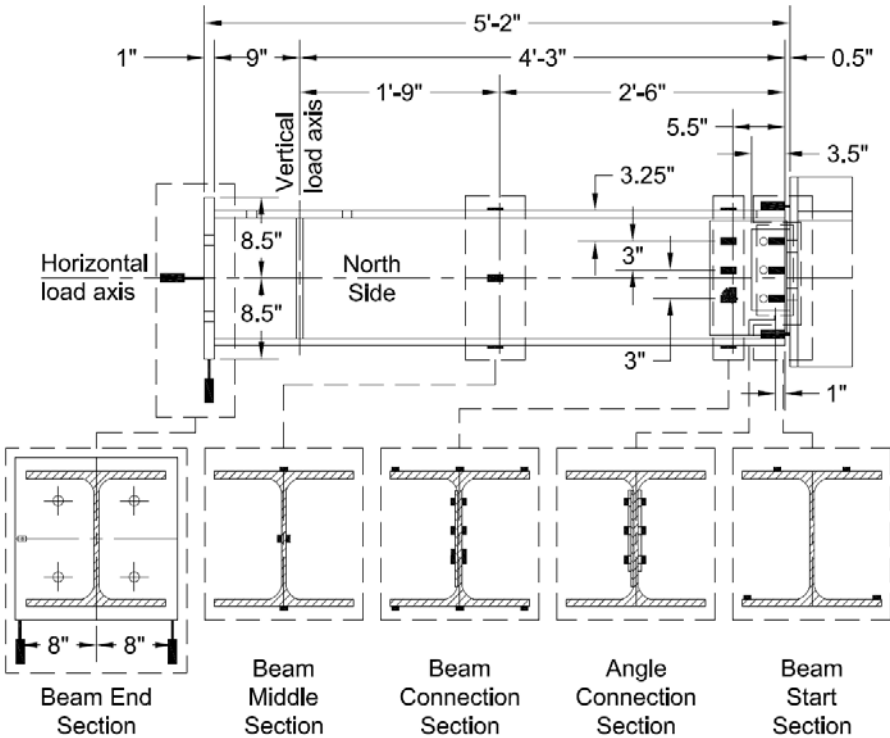


Figure 5.4: Instrumentation sections of the laboratory test setup (north view)

More specific information about the strain gauges and the displacement sensors used can be found in Table 5.5 and Table 5.6. All strain gauges and displacement sensors as well as the load cells were connected to a data acquisition system and data was sampled at 10 Hz during loading.

Table 5.2: Uniaxial strain gauge instrumentation label details

<b>Label</b>	<b>Part</b>	<b>Section</b>	<b>Location 1</b>	<b>Location 2</b>	<b>Location 3</b>
ACTN	Angle	Connection	Top	North	-
ACMN	Angle	Connection	Middle	North	-
ACBN	Angle	Connection	Bottom	North	-
ACTS	Angle	Connection	Top	South	-
ACMS	Angle	Connection	Middle	South	-
ACBS	Angle	Connection	Bottom	South	-
BCTFN	Beam	Connection	Top	Flange	North
BCTFC	Beam	Connection	Top	Flange	Center
BCTFS	Beam	Connection	Top	Flange	South
BCBFN	Beam	Connection	Bottom	Flange	North
BCBFC	Beam	Connection	Bottom	Flange	Center
BCBFS	Beam	Connection	Bottom	Flange	South
BCWTN	Beam	Connection	Web	Top	North
BCWMN	Beam	Connection	Web	Middle	North
BCWTS	Beam	Connection	Web	Top	South
BCWMS	Beam	Connection	Web	Middle	South
BMTFC	Beam	Middle	Top	Flange	Center
BMBFC	Beam	Middle	Bottom	Flange	Center
BMWCN	Beam	Middle	Web	Center	North
BMWCS	Beam	Middle	Web	Center	South

Table 5.3: Rosette strain gauge instrumentation label details

<b>Label</b>	<b>Part</b>	<b>Section</b>	<b>Location 1</b>	<b>Location 2</b>	<b>Location 3</b>	<b>Other</b>
BCWBNH	Beam	Connection	Web	Bottom	North	Horizontal
BCWBN45	Beam	Connection	Web	Bottom	North	45 Degree
BCWBNV	Beam	Connection	Web	Bottom	North	Vertical
BCWBSH	Beam	Connection	Web	Bottom	South	Horizontal
BCWBS45	Beam	Connection	Web	Bottom	South	45 Degree
BCWBSV	Beam	Connection	Web	Bottom	South	Vertical

Table 5.4: Displacement sensors instrumentation label details

<b>Label</b>	<b>Part</b>	<b>Section</b>	<b>Location 1</b>	<b>Location 2</b>	<b>Location 3</b>	<b>Other</b>
BSTFND	Beam	Start	Top	Flange	North	Displacement
BSTFSD	Beam	Start	Top	Flange	South	Displacement
BSBFND	Beam	Start	Bottom	Flange	North	Displacement
BSBFSD	Beam	Start	Bottom	Flange	South	Displacement
BECNHD	Beam	End	Center	North	Horizontal	Displacement
BENVD	Beam	End	North	Vertical	-	Displacement
BESVD	Beam	End	South	Vertical	-	Displacement

Table 5.5: Strain gauge information

<b>Sensor type</b>	<b>Size</b>	<b>Resistance</b>	<b>Angle</b>	<b>Manufacturer</b>
Uniaxial Strain Gauge	¼"	350 Ω	N/A	Micro-Measurements®
Strain Gauge Rosette	¼"	350 Ω	45 Degree	Micro-Measurements®

Table 5.6: Displacement sensor information

<b>Label</b>	<b>Sensor type</b>	<b>Range</b>	<b>Model</b>	<b>Manufacturer</b>
BSTFND	Linear Potentiometers	½”	404 Series	TT Electronics
BSTFSD	Linear Potentiometers	½”	404 Series	TT Electronics
BSBFND	Linear Potentiometers	½”	404 Series	TT Electronics
BSBFSD	Linear Potentiometers	½”	404 Series	TT Electronics
BECNHD	Linear Position Transducer	5”	PA-5-DS-L3M-	UniMeasure, Inc.
BENVD	Linear Variable Differential Transformer (LVDT)	4”	DCT 2000	RDP Group
BESVD	Linear Variable Differential Transformer (LVDT)	4”	DCT 2000	RDP Group

### 5.2.1.1 Angle Connection Section

Six uniaxial strain gauges were attached on top of the connection angles as shown in Figure 5.5 and 5.6. The strain gauges were placed between the beam web to angle bolts and the other leg of the angle. The gauges were aligned with the bolts and placed on both connection angles. The strain gauges measured longitudinal strain (horizontal strain). These gauge labels are: ACTN/S (north/south), ACMN/S, ACBN/S for the top, middle, and bottom gauges, respectively.

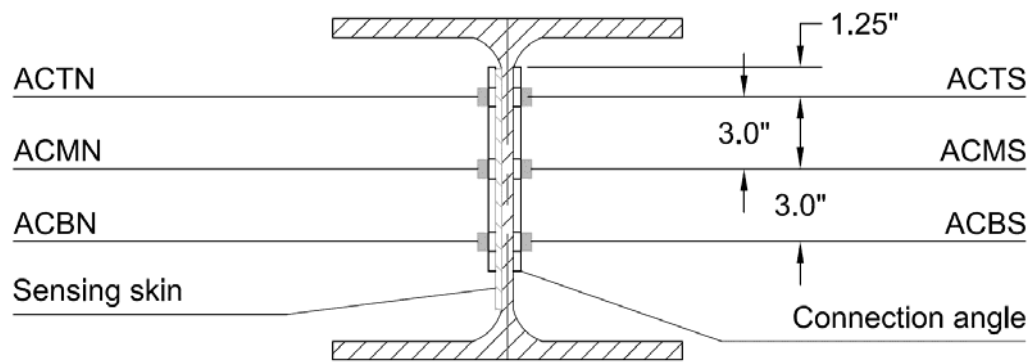


Figure 5.5: Angle connection instrumentation section schematic

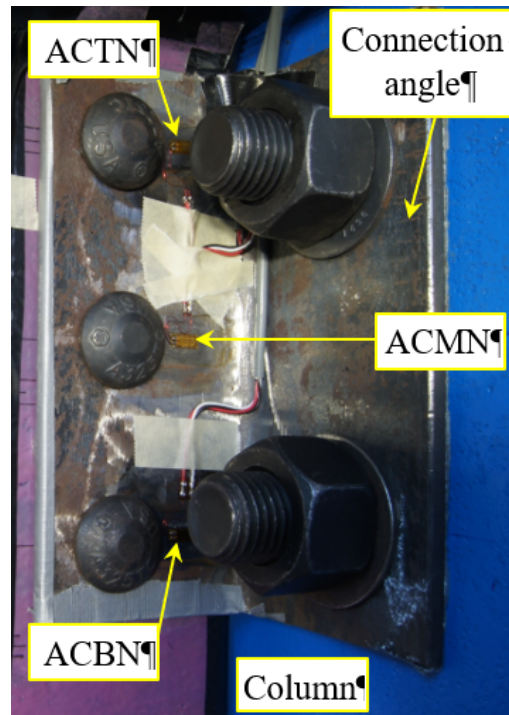


Figure 5.6: Angle connection instrumentation

### 5.2.1.2 Beam Start Section

Four displacement sensors were used to measure the horizontal displacement of the beam flanges at the end of the beam adjacent to the column (i.e. measuring the

gap between the end of the beam and the flange of the column) in the locations shown in Figure 5.7. Two displacement sensors measured displacements of the top of the top flange (labeled BSTFND and BSTFSD) and the other two sensors measured displacements of the top of the bottom flange (labeled BSBFND and BSBFSD).

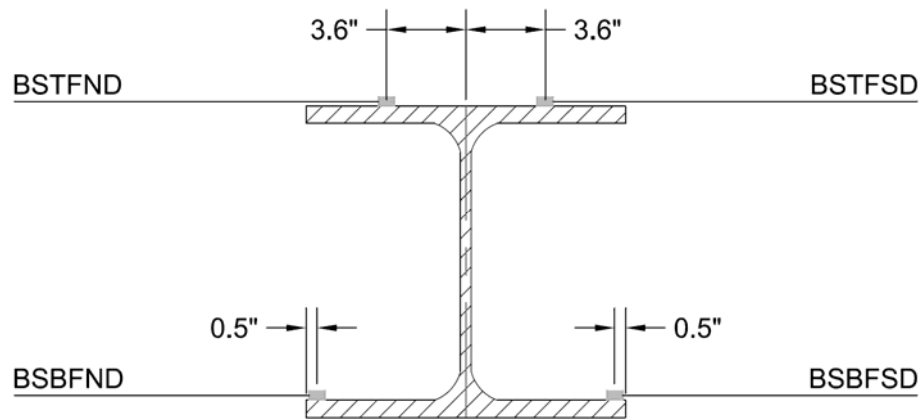


Figure 5.7: Beam start instrumentation section schematic

### 5.2.1.3 Beam Connection Section

This beam section was closest to the connection area and was therefore densely instrumented as shown in Figure 5.8, using 10 uniaxial strain gauges and two strain rosettes. The flanges of the beam were instrumented using three uniaxial strain gauges on each flange (BCTFN/C/S and BCBFN/C/S). The strain gauges on the web were aligned with the bolt holes, similar to the angle connection strain gauges. The top and middle strain gauges (BCWTN/S and BCWMN/S) were uniaxial strain gauges whereas the bottom strain gauges were two strain rosettes. The rosettes are fabricated by stacking three uniaxial strain gauges on top of each other with a 45-degree angle in between them. The used strain rosettes (Type: CEA-09-125UR-350) were

manufactured by Micro-Measurements<sup>®</sup>. The horizontal strain gauge of the rosettes (BCWBNH / BCWBSH) were aligned with the bottom bolts. The strain gauges on the north side of the beam were attached to the sensing skin as shown in Figure 5.8 and in Section 5.2.2 and the strain gauges on the south side of the beam were attached directly to the steel surface of the beam.

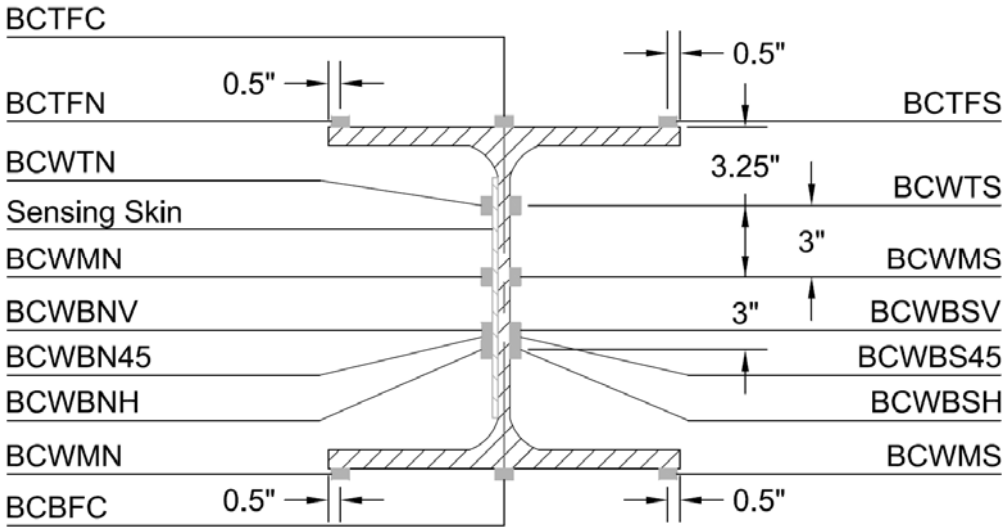


Figure 5.8: Beam connection instrumentation section schematic

**5.2.1.4 Beam Middle Section**

This cross-section was instrumented with 4 uniaxial strain gauges, as shown in Figure 5.9. Two of the strain gauges were bonded to the center of the top flange (BMTFC) and the center of the bottom flange (BMBFC), respectively. The other two strain gauges were placed at the mid-height of the beam on both sides of the web (BMWCN and BMWCS). This section was placed at the mid span of the beam to capture global stresses away from the connection area.

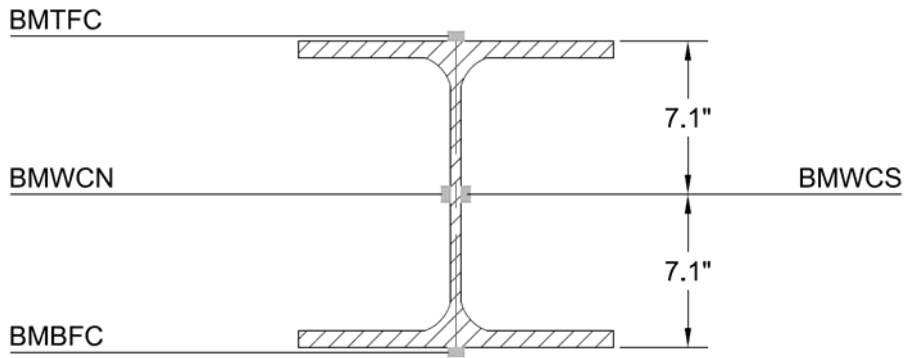


Figure 5.9: Beam middle instrumentation section schematic

### 5.2.1.5 Beam End Section

This section was used to capture the beam end displacements of the laboratory test setup in the horizontal as well as the vertical directions. Therefore, three displacement sensors were placed in this section as shown in Figure 5.10. Two of the sensors (BENVD and BESVD) measured displacement of the end plate in the vertical direction. The third sensor (BECNHD) was attached to the beam end plate and measured horizontal displacements.

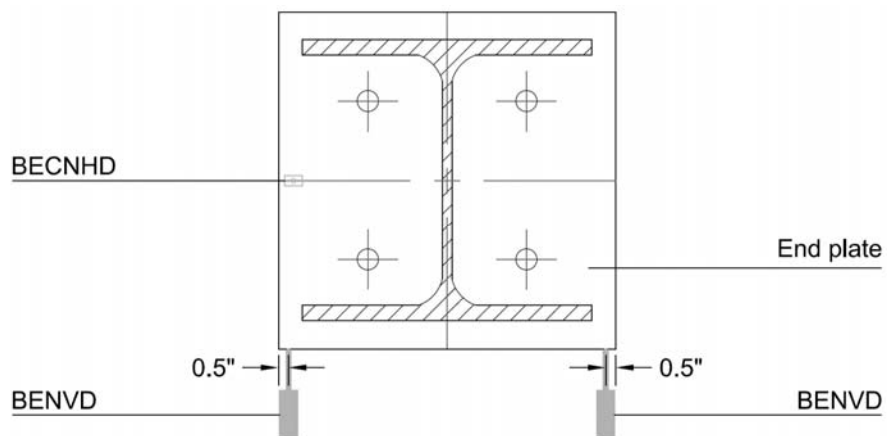


Figure 5.10: Beam end instrumentation section schematic

### 5.2.2 Carbon Nanotube-Based Sensing Skin Installation on the Test Setup Beam

A CNT-based sensor was installed in the connection area of the test beam to evaluate the capability of this novel technique for inferring strain. The sensing skin was fabricated using the same method as described in Section 4.1 with a width of 203 mm (8 in) and a height of 305 mm (12 in). The sensing skin was attached to the test beam in the connection area, as shown in Figure 5.11, using a two-part epoxy paste adhesive (HYSOL 9309.3NA, Henkel Corporation). The epoxy forming this adhesive layer was applied to the test beam once the test beam was cleaned.



Figure 5.11: Adhesive layer application to install the sensing skin

Once the adhesive layer was applied to the test beam, the sensing skin was put in place and covered with a breather layer, as shown in Figure 5.12. The entire area around the protective layer was enclosed to create a vacuum bag. Using a hose and an electrical pump, a vacuum was created to bond the sensing skin uniformly to the steel beam. The sensing skin was left in the vacuum bag for 24 hours.

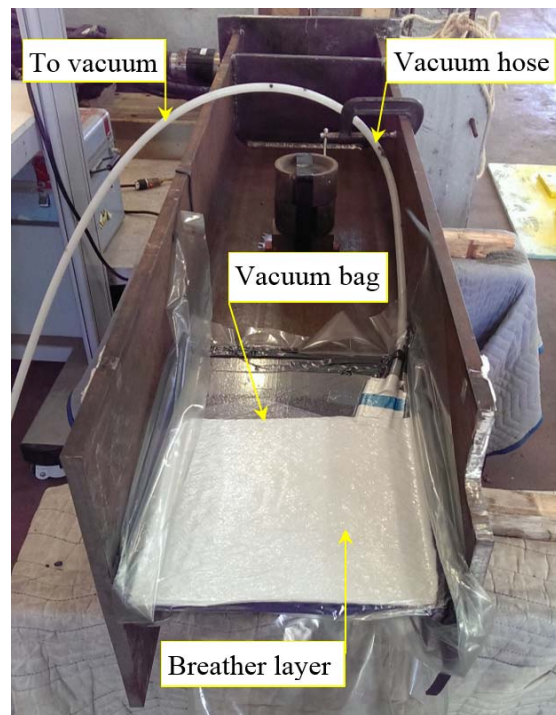


Figure 5.12: Bonding the sensing skin to the beam using the vacuum bagging method

Once the sensing skin was attached to the test beam, the vacuum bag and the protective layer was removed. Next the sensing skin was removed from the bolt hole areas and the bolt holes were coated using a nonconductive coating (M-Coat, Micro Measurements) as shown in Figure 5.13. To connect the sensing skin to the data

acquisition system, nine electrodes were created on the sensing skin using conductive silver paint (Flash Dry, SPI Supplies, West Chester, Pennsylvania) and connected to wires. The electrodes were labeled with an “E” following an arbitrary number as a subscript as shown in Figure 5.13 and 5.14. The nine electrodes were equally spaced in a 3 by 3 array along the height of the web (127 mm (5 in.) and along the length of the sensing skin (102 mm (4 in.)) as shown in Figure 5.13. Six of the electrodes ( $E_1 - E_6$ ) were placed on the longitudinal surface of the web near the connection, but not covered by the connection angle. Three of the electrodes ( $E_7 - E_9$ ) were placed on the cross-section of the web, as shown in Figure 5.13. The cross-section surface of the beam web was the only location where electrodes could be placed directly in the connection since every other location on the beam was covered by the connection angles. Finally, the conventional strain gauges (BCWTN, BCWMN, BCWBNH/45/V) were attached to the sensing as shown in Figure 5.8 and Figure 5.13.

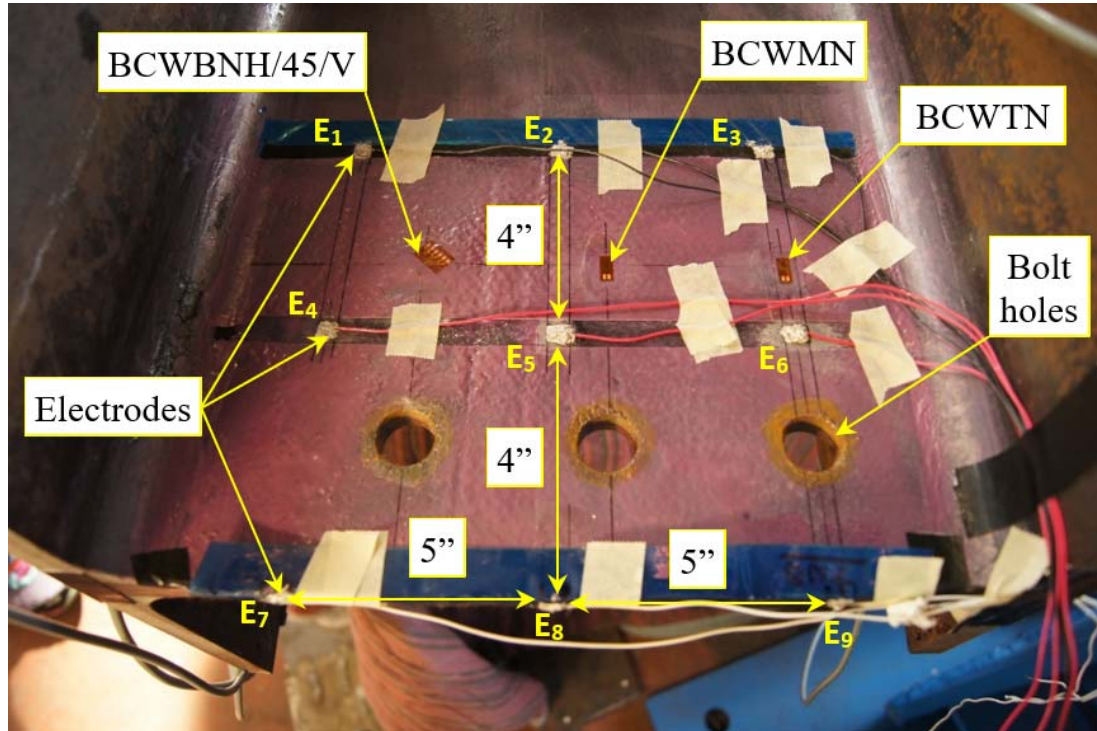


Figure 5.13: Installed sensing skin on the start of the beam including electrodes and strain gauges

Since the sensing skin had to be completely electrically insulated, the connection angle and the web bolts were electrically insulated using electrical tape and duct tape as shown in Figure 5.14. Furthermore, the electrodes of the sensing skin were protected and the final instrumented connection detail was shown in Figure 5.14.

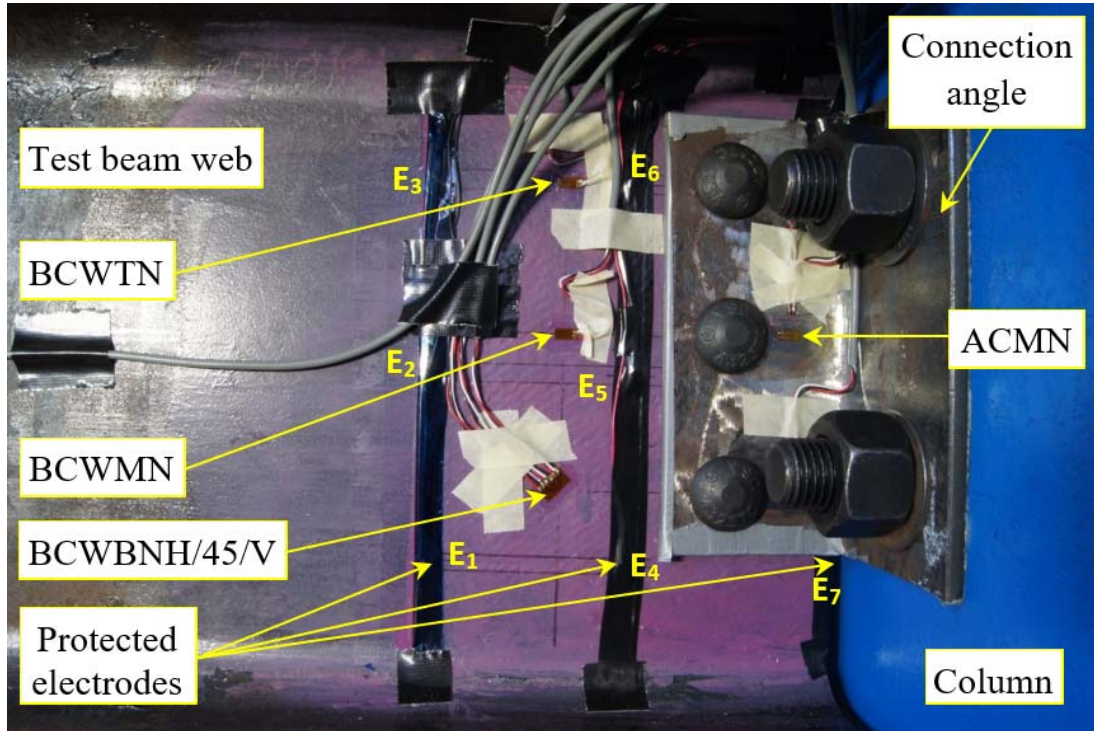


Figure 5.14: Final beam end instrumentation with electrically insulated connection angle (north view)

### 5.3 Load Tests

Once the laboratory test setup was fabricated, instrumented and installed, the setup was tested in three different configurations. First, axial load (tension and compression) was applied to the test beam as described in more detail in Section 5.3.1. The strong axis bending test setup configuration as explained in Section 5.3.2 and weak axis bending of the test setup was evaluated, as described in Section 5.3.3. For each configuration at least three tests were performed to check the repeatability of the data, which was confirmed. Therefore, only one set of test data is shown in the following subsections.

### 5.3.1 Axial Load Test Setup Configuration

For the axial load tests, a hydraulic actuator with a capacity of 667 kN (150 kips) was oriented horizontally and attached to the test setup as shown in Figure 5.15. The actuator was connected to a steel “support member” on the east side of the test setup. This member was connected to a testing frame bolted to the laboratory strong floor. More detail about dimensions of the support member and the custom actuator connection are given in (Wennick 2016).

The test beam was loaded in tension and compression using the attached horizontal actuator. The tests were run in load control and the applied force was measured using a load cell, with a capacity of 667 kN (150 kips), which was mounted between the actuator and the actuator attachment. The axial load test setup was shown in Figure 5.15.



Figure 5.15: South view of the laboratory test setup, axial load configuration

### **5.3.2 Strong Axis Bending Test Setup Configuration**

A preliminary finite element model of the test setup showed that parts of the connection yield at a very low load. Therefore, it was decided to use a manual hydraulic jack to apply vertical force to the test beam as shown in Figure 5.16, so that a lower magnitude of load could be more gradually applied compared to using the actuator. The location of the jack along the length of the beam was shown in Figure 5.4. A 222 kN (50 kip) load cell was placed between the manual hydraulic jack and a piece of wood (supporting the beam) to record the applied vertical force. The strong axis bending tests were conducted in displacement control, i.e. force was applied until a defined displacement (3.18 mm, 1/8 in.) was reached. Then data at this displacement was recorded for 30 seconds. This step was repeated until the maximum displacement (50.8 mm (2 in.) was reached. The maximum displacement limit was defined to avoid yielding of any parts of the test setup based on preliminary FEA.

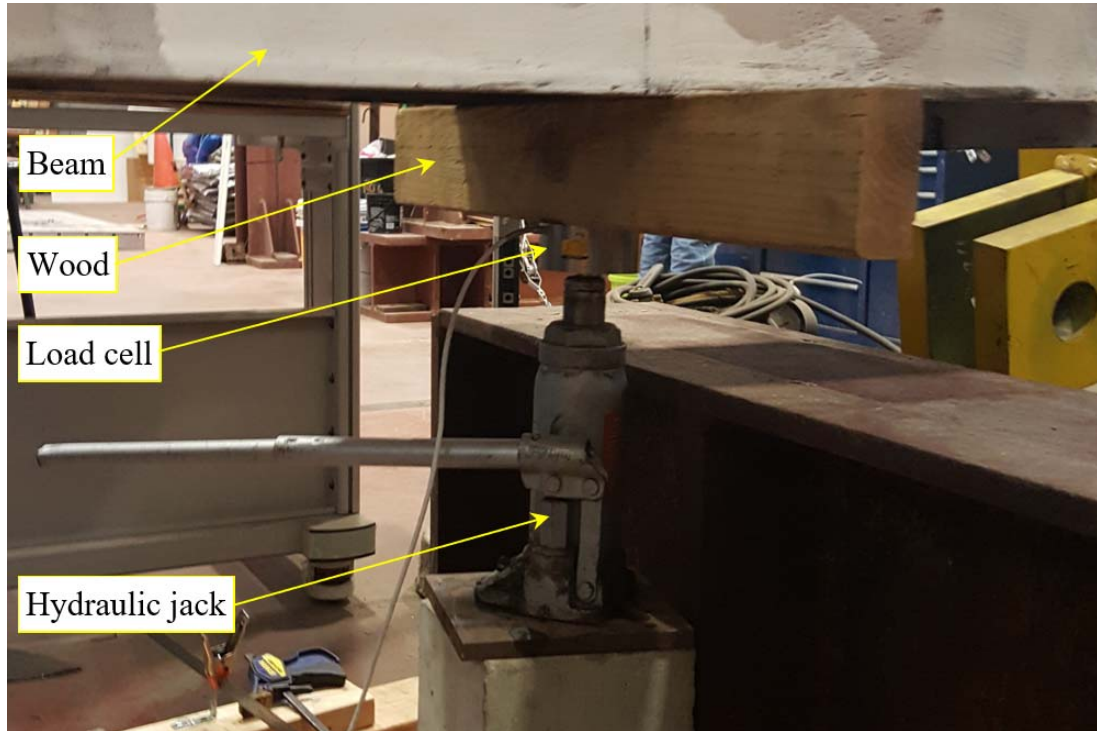


Figure 5.16: South view of the manual hydraulic jack, strong axis bending configuration

### 5.3.3 Weak Axis Bending Test Setup Configuration

For the weak axis testing, the actuator attachments were removed and the test beam was rotated  $90^\circ$  as shown in Figure 5.17. After the beam was rotated, the top flange of the test beam was located on the north side and the bottom of the beam on the south side. Similar to the strong axis bending tests, the vertical load for the weak axis test was applied using a manual jack. The load was applied to the flanges using a 2 in. x 2 in. wood cross-section to transfer the force between the jack and the flanges.



Figure 5.17: South view of the laboratory test setup, weak axis bending configuration

#### 5.4 Test Results

For the following test results the collected strain data was converted to stress using Hooke's law with an assumed Young's modulus of 200,000 MPa (29,000 ksi). The collected time domain data was averaged for each load step to obtain the graphs shown in Figure 5.18 through 5.23. Furthermore, in the following figures, the strain gauges on the same side of the web of the test beam were plotted in the same color (north = red, south = black). Also, the gauges at the same location (but opposite sides) were plotted with the same marker.

Since the purpose of the lab test setup was to validate the finite element model described in Chapter 6 it was important to not yield any parts of the test setup under each loading configuration. Therefore, several elastic tests were performed for the

three different loading scenarios (i.e. axial force, strong axis bending, and weak axis bending). The obtained data was compared to the preliminary finite element models. During the comparisons it became obvious that the electrically insulated bolts passing through the beam and the insulated connection angles had an unknown influence on the test setup that resulted in test data that did not compare favorably to the analytical data. Therefore, the insulated angles and bolts were replaced with uninsulated ones. This step improved the correlation between lab data and finite element model drastically. However, it also made it temporarily impossible to collect data with the CNT-based sensor.

#### **5.4.1 Axial Force Tests**

The axial force test was divided into tension and compression tests. Both tests were force controlled and a maximum of 22 kN (5 kips) was applied. The results for the tension and the compression tests were similar, therefore only the tension test results were included. Furthermore, since the test setup was used mainly to validate the finite element model, the following results were used to check if the test setup displayed any unexpected behavior and to compare the results to theoretical values where possible.

The theoretical uniaxial stress for a 22 kN (5 kip) load was calculated to be 1.17 MPa (0.17 ksi) using basic solid mechanics, i.e.  $P/A$ , where  $P$  was the load and  $A$  was the area of the cross section ( $18.8 \cdot 10^3 \text{ mm}^2$  [ $29.1 \text{ in}^2$ ]). If the eccentricity of the connection was taken into account, the total stress for BCWTN and BCWTS was 1.3 MPa (0.19 ksi). The stress due to eccentricity of the connection was calculated as follows,  $\sigma = M \cdot c / I$ , or  $\sigma = P \cdot e \cdot c / I$ , where  $P$  was the axial load,  $e$  was the eccentricity (21.6 mm [0.85 in]),  $c$  was the distance between the centerline and the gauge location

(97.8 mm [3.85 in]), and  $I_x$  was the moment of inertia for the strong axis ( $462 \times 10^6 \text{ mm}^4$  [1110 in<sup>4</sup>]).

The data for the beam connection gauges for the tension test were shown in Figure 5.18. It can be seen that the gauge values at the final axial load are much higher than the theoretically calculated value by 1.3 MPa [0.19 ksi]. Furthermore, the stress difference between top, middle, and bottom strain gauge pairs (e.g., BCWT and BCWM and BCWB) indicate a moment being applied to the connection as was expected due to the eccentricity of the connection.

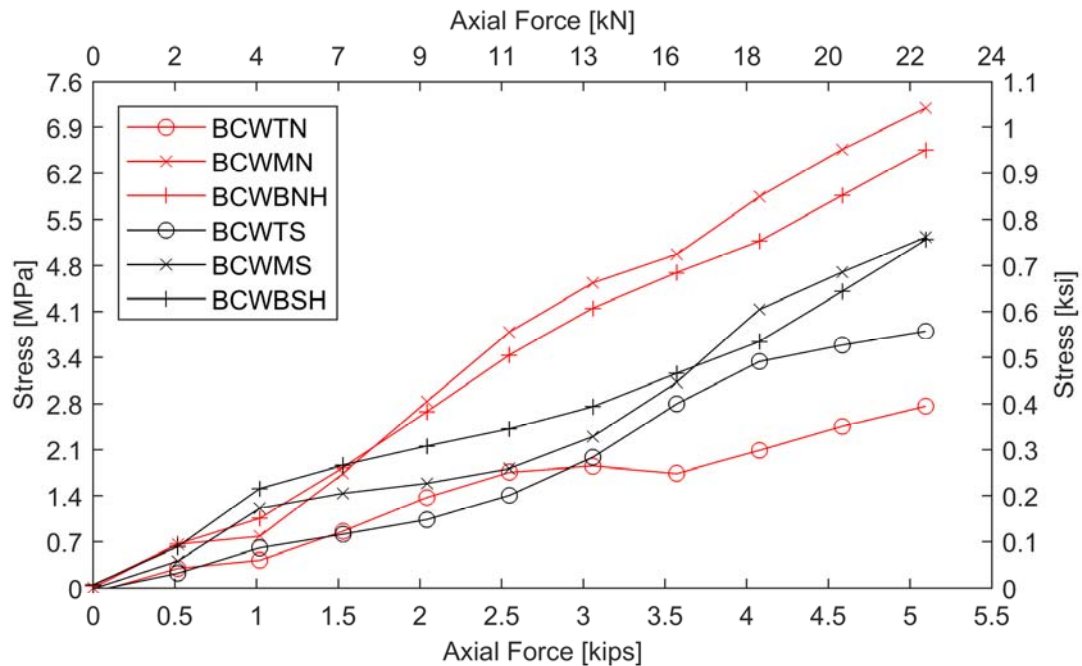


Figure 5.18: Beam connection cross-section stress data for applied axial tension force

The beam middle stress data for the axial load test were shown in Figure 5.19. The obtained stress values are close to the theoretically calculated stress value for this

loading scenario. This was expected, since the beam middle gauges are further away from the connection and associated stress concentration.

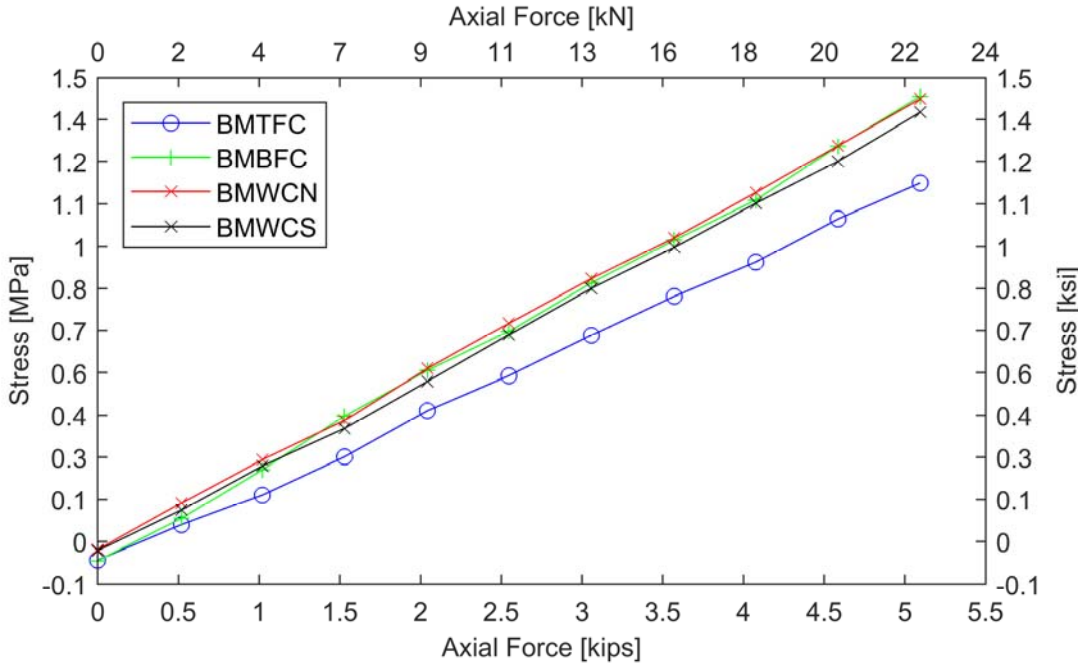


Figure 5.19: Beam middle cross-section stress data for applied axial tension force

**5.4.2 Strong Axis Bending Tests**

The theoretical stress for a vertical force of 13 kN (3 kips) was calculated to be 3.24 MPa (0.47 ksi) for BCWTN and BCWTS. The stress was calculated using the same method as described in Section 5.4.1.

The beam connection cross-section data for the strong axis test were shown in Figure 5.20. During the different tests of the laboratory test setup, some of the installed strain gauges were damaged. For the following plots BCWTS and BCWBSH were missing. Similar to the previous section, the laboratory stresses were much

higher than the theoretical stress. However, the data indicates moment at the cross-section, which was expected.

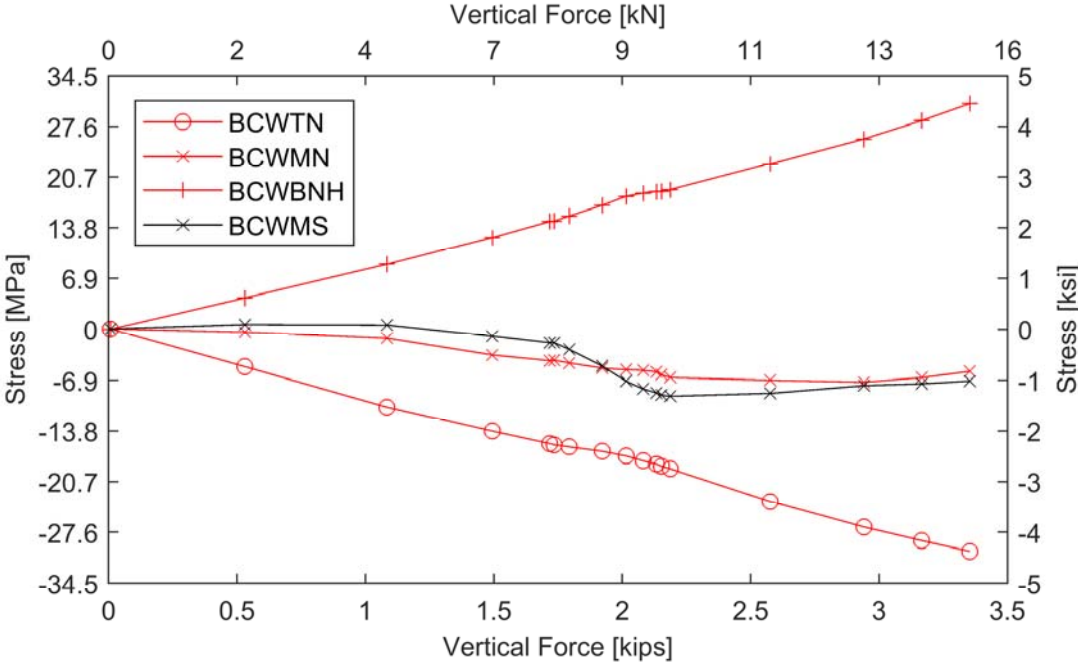


Figure 5.20: Beam connection cross-section stress data for applied strong axis bending moment

For the beam middle cross-section, the theoretical stress value was 2.76 MPa (0.40 ksi) for gauge BMTFC. This value is very similar to the value found in the lab data shown in Figure 5.21. The beam middle data shows similar trends to the beam connection data.

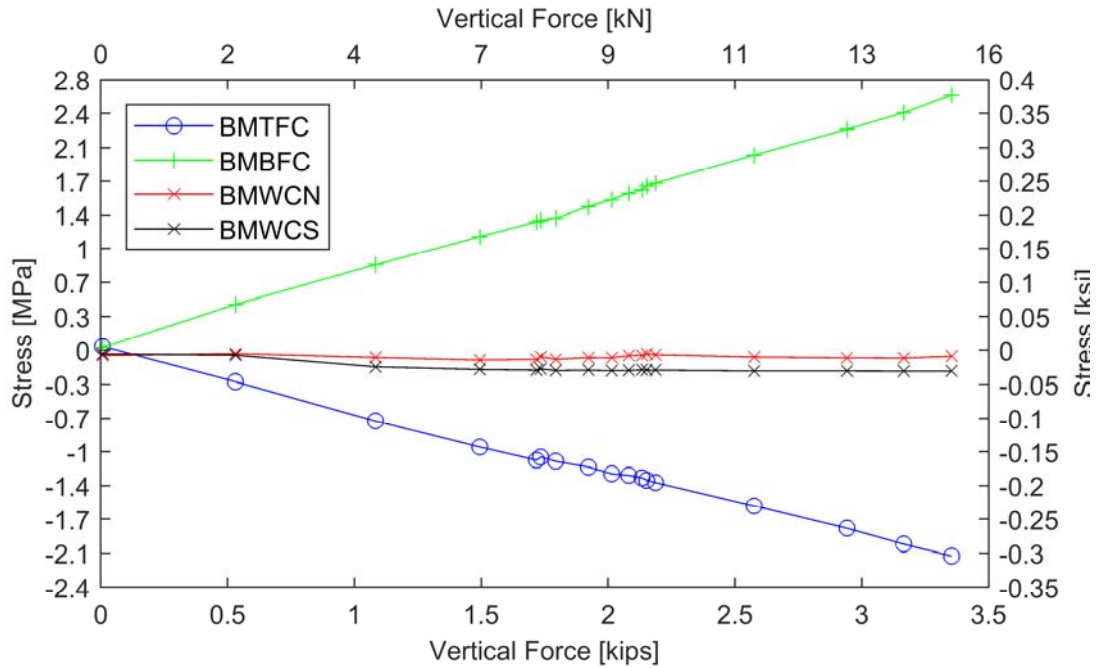


Figure 5.21: Beam middle cross-section stress data for applied strong axis bending moment

For the strong axis test, the beam start displacement sensor data was compared to theoretical beam start displacements. The theoretical values were obtained by selecting a pivot point and displacing the end of the beam in a CAD software assuming rigid body motion and measuring the resulting beam start displacement. The results are shown in Figure 5.22. The different theoretical values shown were measured by choosing different centers of rotation. The center of rotation for the theoretical value was selected to be at the center of the middle connection bolt, the center of the bottom connection bolt, and the center of the top connection bolt. When comparing the displacement sensor data from the lab to the theoretical values, it can be seen that the center of rotation for the laboratory test setup was between the bottom and the middle bolt. These results were unexpected, since it was assumed the

connection would rotate about the center of the middle bolt. However, the lab results were plausible, since the connection was not at the beam center and different bolts may have been subjected to different pre-tension forces.

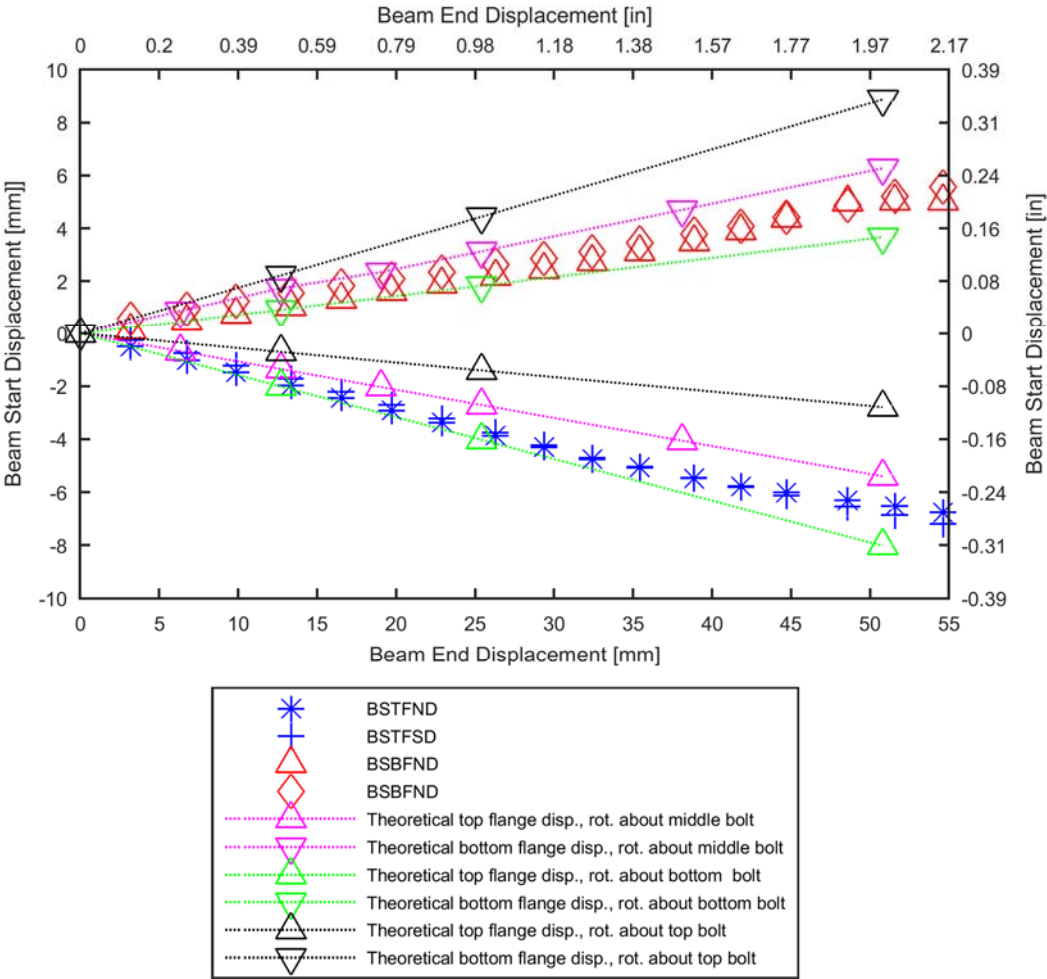


Figure 5.22: Beam start displacement data compared to theoretical displacement data for applied strong axis bending moment

### 5.4.3 Weak Axis Bending Tests

For the weak axis test only a very small force was needed to induce a significant displacement at the end of the test beam. Therefore, the test force was kept small to keep all parts of the test setup elastic.

The theoretical stress data was calculated for both the beam connection and the beam middle gauge cross-sections. The computed stress was 0.21 MPa (0.03 ksi) for the gauges in the connection cross-section and 0.07 MPa (0.01 ksi) for the gauges in the middle cross-section. The data for the beam middle cross-section is not shown, since all data values were very close to zero. The laboratory stress data for the beam connection cross-section were plotted in Figure 5.23. Similarly, to the previous test data (axial and strong axis bending) the recorded stresses close to the connection exceed the theoretically calculated values.

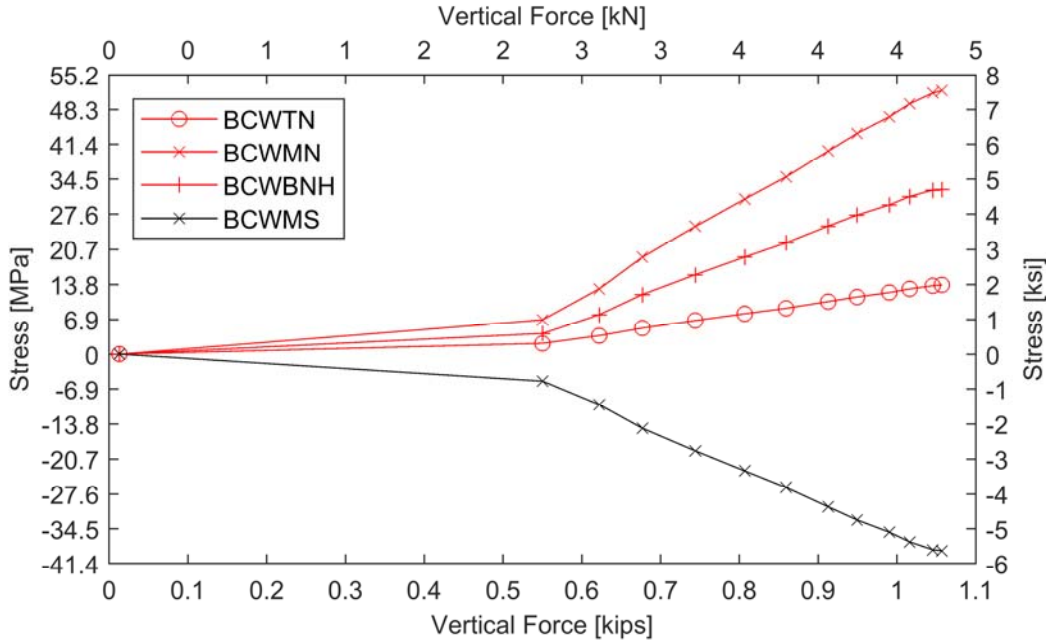


Figure 5.23: Beam connection cross-section stress data for applied weak axis bending moment

## 5.5 Conclusion

To validate the finite element model of a connection area, a full-scale laboratory test setup was created. For the test setup, one of the instrumented connections of the Purnell Hall Addition was replicated and densely instrumented. The selected connection was a beam-to-column connection that used two angles as shear connectors. The test setup was instrumented using 20 uniaxial strain gauges, two 45° strain rosettes, and 7 displacement sensors with most of the strain gauges located in the connection area of the test setup. Furthermore, a CNT-based sensor was installed on the beam in the connection area. The test setup was tested using three loading configurations. First, axial compression and tension loads were applied using a horizontal hydraulic actuator. Second, strong axis bending moment was applied using a manual hydraulic jack, and third, weak axis moment was applied using the same manual hydraulic jack.

The collected data was compared to theoretically calculated values using simple solid mechanics equations. It was found that the collected strain data compared well to the theoretical values at mid-span of the beam (762 mm (2 ft. 6 in.) away from the connection). However, strain gauge data from the connection area was higher for all load test data compared to the theoretically calculated values.

These test results confirmed that stresses in connection areas cannot be calculated using conventional basic solid mechanics equations but follow St. Venant's principle. Therefore, to quantify the complex stress distribution in a connection area, it was necessary to use a finite element model to extrapolate construction stresses into a connection area. Furthermore, using the test data of the full-scale test to validate the finite element results was a viable option.

## **Chapter 6**

### **FINITE ELEMENT ANALYSIS**

The last part of this research was to investigate if connection areas of structural steel members could be reused. Current practice in the reuse industry is to cut off connection areas and only reuse the leftover part of the steel member. However, doing so reduces the length of the steel member and therefore its reuse potential.

To quantify stresses in connection areas during construction, strain gauges were placed in the vicinity of connections during field instrumentation of the three buildings. Furthermore, one of the steel member connections instrumented in the Purnell Hall Addition (the Girder to Long Column connection, see Figure 5.1 and 5.2) was replicated in the University of Delaware Structural Laboratory and densely instrumented as described in Chapter 5. Additionally, a finite element model (FEM) of the test setup was created using ABAQUS, as explained in Section 6.1. Next the FEM was validated using laboratory test setup results from Chapter 5 and the findings were summarized in Section 6.2.

To extrapolate connection area field data, the connection area of the Girder to Long Column connection of the Purnell Hall Addition (see Figure 3.9 for instrumentation details) was modeled using FEA and the FEM was loaded using field data results and the following process. Once the FEM was validated, different loads (axial force, strong and weak axis bending moments) were individually applied to the FEM and the resulting stresses were combined using superposition. The superposition data from the FEM was compared to field data strain gauge values to find the best

match between field data and FEM superposition data. The loading conditions associated with the selected superposition stress values were then applied to the FEM of the connection and the resulting FEM stress values were analyzed for potential yielding of the connection area due to field data loadings. The subsequent results are discussed in more detail in Section 6.3.

## **6.1 Finite Element Model Overview**

The FEM for this project was created using ABAQUS/Standard Version 6.14-1 (ABAQUS, 2015a). The FEM was a replica of the laboratory test setup described in Chapter 5 and an overview of the model is shown in Figure 6.1. The test setup as well as the FEM consisted of a beam (W360x147 [W14x99]), a column (steel built-up section), two connection angles (L100x100x8 [L4x4x5/16]), four column to connection angle bolts (M30 x 90 [ $\phi$ 1 1/4"x3 1/2"]), three beam to connection angle bolts (M20 x 65 [ $\phi$ 3/4"x2 1/2"]), a custom made vertical load attachment, and a custom made horizontal load attachment. The FEM was created using 8-node reduced integration linear brick and 6-node linear triangular prism solid elements. For the brick elements, the reduced integration option was used to save computational time. A model using brick elements without the reduced integration formulation provided similar results but at a much higher computational cost. For the triangular prism the full integration element was used since this was the only available option in ABAQUS.

The FEM parts and mesh are described in more detail in Section 6.1.1. Each part of the FEM was modeled using the material that was used in the laboratory test setup and the different material input parameters are described in Section 6.1.2. To keep the column from moving, boundary conditions were used as described in Section

6.3. Furthermore, the different parts of the FEM were held together by applying bolt pretension forces to the beam and the column bolts as well as defining interactions between the different parts as described in Section 6.1.3 and 6.1.4. Lastly, the pretension bolt load and three different loads (i.e. axial force, strong and weak axis bending moments) were applied in two steps as described in Section 6.1.4.

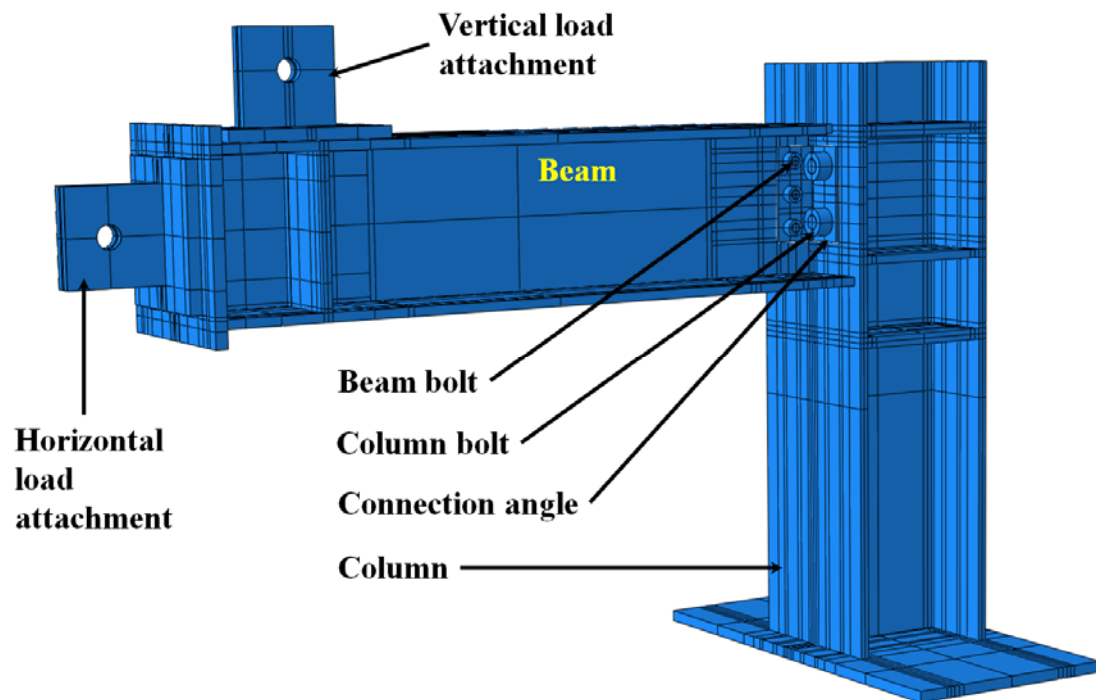


Figure 6.1: Annotated Overview of FEM of the laboratory test setup (isometric view)

### 6.1.1 Parts and Mesh

The FEM of the laboratory test setup was modeled using 11 individual parts, the beam, the column, two connection angles, three beam bolts and four column bolts. The model was modeled using two mesh seed sizes (2.5 mm (0.1 in.) and 12.7 mm (0.5 in.) respectively), and two finite element elements, C3D8R and C3D6 resulting in

a total of 661,000 finite element nodes. The different model parts are described in more detail in the following paragraphs.

The beam of the FEM model was created using W360x147 [W14x99] dimensions with a length of 1524 mm (5 ft.). More dimensions for this part can be found in AISC (2017). To simplify the meshing of the beam, the fillets of the hot rolled W-section were neglected; this reduced the cross-section properties of the beam, which was considered conservative. The vertical and horizontal load attachment as well as the stiffeners were modeled as part of the beam. The beam was modeled using A992 steel, the load attachment and the stiffeners were modeled using A36 steel as described in Table 6.1.

The beam was separated in to two meshing sections. Since the connection area was the main focus of this model it was meshed using a small mesh of 2.5 mm (0.1 in.). To reduce the computational demands for the model, only 254 mm (10 in.) from the start of the beam on the connection area side were meshed that densely. The rest of the beam including the load attachments and stiffeners were meshed with a mesh seed size of 12.7 mm (0.5 in.). Two types of elements were used to mesh the beam part, the C3D8R and the C3D6 element. The C3D6 elements were only used in the transition area between the different mesh sizes. Using these elements and the described mesh sizes, a total of 393,000 FEM nodes were created for this part.

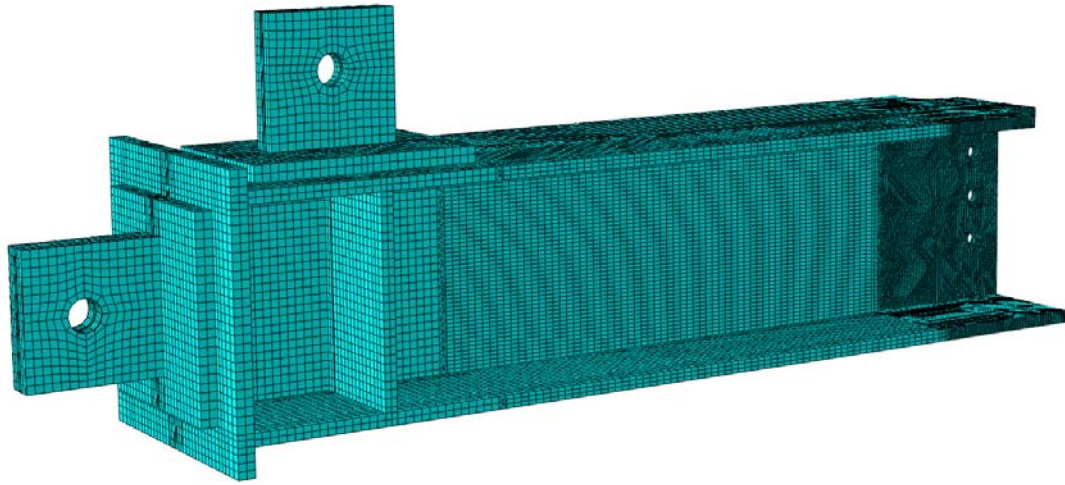


Figure 6.2: FEM of the beam with mesh

The column was modeled using dimensions measured from the laboratory test setup and A36 steel. The overall height of the column was 1384 mm (4 ft. – 6.5 in.), the built-up section had a depth of 362 mm (1 ft. – 2.25 in.) and a width of 378 mm (1 ft. – 2.875 in.). The column did not include the brace that was present in the laboratory setup (see Figure 5.3) to save computational time when running the model. However, the brace was modeled using springs as described in Section 6.1.3. Similar to the beam, the column was modeled using two different mesh sizes, 2.5 mm (0.1 in.) and 12.7 mm (0.5 in.) respectively. The same mesh elements (C3D8R generally and C3D6 for transition areas between mesh sizes) were used to mesh the column, which resulted in a total of 179,000 nodes.

Similar to the beam and the column, the connection angle was modeled using dimensions of the laboratory test setup, an L100x100x8 [L4x4x5/16] cross section with a length of 216 mm (8.5 in.) as shown in Figure 6.4. The fillets of the angle cross section were not modeled for simplicity and because it was conservative (due to

reduced cross-sectional area. The connection angle was meshed using a 2.5 mm (0.1 in.) seed size and C3D8R elements. This resulted in a total of 28000 nodes per connection angle.

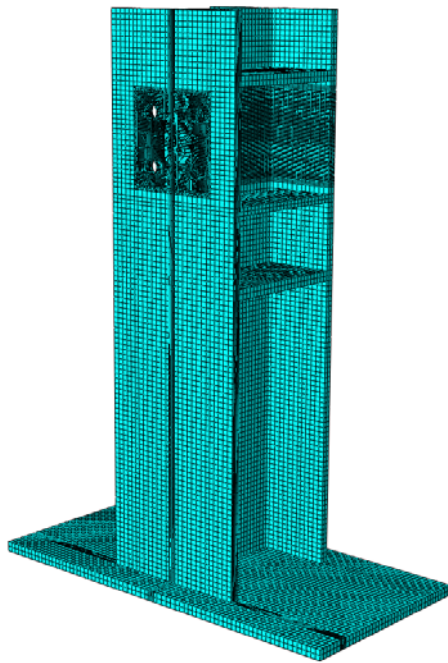


Figure 6.3: FEM of the column including mesh

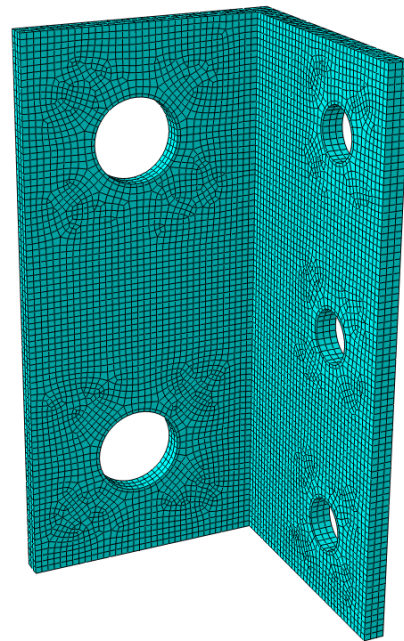


Figure 6.4: FEM of the connection angle including mesh

The column bolts (M30 x 90 [1-1/4"  $\varnothing$  x 3-1/2"]) and the beam bolts (M20 x 65 [3/4"  $\varnothing$  x 2 1/2"]) were both modeled using a mesh size of 2.5 mm (0.1 in.). The C3D6 elements were used along the longitudinal bolt axis and C3D8R elements were used elsewhere. This resulted in 4845 nodes for each column bolt and 4557 nodes for each beam bolts.

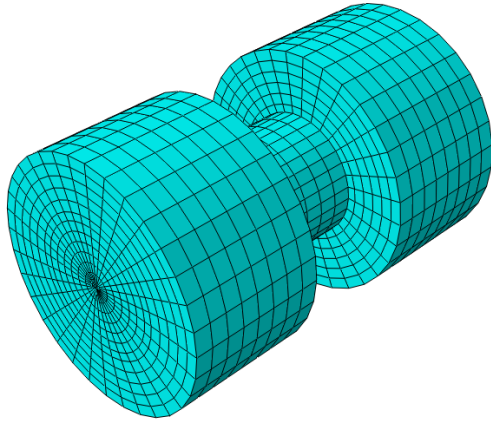


Figure 6.5: FEM of the column bolt including mesh

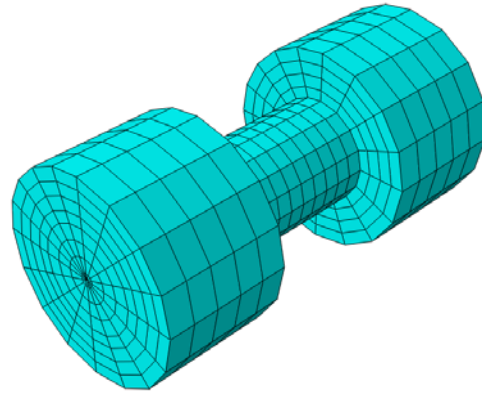


Figure 6.6: FEM of the beam bolt including mesh

### 6.1.2 Materials

The different materials used in the FEM were listed in Table 6.1. All materials were modeled as elastic-plastic materials with strain hardening. Young's modulus, Poisson's ratio, the minimum specified engineering yield stress, and the minimum specified engineering ultimate stress for each FEM part are listed in Table 6.1. Detailed stress versus strain values for each material are listed in Tables 6.2 through 6.4. Both engineering and true stress and strain values are provided since ABAQUS requires the true material properties. The stress-strain data for the beam (Grade 345 (A992)) was obtained from Barth et al. (2005), which was based on material testing of this material for the purpose of determining FEA input. The inputs from the other materials were determined based on applying Barth et al.'s philosophy to their minimum specified yield and ultimate strengths. Each material, except the bolts, was

obtained from previous research projects since no material tests were performed for the laboratory test setup.

Table 6.1: Material properties of FEM parts

<b>Part</b>	<b>Material</b>	<b>Young's Modulus [MPa] (ksi)</b>	<b>Poisson's Ratio</b>	<b>Yield Stress [MPa] (ksi)</b>	<b>Ultimate Stress [MPa] (ksi)</b>	<b>Table for Constitutive Model</b>
Beam	A992	200,000 (29,000)	0.3	345 (50.0)	475 (68.9)	Table 6.2
Column Bolt	A325	200,000 (29,000)	0.3	558 (81.0)	724 (105)	Table 6.3
Beam Bolt	A325			634 (92.0)	827 (120)	
Beam End Plate						
Beam Stiffener						
Column						
Connection Angle	A36	200,000 (29,000)	0.3	248 (36.0)	400 (58.0)	Table 6.4
Vertical load attachment						
Horizontal load attachment						

Table 6.2: Beam constitutive model (A992)

Engineering			True		
Stress [MPa]	Stress [ksi]	Strain [mm/mm]	Stress [MPa]	Stress [ksi]	Plastic Strain [mm/mm]
0	0	0	0	0	0
345	50.0	0.002	345	50.1	0.000
354	51.3	0.011	358	51.1	0.009
448	65.0	0.030	462	66.9	0.027
475	68.9	0.300	618	89.6	0.259

The bolt yield stress and ultimate stress were selected based on ASTM A325-14 (2014). The two bolts had different stress-strain data because the bolt sizes were different (the Beam Bolt diameter was under 25.4 mm (1in.) and the Column Bolt diameter was over 25.4 mm (1in.)).

Table 6.3: Bolt Constitutive Model (A325)

Part	Engineering			True		
	Stress [MPa]	Stress [ksi]	Strain [mm/mm]	Stress [MPa]	Stress [ksi]	Plastic Strain [mm/mm]
<b>Column Bolt</b>	0	0	0	0	0	0
	558	81.0	0.003	560	81.2	0.000
	655	95.0	0.015	665	96.4	0.012
	655	95.0	0.030	675	97.9	0.026
	724	105	0.140	825	120	0.127
<b>Beam Bolt</b>	0	0	0	0	0	0
	634	92.0	0.003	636	92.3	0.000
	724	105	0.015	735	106	0.011
	724	105	0.030	746	108	0.026
	827	120	0.140	943	137	0.126

Table 6.4: Plate material properties (A36)

Stress [MPa]	Engineering		Stress [MPa]	True	
	Stress [ksi]	Strain [mm/mm]		Stress [ksi]	Plastic Strain [mm/mm]
0	0	0	0	0	0
248	36.0	0.001	249	36.0	0.000
255	37.0	0.014	259	37.5	0.013
345	50.0	0.032	356	51.6	0.030
400	58.0	0.120	448	65.0	0.111

### 6.1.3 Boundary Conditions and Interactions

The FEM was restrained from moving using displacement boundary conditions at the bottom plate of the column and spring connectors on the column as shown in Figure 6.7. The displacement boundary conditions at the bottom of the column were displacement boundary conditions that restrained the movement of the test setup in all directions ( $U_x = 0$ ,  $U_y = 0$ , and  $U_z = 0$ ) at the two locations where the specimen was connected to the laboratory strong floor. Furthermore, the column brace of the laboratory test setup was modeled using spring elements at the locations shown in Figure 6.7. At each of these locations, three spring elements were attached to the column, one for each coordinate direction. The stiffness of the brace was calculated by assuming the brace acted as a fixed end cantilever for each direction and each spring ( $k_x = 20,840$  kN/m (119 kip/in.),  $k_y = 10,858$  kN/m (62 kip/in.),  $k_z = 1,506$  kN/m (8.60 kip/in.)) and the value was used as spring stiffness in the spring elements of the FEM. Seven spring elements were attached to the column and were arranged in the same pattern as the I-shaped brace was attached to the column in the laboratory test setup. This arrangement reduced stress concentrations at the nodes, where the springs were attached to the column, and forced the column flange to act similar to the flange in the test setup.

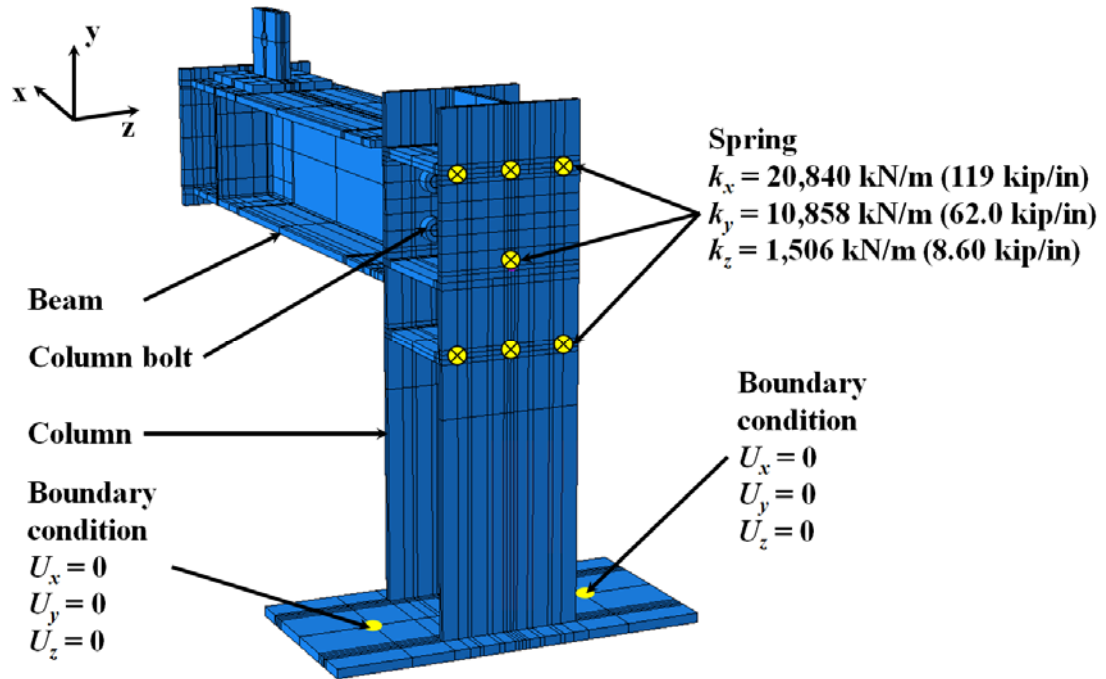


Figure 6.7: FEM boundary condition and spring element locations

The different FEM parts described in Section 6.1.1 were connected using the modeled column and beam bolts and the connection angles. The parts were held together by applying bolt pretension loads in the first step of the finite element analysis as described in Section 6.1.4. To achieve a realistic behavior of the connection, surface to surface interactions between the different parts were modeled using two different contact behaviors (described below). The interaction surfaces are identified in Figure 6.8 and 6.9. Surfaces were defined between bolt heads and connection angles, bolt heads and column flanges, bolt shafts and column holes and connection angle holes, bolt shafts and beam web holes and connection angle holes, connection angle flanges and beam webs, as well as connection angle flanges and the column flange.

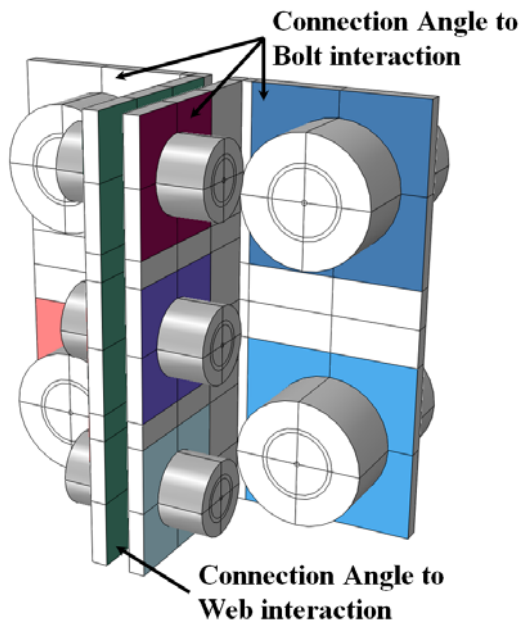


Figure 6.8: Connection angles and bolt interactions surfaces

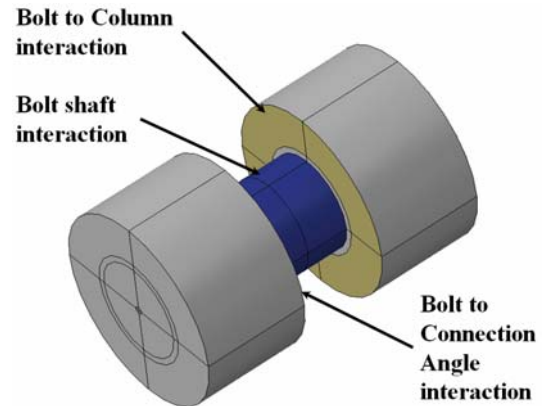


Figure 6.9: Bolt interaction surfaces

The normal behavior of the connection described the interaction between two parts when normal forces (perpendicular forces) were applied to the surface. The normal behavior was defined as “hard contact” with allowed separation after contact. This behavior ensures that two defined surfaces cannot penetrate each other (i.e. “hard contact”) and that the surfaces can separate again once they touched. This behavior was defined since it accurately models the behavior of steel to steel surface interactions when applying normal forces.

The second behavior of a steel connection that had to be modeled was the tangential behavior. This behavior models the interaction between two surfaces when they move across each other, commonly known as friction between two surfaces. To

define this interaction in ABAQUS the “penalty” method was utilized as the friction formulation with a friction coefficient of 0.3. The “penalty” method permits some relative motion of two surfaces as described in ABAQUS user manual (ABAQUS, 2015) . This friction formulation and friction coefficient were found to be common for structural steel connections during the literature review in Section 2.4.

#### **6.1.4 Steps and Applied Loads**

Two different steps were used to apply loads to the FEM. During the first step, the pretension load for the beam and column bolts were applied and in the second step, the external load was applied to model. The two steps were necessary, since the pretension load in the bolts had to be applied first to create interactions between the bolts, the connection angles, the beam, and the column. Nonlinear geometry was considered in both steps.

The pretension forces in the bolts were modeled using the “Bolt Load” load type in ABAQUS. Using this method, a defined bolt pretension load can be applied to the shaft cross section. The bolt pretension loads were selected from the Steel Construction Manual (American Institute of Steel Construction (AISC), 2017) Table J3.1. This table defines the minimum pretension loads for the diameter of the beam bolts (M20 (3/4”  $\varnothing$ )) as 125 kN (28 kips) and for the diameter of the column bolts (M30 (1-1/4”  $\varnothing$ )) as 316 kN (71 kips). The bolt loads were applied to the model in a static step.

The external forces were applied at the load attachment holes and the beam stiffener as shown in Figure 6.10. The loads were applied in a second step, after bolt pretension was applied to the bolt in the first step, using a static step. The loads were applied using a uniform pressure that was applied over half the load attachment hole

area for the vertical and the axial force and the beam stiffener area (stiffener thickness \* height) for the lateral force causing weak axis loading. The applied load varied from 2.67 kN (0.6 kips) for the weak axis load (WAL in Figure 6.10) to 26.7 kN (6 kips) for the strong axis load (SAL in Figure 6.10), to 89 kN (20 kips) for the axial load (AL in Figure 6.10). These load ranges were selected to keep the FEM in an elastic range (i.e. no yielding occurred in any parts of the FEM).

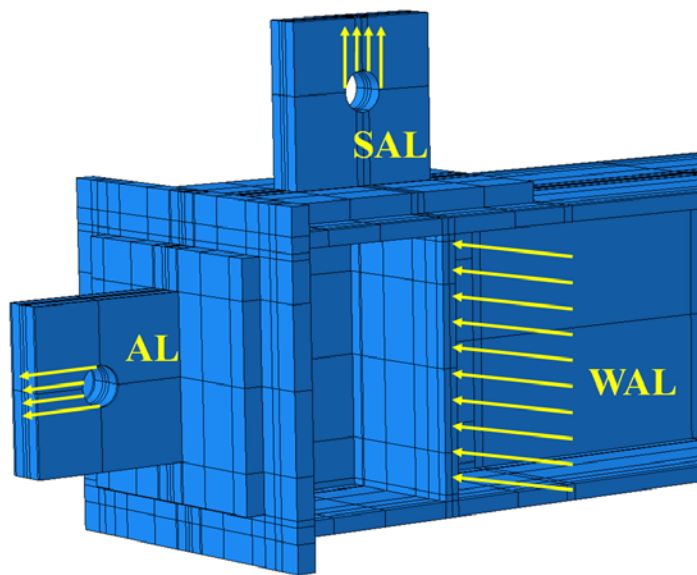


Figure 6.10: Load application locations

## 6.2 Finite Element Model Validation

The FEM was validated using the laboratory test data described in Chapter 5. Since this FEM was focused on the connection area, data from six connection area strain gauges (BCWTN/S (North/South), BCWMN/S, BCWBNH, and BCWBSH, see Figure 5.7) were used for this validation process. However, since the FEM results were the same on both sides of the web of the beam for the axial load test and the

vertical load test (the FEM was symmetrical about the x-axis) the strain gauges on opposing sides of the web but same longitudinal and vertical positions were averaged for these two tests. For the weak axis load test (WAL, Figure 6.10), the strain gauge data on opposing sides of the web were different and therefore used independently in the validation.

Three differences between the FEM and the laboratory test setup had to be considered for the validation of the FEM. First, the CNT-based sensor installed on the test setup (Section 5.2.2) was not included in the FEM. The sensing skin was installed on only one side of the laboratory setup beam introducing a small eccentricity into the connection. Second, the friction coefficient of the sensing skin was unknown but most likely differed from the friction coefficient of steel. Finally, the bolt pretension loads for the laboratory test setup were unknown. The bolts were tightened by hand as tight as possible using a wrench and a wrench extension. However, the applied force was not measured and is therefore unknown. Since the friction coefficient and the bolt loads for the laboratory setup were unknown, the previously defined values were used (0.3 for the friction coefficient, a beam bolt load of 125 kN (28 kips) and a column bolt load of 316 kN (71 kips) as described in Sections 6.1.3 and 6.1.4, respectively). The influence of the sensing skin in the connection was discussed in Section 6.2.3, and the influence of the friction coefficient and the beam bolt loads on the FEM results were discussed in Section 6.2.4.

For the FEM validation figures in this section the strain gauge data of the laboratory test was displayed as colored symbols without a line between the measurement points. The FEM data was displayed in black and with connection lines.

The FEM data used the same symbols as the laboratory test setup to indicate the location of the strain gauges on the test setup and the FEM.

### **6.2.1 Axial Load**

Since the axial load test was performed in load control (as described in Section 5.3.1) and the horizontal displacements were very small, the FEM data was compared to the laboratory test data in an axial force versus stress plot as shown in Figure 6.11. The FEM data is similar to the laboratory test data at the middle of the beam and all values follow the same trend. The laboratory gauge data and the FEM data are within 12 % for the last laboratory test value at 22.50 kN (5.06 kips), which was the biggest difference between the laboratory result and the FEM for the axial load test.

Both the bottom and the middle strain gauge values were similar to each other which was expected when a uniaxial tension load was applied. The top gauge results were lower than the other two gauge results, which was found in the laboratory data and the FEM data. This was due to the eccentricity in the connection as described in Section 5.4.1 and further supports the accuracy of the connection modeling.

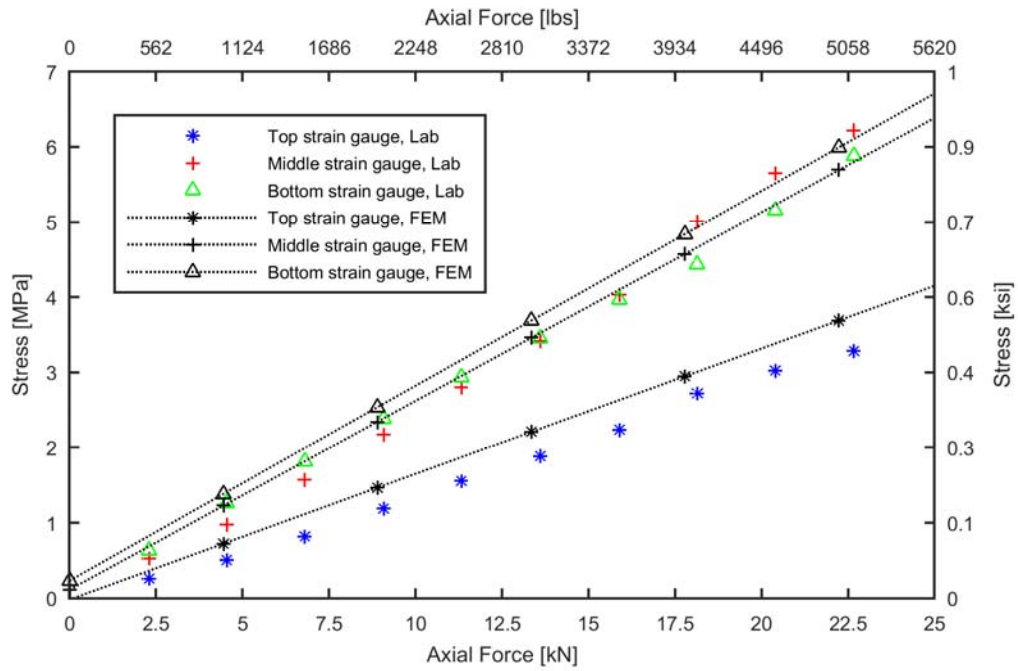


Figure 6.11: FEM validation at the middle of the beam using axial load test results

### 6.2.2 Strong Axis Load (Strong Axis Bending)

The laboratory strong axis load test was run in displacement control using the manual hydraulic jack as described in Section 5.3.2. Therefore, the laboratory test data and the FEM data were compared using a displacement versus stress plot, shown in Figure 6.13. The displacement values for the x-axis were measured at the end of the laboratory test beam using an average of BENVD and BESVD data (see Section 5.2.1.5) as shown in Figure 6.12.

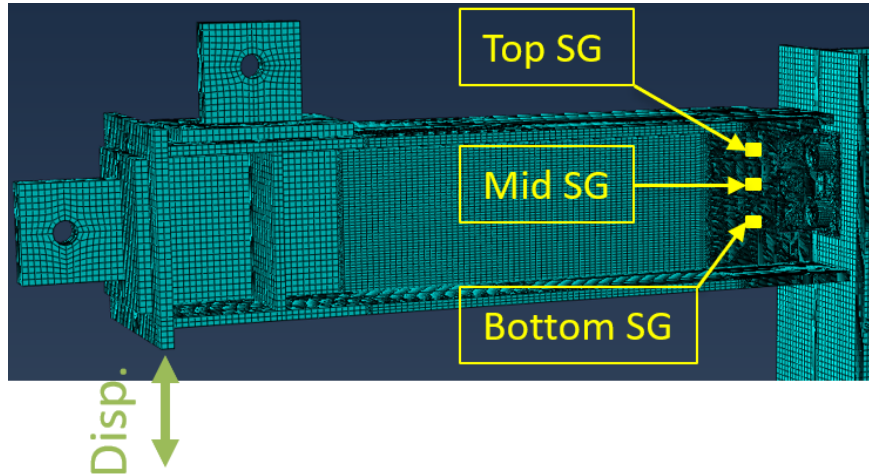


Figure 6.12: Location of displacement sensor and strain gauges for vertical tests

The signs (i.e. compression or tension) for all three strain gauges (Lab and FEM) was as expected, since a positive moment was applied to the beam that resulted in tension stresses at the bottom of the connection and compression stresses at the top of the connection. Also, the centerline was not aligned with the center bolt of the connection. This eccentricity created compression stress in the center strain gauge because the strain gauge was located above the beam centerline. The FEM shows a tension stress at the middle location, which was attributed to different pretension forces in the beam bolts in the laboratory setup. The different pretension forces caused the center of rotation of the connection to shift, which resulted in a tension stress instead of a compression stress in the middle location. The different pretension forces and are discussed in more detail in Subsection 6.2.4.

Both data sets followed similar trends during the entire test, however, the laboratory test data had consistently smaller stress values than the FEM data at a given displacement. This indicates the laboratory specimen was less stiff than assumed when

using the input values discussed above. The biggest stress difference between strain gauge data and FEM data using the input values discussed above was 15.0 MPa (2.18 ksi) for the top strain gauge data set, 13.3 MPa (1.93 ksi) for the bottom strain gauge data set, and 10.3 MPa (1.50 ksi) for the middle strain gauge data set.

Three distinctive phases can be seen in the FEA data in Figure 6.13. First, the stress in both the top and bottom location increase rapidly between 0 and 7.00 mm (0.28 in.) of vertical displacement. During this phase the applied force was transferred from the beam via the friction forces in the connection resulting from the bolt pre-tensioning step. Once the applied force (resulting from the increased displacement at the end of the beam) was greater than the friction resistance in the connection, the connection components moved relatively freely from their original position until the bolt and other connection components were in contact, then resulting in greater stiffness. The relatively free movement of the beam occurred between 7.00 and 23.8 mm (0.28 in. and 0.94 in., Figure 6.13). Once the bolts are bearing against the beam the applied load is transferred via the bolts until the maximum load was reached. However, the data shown in Figure 6.13 was limited to include only the first 55 mm (2.2 in.) because the laboratory test setup displacement was limited to 50.8 mm (2 in.).

Both the laboratory data and the FEM data followed the same stress versus displacement trend throughout the three phases described above: resistance from friction, slip, resistance from bolt contact (Figure 6.13). Furthermore, the top and the bottom strain gauges of the lab data and FEM data had the same sign (i.e. compression and tension), although the middle gauge did not. Therefore, the laboratory test data validated the FEM data for this loading condition. However, the differences between

the magnitudes of the laboratory stress data and the FEM stress data are discussed in more detail in Section 6.2.4.

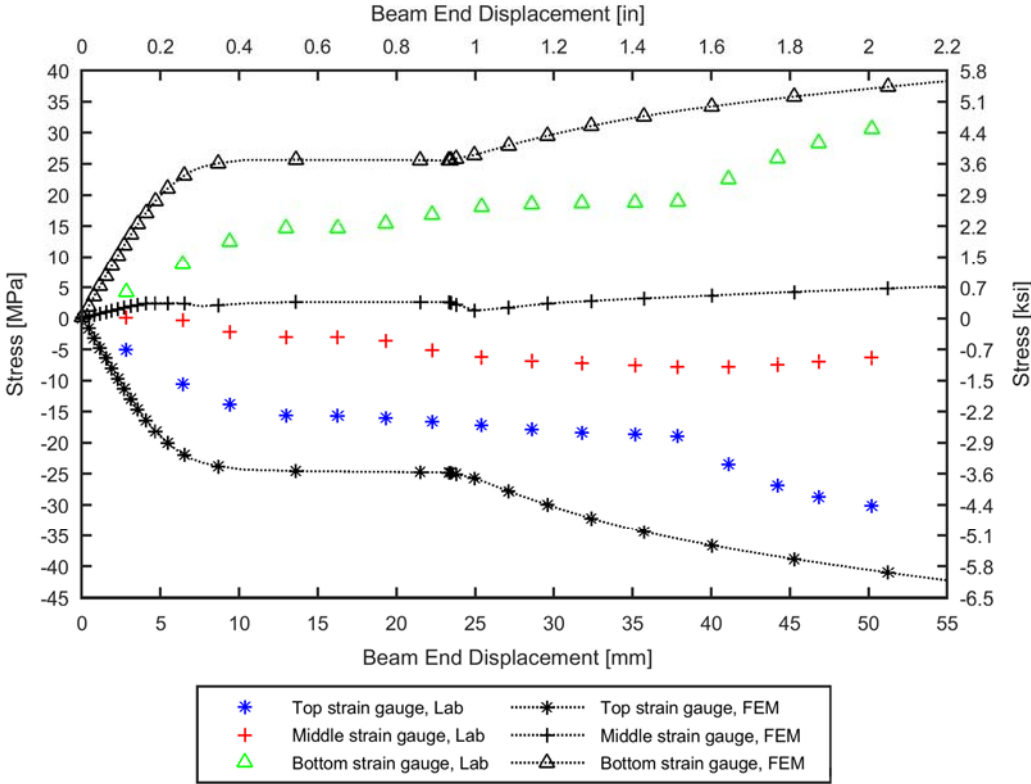


Figure 6.13: Validation of the FEM using vertical displacement test results

### 6.2.3 Weak Axis Load (Weak Axis Bending)

The weak axis load test of the laboratory test setup was performed in displacement control using a manual hydraulic jack as described in Section 5.3.3. The laboratory test data was compared to the FEM data in Figure 6.14. For the weak axis load test the strain gauges on both sides of the web of the laboratory setup were included in the figure, since one side of the web was in compression and the other side

in tension. However, since this test was the last test performed on the setup, some of the strain gauges were damaged before this test and their results were not used. These strain gauges were not replaced since symmetry was assumed in the test setup. Therefore, only the middle strain gauge results were available for both sides of the web.

As expected, the strain gauges on the north side were in tension and the strain gauge on the south side of the web was in compression, as shown in Figure 6.14. The north middle laboratory strain gauge had a higher magnitude than the south middle laboratory strain gauge by 13.2 MPa (1.91 ksi) at 37.7 mm (1.48 in.) of applied displacement where the FEM value at these locations and at the same displacement differed only by 3.03 MPa (0.44 ksi). The difference in the FEM data may be viewed as unexpected, but was determined to be a result of the web being pressed against the connection angle on the compression side and lesser contact on the tension side. The larger difference in lab strain gauge data can be explained by the presence of the sensing skin that was bonded to the north side of the connection. Since the strain gauges on the north side of the test setup were attached to the sensing skin, the distance between the center of the web and the strain gauge increased which increases the stress at the location. The two different stress values were used to calculate the difference between the distances between the neutral axis of the web of the beam and the strain gauge locations (half the web thickness on the south side and half the web thickness plus the thickness of the sensing skin plus thickness of adhesive layer on the north side). The obtained additional eccentricity from the sensing skin was 2.10 mm (0.08 in.) which was a reasonable value for the thickness of the sensing skin including the adhesive layer.

The laboratory test results and the FEM results follow the same trend (linear for the first 25 mm (1 in.) and then softening) for all four strain gauge locations. The maximum difference between two values was 15.0 MPa (2.18 ksi) between the middle strain gauge (S) values at 37.7 mm (1.45 in.), a 40% difference between the FEM and the laboratory setup results. Furthermore, the three different magnitudes of stresses for the north side gauges was unexpected based on basic solid mechanics assumptions. However, since both the laboratory data and the FEM show the same trends (i.e. different magnitudes of stress in all three gauges) it was implied that most of the force was transferred through the middle bolt of the connection.

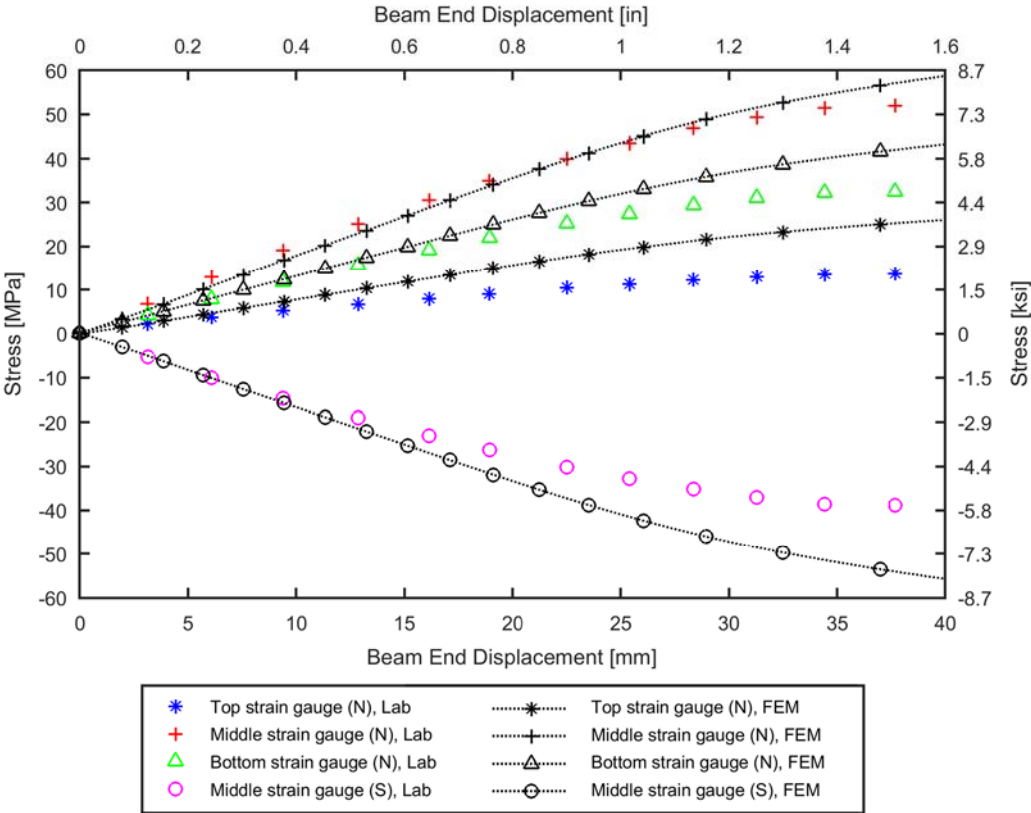


Figure 6.14: Validation of the FEM using horizontal displacement test results

#### **6.2.4 Influence of Bolt Pretension Load and Friction Coefficient**

The bolt pretension applied to the beam bolts as well as the friction coefficient defined for the contact interactions had a large influence on the FEM results as shown in Figure 6.15. The figure shows the laboratory test data, the FEM data from Section 6.2.2 with a beam bolt pretension load (BBL) of 125 kN (28 kips) and a friction coefficient (FC) of 0.30, FEM result for a BBL of 125 kN (28 kips) and a FC of 0.05, and FEM results for a BBL of 93 kN (21 kips) and a FC of 0.25. The BBL of 125 kN (28 kips) was taken from the Steel Construction Manual (AISC, 2017) as the minimum pretension load. Since the laboratory test setup bolts were tightened by hand a 25% reduction of the BBL was assumed for the other model. The friction coefficients of 0.30 and 0.25 were taken from the literature (see Section 2.4 for the FEM literature review) and the value of 0.05 was selected to simulate frictionless behavior as a theoretical lower bound without creating problems for the FEA solver. The column bolt load were kept constant at 316 kN (71 kips), the (AISC, 2017) minimum pretension load to limit the parameters that were changed at the same time.

The recorded stresses for the different FEMs were significantly different. For example, at 15 mm (0.60 in.) displacement the stress recorded for the maximum bottom gauge stress was 25.7 MPa (3.73 ksi) in the BBL = 125 kN and FC = 0.30 FEM and 4.43 MPa (0.64 ksi) for the lowest FEM with FC = 0.05.

However, all FEM models have similar phases (resistance from friction, slip, then resistance from bolt contact, as described in Section 6.2.2). First, the applied force overcomes the initial friction force in the connection, then the bolts slide into bearing (beam hole to bolts), then some more friction resistance in the connection has to be overcome until the bolts slide into bearing with the connection angles (the second phase was not observed in Section 6.2.2 results). These steps were very

distinguishable for the BBL = 93 kN model (dash dotted line in Figure 6.15). First slip occurs between 4.2 mm (0.17 in.) and 19.4 mm (0.76 in.) and the second slip between 32.9 (1.30 in.) mm and 47.2 mm (1.86 in.) of vertically applied displacement at the end of the test beam. The phases were also very distinguishable for the BBL = 125 kN with a FC of 0.05 FEM. However, the BBL = 125 kN with a FC of 0.30 FEM data shown on the plot only displayed the first slip phase.

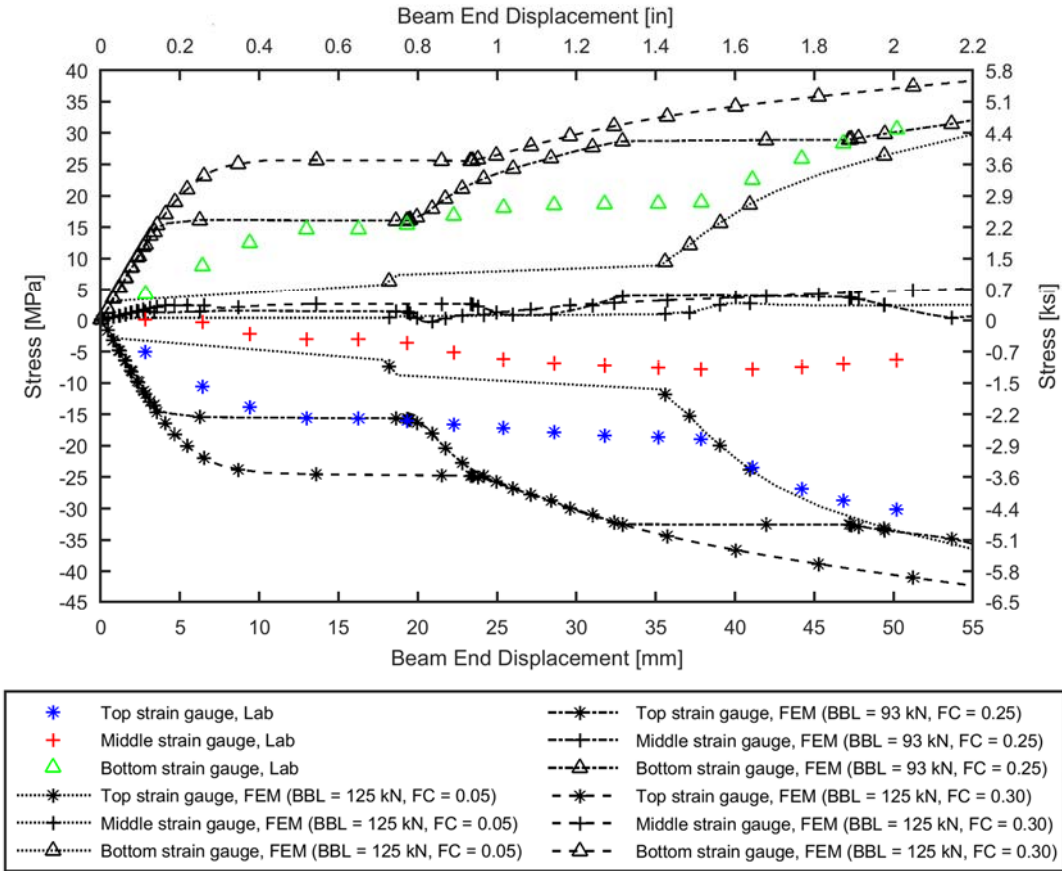


Figure 6.15: Vertical load laboratory test data compared to FEM data with different beam bolt loads and friction coefficients

Changing the bolt pre-tension and the friction coefficient had a significant influence on the behavior of the FEM model as was shown in Figure 6.15. However, the initial slope of the FEM data between 0 and 5 mm (0.20 in.) stayed the same for all three pre-tension and friction combinations. To change this slope, the beam bolt pre-tensions were changed individually to simulate a situation where one or multiple bolts were not tightened to the specified pretension force. This approach was selected based on the horizontal displacement data from the laboratory test setup (as described in Section 5.4.2 and Figure 5.22). The laboratory data showed that the center of rotation of this connection was between the middle and the bottom bolt, lower than where this occurred in the preliminary FEA. Therefore, to move the center of rotation of the connection different beam bolt pre-tension forces had to be used.

To show the effect of bolts with less pretension force on the FEM results, four new FEM models were created. The obtained stress results for the top strain gauge location were compared to the lab data and the FEM with a BBL of 125 kN (28 kips) and a friction coefficient of 0.30 as shown in Figure 6.16. The first new FEM model had a top bolt load of 0.4 kN (0.1 kips), a middle and bottom bolt load of 125 kN (28 kips), and a friction coefficient of 0.30. The top bolt load simulated a bolt that was not tightened at all and prevented FEM solver errors at the same time. The second new FEM model had a bottom bolt load of 0.4 kN (0.1 kips), a middle and top bolt load of 125 kN (28 kips), and a friction coefficient of 0.30. The third new FEM model had a top and middle bolt load of 0.4 kN (0.1 kips), a bottom bolt load of 125 kN (28 kips), and a friction coefficient of 0.30. This model simulated a situation where the top and the middle bolt were not tightened at all. The final new FEM model had a top bolt load

of 22 kN (kips), a middle bolt load of 44 kN (10 kips), a bottom bolt load of 125 kN (28 kips), and a friction coefficient of 0.30.

All models except one completed the analysis successfully. The model with a bottom bolt load of 0.4 kN (0.1 kips) did not complete the analysis and therefore, the corresponding results in the following figures (Figures 6.16 through 6.17) end after a displacement of 10 mm (0.4 in.).

Changing the bolt load in the different bolts had a significant impact on the stress results in the top strain gauge location as shown in Figure 6.16. Changing the bolt load in selected beam bolts changed the slope of the initial data, which was the desired outcome of the new FE models. The most significant change was the drop in magnitude of stress between the model with a bolt force of 125 kN (28 kips) in all three beam bolts and the new FE models. Furthermore, changing the bolt load in individual bolts, changed the behavior of the connection, i.e. slip distances and slip sequences. This was expected since a lower pretension load in a bolt reduces the force required to overcome the friction force.

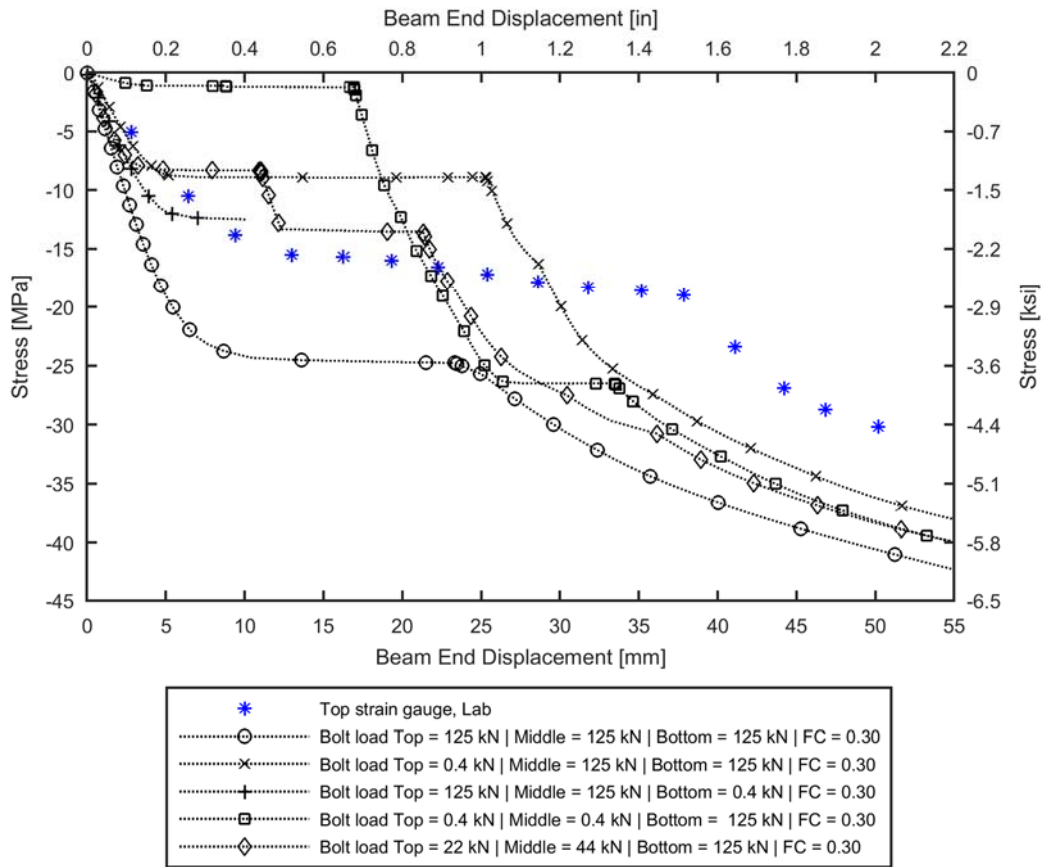


Figure 6.16: Vertical load laboratory test data (top strain gauge data only) compared to FEM data with different beam bolt loads

The stress values for the bottom strain gauge location are shown in Figure 6.17. The obtained results were similar to the top strain gauge location results. However, the obtained stresses were in tension instead of compression. Similar to the top strain gauge location data, the slope of the obtained data changed during the first 5 mm (0.2 in.).

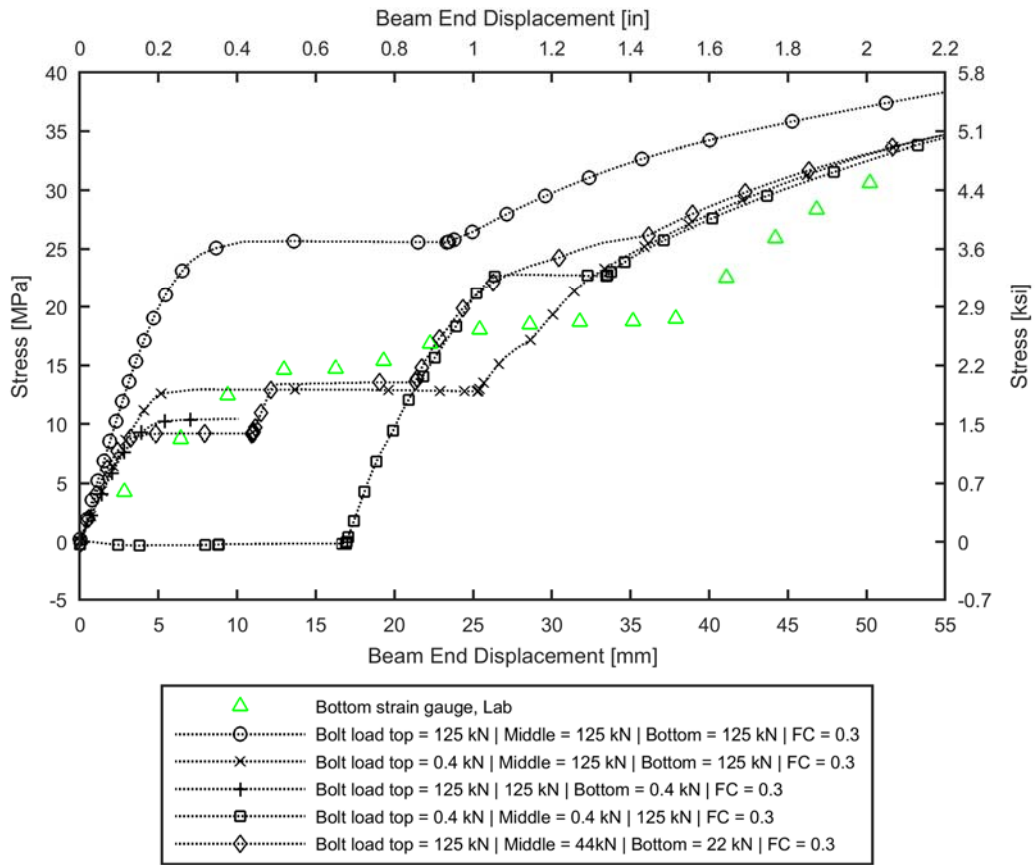


Figure 6.17: Vertical load laboratory test data (bottom strain gauge data only) compared to FEM data with different beam bolt loads

The new FEM results for the middle strain gauge location are shown in Figure 6.18. The stresses obtained from the models with significantly less pretension bolt loads (i.e. 0.4 kN (0.1 kips) in the top or bottom bolt) were higher at the middle location. This was expected. Because the bolt pretension load in the top or the bottom bolt were small, the applied load was transferred through the other two bolts (bottom and middle bolt, or top and middle bolt, respectively) resulting in a higher stress at the middle strain gauge location.

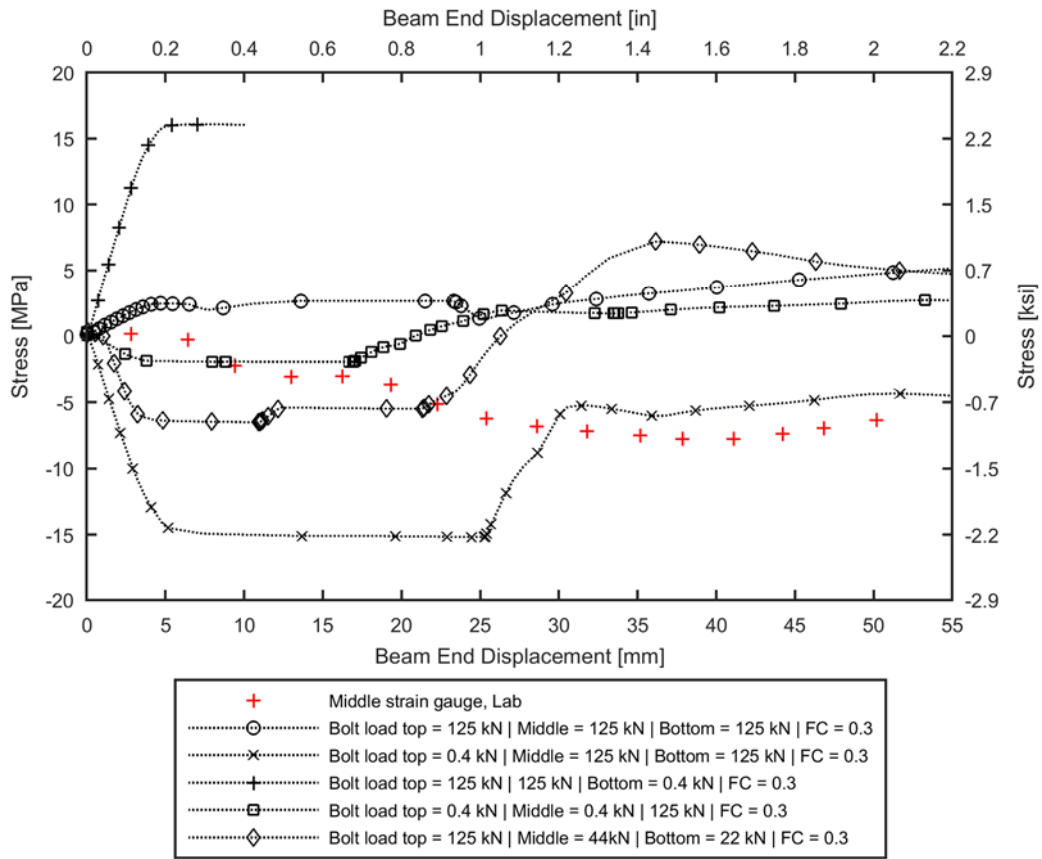


Figure 6.18: Vertical load laboratory test data (middle strain gauge data only) compared to FEM data with different beam bolt loads

The different stress magnitudes but similar connection behavior showed how important the beam bolt pretension load and the friction coefficient were to accurately model a bolted connection. Since the friction coefficient for steel to steel interactions is given as 0.30 in the literature (see Section 2.4 for the literature review) and the bolt pretension loads for the used bolts were provided in the Steel Construction Manual (AISC, 2017), as described in Section 6.1.4 these values were used for the FEM in the following section. These values were used, since in the following section the FEM is used to obtain construction-induced stresses in the connection area of a steel member,

and the selected pretension loads and the friction coefficient were assumed to represent the most accurate field condition values (bolts tightened to the prescribed values and steel on steel friction), even though they did not provide the most accurate results for the validation model.

### **6.3 Connection Field Data Evaluation Using the Finite Element Model**

Connection areas of structural steel members would ideally be included in reused structural steel members. Therefore, connection area stresses during the construction phase of a building need to be known. However, the stress distribution in connection areas is complex, resulting in the peak stresses likely being in locations close to bolt holes that are difficult to instrument during the construction process of a building. To resolve this problem, field strain gauge data collected close to a connection area are used in combination with an FEM of said connection to find the maximum stresses in the connection. The validated FEM from Section 6.1 and 6.2 was used to extrapolate connection area strain gauge field data, collected during the construction of the Purnell Hall Addition (as a proof of concept), to find the maximum and minimum stresses in the given connection area using the process shown in Figure 6.19 and explained in more detail in the following paragraph.

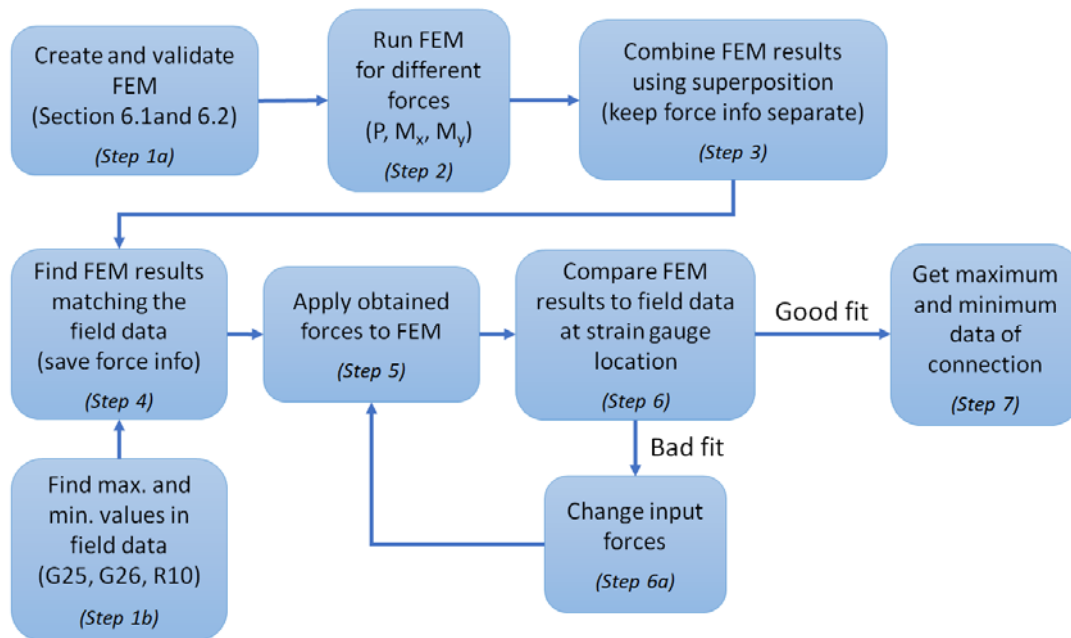


Figure 6.19: Flowchart of the field data extrapolation process using an FEM

Once the FEM was validated (Step 1a, Figure 6.19), six different forces were applied to the FEM (Step 2). An axial compression and tension force (AL) of 89.0 kN (20 kips), a vertical force up and down (SAL) of 26.7 kN (6 kips) that produced a positive or a negative strong axis moment in the connection, and a transverse force to the back and to the front of the beam stiffener (WAL) of 2.67 kN (0.6 kips) that produced a positive and negative weak axis moment in the connection were applied to the FEM at the loading points described in Section 6.1.4. These load ranges were selected to keep the FEM in an elastic range (i.e. no yielding occurred in any parts of the FEM). The loads were applied in increments of 0.89 kN (0.20 kips) for the axial force, 0.27 kN (0.06 kips) for the vertical force, and 0.027 kN (0.006 kips) for the horizontal load.

The longitudinal stresses at the same locations where strain gauges were located in the connection area of the steel member during the field instrumentation were obtained from the FEA (see G25, G26, and R10 in Figure 3.8 Section A-A for location of strain gauges in the field). The obtained FEM stress results for the three strain gauge locations and the three applied forces were combined using superposition of every possible force combination. An example of the superposition of one possible force combination is shown in Figure 6.20. These loads are then varied by one increment, one at a time, to form additional possible force and stress combinations. Each of these force combinations serve as different rows in a “superposition matrix”.

AL	SAL	WAL	$\sigma_{G25}$	$\sigma_{G26}$	$\sigma_{R10}$
[kN (kips)]	[kN (kips)]	[kN (kips)]	[MPa (ksi)]	[MPa (ksi)]	[MPa (ksi)]
$P_i$	0	0	$v_1$	$v_2$	$v_3$

+

AL	SAL	WAL	$\sigma_{G25}$	$\sigma_{G26}$	$\sigma_{R10}$
[kN (kips)]	[kN (kips)]	[kN (kips)]	[MPa (ksi)]	[MPa (ksi)]	[MPa (ksi)]
0	$SAL_i$	0	$v_4$	$v_5$	$v_6$

+

AL	SAL	WAL	$\sigma_{G25}$	$\sigma_{G26}$	$\sigma_{R10}$
[kN (kips)]	[kN (kips)]	[kN (kips)]	[MPa (ksi)]	[MPa (ksi)]	[MPa (ksi)]
0	0	$WAL_i$	$v_7$	$v_8$	$v_9$

=

AL	SAL	WAL	$\sigma_{G25}$	$\sigma_{G26}$	$\sigma_{R10}$
[kN (kips)]	[kN (kips)]	[kN (kips)]	[MPa (ksi)]	[MPa (ksi)]	[MPa (ksi)]
$P_i$	$SAL_i$	$WAL_i$	$v_1 + v_4 + v_7$	$v_2 + v_5 + v_8$	$v_3 + v_6 + v_9$

Figure 6.20: Example rows of the superposition matrix

In Figure 6.20 a six-column matrix was created with the different force components (i.e. axial load (AL), strong axis load (SAL), and weak axis load (WAL)) kept separate in the first three columns and the stress values for the three strain gauges (G25, G26, and R10) in the last three columns. Each of the three applied loads resulted in three different FEM strain gauge values ( $v_1 - v_9$ ). The strain gauge values from three different loadings were superimposed and the obtained results were given as the final row of the superposition matrix (for example:  $\sigma_{G25} = v_1 + v_4 + v_7$ ). This process was repeated for all applied load increments, varying each load increment one at the time. This superposition matrix was later used to find matching stresses between the field data and the FEM data (Step 4).

The laboratory test setup and the FEM were both a replica of the Girder to Long Column connection shown in Figure 3.8 Section A-A. Therefore, sustained field strain gauge data from G25, G26, and R10 were used for this evaluation of connection area stresses. The maximum and minimum of each of the three strain gauges were found in the collected field data. The stress values for all three strain gauges (G25, G26, and R10) at the same timestamps as the maximum and minimum values were saved (Step 1b in Figure 6.19).

Once the maximum field stresses for all three strain gauges were known, the closest FEM stress values in the superposition matrix were found (Step 4). Therefore, the root mean square error (RMSE) between the field data values (for example: maximum value of G25, and the corresponding values for G26 and R10) and the stress values of the entire superposition matrix were calculated. This resulted in a RMSE vector with an RMSE value for every row of the superposition matrix. To find the best fit between the field data and the FEM data, the minimum value of the RMSE vector

was found and the corresponding force components from the superposition matrix were recorded. This step was repeated for each field data maximum and minimum value.

Next, the recorded force components (from the previous step) for each field data maximum and minimum value was applied to the FEM for the ultimate purpose of determining the stresses at locations other than the gauge locations. Each FEM was analyzed and the stress results at the selected strain gauge locations were extracted. The extracted FEM results were compared to the maximum field data values and it was decided if the FEM data was a good fit (difference between each stress value of maximum 1 MPa (0.15 ksi)) or a bad fit (Step 6). A bad fit could have happened since the superposition matrix contained a finite amount of force combinations. If the FEM data was a bad fit, the input force components were adjusted (by increasing or decreasing each force component based on the difference between the obtained FEM stress data and the field data) and a new FEM model was analyzed as shown in Figure 6.19 (Step 6a). Once the FEM was a good fit, the von Mises stress and maximum and minimum principle stresses throughout the connection for each load case corresponding to a minimum (maximum compression value) and maximum (maximum tension) at G25, G26, or R10 were found (Table 6.5). Furthermore, the member forces corresponding to these maximums and minimums that were obtained from the optimization process are listed in Table 6.5.

The FEM results were organized and labeled based on the used model. However, the obtained result (i.e. von Mises criterion, maximum, and minimum principal stress data) did not occurred at the given strain gauge locations but anywhere in the connection area (close to the bolt holes in the beam).

Table 6.5: FEM result summary

<b>FEM model data from field strain gauge</b>	<b>Applied axial load [kN] (kip)</b>	<b>Applied strong axis moment [kNm] (kip*in)</b>	<b>Applied weak axis moment [kNm] (kip*in)</b>	<b>von Mises stress [MPa] (ksi)</b>	<b>Maximum principal stress [MPa] (ksi)</b>	<b>Minimum principal stress [MPa] (ksi)</b>
G25 <sup>a</sup> max	-69.9 (15.7)	0.73 (6.4)	-0.04 (-0.31)	175 (25.4)	56.4 (8.18)	-203 (-29.5)
G25 <sup>a</sup> min	-27.6 (-6.2)	-3.97 (-35.1)	-0.13 (-1.17)	156 (22.7)	26.9 (3.90)	-182 (-26.3)
G26 <sup>a</sup> max	41.9 (9.4)	-2.25 (-19.9)	-0.10 (-0.88)	159 (23.1)	40.3 (5.84)	-216 (-31.4)
G26 <sup>a</sup> min	-15.1 (-3.4)	3.63 (32.2)	-0.30 (-2.65)	154 (22.4)	36.5 (5.29)	-180 (-26.2)
R10 <sup>a</sup> max	41.8 (9.4)	2.31 (20.5)	-0.46 (-4.09)	176 (25.5)	65.2 (9.46)	-198 (-28.8)
R10 <sup>a</sup> min	-29.4 (-6.6)	-3.64 (-32.2)	-0.07 (-0.58)	156 (22.6)	23.2 (3.36)	-181 (-26.3)

<sup>a</sup> See Figure 3.8 for strain gauge location

From Table 6.5 it can be seen that the highest von Mises stress in the FEM of the beam was 176 MPa (25.5 ksi) and the maximum absolute principal stress was 216 MPa (31.4 ksi). These stresses were located in the bolt hole areas of the beam as shown in Figure 6.21. At these locations the high multiaxial stresses result from the pressure of the bolt pretension force, contact interaction between the bolt shaft and the beam, and from externally applied loads. From the result summary (Table 6.5) it can be seen that none of the FEM models indicated any yielding in the connection area of the analyzed beam.

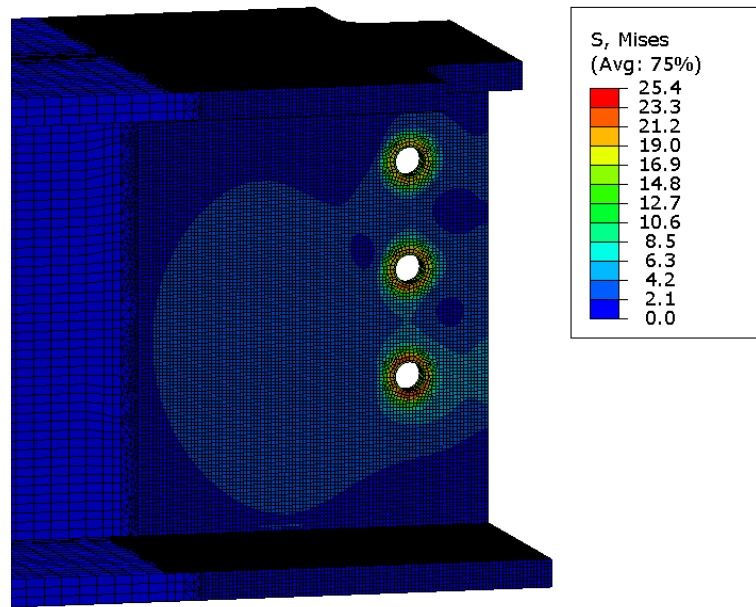


Figure 6.21: FEM contour plot of von Mises stresses for R10 max model (worst-case loading)

#### 6.4 Finite Element Analysis Conclusions

To quantify stresses in the connection area of a steel member, a three-dimensional FEM was created using ABAQUS. The FEM was modeled using 4 individual parts comprised of solid elements that were connected using the modeled bolts, bolt pretension forces and contact interactions. The material for each part was defined as an elastic-plastic material with strain hardening and the yield and ultimate stress of each material was summarized in Table 6.1. The bolt pretension forces for the column bolts were set at 316 kN (71 kips) and for the beam bolts at 125 kN (28 kips), based on values provided in the Steel Construction Manual (AISC, 2017). The contact interaction between the bolts, the connection angles, the beam, and the column were defined using a “hard” contact interaction for perpendicular interactions and with a friction interaction for tangential interactions. The friction coefficient was set at 0.30

for steel to steel interactions. The FEM model was modeled based on the laboratory test setup described in Chapter 5. Therefore, the same boundary conditions were defined. However, the column brace from the test setup was modeled using “node to ground” springs with the spring stiffnesses calculated based on the stiffness of the brace in all three global directions ( $k_x$ ,  $k_y$ , and  $k_z$ ).

The created FEM was validated using the laboratory test setup results described in Section 5.4 for axial load, strong axis moment, and weak axis moment. The FEM and the test setup results for the axial load test were within 12%. However, the results for the vertical load test and the horizontal load test were within 90% and 40%, respectively. These big differences in stresses were attributed to the differences in the beam bolt pre-tension loads and the differences in the friction coefficient between the FEM and the laboratory setup as described in Section 6.2.4. However, the FEM bolt loads and friction coefficient were not changed relative to the preliminary values when applying the FEA model to other loading scenarios, since these preliminary values were most likely observed in a connection in a steel building.

After the FEM was validated, it was used to extrapolate field stress data, collected during the Purnell Hall Addition instrumentation, to assess the maximum stresses in a connection during construction. The FEM was a replica of one of the connections instrumented for the Purnell Hall Addition. Therefore, the maximum and minimum strain gauge field data of said connection were found and the best fit between the field data and FEM results at the same location were chosen using the process described in Figure 6.19. The FEM with the best fit was used to find maximum stresses during the construction process of the Purnell Hall Addition in the instrumented connection area. The maximum von Mises stress in the FEM of the beam

was 176 MPa (25.5 ksi) and the maximum absolute principal stress was 216 MPa (31.4 ksi). Both of these values were lower than the yield stress of 345 MPa (50 ksi) of the instrumented steel beam by 37%. Therefore, the connection area did not yield during the construction phase of the Purnell Hall Addition and could be included when reusing the beam in the future.

## **Chapter 7**

### **SUMMARY AND CONCLUSIONS**

#### **7.1 Summary**

To assess the reuse capability of structural steel members, 13 steel members in three different steel framed buildings were instrumented using strain gauges. The collected strain data was processed and analyzed for potential yielding of the instrumented locations (i.e. local yielding of the steel at the strain gauge location). Member forces were calculated and combined to assess if a steel member may be likely to fail by combinations of yielding and buckling due to combined member forces. Furthermore, a CNT-based sensor was installed on one of the steel members to show that this type of sensors can be installed in the field to infer strain. Sensing skin data was collected and compared to strain gauge data from the same connection area.

To quantify stresses in connections, a finite element model of one of the instrumented beam-to-column connections was created and validated using a laboratory test setup. The laboratory test setup was a replica of the instrumented beam-to-column connection from the field. Once the finite element model was validated it was used to extrapolate strain gauge field data collected in the vicinity of the connection to assess if parts of the connection yielded during the construction process.

##### **7.1.1 Field Data Summary**

A total of 13 structural steel members, in three different buildings (Purnell Hall Addition, STAR Tower, and BPI Building) were instrumented at the steel fabrication

location before the steel members were installed in the buildings. For the field instrumentation, a wireless sensor network was connected to 40 strain gauges per building and a novel CNT-based sensor in one of the building (BPI Building). Continuous strain and temperature data were collected using the strain gauges and temperature sensors located in the WSN nodes. For all three buildings a total of 3 billion strain and 744 million temperature data points were collected.

The collected data was processed, zeroed, converted to stress, and categorized into impact and sustained stress values. The absolute maximum stress value was 160 MPa (-23.2 ksi) at the top of the Short Column of the Purnell Hall Addition. This value was 46.4 % of the yield stress of 345 MPa (50 ksi) for the instrumented steel member.

The calculated member forces (axial force, strong and weak axis bending) for the three buildings were calculated using two approaches. One approach used data from three strain gauges, located in the same cross section of a member, and solid mechanics principles to calculate the member forces. The second approach used an optimization process and data from at least seven strain gauges to calculate the member forces. The two methods were labeled “three-gauge” approach and the “optimization” approach and were discussed in more detail in Section 3.2.5.

The calculated maximum axial force was a compression force of -1690 kN (-380 kip) in the 1<sup>st</sup> Floor Column of the BPI Building. The maximum strong axis bending moment was 203 kNm (150 kip\*ft) at midspan of the STAR Tower girder. The weak axis moments were smaller than the strong axis moments, the maximum weak axis moment was 42.0 kNm (31 kip\*ft) and calculated for the 1<sup>st</sup> Floor Column of the BPI Building. However, unexpected bending moments in the columns were

recorded. The higher than expected moments could be due to eccentric loading of the columns during the construction process or temperature influence in the field data.

The calculated member forces were evaluated using the AISC Steel Construction Manual (AISC, 2017), Chapter H with modifications to assess yielding. The maximum combination of member forces for each gauge set was found as well as the yield capacity for each steel member. The maximum values were found to be 0.55 for the Purnell Hall Addition data, 0.32 for STAR Tower data, and 0.30 for the BPI Building. All ratios were below 1.0 and therefore indicated that the members did not experience any yielding during the construction phase.

### **7.1.2 Carbon Nanotube-Based Sensor Summary**

Carbon nanotube-based sensors with multiple electrodes have not been used previously in the field for structural engineering applications. Therefore, this project was used to prove the concept of installing pre-manufactured CNT-based sensors in the field (not under laboratory conditions) and to collect data from the sensor via a commercially available WSN.

To collect strain data in the connection area of a steel member, a sensing skin was bonded to the 6<sup>th</sup> Floor Girder of the BPI Building at the steel fabricator's facilities. The instrumented girder was installed in the BPI Building and two sets of data were collected. The collected data was assessed and compared to strain gauge data that was collected in the same connection area on the opposite side of the web of the sensing skin.

This project established the possibility of installing CNT-based sensors with multiple electrodes in the field to a steel member without laboratory conditions. Furthermore, the voltage measurement data had a lower noise content than the

commercially bought strain gauges which was unexpected but positive. Furthermore, the collected voltage data recorded a data event at the same time as the strain gauges did, showing the monitoring capabilities of the sensing skin. Also, the sensing skin showed different voltage measurements during the data events at different electrode locations, showing the capability of the sensing skin to capture distributed strain behavior in a connection area.

### **7.1.3 Laboratory Test Setup Summary**

To validate the finite element model of a connection area, a full-scale laboratory test setup was created. For the test setup, one of the instrumented connections of the Purnell Hall Addition was replicated and densely instrumented. The selected connection was a beam-to-column connection that used two angles as shear connectors. The test setup was instrumented using 20 uniaxial strain gauges, two 45° strain rosettes, and 7 displacement sensors with most of the strain gauges located in the connection area of the test setup. Furthermore, a CNT-based sensor was installed on the beam in the connection area. The test setup was tested using three loading configurations. First, axial compression and tension loads were applied using a horizontal hydraulic actuator. Second, strong axis bending moment was applied using a manual hydraulic jack, and third, weak axis moment was applied using the same manual hydraulic jack.

The collected data was compared to theoretically calculated values using simple solid mechanics equations. It was found that the collected strain data compared well to the theoretical values at midspan of the beam (762 mm (2 ft. 6 in.) away from the connection). However, strain gauge data from the connection area was higher for all load test data compared to the theoretically calculated values.

These test results confirmed that stresses in connection areas cannot be calculated using conventional solid mechanics equations. Therefore, it was necessary to use a finite element model to extrapolate construction stresses into a connection area. Furthermore, using the test data of the full-scale test to validate the finite element results was a viable option.

#### **7.1.4 Finite Element Analysis Summary**

To quantify stresses in the connection area of a steel member, a three-dimensional finite element model was created using ABAQUS. The FEM was modeled using four individual parts (one beam, one column, and two connection angles) comprised of solid elements that were connected using seven modeled bolts (three beam bolts and four column bolts), bolt pretension forces and contact interactions. The material for each part was defined as elastic-plastic with strain hardening. Furthermore, bolt pretension forces in the column and beam bolts in combination with contact interaction between the bolts, the connection angles, the beam, and the column were used to model the FEM connection.

The created FEM was validated using the laboratory test setup results for axial load, strong axis moment, and weak axis moment. The FEM and the laboratory test setup results for the axial load test were within 12%. However, the results for the strong axis load test and the weak axis load test were within 90% and 40%, respectively. The differences between the FEM and lab setup data for the strong axis and the weak axis load tests were attributed to differences in bolt pretension forces between the FEM and the laboratory test setup as well to an unknown friction coefficient for the laboratory test setup connection due to the presence of the sensing skin. The pretension force and the friction coefficient in the FEM were adjusted to get

a better fit between the FEM and the test setup to confirm the model was valid. However, values used in the FEM were those most likely to occur during construction of a building.

After the FEM was validated, it was used to extrapolate stresses (in the Purnell Hall Addition) to more locations than feasible to physically instrument, to assess the maximum stresses in a connection during construction. The FEM was a replica of one of the connections instrumented for the Purnell Hall Addition. The FEM with the best fit (between field data and FEM results) was used to find maximum stresses during the construction process of the Purnell Hall Addition in the instrumented connection area. The maximum von Mises stress in the FEM of the beam was 176 MPa (25.5 ksi). This value was lower than the yield stress of 345 MPa (50 ksi) of the instrumented steel beam by 49%. Therefore, the connection area did not yield during the construction phase of the Purnell Hall Addition and could be included with confidence when reusing the beam in the future.

## **7.2 Conclusions**

Based on the collected field data (from strain gauge data and CNT-based sensor data), the results from the laboratory test setup, and the analytical results from the finite element model, the following conclusions were drawn:

- The overall maximum absolute impact stress was 149 MPa (21.6 ksi), in G34 in the connection area of the 6<sup>th</sup> Floor Girder of the BPI Building.
- The overall maximum absolute sustained value was 160 MPa (23.2 ksi) at the top of the Short Column of the Purnell Hall Addition. This value was 46.4 % of the yield stress of 345 MPa (50 ksi) for the instrumented steel member.

Therefore, it can be concluded that none of the instrumented areas reached yielding.

- The maximum absolute principal stress in the FEM was 216 MPa (31.4 ksi) and therefore lower than the yield stress of 345 MPa (50 ksi) of the instrumented steel beam by 37%. Therefore, the connection area did not yield during the construction phase of the Purnell Hall Addition and could be included when reusing the beam in the future.
- The field data of the Purnell Hall Addition were also analyzed by construction phases, with three phases categorized as pre-concrete, during-concrete, and post-concrete. This showed that, as expected, the stresses were generally increasing and the variability in stress was generally decreasing throughout construction.
- The maximum axial compression and tension forces were recorded in the BPI Building columns. The maximum compression force of -1690 kN (-380 kip) was calculated for 1<sup>st</sup> Floor Column of the BPI Building and the maximum tension force of 296 kN (49.5 kip) for the 5<sup>th</sup> Floor column of the BPI Building.
- The maximum strong axis bending moment was 203 kNm (150 kip\*ft) at the center of the STAR Tower girder. And the maximum weak axis moment was 42.0 kNm (31 kip\*ft) and calculated for the 1<sup>st</sup> Floor Column of the BPI Building.
- Combined member forces at each gauge set, using (AISC, 2017) calculations that were modified to use yield capacity limits instead of plastic limits, showed that the member capacity for combined force effects was not reached in any

combination. All ratios were below 1.0 which indicated that none of the instrumented steel members were compromised for reuse during the construction phase.

- A test setup was created to validate the finite element model of a connection in the Purnell Hall Addition. The test results from the laboratory test setup proved that stresses in connection areas cannot be calculated using conventional solid mechanics equations.
- The finite element model was validated using laboratory test results. It was shown that bolt pretension loads and friction coefficient had an immense influence on the finite element results.

### **7.3 Lessons Learned**

The following lessons were learned during the instrumentation of the three steel buildings. This section was split into two subsections. The first subsection (7.3.1) lists things that were instrumental to the success of the instrumentation project that were implemented by the researchers. The second subsection (7.3.2) lists items that were implemented by the researchers during the project on short notice or that were learned in hindsight.

#### **7.3.1 Instrumental Steps Taken for the Building Instrumentation**

- Things to consider when selecting a building for instrumentation:
  - Building owner knows exactly what is planned for the instrumentation and what data will be collected.
  - Building owner agrees completely with planned instrumentation.
  - Building is located in close proximity for quick troubleshooting.

- Communicate with the construction company early:
  - Make sure project managers know all stages of the instrumentation.
  - The more information the project managers know, the better they can assist you.
  - Talk to the construction company about access to the building site.
  - Always make sure the construction company knows when you are onsite.
  - Safety is top priority for construction companies. Always keep this in mind.
- Communicate with the steel fabricator early:
  - Make sure steel fabricator knows the selected steel members to set aside after fabrication.
  - Talk to the steel fabricator about where the beams can be instrumented and the expected time involved for instrumentation.
- Communicate with the erection company early:
  - Make sure they know what is on the steel members (WSN nodes, wires, strain gauges).
  - Ask them for consent that they are in pictures.
- Thing to consider for the data collection laptop, the data collection beacon, and the camera:
  - Must have access to electricity.
  - Must be protected from weather.
  - Data collection beacon should be placed as close as possible to the instrumented steel members. The erected steel members surrounding

- the instrumented steel members interfere with the wireless signal of the WSN reducing the range of the WSN greatly.
- Data collection laptop should be connected to the internet for remote connection.
  - Talk to construction company about possible locations in the jobsite trailer or on the building site.
  - Camera and data collection beacon should be connected to the same laptop to avoid timestamp differences.
  - Make sure the wireless sensor nodes connect to the data collection beacon:
    - Wireless range provided by WSN manufacturer is usually measured without any obstacles blocking the signal.
    - Test the WSN range in existing buildings (with obstacles) to obtain a more accurate range estimate.
    - Test the WSN at the building site of the instrument building. Connect a wireless node to the beacon in the area where the instrumented steel members will be located and check the wireless signal.
    - Building steel members reduce the WSN range significantly.
    - Cold weather can significantly decrease the battery life in your WSN nodes. During the Purnell Hall instrumentation, one set of batteries was used to collect data during the entire project (two month of data collection). For the BPI Building project, multiple battery sets were used due to temperature and due to the big distance between the data collection beacon and the longer distance between the data collection beacon and the WSN nodes.

- If sensors don't connect to the data collection beacon, consider changing the location of the beacon or if possible, change the selected steel members to a member that is located in a more favorable position relative to the data collection beacon.
- Things to consider for the steel member instrumentation:
  - Keep the instrumentation equipment protected by placing it on the web and the inside flanges of W-sections.
  - Run instrumentation wires along the top fillet of the W-sections to keep the wires protected when steel workers walk on web or on flanges during steel installation.
  - The three gauge layout used for the instrumentation resulted in good results when torsion was low. Using more than three strain gauges in a cross section resulted in additional valuable information (with respect to torsion, temperature, and neutral axis).
  - Rosette strain gauges provide valuable information a specific point. However, since strain rosettes need three strain gauges in a very small area it could be argued that the rosettes be replaced by one strain gauge at the specified location and the other two strain gauges moved to other location.

### **7.3.2 Lessons Learned After the Instrumentation**

- During the time when the steel members are delivered to the building site and put in place, it is important to be on site to immediately deal with occurring problems. This will assure continuous data collection during the erection process.

- Construction site access should be granted during the time when the steel members are erected to record the exact process.
- The construction site camera should record everything that is happening in the area of the instrumented members (i.e. local events) and everything that is happening on the entire construction site (i.e. global events). This might require multiple construction site cameras for best results.
- Construction site camera and WSN should be synced to the same time to optimize correlation between data events and images.
- A WSN could be considered where the data is saved to the WSN nodes (local SD card) and collected sporadically (by the user) instead of a WSN where the data is transmitted continuously to a data collection laptop. This would avoid the need of constant connectivity between the data collection laptop and the WSN nodes.

#### **7.4 Future work**

To fully understand the collected field data and to further reduce the concerns of structural design engineers about reuse of complete structural steel members the following topics should be included in future research:

- Even though a significant time of this research project was spent on temperature influence on the collected field data, more research should be performed in this area. The collected field data should be compared to data from a laboratory test specimen that experienced known thermal loads.
- High axial forces were recorded in horizontal steel members. The axial force was most likely due to temperature and therefore, the influence of

temperature on axial forces during the construction phase of a building should be looked at further.

- Data should be collected periodically during the service life of the BPI Building to assess if any of the instrument steel members yield during their service life to ensure their reuse capability.
- More finite element models of different building connections should be modeled and analyzed for yielding using the collected field data.
- This research used the elastic limit (i.e. yield stress) as upper limit to evaluate if a steel member can be reused. However, it is assumed that localized yielding would not greatly impact the reuse potential of a steel member. This hypothesis should be further analyzed to increase the reusability potential of structural steel members.

## REFERENCES

- ABAQUS. (2015a). Dassault Systems Simulia Corp., Providence.
- ABAQUS. (2015b). *Analysis user's manual v6.14*. Dassault Systems Simulia Corp., Providence, USA.
- Ahmed, A., Kishi, N., Matsuoka, K., and Komuro, M. (2001). "Nonlinear Analysis on Prying of Top-and Seat-Angle Connections." *Journal of applied mechanics*, 4, 227–236.
- American Institute of Steel Construction (AISC). (2012). *Structural Steel: An Industry Overview*. 12.
- American Institute of Steel Construction (AISC). (2017). *Manual of Steel Construction*. Chicago, IL.
- American Iron and Steel Institute (AISI). (2018). *Profile 2018*. 40.
- ASCE/Structural Engineering Institute (ASCE/SEI). (2016). *Minimum design loads for buildings and other structures*. ASCE/SEI 7-16, ASCE, Reston, VA.
- ASTM A325-14. (2014). *Standard Specification for Structural Bolts, Steel, Heat Treated, 120/105 ksi Minimum Tensile Strength (Withdrawn 2016)*. ASTM International, West Conshohocken, PA.
- Barth, K. E., White, D. W., Righman, J. E., and Yang, L. (2005). "Evaluation of web compactness limits for singly and doubly symmetric steel I-girders." *Journal of Constructional Steel Research*, 61(10), 1411–1434.
- Brimacombe, L., Coleman, N., and Honess, C. (2005). "Recycling, reuse and the sustainability of steel." *Millenium Steel*, (446), 3–7.
- Bursi, O. S., and Jaspart, J. P. (1998). "Basic issues in the Finite element simulation of extended end plate connections." *Computers and Structures*, 22.
- Chou, T.-W., Gao, L., Thostenson, E. T., Zhang, Z., and Byun, J.-H. (2010). "An assessment of the science and technology of carbon nanotube-based fibers and composites." *Composites Science and Technology*, 70(1), 1–19.

- Citipitioglu, A. M., Haj-Ali, R. M., and White, D. W. (2002). "Refined 3D finite element modeling of partially-restrained connections including slip." *Journal of Constructional Steel Research*, 58(5–8), 995–1013.
- Cooper, D. R., and Gutowski, T. G. (2017). "The Environmental Impacts of Reuse: A Review: The Environmental Impacts of Reuse: A Review." *Journal of Industrial Ecology*, 21(1), 38–56.
- Dai, H., Gallo, G. J., Schumacher, T., and Thostenson, E. T. (2016). "A Novel Methodology for Spatial Damage Detection and Imaging Using a Distributed Carbon Nanotube-Based Composite Sensor Combined with Electrical Impedance Tomography." *Journal of Nondestructive Evaluation*, 35(2).
- Dai, H., Thostenson, E., and Schumacher, T. (2015). "Processing and Characterization of a Novel Distributed Strain Sensor Using Carbon Nanotube-Based Nonwoven Composites." *Sensors*, 15(7), 17728–17747.
- Densley Tingley, D., Cooper, S., and Cullen, J. (2017). "Understanding and overcoming the barriers to structural steel reuse, a UK perspective." *Journal of Cleaner Production*, 148, 642–652.
- Dunant, C. F., Drewniok, M. P., Sansom, M., Corbey, S., Allwood, J. M., and Cullen, J. M. (2017). "Real and perceived barriers to steel reuse across the UK construction value chain." *Resources, Conservation and Recycling*, 126, 118–131.
- Eckelman, M. J., Brown, C., Troup, L. N., Wang, L., Webster, M. D., and Hajjar, J. F. (2018). "Life cycle energy and environmental benefits of novel design-for-deconstruction structural systems in steel buildings." *Building and Environment*, 143, 421–430.
- Fujita, M., and Iwata, M. (2008). "Reuse system of building steel structures." *Structure and Infrastructure Engineering*, 4(3), 207–220.
- Gallo, G. J., and Thostenson, E. T. (2016). "Spatial damage detection in electrically anisotropic fiber-reinforced composites using carbon nanotube networks." *Composite Structures*, 141, 14–23.
- Gorgolewski, D. M., Straka, V., Edmonds, J., and Sergio, C. (2006). *Facilitating Greater Reuse and Recycling of Structural Steel in the Construction and Demolition Process*. Final Report, Canadian Institute of Steel Construction and Ryerson University, Toronto, 112.

- Green, P., Sputo, T., and Higgins, A. (2005). "Design of All-Bolted Extended Double Angle, Single Angle, And Tee Shear Connections." 430.
- Hantouche, E. G., and Sleiman, S. A. (2016). "Response of double angle and shear endplate connections at elevated temperatures." *International Journal of Steel Structures*, 16(2), 489–504.
- Iijima, S. (1991). "Helical microtubules of graphitic carbon." *Nature*, 354(6348), 56–58.
- Keller, P., McConnell, J., Schumacher, T., and Thostenson, E. T. (2019). "Construction Stress Monitoring using a Wireless Sensor Network to Evaluate Reuse Potential of Structural Steel." *Journal of Structural Engineering*.
- Kishi, N., Ahmed, A., Yabuki, N., and Chen, W. F. (2001). "Nonlinear finite element analysis of top- and seat-angle with double web-angle connections." *Structural Engineering and Mechanics*, 12(2), 201–214.
- Matis, P., Martin, A., McGetrick, P., and Robinson, D. (2018a). "Modelling and experimental testing of interlocking steel connection behaviour." *Life Cycle Analysis and Assessment in Civil Engineering: Towards an Integrated Vision: Proceedings of the Sixth International Symposium on Life-Cycle Civil Engineering (IALCCE 2018), 28-31 October 2018, Ghent, Belgium*.
- Matis, P., Martin, A., Robinson, D., and McGetrick, P. (2018b). "The effect of frictional contact properties on intermeshed steel connections." *Civil Engineering Research in Ireland 2018 conference (CERI 2018)*, Civil Engineering Research Association of Ireland, 547–553.
- MATLAB and Global Optimization Toolbox Release 2017b*. (n.d.). The MathWorks, Inc., Natick, MA.
- McBrien, M., Serrenho, A. C., and Allwood, J. M. (2016). "Potential for energy savings by heat recovery in an integrated steel supply chain." *Applied Thermal Engineering*, 103, 592–606.
- McConnell, J., Schumacher, T., Thostenson, E. T., Wennick, T., and Keller, P. (2014). "Evaluating Structural Steel for Reuse through Field Monitoring." *IABSE Symposium Report*, International Association for Bridge and Structural Engineering, 3174–3181.
- National Oceanic and Atmospheric Administration (NOAA). (2019). "2018 was 4th hottest year on record for the globe." <<https://www.noaa.gov/news/2018-was-4th-hottest-year-on-record-for-globe>> (Feb. 12, 2019).

- New Steel Construction. (2010). "The carbon footprint of steel." *newsteelconstruction.com*.
- Pirmoz, A., Daryan, A. S., Mazaheri, A., and Darbandi, H. E. (2008). "Behavior of bolted angle connections subjected to combined shear force and moment." *Journal of Constructional Steel Research*, 64(4), 436–446.
- Pongiglione, M., and Calderini, C. (2014). "Material savings through structural steel reuse: A case study in Genoa." *Resources, Conservation and Recycling*, 86, 87–92.
- Quayyum, S., and Hassan, T. (2017). "Initial Residual Stresses in Hot-Rolled Wide-Flange Shapes: A Computational Technique and Influence on Structural Performances." *Journal of Structural Engineering*, 143(5), 04017013.
- Saedi Daryan, A., and Yahyai, M. (2009). "Modeling of bolted angle connections in fire." *Fire Safety Journal*, 44(7), 976–988.
- Schumacher, T., and Thostenson, E. T. (2014). "Development of structural carbon nanotube-based sensing composites for concrete structures." *Journal of Intelligent Material Systems and Structures*, 25(11), 1331–1339.
- Seaburg, P. A., and Carter, C. J. (2003). *AISC Steel Design Guide Series #9, Torsional Analysis of Structural Steel Members*. American Institute of Steel Construction, Chicago, IL.
- Shi, G., Shi, Y., Wang, Y., and Bradford, M. A. (2008). "Numerical simulation of steel pretensioned bolted end-plate connections of different types and details." *Engineering Structures*, 30(10), 2677–2686.
- STAAD.Pro*. (8i). Bentley Systems, Inc., Exton, PA.
- Steel Recycling Institute. (2015). "Waste in Place Fact Sheet." Keep America Beautiful, Inc.
- Swanson, J. A., Kokan, D. S., and Leon, R. T. (2002). "Advanced finite element modeling of bolted T-stub connection components." *Journal of Constructional Steel Research*, 58(5–8), 1015–1031.
- Takhirov, S. M., and Popov, E. P. (2002). "Bolted large seismic steel beam-to-column connections Part 2: numerical nonlinear analysis." *Engineering Structures*, 24(12), 1535–1545.

- Themelis, N. J., and Mussche, C. (2014). “2014 ENERGY AND ECONOMIC VALUE OF MUNICIPAL SOLID WASTE (MSW), INCLUDING NON-RECYCLED PLASTICS (NRP), CURRENTLY LANDFILLED IN THE FIFTY STATES.” 40.
- Thostenson, E. T., and Chou, T.-W. (2006). “Carbon Nanotube Networks: Sensing of Distributed Strain and Damage for Life Prediction and Self Healing.” *Advanced Materials*, 18(21), 2837–2841.
- Thostenson, E. T., Ren, Z., and Chou, T.-W. (2001). “Advances in the science and technology of carbon nanotubes and their composites: a review.” *Composites Science and Technology*, 61(13), 1899–1912.
- Trutor, B. (2013). “Measuring Voltages Above 3 Volts.” LORD Corporation.
- U.S. Department of Energy Industrial Technologies Program. (2008). *Waste Heat Recovery: Technology and Opportunities in U.S. Industry*. 112.
- U.S. Environmental Protection Agency (USEPA). (2018). *Inventory of U.S. Greenhouse Gas Emissions and Sinks: 1990 -2016*. 655.
- U.S. Green Building Council (USGBC). (2018). *LEED v4 for Building Design and Construction*. USGBC, Washington, D.C.
- USEPA, O. (2016). “Climate Change Indicators: U.S. Greenhouse Gas Emissions.” *US EPA, Reports and Assessments*, <<https://www.epa.gov/climate-indicators/climate-change-indicators-us-greenhouse-gas-emissions>> (Feb. 9, 2019).
- Wang, L., Webster, M. D., and Hajjar, J. F. (2019). “Pushout tests on deconstructable steel-concrete shear connections in sustainable composite beams.” *Journal of Constructional Steel Research*, 153, 618–637.
- Webster, M. D., Meryman, H., Slivers, A., Rodriguez-Nikl, T., Lemay, L., Simonen, K., Trivedi, H., Maclise, L., Kestner, D., Bland, K., Lee, W., and Lorenz, E. (2012). *Structure and Carbon – How Materials Affect the Climate*. SEI Sustainability Committee; Carbon Working Group, 75.
- Weigand, J. M., Liu, J., and Main, J. A. (2016). “Modeling of Double-Angle Connections for Robustness Evaluation of Steel Gravity Frames.” *International Workshop on Connections in Steel Structures 2016*, Boston, MA, 10.

- Weisenberger, G. (2010). "The Fabrication Factor." *Modern Steel Construction*, 50, 56–57.
- Wennick, T. (2016). "Measuring Strains During Construction of a Steel Building using a Wireless Sensor Network." University of Delaware, Newark, DE.
- Winters-Downey, E. (2010). "Reclaimed Structural Steel and LEED Credit MR 3 – Materials Reuse." 3.
- Yellishetty, M., Mudd, G. M., Ranjith, P. G., and Tharumarajah, A. (2011). "Environmental life-cycle comparisons of steel production and recycling: sustainability issues, problems and prospects." *Environmental Science & Policy*, 14(6), 650–663.
- Yeung, J., Walbridge, S., and Haas, C. (2015). "The role of geometric characterization in supporting structural steel reuse decisions." *Resources, Conservation and Recycling*, 104, 120–130.

**Appendix**

**COPYRIGHT RELEASE FORM FOR USED FIGURES**

**GHGInventory** <ghginventory@epa.gov>  
To: "phkeller@udel.edu" <phkeller@udel.edu>

Mon, Feb 11, 2019 at 2:21 PM

Dear Philipp,

Thank you for your interest in the U.S. Greenhouse Gas Inventory. The Inventory document is a publicly available document and free to use for your dissertation. We ask though that you provide attribution to EPA for your reference.

To reference the Inventory report, it is best to cite the U.S. Environmental Protection Agency as the author. The Inventory documents posted on the EPA website have date stamps associated with them and would be the appropriate publication dates for citing: <https://www.epa.gov/ghgemissions/inventory-us-greenhouse-gas-emissions-and-sinks-1990-2016>. We appreciate use of the appropriate citation style for government websites using MLA, APA, Chicago style, etc. as applicable.

In addition, some charts and tables are also available at the following website: <https://www3.epa.gov/climatechange/ghgemissions/inventoryexplorer/>

Thank you

John Steller  
U.S. Greenhouse Gas Inventory Team

--

Submitted on 02/11/2019 12:56PM  
Submitted values are:

Name: Philipp Keller  
Email Address: [phkeller@udel.edu](mailto:phkeller@udel.edu)  
Comments:  
Hi there,

My name is Philipp Keller and I am a PhD student at the University of Delaware. I'm currently writing my dissertation and I would like to use some of the figures published in the following report:

Inventory of U.S. Greenhouse Gas Emissions and Sinks: 1990 -2016

I couldn't find any copyright information in the report and was wondering if you have any information on how I can get permission to use these figures.

Thank you very much for your time and your help!

Best regards,  
Philipp Keller

Figure A.1: Copyright release for all figures from (U.S. Environmental Protection Agency (USEPA) 2018)



INFORMATION SHEET FOR REQUESTS TO PRINT/REPRINT COPYRIGHTED MATERIALS

(PLEASE SUBMIT AN INFORMATION SHEET FOR EACH GRAPHIC OR WRITTEN WORK FOR WHICH PRINTING/REPRINTING PERMISSION IS REQUESTED)

Name of party requesting reprint permission Philipp Keller

Date of Request: 02/08/2019

Type of Business: University of Delaware

Address: 281 Dupont Hall, Newark, DE 19716

Contact: Philipp Keller Contact Title: Mr.

Phone: 541-250-2336 Fax: - E-mail: phkeller@udel.edu

What graphic, figure or written material do you seek permission to print/reprint? (provide specific information including source of original material, page number, and attach a copy of the actual material intended for use):

From: Profile 2018, 2017 Steel Shipments\* by Market Classification  
in F. 8

Name of publication for which reprint/publishing permission is requested (include page if applicable, publisher, intended date, length of use):

Doctoral dissertation submitted to the University of Delaware

Description\* of intended use of the material you request to reprint/publish (specify for example, educational publication, website, etc.):

Educational publication (Dissertation)

I hereby certify and confirm that the information provided herein is true and accurate.

Signature: [Signature]  
Name: Philipp Keller  
Title: \_\_\_\_\_  
Date: 02/08/2019

AISI Approval:  
Signature: [Signature]  
Name: JIMMY GILL  
Title: CHIEF ECONOMIST  
Date: 2/11/19

Figure A.2: Copyright release form for Figure 1.4 (AISI, 2018)